



# Resonant Piezoelectric Shunt Damping of Structures

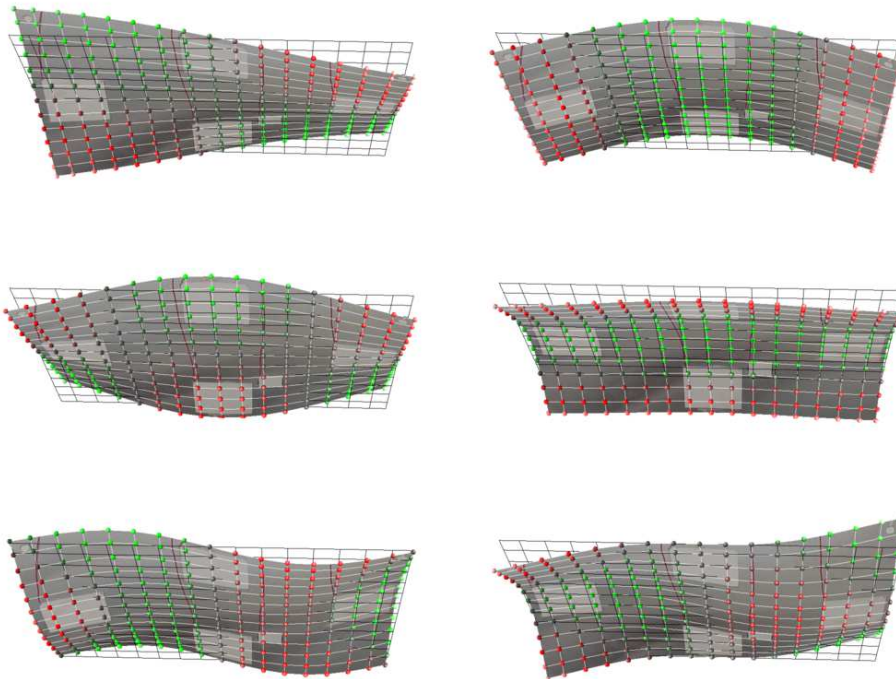
Johan Frederik Toftekær

PhD Thesis



# Resonant Piezoelectric Shunt Damping of Structures

Johan Frederik Toftekær



DEPARTMENT OF MECHANICAL ENGINEERING  
SECTION OF SOLID MECHANICS  
TECHNICAL UNIVERSITY OF DENMARK  
SEPTEMBER 2019

Section of Solid Mechanics  
Department of Mechanical Engineering  
Technical University of Denmark  
Nils Koppels Allé, Building 404  
DK-2800 Kongens Lyngby,  
Denmark

# PREFACE

This thesis is submitted in partial fulfilment of the Ph.D. degree from the Technical University of Denmark (DTU). The work has been carried out at the Section of Solid Mechanics, Department of Mechanical Engineering at DTU and during a five month stay in France at Supmèca in Paris and the University of Technology of Compiègne. The work has been performed in the period of October 2016 to september 2019 under the supervision of main supervisor Associate Professor Jan Høgsberg and co-supervisors Professor Dr. Techn. Steen Krenk and Professor Ayech Benjeddou.

I would like to thank Jan Høgsberg for his great support and for being a source of inspiration since I began my studies at DTU more than eight years ago. Furthermore, I would like to thank him for granting me a lot of freedom during the Ph.D. project, while still being very engaged in my day to day work. I would like to express me deep gratitude to Ayech Benjeddou for being so welcoming during my stay in France and for his untiring proof reading and help with writing papers, preparing presentations and understanding the properties of piezoelectric materials. I also owe my deep gratitude to Steen Krenk for supervising me during my master thesis at DTU, for always taking his time to assist me during the Ph.D. and for being the one who introduced me to the world of research.

I want to thank all of my present and former colleagues in the Section of Solid Mechanics at DTU. I have truly enjoyed the international work environment and the great social life, which has made it a pleasure to come to the office and to stay long hours. I am grateful to the people I have shared office with during my Ph.D. and a special thank you to Morten Andersen for proofreading parts of this thesis and in general for always being helpful. I would also like to thank my colleagues in France, who quickly included me in their lives and social activities.

On a personal level, I would like to thank my family and girlfriend for always supporting me during the Ph.D. and my parents for never putting pressure on me, but still motivating me in achieving my goals. Finally, a very special thank you to my girlfriend Lina who moved to Denmark for me and endured me during the three years of Ph.D., by being supportive and by always believing in me.

Kongens Lyngby, September 2019



Johan Frederik Toftekær



# ABSTRACT

Excessive resonance vibrations of large civil engineering structures are effectively mitigated by the resonant mechanical absorber, while the damping of medium to small sized structures may be mitigated more efficiently by the electromechanical absorber. The latter is often designed as a pair of electrically shunted piezoceramic patches glued directly to the vibrating structure. Mechanical energy is hereby converted into electrical energy which is led in to the shunt consisting of an inductance tuned to secure a maximum energy dissipation in an electric resistance.

The present thesis concerns numerical modeling of piezoelectric absorbers bonded to general plate-like structures and the derivation of a precise shunt tuning procedure, which is practical in terms of numerical and experimental implementation. The thesis is organized in three parts, respectively, covering the development of a numerical model, the derivation of optimum shunt tuning and the experimental implementation, wherein a beam and a plate example are used throughout the thesis to validate the numerical models and proposed tuning methods.

In the first part, a numerical model describing general plate-like structures with pairs of co-located piezoceramic patches is developed. As the piezoceramic patch bonded to a plate surface mainly influences the plate vibration through the moments generated by the in-plane patch deformations, a plane stress-reduction of the full piezoceramic properties is introduced. Subsequently, the electrode equipotentiality and electric wiring of the piezoceramic patches are modeled and a governing vibration problem is obtained. The same vibration problem is governing in a commercial finite element program and two eigenvalue problems associated with the short and open circuit (SC and OC) piezoelectric absorbers are then considered to determine the effective electromechanical coupling of the considered beam and plate examples.

In the second part, a modal representation of the mechanical displacements in the governing vibration problem is introduced, whereby the mechanical equations uncouple. However, because of the piezoelectric shunt the electric domain couples the modal equations. An approximation of the contribution from the non-resonant vibration modes is therefore introduced by an additional term to the inherent piezoelectric capacitance. This additional correction term is determined from the solution to the SC and OC eigenvalue problems, while a third eigenvalue problem may be evaluated to determine a specific non-resonant inertia effect. This method is implemented in the developed numerical model and in a commercial finite element program, whereby single- and multi-mode tuning of multiple piezoelectric absorbers are demonstrated for the considered beam and plate examples.

In the final part, the proposed shunt tuning procedure is shown suitable for experimental implementation, where it requires the acquisition of two absorber response in the SC and OC limits. Good correlation between the numerical and experimental results and shunt tuning is demonstrated for the beam and plate examples and it is shown that the omission of the non-resonant modes contribution leads to detuning of the absorbers and reductions in the attainable damping.



# RESUMÉ

Resonante svingninger i store konstruktioner er effektivt dæmpet ved brugen af resonante mekaniske dæmpere, mens dæmpning af mellemstore til små konstruktioner dæmpes mere effektivt med den elektromekaniske dæmper. Sidstnævnte er ofte designet som et par af piezokeramiske skiver tilsluttet en elektrisk shunt og limet direkte på den svingende konstruktion. Mekanisk energi omdannes herved til elektrisk energi, der føres ind i den elektriske shunt, som består af en induktans tunet til at sikre en maksimal energiafsætning i en elektrisk modstand.

Denne afhandling omhandler numerisk modellering af piezoelektriske dæmpere fastgjort til generelle plade konstruktioner og udledningen af en præcis metode for den optimale shunt-tuning, som er praktisk med hensyn til numerisk og eksperimentel implementering. Afhandlingen er organiseret i tre dele som dækker over udviklingen af en numerisk model, udledningen af optimal shunt-tuning og eksperimentel implementering, et bjælke- og plade eksempel er brugt gennem afhandlingen til at validere de numeriske modeller og den foreslåede shunt-tuning.

Den første del adresserer udviklingen af en numerisk model, der beskriver generelle plade konstruktioner med par af piezokeramiske skiver. En plan spændingsreduktion af de fulde piezokeramiske egenskaber er benyttet, idet den piezokeramiske skive limet til en pladeoverflade hovedsageligt influerer pladens bøjningssvingninger gennem de plane skive deformationer. Derefter er den piezoelektriske elektrode og de elektriske forbindelser af de piezokeramiske skiver modelleret, hvorved et styrende vibrationsproblem er opnået. Det samme vibrationsproblem er styrende i et kommercielt element metode program, hvorved to tilhørende egenverdiproblemer for kortsluttede- og åbne piezoelektriske kredsløb (SC og OC) er betragtet til bestemmelsen af den effektive elektromekaniske kobling for bjælke- og plade eksemplerne.

I den anden del indføres en modal repræsentation af de mekaniske frihedsgrader i det generelle vibrationsproblem, hvorved de mekaniske ligninger afkobles, mens de modale ligninger kobles på grund af den piezoelektriske shunt i det elektriske domæne. En approksimation af indflydelsen fra de ikke-resonante svingningsformer indføres derfor ved et ekstra bidrag til den piezoelektriske kapacitans. Dette bidrag er baseret på løsningen til det SC og OC egenverdiproblem, mens et tredje egenverdiproblem kan evalueres til bestemmelsen af den specifikke ikke-resonante inertieffekt. Tuningsmetoden er implementeret i den udviklede numeriske model og i et kommercielt element metode program, hvor dæmpning af en enkel og flere svingningsformer for bjælke- og plade eksemplerne er demonstreret ved brugen af piezoelektriske absorbere.

I den sidste del eftervises de udledte shunt-tuningsmetoder eksperimentelt, hvor der kræves data opsamling af to absorber respons i de SC og OC grænser. God sammenhæng mellem de numeriske og eksperimentelle resultater og den korresponderende shunt-tuning er demonstreret for bjælke- og plade eksemplerne og det er vist at udeladelsen af bidraget fra de ikke-resonante svingningsformer fører til en suboptimal tuning af de piezoelektriske absorbere og reduktion i den opnåelige dæmpning.



# PUBLICATIONS

## Journal papers

- [P1] J.F. Toftekær, A. Benjeddou, J. Høgsberg, S. Krenk, Optimal piezoelectric resistive-inductive shunt damping of plates with residual mode correction, *Journal of Intelligent Material Systems and Structures*, **29** (2018) 3346-3370.
- [P2] J.F. Toftekær, A. Benjeddou, J. Høgsberg, General numerical implementation of a new piezoelectric shunt tuning method based on the effective electromechanical coupling coefficient, *Mechanics of Advanced Materials and Structures*, Epub: January 25, 2019; <https://doi.org/10.1080/15376494.2018.1549297>.
- [P3] J.F. Toftekær, J. Høgsberg, Multi-mode piezoelectric shunt damping with residual mode correction by evaluation of modal charge and voltage, *Journal of Intelligent Material Systems and Structures*, Accepted, JIM-19-319.
- [P4] J.F. Toftekær, J. Høgsberg, Experimental validation of piezoelectric shunt tuning method with residual mode correction for damping of plate-like structures, *Journal of Intelligent Material Systems and Structures*, Submitted, JIM-19-388.

## Conference papers

- [C1] J.F. Toftekær, A. Benjeddou, J. Høgsberg, New piezoelectric shunt tuning method based on the effective electromechanical coupling coefficient: Validation and 3D implementation, *Proceedings of 7th International Symposium on Aircraft Materials*, April 24-26, 2018, Compiègne, France
- [C2] J.F. Toftekær, J. Høgsberg, Resonant piezoelectric shunt tuning based on the electric current and voltage response to pseudo-random vibration excitation, *Proceedings of 9th ECCOMAS Thematic Conference on Smart Structures and Materials*, July 8-11, 2019, Paris, France

## Additional contributions

- [A1] J.F. Toftekær, J. Høgsberg, Vibration suppression of plates by optimally calibrated piezoelectric RL shunt damping, *Poster, 16th DCAMM Symposium*, March 13-14, 2017, Middelfart, Denmark.

- [A2] J.F. Toftekær, A. Benjeddou, J. Høgsberg, S. Krenk, Vibration suppression of plates by optimally calibrated piezoelectric RL shunt damping, *Proceedings of 8th ECCOMAS Thematic Conference on Smart Structures and Materials*, June 5-8, 2017, Madrid, Spain
- [A3] J.F. Toftekær, A. Benjeddou, J. Høgsberg, S. Krenk, Optimal piezoelectric RL shunt damping of plates with residual mode correction, *Poster, Journées Jeunes Chercheurs en vibrations, Acoustique et Bruit*, November 16-17, 2017, Paris, France.
- [A4] J.F. Toftekær, J. Høgsberg, Multi-Mode Piezoelectric Shunt Damping of Plate-Like Structures, *Extended abstract, 30th International Conference on Adaptive Structures and Technologies*, October 7-11, 2019, Montreal, Canada
- [A5] J.F. Toftekær and J. Høgsberg Experimental data for Validation of Piezoelectric Shunt Tuning with Residual Mode Correction: Damping of Plate-Like Structures, *Mendeley Data*, Epub 30 September 2019, <http://dx.doi.org/10.17632/c4zgfwdwvk7.1>



# CONTENTS

<b>1</b>	<b>Introduction</b>	<b>1</b>
1.1	Piezoelectric absorber . . . . .	2
1.2	Resonant shunt . . . . .	3
1.3	Objectives and outline . . . . .	4
<b>2</b>	<b>Finite element modeling</b>	<b>5</b>
2.1	Piezoceramic patch . . . . .	5
2.2	Plate-piezo model . . . . .	8
2.3	Commercial FE software . . . . .	11
2.4	Electromechanical coupling . . . . .	13
2.5	Numerical examples . . . . .	14
<b>3</b>	<b>Resonant shunt damping</b>	<b>21</b>
3.1	Single piezoelectric absorber . . . . .	22
3.2	Multiple piezoelectric absorbers . . . . .	25
3.3	Single-mode damping . . . . .	27
3.4	Multi-mode damping . . . . .	31
3.5	Numerical examples . . . . .	33
<b>4</b>	<b>Experimental validation</b>	<b>39</b>
4.1	Current and voltage response . . . . .	40
4.2	Shunt tuning . . . . .	42
4.3	Inductance . . . . .	44
4.4	Frequency response analysis . . . . .	46
<b>5</b>	<b>Conclusions</b>	<b>51</b>
	<b>References</b>	<b>53</b>

# 1. INTRODUCTION

Pedestrians walking on a bridge, the turbulence of the wind on a wing and the acoustic pressure on a window, are all harmonic type loads, which may synchronize with a resonance of the host structure causing excessive vibrations that may lead to fatigue, acoustic problems or structural failure. In these cases the introduction of additional damping is required and may be achieved by the installment of resonant absorber devices. The resonant absorber is calibrated to counteract the structural motions around a targeted resonant frequency, whereby the vibration energy is effectively dissipated as heat in a viscous damper unit. For large-scale civil engineering structures the use of traditional tuned mass- or inerter based absorbers are beneficial, while for moderate to small structures the vibrations may be mitigated more efficiently by use of electromechanical absorber devices. For both the mechanical and electromechanical absorbers a precise frequency tuning is vital for the final damping performance, which therefore must be based on a model that accurately describes the structure-absorber interaction around the targeted vibration mode. By discretising the structure and the absorber(s) by finite elements (FE) the optimum absorber tuning may be obtained by evaluating the corresponding eigenvalue problem. However, the exact absorber tuning requires the evaluation of the full range of eigenvalues (frequencies) and eigenvectors (mode shapes), which is computational undesirable, whereby a modal reduction of the full numerical FE-model is often introduced. The simplest modal reduction is obtained by assuming that the influence from the non-resonant vibration modes on the response around the target mode is negligible. The full numerical model can hereby be reduced to a two degrees of freedom (DOF) system, from which the optimum absorber tuning may be derived explicitly. However, as it has been demonstrated for the tuning of mass- or inerter based absorbers in [31] the idealized single mode representation of the structure-absorber system may lead to an inaccurate absorber tuning and a reduction in the attainable damping. Instead, two correction terms accounting for the flexibility and inertia effects from the non-resonant vibration modes around the target mode is shown to modify the absorber tuning such that the desired damping level is obtained. In [24] it is shown that these flexibility and inertia correction terms are equivalent to capacitance and inductance corrections, which alter the optimum electromechanical absorber tuning.

## 1.1 Piezoelectric absorber

The electromechanical absorber is often designed by a single (or several) piezoceramic patch(es) with a specific polarization and two surface electrodes connected to an electric circuit or shunt. The shunted piezoceramic patch is then glued to a vibrating structure, whereby an amount of the vibration energy is converted into electric energy by the piezoceramic material and subsequently dissipated in the electric shunt. The conversion of mechanical to electrical energy is governed by the electromechanical coupling properties of the piezoceramic patch and the specific structure-piezo interaction. In resonance the rate of converted energy is described by the so-called effective electromechanical coupling coefficient (EMCC), which is defined as the relative difference between the modal strain energies associated with short- and open circuit (SC and OC) piezoelectric electrodes [26]. The inherent electromechanical coupling properties of the piezoceramic patch implies three fundamental coupling modes given by in- and out-of-plane deformations and transverse shear deformations for the piezoceramic patch polarized perpendicular to the major patch surfaces. The three electromechanical coupling modes are restricting for the applications of the piezoelectric absorber. An example for the respective use of each coupling mode is shown in Figure 1.1, for (a) the in-plane coupling in a pair of co-located piezoceramic patches [20], (b) the out-of-plane coupling in a stacked transducer [44] and (c) the shear coupling in a sandwich beam configuration [4].

Piezoelectric absorbers exploiting the in-plane electromechanical coupling mode in Figure 1.1(a) are beneficial for the damping of a wide range of structural elements, such as beams [20], plates [40] and shells [32], where bending or twisting may cause in-plane deformations of the surface bonded piezoceramic patches. For the damping of general plate-like structures the electromechanical coupling is conveniently increased by using a pair of piezoceramic patches placed on both sides of the plate. The two co-located piezoceramic patches may then be employed as sensor/actuator pairs in active feedback vibration control [1, 41, 28, 43] or be connected and wired to semi-active [13, 14, 7, 8] or passive [20, 25, 53, 54] resonant shunts. The electromechanical coupling may be further increased by optimizing the position, shape and size of the piezoelectric absorber [37, 15], while the optimum absorber configuration may be influenced by the inherent structural damping [46] and non-linearities [47, 34].

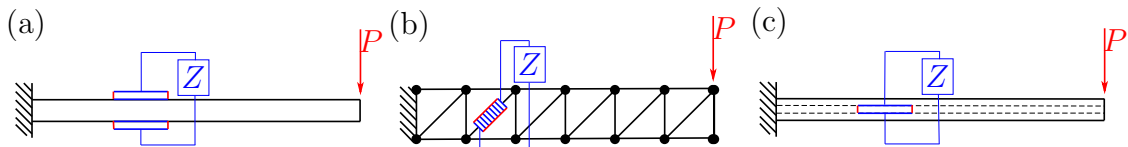


Figure 1.1. Applications activating the (a) in-plane, (b) out-of-plane and (c) out-of-plane shear electromechanical coupling deformation modes of a piezoceramic patch.

## 1.2 Resonant shunt

The resonant shunt consists of an inductance ( $L$ ) and a resistance ( $R$ ) connected in series [20] or in parallel [53] with the piezoceramic patch(es) as seen in Figure 3.3. In both cases the inductance is tuned to secure a desired absorber frequency, while the resistance ( $R$ ) is chosen subsequently to obtain optimum energy dissipation around the targeted vibration mode [18]. The absorber frequency is defined by the inverse product of the shunt inductance and the inherent blocked piezoelectric capacitance  $C_p^S$ , whereby the shunt inductance is tuned in order to match the absorber and target structural frequencies. The single mode truncation implies equality between the absorber and target frequencies, whereby the inductance is tuned directly from the blocked capacitance  $C_p^S$  [20, 53, 38, 10, 55, 49, 22, 45]. However, by including the effects from the non-resonant vibration modes this tuning becomes inadequate. Instead, an effective modal capacitance containing the contribution from the residual (non-resonant) vibration modes modifies the absorber frequency, that should be matched with the target frequency. In [42, 13, 43] the effective capacitance  $C(\omega)$  of a piezoelectric element bonded to a vibrating structure is found to be in between the blocked  $C_p^S$  and a static capacitance  $C_p^0$  obtained by the piezoelectric charge to voltage ratio in the static limit. This implies that the effective capacitance  $C(\omega)$  is close to the static capacitance  $C_p^0$  at low frequencies, while it approaches the blocked capacitance  $C_p^S$  for increasing frequencies. In [42] a blocked modal capacitance is further proposed but considered impractical to determine experimentally as it should be measured for blocked modal coefficients. Subsequently, the influence from the residual vibration modes has been accounted for numerically by modifying the blocked capacitance by the influence from higher vibration modes in [7, 8], through a theoretical study of the influence from an increasing number of modes in [19] and by the evaluation of explicit quasi-static and quasi-dynamic correction terms in [23, 24]. In all cases the main objective is to describe an effective capacitance for the piezoelectric absorber bonded to a structure vibrating in a targeted resonant mode, which is then used for the tuning of the corresponding resonant shunt.

The shunt inductance is often emulated actively by use of operational amplifiers in a so-called synthetic inductor [16], as the design of passive inductors with high inductance traditionally has been considered impractical. The use of the synthetic inductor has permitted easy adjustment of the emulated inductance, whereby the demand for a precise prior shunt tuning has been inessential. Furthermore, the use

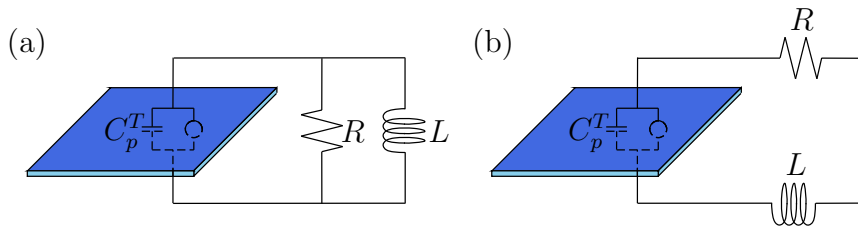


Figure 1.2. Parallel and series (a,b) shunted piezoceramic patch with free capacitance  $C_p^T$ .

of the active resonant shunt has led to the proposal for improved shunts in terms of actively emulated negative capacitance [9, 13, 7] or switch damping [14]. However, a practical design of the pure passive inductor with high inductance has recently been demonstrated by winding a copper wire around a magnetic coil [33], permitting the pure passive resonant shunt. While pure passive shunt damping is attractive because of the inherent stability, it seemingly requires a precise prior inductance tuning to determine the exact number of coil wire turns, which may only be achieved by including the contribution from the residual vibration modes.

### 1.3 Objectives and outline

The objectives of the present work is to develop a plate-piezo FE-model capable of describing the full electromechanical behavior of shunted and interconnected piezoceramic patches bonded to plate-like structures. The model is then used to verify the optimum shunt calibration method with residual modes corrections in [24]. Furthermore, it is the aim to implement the shunt calibration procedure [24] in a general commercial FE-software supporting electromechanical analysis. This requires a consistent reformulation of the calibration method [24] in terms of variables available in any FE-software. Finally, the developed FE-model, proposed shunt tuning procedures and implementation in commercial FE-software will be validated by experiments on plate-like structures with multiple piezoelectric absorbers.

The present thesis comprises an introductory summary, four attached journal papers [P1]-[P4] and two conference papers [C1]-[C2]. The summary is organized in four chapters and a conclusion. Initially, the assumptions leading to the development of the plate-piezo FE-model in [P1] is presented. This concerns particularly a plane stress-reduction of the full three dimensional (3D) electromechanical properties of the piezoceramic patch(es) and the implementation of the equipotential condition and wiring of the piezoelectric electrodes. The SC and OC frequencies evaluated with the piezo-plate FE-model are then compared to numerical benchmark values obtained with a full 3D FE-model in the commercial FE-software ANSYS [P2]. Next, a modal representation of the general vibration problem for a structure with piezoelectric absorbers is introduced and used to identify the coupling between the resonant and the non-resonant vibration modes. Two new methods for the practical evaluation of the residual modes contribution are then proposed and obtained from variables available in commercial FE-software [P2-P3] or experimental measurements [P4]. The modal reduced electromechanical structure is hereby used to derive the final piezoelectric shunt tuning [P3], which is demonstrated numerically by the plate-piezo and full 3D FE-models for single- and multi-mode damping. Finally, it is demonstrated how the required shunt tuning parameters may be obtained from experimental measurements of the piezoelectric SC current and OC voltage response to a specific dynamic excitation load [P4]. The experimental shunt tuning method is then verified for the same examples analyzed numerically by the plate-piezo and 3D FE-models, enabling a final experimental validation of the shunt tuning and damping performance obtained with the numerical models.

## 2. FINITE ELEMENT MODELING

An accurate numerical model considering the full three-dimensional (3D) piezoceramic properties and the electromechanical interaction is crucial for achieving a precise piezoelectric shunt tuning. A plate-piezo FE-model has therefore been developed in [P1] for the analysis of piezoelectric shunt damping of plate-like structures. The model uses a plane stress-reduction of the full 3D piezoceramic material properties and accounts for the electrode equipotentiality, specific polarization and wiring of the piezoceramic patches [11]. A thorough review of FE techniques for the modeling of piezoelectric structural elements is provided in [3]. The host plate-like structure is approximated by use of Kirchoff plate bending kinematics, whereas the coupling to the surface bonded piezoceramic patches is established by transforming the electric forcing from the patches to the equivalent moment contributions in the plate model. This finally leads to a governing vibration problem which is considered in the following chapter for the derivation of optimum piezoelectric shunt tuning.

Full 3D modeling of piezoelectric absorbers in the commercial FE-software ANSYS is considered subsequently and used to validate the developed plate-piezo FE-model by the analysis of two benchmark problems, considered experimentally in [P4] and chapter 4.

### 2.1 Piezoceramic patch

A piezoceramic patch is a transverse isotropic material with the constitutive relations (for a polarization along the 3-direction),

$$\begin{Bmatrix} T_1 \\ T_2 \\ T_3 \\ T_4 \\ T_5 \\ T_6 \end{Bmatrix} = \begin{bmatrix} c_{11}^E & c_{12}^E & c_{13}^E & 0 & 0 & 0 \\ c_{12}^E & c_{11}^E & c_{13}^E & 0 & 0 & 0 \\ c_{13}^E & c_{13}^E & c_{33}^E & 0 & 0 & 0 \\ 0 & 0 & 0 & c_{55}^E & 0 & 0 \\ 0 & 0 & 0 & 0 & c_{55}^E & 0 \\ 0 & 0 & 0 & 0 & 0 & c_{66}^E \end{bmatrix} \begin{Bmatrix} S_1 \\ S_2 \\ S_3 \\ S_4 \\ S_5 \\ S_6 \end{Bmatrix} - \begin{bmatrix} 0 & 0 & e_{31} \\ 0 & 0 & e_{31} \\ 0 & 0 & e_{33} \\ 0 & e_{15} & 0 \\ e_{15} & 0 & 0 \\ 0 & 0 & 0 \end{bmatrix} \begin{Bmatrix} E_1 \\ E_2 \\ E_3 \end{Bmatrix} \quad (2.1)$$

$$\begin{Bmatrix} D_1 \\ D_2 \\ D_3 \end{Bmatrix} = \begin{bmatrix} 0 & 0 & 0 & 0 & e_{15} & 0 \\ 0 & 0 & 0 & e_{15} & 0 & 0 \\ e_{31} & e_{31} & e_{33} & 0 & 0 & 0 \end{bmatrix} \begin{Bmatrix} S_1 \\ S_2 \\ S_3 \\ S_4 \\ S_5 \\ S_6 \end{Bmatrix} + \begin{bmatrix} \epsilon_{11}^S & 0 & 0 \\ 0 & \epsilon_{11}^S & 0 \\ 0 & 0 & \epsilon_{33}^S \end{bmatrix} \begin{Bmatrix} E_1 \\ E_2 \\ E_3 \end{Bmatrix} \quad (2.2)$$

between the mechanical stresses  $\{T\}$  and strains  $\{S\}$  and the electric displacements  $\{D\}$  and fields  $\{E\}$ , respectively. The material properties are defined by six independent elastic stiffness components  $C_{11}^E$ ,  $C_{12}^E$ ,  $C_{13}^E$ ,  $C_{33}^E$ ,  $C_{55}^E$  and  $C_{66}^E$ , three piezoelectric coupling coefficients  $e_{31}$ ,  $e_{33}$  and  $e_{15}$  and two blocked dielectric constants  $\epsilon_{11}^S$  and  $\epsilon_{33}^S$ . The indices of the piezoelectric coupling coefficients refer to the coupling between the applied electric field and the mechanical strain deformation mode, leading to the three fundamental electromechanical coupling modes shown in Figure 2.1.

For the piezoceramic patch(es) bonded to one of the major surfaces of a vibrating plate, the electromechanical coupling mode in Figure 2.1(b) between in-plane strains and electric field in the 3-direction is dominating. The piezoceramic material behavior is thereby beneficially represented by the plane stress-reduced mechanical and electrical properties. The plane stress-assumption yields vanishing transverse stresses  $T_3 = T_4 = T_5 = 0$ , whereby (2.1) and (2.2) can be reduced to

$$\begin{Bmatrix} T_1 \\ T_2 \\ T_6 \\ \bar{D}_3 \end{Bmatrix} = \begin{bmatrix} \bar{c}_{11}^E & \bar{c}_{12}^E & 0 & -\bar{e}_{31} \\ \bar{c}_{12}^E & \bar{c}_{11}^E & 0 & -\bar{e}_{31} \\ 0 & 0 & c_{66}^E & 0 \\ \bar{e}_{31} & \bar{e}_{31} & 0 & \bar{\epsilon}_{33}^S \end{bmatrix} \begin{Bmatrix} S_1 \\ S_2 \\ S_6 \\ E_3 \end{Bmatrix} = \begin{bmatrix} \bar{C}^E & -\bar{e}_3 \\ \bar{e}_3 & \bar{\epsilon}_{33}^S \end{bmatrix} \begin{Bmatrix} \bar{S} \\ E_3 \end{Bmatrix} \quad (2.3)$$

with the plane stress-reduced SC stiffness, coupling coefficients and dielectric constants given as

$$\bar{c}_{11}^E = c_{11}^E - \frac{(c_{13}^E)^2}{c_{33}^E}, \quad \bar{c}_{12}^E = c_{12}^E - \frac{(c_{13}^E)^2}{c_{33}^E}, \quad \bar{e}_{31} = e_{31} - e_{33} \frac{c_{13}^E}{c_{33}^E}, \quad \bar{\epsilon}_{33}^S = \epsilon_{33}^S + \frac{e_{33}^2}{c_{33}^E} \quad (2.4)$$

By considering the electric quasi-static equilibrium and boundary conditions in [P1] the variational formulation for the piezoceramic patch may be written as

$$\int_{\Omega_p} \{\delta \bar{S}\}^t \{\bar{T}\} d\Omega_p - \omega^2 \int_{\Omega_p} \{\delta u\}^t \rho_p \{u\} d\Omega - \int_{\Omega_p} \delta E_3 D_3 d\Omega_p = \int_{A_p} \{\delta \varphi\}^t \{q\} dA_p \quad (2.5)$$

assuming mechanically unloaded vibrations with harmonic solutions of the form  $\{u\} = \{u\} e^{i\omega t}$ , while  $(\dots)^t$  represents the transpose operation. Furthermore,  $t_p$  is the patch thickness,  $A_p$  is the surface electrode area,  $\Omega_p = A_p t_p$  is the volume and  $\rho_p$  is the material density, while  $\{\varphi\}$  and  $\{q\}$ , respectively, contain the electric potentials

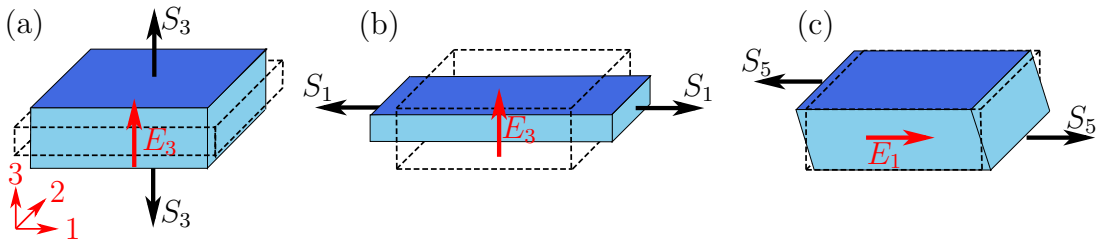


Figure 2.1. Electromechanical coupling modes for a piezoceramic patch with two surface electrodes (dark blue color) and polarization in the 3-direction.

and surface charge densities for the two surface electrodes. The in-plane strains  $\{\bar{S}\}$  and the electric field  $E_3$  may then be described by the in-plane displacements  $\{u\}$  and the electrode potentials  $\{\varphi\}$  as

$$\{\bar{S}\} = \{\nabla\}_p \{u\} \quad , \quad E_3 = -\{\nabla\}_\varphi \{\varphi\} \quad (2.6)$$

where  $\{\nabla\}_p$  is the derivative operator and  $\{\nabla\}_\varphi$  the vector enforcing the constant field assumption in [P1]. Hereby, the variational formulation (2.5) can be written in terms of the mechanical displacements and electric potentials

$$\begin{aligned} \left\{ \begin{array}{c} \{\delta u\} \\ \{\delta \varphi\} \end{array} \right\}^t \int_{A_p} \left[ \begin{array}{c|c} \{\nabla\}_p^t [\bar{C}^E] t_p \{\nabla\}_p - \omega^2 \rho t_p & \{\nabla\}_p^t \{\bar{e}_3\} t_p \{\nabla\}_\varphi \\ \hline \{\nabla\}_\varphi^t \{\bar{e}_3\} t_p \{\nabla\}_p & -\{\nabla\}_\varphi^t \bar{e}_{33}^S t_p \{\nabla\}_\varphi \end{array} \right] dA_p \left\{ \begin{array}{c} \{u\} \\ \{\varphi\} \end{array} \right\} \\ = \int_{A_p} \left\{ \begin{array}{c} \{\delta u\} \\ \{\delta \varphi\} \end{array} \right\}^t \left\{ \begin{array}{c} \{0\} \\ -\{Q\} \end{array} \right\} dA_p \end{aligned} \quad (2.7)$$

by use of the plane stress-reduced constitutive relations in (2.3). The in-plane piezoceramic element in Figure 2.2 has then been proposed from [P1] to describe the plate bonded piezoceramic patch. The element stiffness, mass, coupling and capacitance matrices follow from (2.7) and the nodal shape functions  $[N]_p$  in [P1] as

$$\begin{aligned} [M_p^e] &= \int_{A_p^e} [N]_p^t \rho_p t_p [I]_2 [N]_p dA_p^e \\ [K_p^e] &= \int_{A_p^e} (\{\nabla\}_p [N]_p)^t [\bar{C}^E] t_p (\{\nabla\}_p [N]_p) dA_p^e \\ [K_{pe}^e] &= \int_{A_p^e} (\{\nabla\}_p [N]_p)^t \{\bar{e}_3\} t_p \{\nabla\}_\varphi dA_p^e \\ [K_e^e] &= \int_{A_p^e} \{\nabla\}_\varphi^t \bar{e}_{33}^S t_p \{\nabla\}_\varphi dA_p^e \end{aligned} \quad (2.8)$$

After assembly of the element matrices and vectors the global equation of motion for the discretized piezoceramic patch can then be written as

$$\begin{bmatrix} K_p - \omega^2 M_p & K_{pe} \\ K_{pe}^t & -K_e \end{bmatrix} \begin{Bmatrix} u_p \\ \varphi_p \end{Bmatrix} = \begin{Bmatrix} f_p \\ -Q \end{Bmatrix} \quad (2.9)$$

where the mechanical  $u_p$  and electrical  $\varphi_p$  variables are organized in the upper and lower set of equations, while  $f_p$  and  $Q$ , respectively, contain the nodal mechanical forces and element electrode charges.

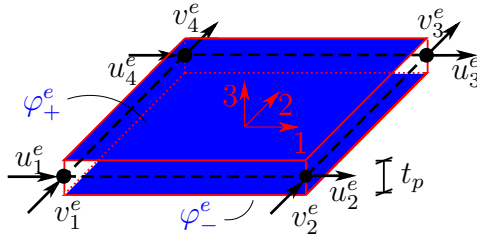


Figure 2.2. Piezoceramic patch element with 8 mechanical and 2 electric DOFs, from [P1].

Finally, the equipotential condition for the surface electrodes of the discretized piezoceramic patch is considered. The electrode equipotentiality states that all element electrode potentials forming a continuous electrode must be identical. In [P1] this has been enforced by defining a boolean matrix  $[P]$ , that determines the relation between the element potentials in  $\{\varphi\}_p$  and the full surface potentials of the top (+) and bottom (-) patch electrodes as

$$\{\varphi\}_p = [P]\{\varphi\}_\pm = \begin{bmatrix} 1 & 0 & \cdots & 1 & 0 \\ 0 & 1 & \cdots & 0 & 1 \end{bmatrix}^t \begin{Bmatrix} \varphi_+ \\ \varphi_- \end{Bmatrix} \quad (2.10)$$

The coupled FE-equations for the discretized piezoceramic patch considering the equipotential condition can thereby be written

$$\begin{bmatrix} K_p - \omega^2 M_p & K_{pe}P \\ (K_{pe}P)^t & -P^t K_e P \end{bmatrix} \begin{Bmatrix} u_p \\ \varphi_\pm \end{Bmatrix} = \begin{Bmatrix} f_p \\ Q_\pm \end{Bmatrix} \quad (2.11)$$

where  $\{Q\}_\pm$  contains the electric charge of the surface electrodes while the quadratic product

$$[P]^t [K_e] [P] = C_p^S \begin{bmatrix} 1 & -1 \\ -1 & 1 \end{bmatrix} \quad , \quad C_p^S = \frac{\bar{\epsilon}_{33}^S A_p}{t_p} \quad (2.12)$$

recovers the blocked capacitance  $C_p^S$  of the plane stress-reduced piezoceramic patch.

## 2.2 Plate-piezo model

For the damping of plate-like structures it is convenient to place the piezoceramic patches in pairs on the two major plate surfaces, whereby the electromechanical coupling is increased and the neutral axis of the plate remains unchanged. The kinematic coupling between a pair of co-located piezoceramic patch elements and the Kirchoff plate bending element used in [P1] is depicted in Figure 2.3. It is here seen

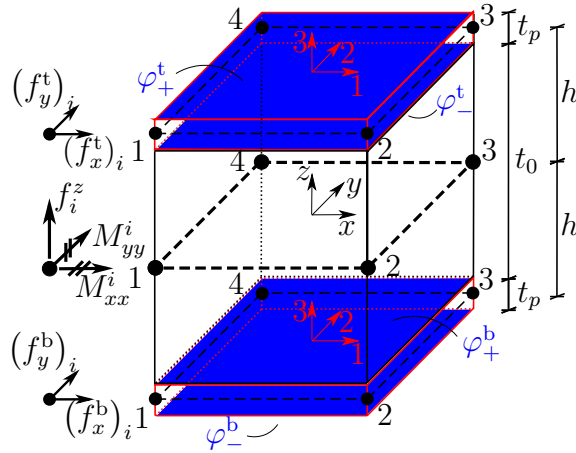


Figure 2.3. Moment equilibrium of plate and piezoceramic patch elements, from [P1].

that the bending moments of the plate element are restricted by the piezoceramic in-plane nodal forces through the moment arm  $h$ . This may be described by the kinematic relations

$$\begin{aligned} M_{xx} &= -hf_y^t + hf_y^b \\ M_{yy} &= hf_x^t - hf_x^b \end{aligned} \quad (2.13)$$

between the plate and the top (t) and bottom (b) piezoceramic patch elements, which are enforced by the establishment of a connectivity matrix  $[W]$  as demonstrated in [P1]. Hereby the mechanically unloaded discrete vibration problem for the plate and piezoceramic patches can be written as

$$\begin{bmatrix} K^E - \omega^2 M & WK_{pe}P & -WK_{pe}P \\ (WK_{pe}P)^t & -P^t K_e P & 0 \\ -(WK_{pe}P)^t & 0 & -P^t K_e P \end{bmatrix} \begin{Bmatrix} U \\ \varphi_{\pm}^t \\ \varphi_{\pm}^b \end{Bmatrix} = \begin{Bmatrix} 0 \\ -Q_{\pm}^t \\ -Q_{\pm}^b \end{Bmatrix} \quad (2.14)$$

in which the resulting elastic stiffness and mass matrices

$$[K^E] = [K_0] + 2[W][K_p][W]^t, \quad [M] = [M_0] + 2[W][M_p][W]^t \quad (2.15)$$

are the plate stiffness  $[K_0]$  and mass  $[M_0]$  matrices altered through the connectivity matrix  $[W]$  by the SC piezoceramic patch stiffness  $[K_p]$  and mass  $[M_p]$ . Since the piezoceramic patches are approximated by pure in-plane elements the bending stiffness and transverse inertia effects of the patches are omitted. For thin patches the bending stiffness becomes insignificant, while the omission of the transverse inertia effects may cause erroneous results. The transverse inertia effects are therefore included in the model by simply lumping the mass of the patches at the relevant DOFs of the system mass matrix according to [P1].

### Piezoelectric polarization and wiring

The piezoceramic patches are co-located in pairs such that they can be electrically connected and thereby dissipate more energy in a resonant shunt, on the condition that the patches are properly wired and polarized according to one of two possible configurations. Either the piezoceramic patches are applied with the same polarization and wired in parallel (SP-PW) with the resonant shunt as in Figure 2.4(a) or the patches are applied with opposite polarization and wired in series (OP-SW) as in Figure 2.4(b). In both cases the shunted piezoceramic patch pair will work as a resulting piezoelectric absorber, while the resulting electromechanical properties and corresponding optimum shunt tuning for the two configurations are substantially different. This is now shown by considering the relation between the electrode potentials for the two patch pair configurations in Figure 2.4. In the following a piezoelectric absorber refers to the shunted patch pair(s) shown in Figure 2.4.

For the SP-PW piezoelectric absorber in Figure 2.4(a) the relations between the potentials are given by

$$\varphi_-^t = \varphi_+^b, \quad \varphi_+^t = \varphi_-^b, \quad V = \varphi_+^t - \varphi_-^t \quad (2.16)$$

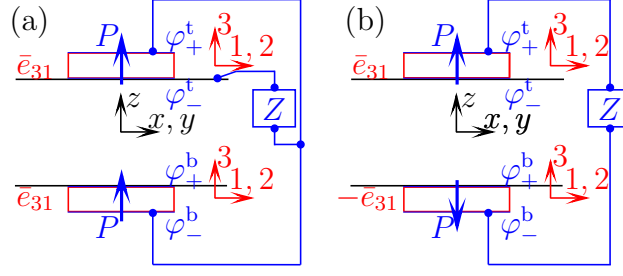


Figure 2.4. Electrically conducting plate structure with a pair of shunted piezoceramic patches (absorber) in the (a) SP-PW and (b) OP-SW configurations, from [P1].

where the last relation introduces the voltage across the electric shunt with the impedance  $Z$ . These relations may then be imposed to the equation of motion (2.14) by establishing the matrix  $[P_\varphi]$  in [P1]. By eliminating the electrode potentials in (2.14) by use of  $[P_\varphi]$  the electromechanical coupling in (2.14) is governed by a vector  $[W]\{k_{pe}\}\tilde{e}_{31}$  while the electric capacitance is described by a (scalar) resulting blocked capacitance  $\bar{C}_p^S$  for the piezoelectric absorber. The resulting blocked capacitance  $\bar{C}_p^S$  and modified piezoelectric coupling coefficient  $\tilde{e}_{31}$  are for the SP-PW piezoelectric absorber hereby readily found as

$$\bar{C}_p^S = 2C_p^S \quad , \quad \tilde{e}_{31} = 2\bar{e}_{31}, \quad (2.17)$$

while the piezoelectric coupling vector  $\{k_{pe}\}$  in the present notation is given as

$$\{k_{pe}\} = [K_{pe}][P] \begin{Bmatrix} 1 \\ -1 \end{Bmatrix} \frac{1}{2\bar{e}_{31}} \quad (2.18)$$

The relations between the potentials for the OP-SW piezoelectric absorber in Figure 2.4(b) are given by

$$\varphi_-^t = \varphi_+^b \quad , \quad \varphi_+^t - \varphi_-^t = \varphi_+^b - \varphi_-^b \quad , \quad V = \varphi_+^t - \varphi_-^b \quad (2.19)$$

where the second condition is valid when two identical and symmetrically positioned piezoceramic patches are assumed. Hereby the new resulting blocked capacitance and modified piezoelectric coupling coefficient,

$$\bar{C}_p^S = \frac{1}{2}C_p^S \quad , \quad \tilde{e}_{31} = \bar{e}_{31} \quad (2.20)$$

are found after eliminating the electrode potentials in (2.14) by use of the new matrix  $[P_\varphi]$  determined from (2.19) in [P1].

It is seen from (2.17) and (2.20) that there is a factor four between the effective blocked capacitances and a factor two between the modified piezoelectric coupling coefficients for the SP-PW and OP-SW piezoelectric absorbers. In the next chapter, it is shown how this influences the corresponding resonant shunt tuning, while the effective electromechanical coupling is the same for the two absorber configurations, as demonstrated in the subsequent numerical examples.

### General vibration problem

For both the SP-PW and OP-SW piezoelectric absorbers the vibration problem (2.14) may be reduced to

$$\left( \begin{bmatrix} K^E & Wk_{pe}\tilde{e}_{31} \\ (Wk_{pe}\tilde{e}_{31})^T & -\bar{C}_p^S \end{bmatrix} - \omega^2 \begin{bmatrix} M & 0 \\ 0 & 0 \end{bmatrix} \right) \begin{Bmatrix} U \\ V \end{Bmatrix} = \begin{Bmatrix} 0 \\ -Q \end{Bmatrix} \quad (2.21)$$

where  $V$  is the voltage across the shunt impedance  $Z$ , while  $Q$  contains the charge with the corresponding time-derivative describing the flow of electric current  $I$ . The off-diagonal terms in (2.21) define the electromechanical coupling vector

$$\{k_{me}^E\} = [W]\{k_{pe}\}\tilde{e}_{31} \quad (2.22)$$

which for the case of multiple piezoelectric absorbers are collected as columns for each absorber in the electromechanical coupling matrix  $[k_{me}^E]$ , while the corresponding resulting capacitances  $(\bar{C}_p^S)_i$  constitute the diagonal of the capacitance matrix  $[C_p]$ . The discrete vibration problem for a plate with multiple piezoelectric absorbers may hereby be written as

$$\left( \begin{bmatrix} K^E & k_{me}^E \\ (k_{me}^E)^t & -C_p \end{bmatrix} - \omega^2 \begin{bmatrix} M & 0 \\ 0 & 0 \end{bmatrix} \right) \begin{Bmatrix} U \\ V \end{Bmatrix} = \begin{Bmatrix} 0 \\ -Q \end{Bmatrix} \quad (2.23)$$

This general vibration problem is considered henceforth for the analysis of electromechanical coupling and for optimum shunt tuning and damping in chapter 3.

## 2.3 Commercial FE software

In [P2] the commercial FE-software ANSYS is used to validate the plate-piezo FE-model developed in [P1] by the analysis of a simple supported plate with a single piezoelectric absorber. In the present chapter the 3D modeling of general electromechanical structures (Figure 3.1) in ANSYS is used to validate the developed plate-piezo FE-model for the case of multiple piezoelectric absorbers attached to a beam and a plate, considered experimentally in [P4] and chapter 4. Furthermore, in chapter 3, the 3D electromechanical ANSYS model is used to verify a proposed shunt tuning method suitable for implementation in any FE-software supporting electromechanical analysis.

By assuming mechanically unloaded harmonic vibrations the variational formulation for the 3D electromechanical structure may be written similarly to (2.5) as

$$\int_{\Omega} \{\delta S\}^t \{T\} d\Omega - \omega^2 \int_{\Omega} \{\delta u\}^t \rho \{u\} d\Omega - \int_{\Omega} \{\delta E\}^t \{D\} d\Omega = \int_{\Gamma_q} \{\delta \varphi\}^t \{q\} d\Gamma_q \quad (2.24)$$

where  $\rho$  is the material density,  $\Omega$  the material volume and  $\Gamma_q$  the area of the electrode where the charge  $q$  is applied or measured. The FE-formulation is then obtained by considering the full 3D constitutive relations in (2.1) and (2.2) and

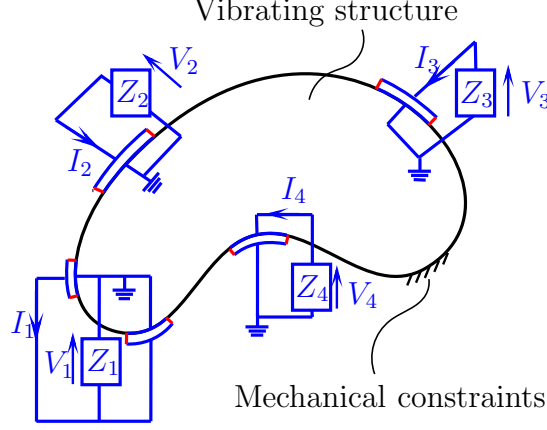


Figure 2.5. Vibrating structure with  $N_p = 4$  piezoelectric absorbers, from [P3].

by approximating the continuous displacements  $\{u\}$  and electric potentials  $\{\varphi\}$  by nodal displacements  $\{U\}$  and potentials  $\{\varphi\}$  via appropriate shape functions. The discrete vibration problem can hereby be represented by the coupled set of equations

$$\left( \begin{bmatrix} K_U^E & K_{U\varphi}^E \\ (K_{U\varphi}^E)^t & -K_\varphi^S \end{bmatrix} - \omega^2 \begin{bmatrix} M & 0 \\ 0 & 0 \end{bmatrix} \right) \begin{Bmatrix} U \\ \varphi \end{Bmatrix} = \begin{Bmatrix} 0 \\ -Q_\varphi \end{Bmatrix} \quad (2.25)$$

from [P2] with  $[K_U^E]$ ,  $[K_{U\varphi}^E]$  and  $[K_\varphi^S]$  containing the stiffness components associated with the mechanical displacements, electromechanical coupling and electric potentials, while  $[M]$  is the system mass matrix.

Next, the equipotential condition is imposed in ANSYS by applying a coupling constraint to all electric potential DOFs that are part of a continuous electrode, whereby the resulting electrode potential is represented in a so-called master node. The wiring between two electrodes is then performed by imposing another coupling constraint on the corresponding two master nodes, whereby the properties are merged in a single node. Hereby, two interface electrodes can be defined for the piezoelectric absorber consisting of several connected piezoelectric domains. It is cumbersome to impose specific relations between the electric master node potentials as it has been done in the developed plate-piezo model. Instead, the voltage between the two interface electrodes of the piezoelectric absorber is simply represented at one of the interface electrodes when the other is electrically grounded. Hereby the discrete vibration problem (2.25) including the electrode's equipotentiality can be written

$$\left( \begin{bmatrix} K_U^E & \bar{K}_{U\varphi}^E & K_{UV}^E \\ (\bar{K}_{U\varphi}^E)^t & -\bar{K}_{U\varphi}^S & -K_{\varphi V}^S \\ (K_{UV}^E)^t & -(K_{\varphi V}^S)^t & -K_V^S \end{bmatrix} - \omega^2 \begin{bmatrix} M & 0 & 0 \\ 0 & 0 & 0 \\ 0 & 0 & 0 \end{bmatrix} \right) \begin{Bmatrix} U \\ \varphi \\ V \end{Bmatrix} = \begin{Bmatrix} 0 \\ 0 \\ -Q \end{Bmatrix} \quad (2.26)$$

in which  $[\bar{K}_{U\varphi}^E]$  and  $[\bar{K}_{U\varphi}^S]$  contain contributions associated with the electric potential DOFs that are not part of an electrode, while  $[K_{UV}^E]$  and  $[K_{\varphi V}^S]$  represent the coupling

to the potential DOFs for the patch electrodes, and  $[K_V^S]$  represent the corresponding dielectric properties. By eliminating  $\{\varphi\}$  from the second set of equations in (2.26) the resulting condensed system matrices

$$\begin{aligned} [K^E] &= [K_{UV}^E] + [\bar{K}_{U\varphi}^E][\bar{K}_\varphi^S]^{-1}[\bar{K}_{U\varphi}^E]^t \\ [k_{me}^E] &= [K_{UV}^E] - [\bar{K}_{U\varphi}^E][\bar{K}_\varphi^S]^{-1}[K_{\varphi V}^S] \\ [C_p] &= [K_V^S] - [K_{\varphi V}^S]^t[\bar{K}_\varphi^S]^{-1}[K_{\varphi V}^S] \end{aligned} \quad (2.27)$$

permit the vibration problem (2.26) to be written in the same form (2.23) as obtained for the plate-piezo model.

## 2.4 Electromechanical coupling

The general vibration problem (2.23) for an elastic structure with  $N_p$  piezoelectric absorbers (Figure 3.1) is characterized by two limiting eigenvalue problems associated with SC and OC absorber electrodes.

In the short circuit (SC) limit the interface electrodes of the piezoelectric absorbers are electrically wired, whereby the voltage in (2.23) vanishes ( $\{V\} = \{0\}$ ). The corresponding SC eigenvalue problem can then be written as

$$([K^E] - \omega_j^2[M]) \{U_j\} = \{0\} \quad (2.28)$$

with SC frequency  $\omega_j$  and mode shape  $\{U_j\}$  for vibration mode  $j$ . The second equation in (2.23) provides a modal charge

$$\{Q_j\} = -[k_{me}^E]^t \{U_j\} \quad (2.29)$$

in the SC limit, which can be viewed as an electric reaction force securing the zero voltage constraint.

In the open circuit (OC) limit no wire connects the absorber interface electrodes, whereby the flow of electric current is prohibited. Since the current is described by the rate of charge, zero current implies zero charge ( $\{Q\} = \{0\}$ ), whereby the OC eigenvalue problem follows from (2.23) as

$$\left( [K^E] + [k_{me}^E][C_p]^{-1}[k_{me}^E]^t - \hat{\omega}_j^2[M] \right) \{\hat{U}_j\} = \{0\} \quad (2.30)$$

where  $\{V\}$  has been eliminated by the second equation in (2.23). Furthermore,  $\hat{\omega}_j$  and  $\{\hat{U}_j\}$  represent, respectively, the OC frequency and mode shape of vibration mode  $j$ . Again, the second equation of the discrete system (2.23) may be considered, which in this case determines a modal voltage

$$\{\hat{V}_j\} = [C_p]^{-1}[k_{me}^E]^t \{\hat{U}_j\} \quad (2.31)$$

which may be seen as an unconstrained electric displacement.

The effective coupling between the mechanical and the electrical domains of the structure with  $N_p$  piezoelectric absorbers is quantified by the rate of convertible energy. When the electromechanical structure resonates in a specific vibration mode  $j$  this rate of convertible energy becomes equivalent to the relative difference between the modal strain energies associated with SC and OC piezoelectric absorbers [50]. The SC and OC modal strain energies are proportional to their respective squared frequencies  $\omega_j^2$  and  $\hat{\omega}_j^2$ , whereby the rate of convertible energy for resonant vibration mode  $j$  may be determined by the effective EMCC [26]

$$\kappa_j^2 = \frac{\hat{\omega}_j^2 - \omega_j^2}{\omega_j^2} \quad (2.32)$$

Hence, the effective EMCC provides a direct measure of the attainable energy dissipation by the piezoelectric absorbers for the vibration mode  $j$ . In the following chapter, the effective EMCC is further shown to be a key parameter for the optimum piezoelectric shunt tuning.

## 2.5 Numerical examples

Two examples have been used in [P1] to demonstrate the accuracy of the developed plate-piezo FE-model. The first example concerns a cantilevered beam with one pair of piezoceramic patches, for which the two first frequencies, effective EMCCs and corresponding optimum shunt tuning has been verified by the corresponding experimental results available in [49]. The second example concerns a simple supported plate also with a single pair of piezoceramic patches, which initially has been investigated analytically in [19], while it has been analyzed subsequently in [C1] and [P2] by use of 3D FEs in ANSYS. Good agreement between the results of the developed plate-piezo model and the full 3D ANSYS model is further demonstrated in [C1] for both examples. Because both examples only consider a single piezoelectric absorber the experimental setups considered in [P4] concerning a free beam and free plate each equipped with four piezoelectric absorbers, are here analyzed by the developed plate-piezo and 3D ANSYS models. The results of the present chapter are subsequently compared to the experimental results obtained in chapter 4.

### Free beam

The first example concerns the free beam with five pairs of co-located piezoceramic patches in Figure 2.6, where four pairs are connected to resonant shunts  $Z_i$ , while the last patch pair is used in the experiment to excite structural vibrations through the voltage input  $V_p$ . The dimensions of the beam and location of the piezoceramic patches can be seen in Figure 2.6, while the material properties of the aluminum beam and piezoceramic material 3625HD are given in [P4].

The free beam is discretized by  $180 \times 12$  plate elements and the patches by  $12 \times 12$  patch elements in the developed plate-piezo FE-model. Similarly the beam is discretized by  $180 \times 12 \times 3$  Solid186 3D FEs and  $12 \times 12$  Solid226 electromechanical

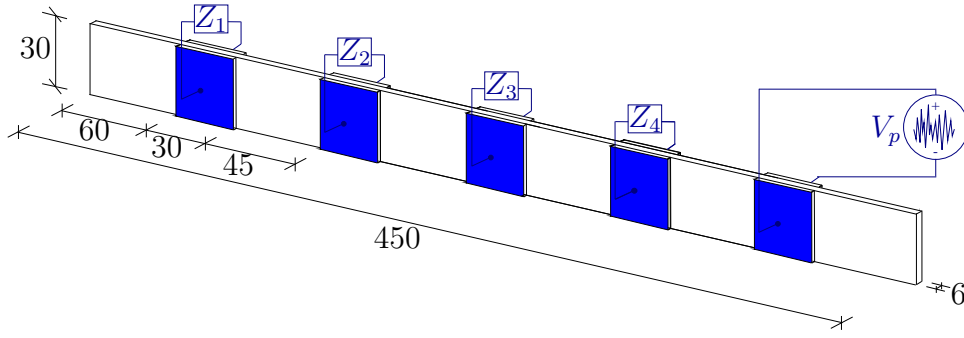


Figure 2.6. Free beam with five pairs of piezoceramic patches. Dimensions in mm.

3D FEs for the piezoceramic patches in ANSYS. The SC ( $f_j = \omega_j/(2\pi)$ ) and OC ( $\hat{f}_j = \hat{\omega}_j/(2\pi)$ ) frequencies and effective EMCCs obtained with the 3D ANSYS model are provided in Table 2.1 for the flexural beam modes 1 to 5, while the corresponding mode shapes can be seen in Figure 2.7. It is seen by the effective EMCCs in Table 2.1 that the rate of convertible energy is significant for the considered flexural vibration modes, particularly for mode 5 in Figure 2.7(e), for which all the piezoelectric absorbers experience maximum curvature. The frequencies and effective EMCCs obtained with the developed plate-piezo model are now compared in Figure 2.8(a,c) by a percentage relative deviation ( $\Delta$ ) to the results in Table 2.1 obtained with the 3D ANSYS model. Good agreement between the frequencies obtained with the plate-piezo and 3D ANSYS models can be seen in Figure 2.8(a) with relative deviations below 3% for the five lowest flexural vibration modes. It is seen that the relative deviation increases proportional with the frequency in Figure 2.8(a), which indicates that higher accuracy of the numerical models may be required for the precise evaluation of higher resonance frequencies. The relative deviations between the squared effective EMCCs based on the plate-piezo and 3D ANSYS models are seen in Figure 2.8(c) to be significantly larger than for the corresponding frequencies. This is because  $\kappa_j^2$  in (2.32) is determined as the relative difference between the squared SC and OC frequencies, and because the deviations on the SC frequencies simply are lower than for those with OC conditions. This means that the SC and OC frequencies need to be very precise for achieving an accurate squared effective EMCC by (2.32). The same conclusion is drawn in [P2] from the convergence study of a 3D ANSYS model. The challenge associated with the accurate evaluation of the effective EMCC is well known and has been discussed extensively in [50, 5].

Table 2.1. SC and OC frequencies and effective EMCCs for flexural vibration modes 1 to 5 of the free beam with five piezoceramic patch pairs, evaluated with 3D FEs in ANSYS.

Mode	1	2	3	4	5
$f_j$ [Hz]	160.59	438.62	852.36	1397.9	2076.0
$\hat{f}_j$ [Hz]	162.44	443.10	859.67	1410.1	2109.5
$\kappa_j^2$ [%]	2.31	2.06	1.72	1.77	3.26

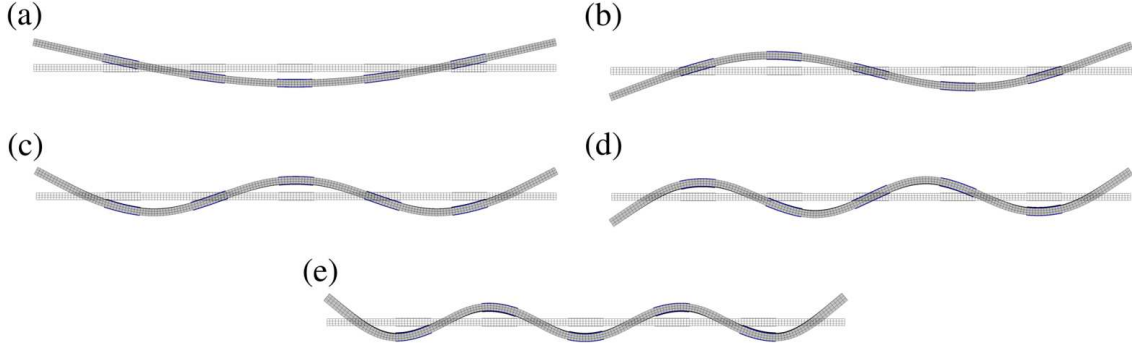


Figure 2.7. Flexural vibration modes 1-5 (a-e) of the free beam (gray) with five piezoelectric patch pairs (blue).

By evaluating the SC and OC eigenvalue problems the modal SC charge (2.29) and OC voltage (2.31) are readily obtained. The modal charge and voltage values provide the individual absorber response for vibration mode  $j$  and they may therefore by their magnitude be used to determine which piezoelectric absorbers are suitable for mitigating vibrations in mode  $j$ . The modal charges and voltages evaluated by the plate-piezo (red bars) and 3D ANSYS (blue bars) models are provided in Figure 2.8(b,d), in which they are normalized by the accumulated modal voltage  $\sum_{i=1}^{N_p} (\hat{V}_j)_i$ . The normalized modal charges in Figure 2.8(b) thus have the dimensions of capacitance, while the modal voltages in Figure 2.8(d) become dimensionless and thereby determine the relative authority of each piezoelectric absorber with respect to vibration mode  $j$ . It is thus seen from the modal voltages in Figure 2.8(d) that

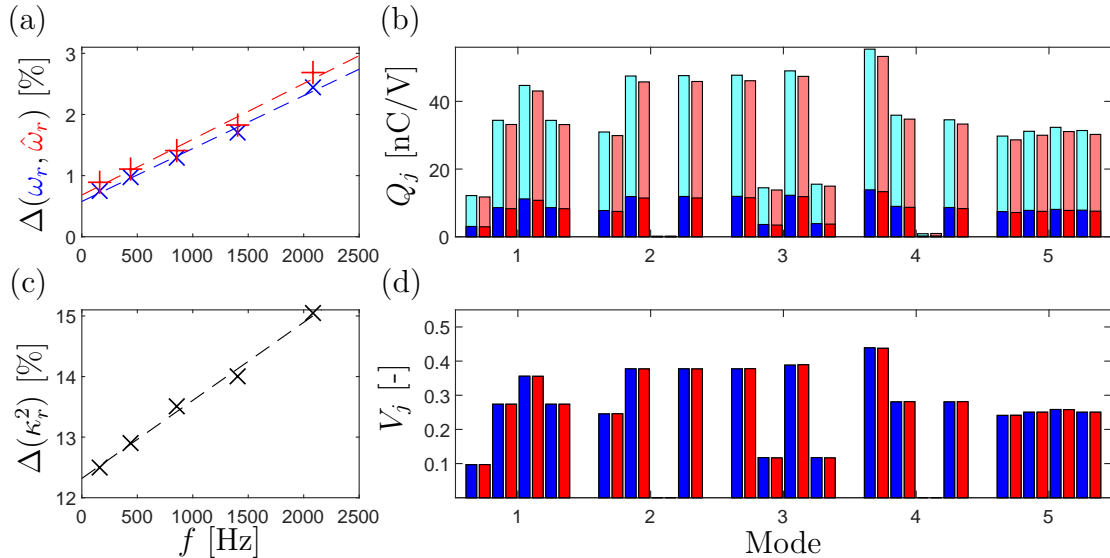


Figure 2.8. Relative deviation for (a) the SC and OC frequencies and (c) the effective EMCC of the free beam and (b,d) the modal charge and voltage based on the 3D ANSYS (blue) and plate-piezo (red) models for the OP-SW (dark) and SP-PW (light) absorbers.

the third absorber has no authority on mode 2 and 4, which also can be seen from the corresponding mode shapes in Figure 2.7(b,d) for which the third absorber is located at a nodal point. Furthermore, it is seen that the four piezoelectric absorbers have almost the same authority on mode 5, which has already been observed by inspection of the corresponding mode shape in Figure 2.7(e). The modal voltage for the OP-SW and SP-PW piezoelectric absorbers are identical since they have been normalized by their respective accumulated modal voltages, while the normalized modal charges are significantly larger for the SP-PW (light red bars) compared to the OP-SW (dark red bars) piezoelectric absorbers. By evaluating the ratio of the SP-PW to OP-SW normalized modal charges a factor of exactly 4 is found, which corresponds to the ratio between the respective resulting blocked capacitances in (2.17a) and (2.20a). Furthermore, a factor of two can be found between the non-normalized modal charges for the SP-PW and OP-SW piezoelectric absorbers, which agrees with the ratio between the corresponding effective piezoelectric coupling coefficients in (2.17b) and (2.20b). Finally, it is seen that the modal charges and voltages obtained by the plate-piezo and 3D ANSYS models are similar, except for slightly underestimated capacitances for the plate-piezo model (red bars) in Figure 2.8(b).

### Free plate

The second example concerns the free plate with five pairs of piezoceramic patches in Figure 2.9. Again, four piezoceramic patch pairs are connected to a resonant

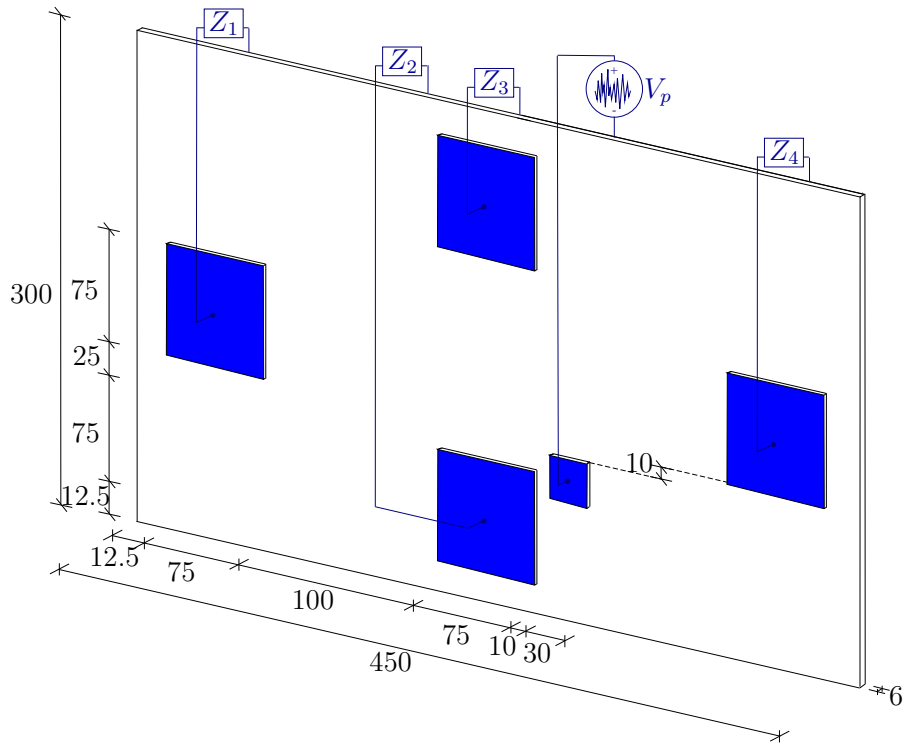


Figure 2.9. Free plate with five pairs of piezoceramic patches. Dimensions in mm.

Table 2.2. SC and OC frequencies and effective EMCCs for the six lowest resonances of the free plate with five piezoceramic patch pairs, evaluated with 3D FEs in ANSYS.

Mode	1	2	3	4	5	6
$f_j$ [Hz]	150.11	155.40	336.91	376.08	417.83	505.17
$\hat{f}_j$ [Hz]	150.11	156.85	339.37	381.32	418.22	513.44
$\kappa_j^2$ [%]	—	1.86	1.46	2.80	0.19	3.30

shunt, while the last patch pair is used experimentally to excite structural vibrations through the voltage input  $V_p$ . The dimensions of the plate and the position of the piezoceramic patches are seen in Figure 2.9, while the respective material properties are provided in [P4].

The plate has been modeled by  $108 \times 72$  plate elements and  $18 \times 18$  patch elements (for the large piezoceramic patches) in the plate-piezo model and by  $108 \times 72 \times 2$  Solid186 3D elements and  $18 \times 18$  Solid226 3D electromechanical elements, respectively, in ANSYS. The SC and OC frequencies and the effective EMCCs obtained in ANSYS are provided in Table 2.2 for the six lowest plate modes, while the corresponding mode shapes can be seen in Figure 2.10.

It is seen that the effective EMCC in Table 2.2 for the first plate vibration mode is vanishing since the four piezoelectric absorbers are either exposed to pure in-plane shear or located in a nodal point of the vibration mode in Figure 2.10(a). The effective EMCC for the fifth vibration mode is also low, while considerable coupling between the mechanical and electrical domains is obtained for modes 2, 3, 4 and 6.

The relative deviations between the frequencies and the effective EMCCs determined from the plate-piezo and 3D ANSYS models are shown in Figure 2.11(a,c), where good agreement between the frequencies can be seen, while the deviations on the effective EMCCs for the two models again are seen to be larger. A linear tendency for the relative deviations with respect to the frequencies is not apparent

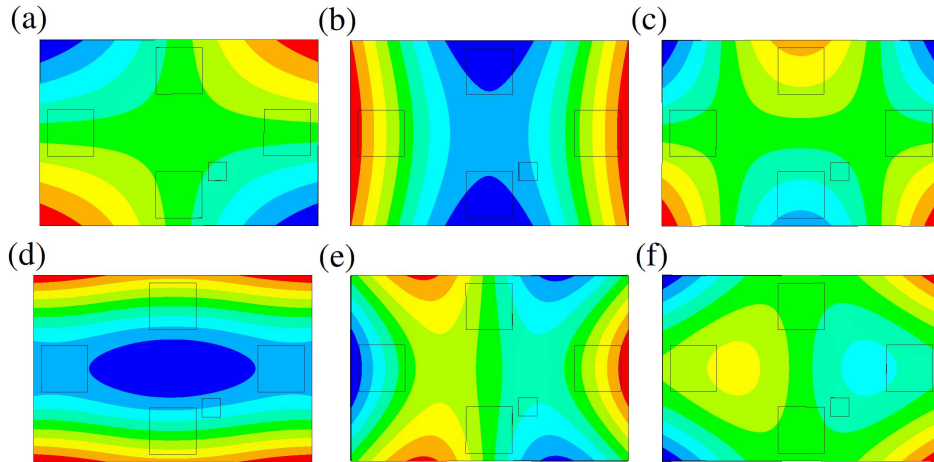


Figure 2.10. Vibration mode 1-6 (a-f) of free plate with five piezoceramic patch pairs.

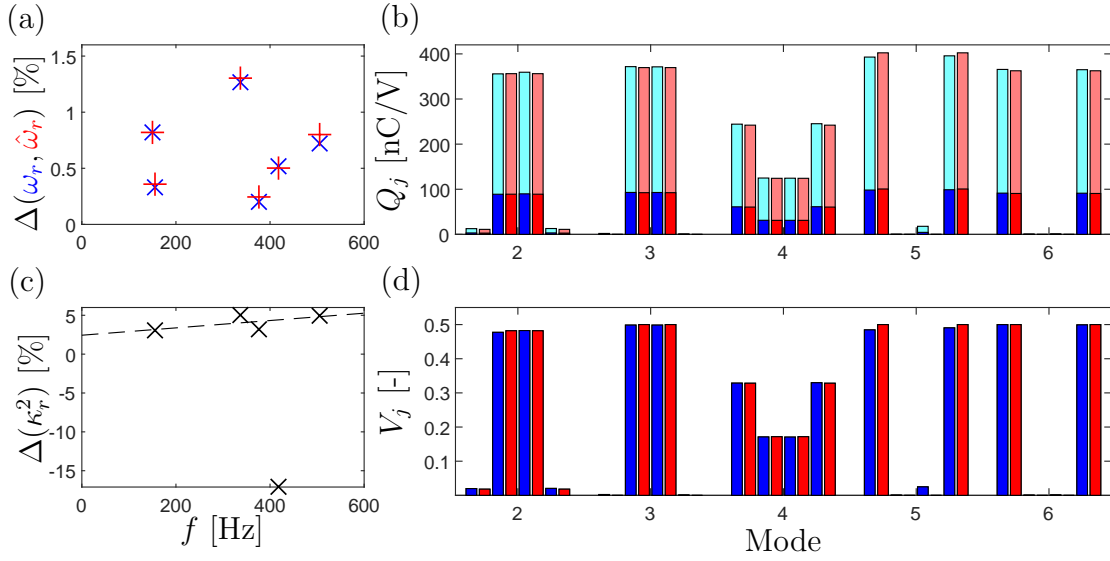


Figure 2.11. Relative deviation for (a) the SC and OC frequencies and (c) the effective EMCC of the free plate and (b,d) the modal charge and voltage based on the 3D ANSYS (blue) and plate-piezo (red) models for the OP-SW (dark) and SP-PW (light) absorbers.

from Figure 2.11(a) as for the free beam, which may be due to the higher complexity of the free plate structure. However, a linear increase of the relative error on the effective EMCCs in Figure 2.11(c) can be seen, when the 5th resonant mode with low electromechanical coupling is neglected.

Finally, the normalized modal SC charge and OC voltage have been provided in Figure 2.11(b,d) for the four piezoelectric absorbers. Again, the normalized modal voltages in Figure 2.11(d) indicate the authority of the individual absorbers on the specific vibration mode  $j$ . It is thus seen that the absorbers 2, 3 have authority on modes 2, 3 and 4, while the absorbers 1, 4 contribute to the electromechanical coupling for modes 4, 5 and 6. The same observations may be obtained from the corresponding mode shapes in Figure 2.10 considering which piezoelectric absorbers experience maximum curvature for the structure vibrating in the specific vibration mode.



### 3. RESONANT SHUNT DAMPING

The resonant shunt initially proposed in [18] consists of an inductance ( $L$ ) and a resistance ( $R$ ) wired in parallel [53] or in series [20]. The resonant shunt is then wired to the interface electrodes of the piezoelectric element(s) to form the resonant piezoelectric absorber, which acts as an equivalent mechanical inerter-based absorber [24] with stiffness, inertance and damping, respectively, represented by the inverse piezoelectric capacitance ( $1/\bar{C}_p^S$ ), shunt inductance ( $L$ ) and shunt resistance ( $R$ ). The absorber frequency hereby follows from the inverse product of the piezoelectric capacitance and shunt inductance, which is tuned by  $L$  to a target mode  $r$  of the vibrating structure. The piezoelectric absorber stiffness given by the inverse of the blocked piezoelectric capacitance is therefore an essential parameter for piezoelectric shunt tuning and decisive for the final level of attainable damping. Hence, the piezoelectric absorber performance may be enhanced by reducing the inherent piezoelectric capacitance by adding an active negative capacitance [9, 13, 7] to the resonant shunt. In the present work the focus has been on the pure passive resonant shunt, whereby the blocked capacitance is considered as a constant property.

The optimum tuning of pure resonant shunts has been studied extensively in the literature. Initially, by assuming a single-mode approximation of the electromechanical structure [20, 53, 38, 10, 55, 49, 22, 45] and subsequently by including the contribution from the non-resonant vibration modes in [13, 23, 24, 19]. In [P1] the optimum shunt tuning method with flexibility and inertia corrections for the non-resonant vibration modes [24] is verified by the numerical analysis of a cantilever beam [48, 49, 14] and a simply supported plate [19] by use of the developed plate-piezo FE-model. Furthermore, an alternative tuning method based on the SC and OC frequencies and the two split mode frequencies obtained for the pure  $L$ -shunt is proposed. In [C1] and [P2] the latter tuning method is implemented in the commercial FE-software ANSYS and analyzed for the same cantilever beam and simple supported plate used in [P1]. Furthermore, in [P2] the damping of plate vibrations by use of multiple interconnected piezoceramic patch pairs has been analyzed. Finally, in [P3] a shunt tuning method, based on the modal absorber response in the SC and OC limits, is derived for  $N_p$  piezoelectric absorbers damping a single or multiple target vibration modes of a simply supported beam. Subsequently, this method has been implemented experimentally in [P4].

In chapter 2 the same governing vibration problem (2.23) for a structure with  $N_p$  piezoelectric absorbers was obtained for the developed plate-piezo and the 3D

ANSYS models and the two limiting eigenvalue problems associated with SC and OC piezoelectric electrodes were analyzed. In the present chapter, the electric charge in the bottom equation of the general vibration problem (2.23) is eliminated by the shunt impedance  $Z$  and voltage  $V$ , whereby the optimum shunt tuning is obtained by introducing a modal representation of the mechanical displacements.

### 3.1 Single piezoelectric absorber

In [P1], [P2] and [C1] the optimum tuning of a single piezoelectric absorber attached to a vibrating structure is considered. It is here the aim to accurately represent the behavior of the full vibrating structure in Figure 3.1(a) around a target mode  $r$  by the modal reduced system in Figure 3.1(b). A modal representation of the mechanical displacements in (2.23) is therefore introduced by  $\{U\} = [U]\{v\}$ , where the matrix  $[U]$  contains the SC mode shapes  $\{U_j\}$  as columns and  $\{v\}$  represents the  $N$  modal coordinates  $v_j$ . Hereby the top set of mechanical equations in (2.23) uncouple and may be written for vibration mode  $j$  as

$$(\omega_j^2 - \omega^2)v_j - \frac{Q_j}{m_j}V = 0, \quad j = 1, 2, \dots, N \quad (3.1)$$

Furthermore, the bottom electric equation in (2.23) can be written as

$$\sum_{j=1}^N Q_j v_j = Q - \bar{C}_p^S V \quad (3.2)$$

which is seen to depend on the full range of modal charges  $Q_j$ . The evaluation of all modal charges is inconvenient and may be associated with high computational costs, whereby a truncation of the sum in (3.2) may be required. It follows from the modal mechanical equations in (3.1) that  $v_j$  is proportional to the voltage  $V$ ,

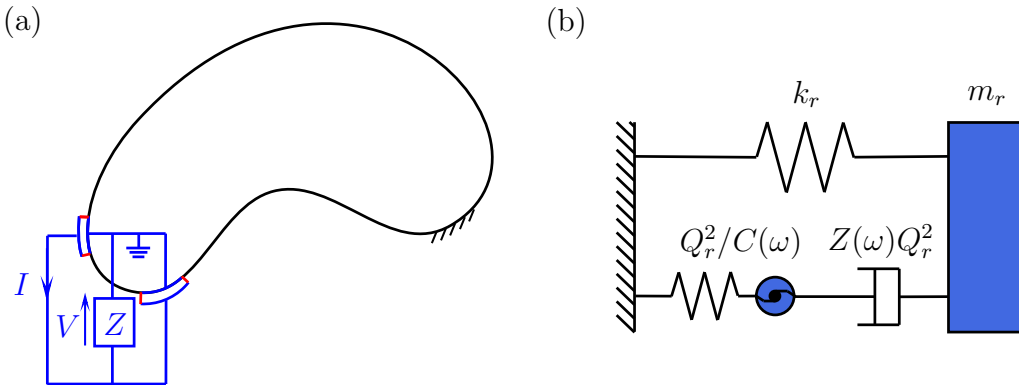


Figure 3.1. Vibrating structure with (a) a single piezoelectric absorber and (b) the corresponding modal reduced model. Frequency dependency of  $Z(\omega)$  is omitted in (a).

whereby the sum over the non-resonant vibration modes in (3.2) contributes with an additional frequency dependent term to the blocked capacitance

$$Q_r v_r = Q - \left( \bar{C}_p^S + \sum_{j \neq r}^N \frac{Q_j^2}{m_j \omega_j^2} \frac{\omega_j^2}{\omega_j^2 - \omega^2} \right) V = Q - C(\omega) V \quad (3.3)$$

The main challenge is hereby associated with the approximation of the frequency dependent effective capacitance  $C(\omega)$  representing the inherent blocked piezoelectric capacitance and the spill-over from the residual vibration modes.

### Residual modes contribution from modified system matrices

In [P1] the electric equivalence to the flexibility and inertia correction terms in [31] is used to approximate the effective capacitance by

$$C(\omega) = \bar{C}_p^S + C'_r - \frac{1}{\omega^2 L'_r} = C_R - \frac{1}{\omega^2 L'_r} \quad (3.4)$$

where  $C_R$  is the flexibility corrected capacitance and  $C'_r$  and  $L'_r$ , respectively represent a correction capacitance and an inductance effect around the target mode  $r$ . These may be evaluated according to [P1] as

$$\begin{aligned} C'_r &= \{k_{me}^E\}^t [K_r]^{-1} [K^E] [K_r]^{-1} \{k_{me}^E\} - \frac{Q_r^2}{\omega_r^2 m_r} \\ \frac{\omega_r^2}{L'_r} &= \{k_{me}^E\}^t [K_r]^{-1} [K^E] [K_r]^{-1} \{k_{me}^E\} - \{k_{me}^E\}^t [K_r]^{-1} \{k_{me}^E\} \end{aligned} \quad (3.5)$$

in which the modified stiffness and mass matrices follow by removing the mass contribution from the target mode  $r$  and making a frequency shift of the stiffness matrix

$$[K_r] = [K^E] - \omega_r^2 [M_r] \quad , \quad [M_r] = [M] - \frac{([M]\{U_r\})([M]\{U_r\})^t}{\{U_r\}^t [M] \{U_r\}} \quad (3.6)$$

By neglecting the non-resonant inertia contribution the pure quasi-static residual mode correction is obtained by  $[K_r] = [K^E]$  in (3.5a).

As demonstrated in [P1] the modal reduced characteristic equation for the target mode  $r$  can hereby be written as

$$\frac{\omega_r^2}{\omega_r^2 - \omega^2} \kappa_R^2 + \frac{1}{i\omega Z(\omega) C_R} - \frac{1}{\omega^2 L'_r C_R} + 1 = 0 \quad (3.7)$$

after eliminating the modal coefficient between (3.3) and (3.1) and introducing the flexibility corrected modal EMCC

$$\kappa_R^2 = \frac{Q_r^2}{m_r C_R \omega_r^2} \quad (3.8)$$

in which the modal mass  $m_r$  is conveniently normalized to unity. Subsequently, the optimum shunt tuning follows in [P1] by considering the specific shunt impedance  $Z(\omega)$  and the principle of equal modal damping [30]. Hereby the shunt inductance is found to depend on the effective capacitance  $C(\omega_r)$  at the SC frequency, while the shunt resistance is tuned by the flexibility corrected capacitance  $C_R$ .

The evaluation of the two non-resonant correction terms in (3.5) provides a robust shunt tuning as demonstrated in [24] and [P1]. However, the method requires that the full electromechanical mass and stiffness matrices are available and simple to modify, which may not be the case when using commercial FE-software. An alternative method for the evaluation of the non-resonant correction parameters in (3.5) has therefore been suggested in [P1] and implemented in the FE-software ANSYS in [C1] and [P2].

### Residual modes contribution from frequencies

The alternative method considers the SC (2.28) and OC (2.30) eigenvalue problems and a third eigenvalue problem associated with the pure  $L$ -shunted piezoelectric absorber. Initially, the same modal approximation in (3.3) is assumed, whereby a governing modal equation is obtained by substituting the modal coefficient  $v_r$  into (3.1),

$$\frac{\omega_r^2 - \omega^2}{\omega_r^2} (Q - C(\omega)V) - \frac{Q_r^2}{m_r \omega_r^2} V = 0 \quad (3.9)$$

This governing equation is then considered in the OC limit with  $Q = 0$ , whereby a modal effective capacitance

$$C_r = C(\hat{\omega}_r) = \frac{Q_r^2}{m_r \kappa_r^2 \omega_r^2} \quad (3.10)$$

may be obtained from the SC and OC frequencies in  $\kappa_r^2$  (2.32) and the modal SC charge  $Q_r$  (2.29) and mass  $m_r$ . As demonstrated in [P1], and previously described, the optimum shunt inductance depends on the effective capacitance  $C(\omega_r)$  at the SC frequency. The pure parallel tuned  $L$ -shunt is thereby introduced by

$$L = \frac{1}{C(\omega_r)\omega_r^2} \simeq \frac{1}{C_r\omega_r^2} \quad (3.11)$$

in which the last approximation  $C(\omega_r) \simeq C_r$  is valid for most practical cases with a limited change in the SC to OC frequencies. The inductance correction  $L'_r$  hereby vanishes in the corresponding characteristic equation, obtained from (3.9), as

$$\omega^4 - (2 + \kappa_R^2)\omega_r^2\omega^2 + \omega_r^4 = 0 \quad (3.12)$$

after elimination of the charge  $Q$  by the impedance relation for the pure  $L$ -shunt. The product and sum of the solutions  $\omega_+^2$  and  $\omega_-^2$  to (3.12) can be written as

$$\omega_+^2\omega_-^2 = \omega_r^4 \quad , \quad \omega_+^2 + \omega_-^2 = (2 + \kappa_R^2)\omega_r^2 \quad (3.13)$$

whereby an alternative flexibility corrected modal EMCC (3.8) is obtained by eliminating  $\omega_r^2$  in (3.13)

$$\kappa_R^2 = \frac{(\omega_+ - \omega_-)^2}{\omega_+ \omega_-} \quad (3.14)$$

The solutions  $\omega_+$  and  $\omega_-$  are the emerging split mode frequencies for the pure  $L$ -shunt, which may be obtained by evaluating the associated eigenvalue problem

$$\left( \begin{bmatrix} K^E & k_{me}^E \\ 0 & 1 \end{bmatrix} - \omega^2 \begin{bmatrix} M & 0 \\ -(k_{me}^E)^t L & \bar{C}_p^{SL} \end{bmatrix} \right) \begin{Bmatrix} U \\ V/L \end{Bmatrix} = \begin{Bmatrix} 0 \\ 0 \end{Bmatrix} \quad (3.15)$$

Hereby the flexibility corrected capacitance  $C_R$ , used for the shunt resistance tuning, is determined from (3.8) by use of the flexibility corrected modal EMCC in (3.14). The capacitance and inductance correction terms for the non-resonant vibration modes (3.5) are thereby simply determined, respectively, as the differences between the flexibility corrected  $C_R$  and blocked  $\bar{C}_p^S$  capacitances and the effective modal  $C_r$  and flexibility corrected  $C_R$  capacitances. The optimum shunt tuning with correction from the residual vibration modes may therefore be obtained by evaluation of the three eigenvalue problems associated with the SC, OC and  $L$ -shunted piezoelectric absorber, which in [C1] and [P2] have been rather easy to implement in commercial FE-software. Furthermore, it was shown in [C1] that the optimum shunt tuning for all practical damping applications may be based exclusively on the effective modal capacitance  $C_r$ , whereby the specific inertia effect from the non-resonant vibration modes is neglected. Using this assumption the correction spring-inerter system  $Q_r^2/C(\omega)$  in Figure 3.1(b) is replaced by a single spring with the stiffness  $Q_r^2/C_r$ , whereby the optimum shunt tuning is obtained from the results of the SC and OC eigenvalue problems.

### 3.2 Multiple piezoelectric absorbers

In [P3] multiple piezoelectric absorbers is considered, see Figure 3.2. The scalar quantities in (3.1) and (3.3) are thereby replaced by matrices and vectors containing the electric properties and DOFs for each piezoelectric absorber. The equations for target mode  $r$  may then be written as

$$\begin{aligned} (\omega_r^2 - \omega^2)v_r - \frac{\{Q_r\}^t}{m_r}\{V\} &= 0 \\ \{Q_r\}v_r + [C(\omega)]\{V\} &= \{Q\} \end{aligned} \quad (3.16)$$

in which  $[C(\omega)]$  contains the effective blocked capacitances in  $[C_p]$  and the contribution from the non-resonant vibration modes. By assuming  $[C(\omega)]$  as diagonal the electric equations in (3.16) decouple, whereby the characteristic equation for the piezoelectric absorber  $i$  follows by elimination of  $v_r$  in (3.16) and  $\{Q\}$  by the impedance relation  $\{V\} = [Z(\omega)]\{Q\}$ ,

$$\frac{\omega_r^2 - \omega^2}{\omega_r^2} \left( \frac{(\hat{V}_r)_i}{i\omega Z_i(\omega)\{\hat{V}_r\}^t\{Q_r\}} + \frac{(\hat{V}_r)_i C_i(\omega)}{\{\hat{V}_r\}^t\{Q_r\}} \right) + \frac{(Q_r)_i}{m_r \omega_r^2} = 0 \quad (3.17)$$

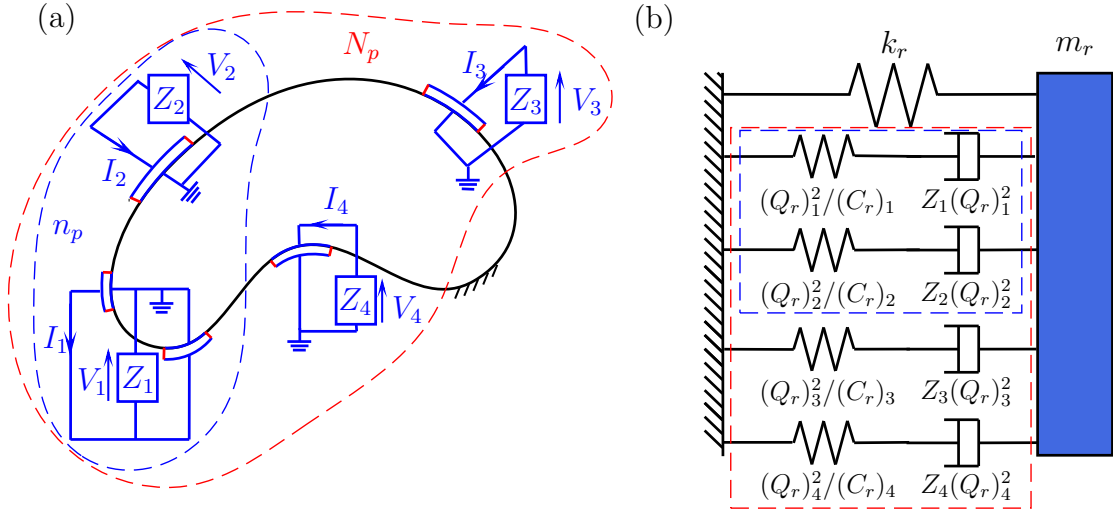


Figure 3.2. Vibrating structure with (a) four piezoelectric absorbers and (b) the corresponding modal reduced model. Frequency dependency of  $Z_i(\omega)$  is omitted.

This characteristic equation is then considered in the OC limit with  $Z_i(\omega) \rightarrow \infty$  in order to determine the effective modal capacitance for the piezoelectric absorber  $i$ ,

$$(C_r)_i = C_i(\hat{\omega}_r^2) = \frac{\{\hat{V}_r\}^t \{Q_r\}}{m_r \omega_r^2} \frac{\omega_r^2}{\hat{\omega}_r^2 - \omega_r^2} \frac{(Q_r)_i}{(\hat{V}_r)_i} \quad (3.18)$$

Using a combined modal projection by multiplying the OC eigenvalue problem in (2.30) with the SC mode shape  $\{U_j\}$  an alternative expression for the effective EMCC in (2.32) is in [P3] obtained as

$$\kappa_j^2 = -\frac{\{Q_j\}^t \{\hat{V}_j\}}{\tilde{m}_j \omega_j^2} \quad (3.19)$$

in which  $\tilde{m}_j$  is an intermediate modal mass. Considering this effective EMCC for the target mode  $r$  it is seen that the expression for the modal effective capacitance (3.18) may be reduced to

$$(C_r)_i = -\frac{(Q_r)_i \tilde{m}_r}{(\hat{V}_r)_i m_r} \simeq -\frac{(Q_r)_i}{(\hat{V}_r)_i} \quad (3.20)$$

where the last approximation  $\tilde{m}_r \simeq m_r$  is valid for most practical problems with limited electromechanical coupling. The effective modal capacitance given by the ratio of the modal SC charge to OC voltage is convenient since it is independent of any specific mode shape normalization, required in (3.10), as long as the SC and OC mode shapes are equally scaled. This also enables the effective modal capacitance (3.20) to be determined directly from experimental measurements as discussed in chapter 4. In [P3] the specific non-resonant inertia effect is neglected, whereby the structure with multiple piezoelectric absorbers in Figure 3.2(a) may be represented

by the reduced mechanical system in Figure 3.2(b), where the effect of the non-resonant vibration modes are contained in the modal effective capacitances  $(C_r)_i$ .

As suggested in [P2] and previously discussed in [42, 13, 43, 7] the effective modal capacitance  $(C_r)_i$  may in many cases be approximated accurately by the static capacitance  $(C_p^0)_i$  measured at low frequency for the piezoelectric absorber bonded to the structure. Numerically the static capacitance may be obtained by applying a voltage between the absorber interface electrodes and solving the associated static problem to determine the corresponding absorber charge response. The static capacitance thereby follows by an expression similar to (3.20)

$$(C_p^0)_i = -\frac{(Q_s)_i}{(V_s)_i} = (C_p^S)_i + \{k_{me}^E\}_i^t [K^E] \{k_{me}^E\}_i \quad (3.21)$$

in which the static charge  $(Q_s)_i$  and voltage  $(V_s)_i$  replaces the modal quantities  $(Q_r)_i$  and  $(\hat{V}_r)_i$ , while it may also be determined by an expression similar to the pure flexibility correction (3.5a), without considering the target modal stiffness  $Q_r^2/(\omega_r^2 m_r)$ .

### 3.3 Single-mode damping

In [P1-P3] the principle of equal modal damping [29, 30] has been considered for the derivation of an optimum resonant shunt tuning. Initially, the characteristic equation for the modal reduced system is derived for either the parallel or the series shunt, which is then compared with the generic equation from [30],

$$\frac{\omega^4}{\omega_r^4} - (2 + 4\chi^2) \frac{\omega^2}{\omega_r^2} + 1 + 4i\lambda\chi \frac{\omega}{\omega_r} \left(1 - \frac{\omega^2}{\omega_r^2}\right) = 0 \quad (3.22)$$

with  $i = \sqrt{-1}$  denoting the imaginary unit. This generic equation ensures equal modal damping through the tuning of the shunt inductance  $L$ , while the subsequent tuning of the shunt resistance  $R$  by  $\lambda = 1/\sqrt{2}$  balances large attainable damping and effective vibration amplitude mitigation.

For a vibrating structure with multiple piezoelectric absorbers (Figure 3.2(a)) the characteristic equation of the modal reduced system considering both the non-resonant flexibility and inertia effects may be written as

$$\left(1 - \frac{\omega^2}{\omega_r^2}\right) \left[ \frac{\omega^2}{\omega_r^2} - i \frac{\omega}{\omega_r} \sum_{i=1}^{N_p} \frac{(\hat{V}_r)_i (Q_r)_i}{\{\hat{V}_r\}_i^t \{Q_r\}_i} \left( \frac{1}{Z_i(\omega)} + \frac{1}{i\omega(L_r)_i} \right) \frac{1}{(C_R)_i \omega_r} \right] + \kappa_R^2 \frac{\omega^2}{\omega_r^2} = 0 \quad (3.23)$$

The optimum shunt tuning then follows by inserting the parallel or series shunt impedance  $Z_i(\omega)$  and writing the characteristic equation in accordance with the generic form (3.22). This is done in [24] and [P1] for the single piezoelectric absorber, where the extension to multiple absorbers is straightforward. However, as demonstrated in [C1] the specific non-resonant inertia effect does not improve the shunt damping performance for most practical cases. Furthermore, for simplicity, the modal reduced system in Figure 3.2(b), deliberately neglecting the specific

non-resonant inertia correction, is considered in the following. The characteristic equation for the modal reduced system in Figure 3.2(b) can be written as

$$\left(1 - \frac{\omega^2}{\omega_r^2}\right) \left(\frac{\omega^2}{\omega_r^2} - i \frac{\omega}{\omega_r} \sum_{i=1}^{N_p} \frac{(\hat{V}_r)_i (Q_r)_i}{\{\hat{V}_r\}^t \{Q_r\}} \frac{1}{Z_i(\omega) (C_r)_i \omega_r}\right) + \kappa_r^2 \frac{\omega^2}{\omega_r^2} = 0 \quad (3.24)$$

in which the effective modal capacitances  $(C_r)_i$  and the effective EMCC  $\kappa_r^2$  replaces, respectively, the flexibility corrected capacitances  $(C_R)_i$  and EMCC  $\kappa_R^2$  in (3.23), while the inertia terms  $(L'_r)_i$  vanishes.

### Parallel shunt

The parallel shunt is equivalent to a series connection of a mechanical dashpot and inerter as seen in Figure 3.3(a), whereby the impedance relation is conveniently expressed in terms of the inverse of the individual contributions,

$$\frac{1}{Z_i^p(\omega)} = \frac{1}{R_i^p} + \frac{1}{i\omega L_i^p} \quad (3.25)$$

with superscript  $p$  referring to the parallel shunt. This impedance is then used in (3.24), which hereby can be written in accordance with the generic form (3.22) as

$$\begin{aligned} \frac{\omega^4}{\omega_r^4} - \left(1 + \kappa_r^2 + \sum_{i=1}^{N_p} \frac{(\hat{V}_r)_i (Q_r)_i (C_r)_i}{\{\hat{V}_r\}^t \{Q_r\} L_i^p \omega_r^2}\right) \frac{\omega^2}{\omega_r^2} + \sum_{i=1}^{N_p} \frac{(\hat{V}_r)_i (Q_r)_i (C_r)_i}{\{\hat{V}_r\}^t \{Q_r\} L_i^p \omega_r^2} \\ + i \frac{\omega}{\omega_r} \sum_{i=1}^{N_p} \frac{(\hat{V}_r)_i (Q_r)_i (C_r)_i}{\{\hat{V}_r\}^t \{Q_r\} R_i^p \omega_r} \left(1 - \frac{\omega^2}{\omega_r^2}\right) = 0 \end{aligned} \quad (3.26)$$

Comparing this characteristic equation with the generic equation (3.22) it is readily seen that the constant term should equal unity, which may only be secured by

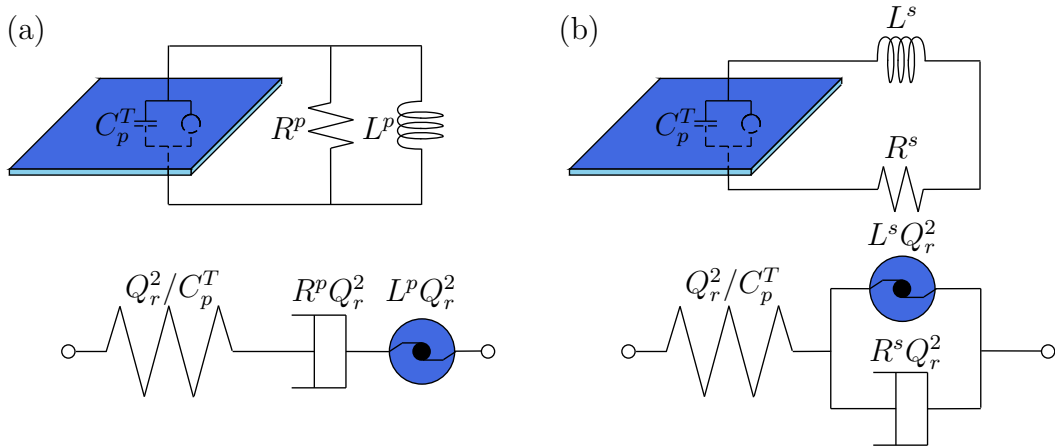


Figure 3.3. Parallel (a) and series (b) shunted piezoceramic patch with free capacitance  $C_p^T$  and their mechanical equivalent systems.

a proper tuning of the shunt inductances  $L_i^p$ . This is achieved by balancing the individual inductance  $L_i^p$  with the respective effective modal capacitance  $(C_r)_i$  and the target mode frequency  $\omega_r$ ,

$$L_i^p = \frac{1}{(C_r)_i \omega_r^2} \quad , \quad R_i^p = \frac{1}{(C_r)_i \omega_r} \sqrt{\frac{1}{2\kappa_r^2}} \quad (3.27)$$

while the optimum resistance is obtained by identifying  $\chi = \kappa_r^2/4$  and comparing the odd-power terms in (3.22) and (3.26).

The optimum parallel inductance tuning (3.27) based on the principle of equal modal damping secures the inverse point relation in (3.13a) for  $R_p \rightarrow \infty$ , whereby the roots for decreasing resistance follow a semicircle into the complex plane until the two root trajectories meet in a bifurcation point, as shown for the single piezoelectric absorber in Figure 3.4(a). Hereafter, one root becomes heavily damped when approaching the imaginary axis, while the other root becomes undamped when terminating at the SC solution for  $R^p \rightarrow 0$ . According to the principle of equal modal damping [30] the optimum resistance is subsequently tuned to secure a reasonable compromise between large modal damping and effective response mitigation, which is obtained in the points on the semi-circle (red crosses) in Figure 3.4 for  $\lambda = 1/\sqrt{2}$ , which are approximately located on the  $\pm 45^\circ$  lines from the SC frequency  $\omega_r$ . The attainable damping may hereby be estimated as  $\zeta_r = \sqrt{1/8\kappa_r^2}$ , while the tuning causes a flat plateau in the absorber response amplitude with unit magnitude, when normalized by the applied modal load  $\{f_r\} = [M]\{U_r\}$ , as seen in Figure 3.4(c). The corresponding normalized structural displacements (red curve) in Figure 3.4(b) are further seen to have a nearly flat plateau around the target mode  $r$  at the level of the dynamic amplification factor  $|\text{DAF}| = 1/(2\zeta_r)$ . Furthermore, the three (dashed, blue, red) curves in Figure 3.4(b) are seen to intersect for two neutral frequencies, at which the structural response is independent of the applied resistance and that the response to the pure  $L$ -shunt (blue line) exhibits a clear anti-resonance point at  $\omega = \omega_r$ , indicating that the inverse point relation in (3.13a) is fulfilled.

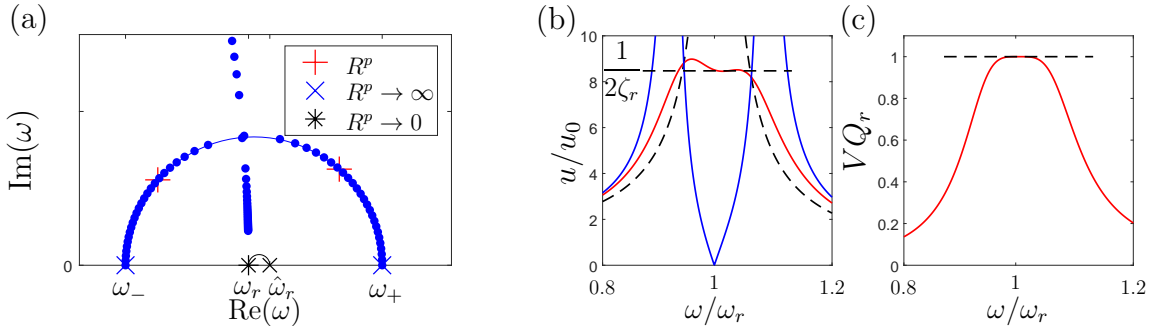


Figure 3.4. Parallel shunt tuning analyzed by (a) root-locus diagram, (b) the normalized displacements for the SC (---),  $L$  (—) and  $LR$ -shunted (—) piezoelectric absorbers and (c) the corresponding  $LR$ -shunted absorber voltage response.

### Series shunt

The series shunt is equivalent to a mechanical dashpot and inerter connected in parallel as shown in Figure 3.3(b), whereby the impedance relation is simply given by the sum of the individual components,

$$Z_i^s(\omega) = R_i^s + i\omega L_i^s \quad (3.28)$$

in which superscript  $s$  refers to the series shunt. This is now used in (3.24), which then can be written in accordance with the generic form (3.22) as

$$\begin{aligned} \frac{\omega^4}{\hat{\omega}_r^4} - \left( 1 + \sum_{i=1}^{N_p} \frac{\{\hat{V}_r\}^t \{Q_r\} (C_r)_i}{(\hat{V}_r)_i (Q_r)_i L_i^s \hat{\omega}_r^2} \right) \frac{\omega^2}{\hat{\omega}_r^2} + \sum_{i=1}^{N_p} \frac{\{\hat{V}_r\}^t \{Q_r\} (C_r)_i}{(\hat{V}_r)_i (Q_r)_i L_i^s \hat{\omega}_r^2 (1 + \kappa_r^2)} \\ + i \frac{\omega}{\hat{\omega}_r} \frac{\sum_{i=1}^{N_p} (Q_r)_i^2 R_i^s}{\sum_{i=1}^{N_p} (Q_r)_i^2 L_i^s \hat{\omega}_r} \left( 1 - \frac{\omega^2}{\hat{\omega}_r^2} \right) = 0 \end{aligned} \quad (3.29)$$

and conveniently expressed in terms of the OC frequencies  $\hat{\omega}_r$ , as discussed in [P3]. The series inductance tuning hereby follows by balancing the individual inductance  $L_i^s$  with the respective effective modal capacitance  $(C_r)_i$  and the altered OC frequency  $\hat{\omega}_r^2(1 + \kappa_r^2)$ ,

$$L_i^s = \frac{1}{(C_r)_i \hat{\omega}_r^2 (1 + \kappa_r^2)} \quad , \quad R_i^s = \frac{1}{(C_r)_i \hat{\omega}_r (1 + \kappa_r^2)} \sqrt{2\kappa_r^2} \quad (3.30)$$

while the series resistance is obtained by identifying  $\chi = \kappa_r^2/4$ , inserting the series inductance in (3.29) and comparing the odd-power terms with those in (3.22).

For the series shunt, the inductance is now tuned such that the two split mode frequencies  $\omega_-$  and  $\omega_+$  for  $R^s \rightarrow 0$  are inverse points to the altered OC frequency  $\hat{\omega}_r \sqrt{1 + \kappa_r^2}$ , whereby the roots for increasing resistance in Figure 3.5(a) follow a semicircle into the complex plane, similarly to the parallel shunt. After the root trajectories meet in a bifurcation point, they split into a heavily damped and an undamped trajectory, with the latter terminating at the OC solution  $\hat{\omega}_r$  for  $R^s \rightarrow \infty$ ,

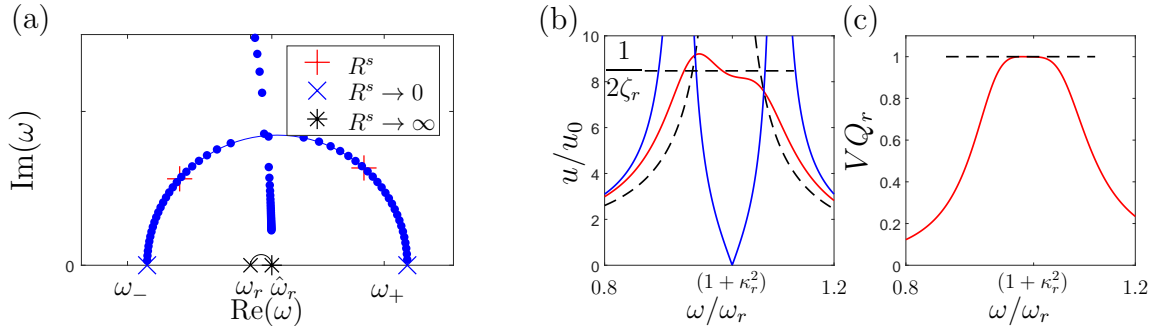


Figure 3.5. Series shunt tuning analyzed by (a) root-locus diagram, (b) the normalized displacements for the OC (--) ,  $L$  (—) and  $LR$ -shunted (—) piezoelectric absorbers and (c) the corresponding  $LR$ -shunted absorber voltage response.

see Figure 3.5(a). It is again seen that the optimum resistance based on the principle of equal modal damping causes a completely flat plateau in the absorber response amplitude in Figure 3.5(c) and a nearly flat plateau for the displacement response (red curve) in Figure 3.5(b) at a level close to the DAF. For the series shunt it is seen that the response curves for the  $L$ - (blue curve) and  $LR$ -shunted (red curve) absorber now intersect with the OC frequency response (black dashed curve) in Figure 3.5(b). Furthermore, the frequency response for the pure  $L$ -shunted absorber (blue curve) in Figure 3.5(b) exhibits an anti-resonance point at  $\omega = \omega_r(1 + \kappa_r^2) = \hat{\omega}_r\sqrt{1 + \kappa_r^2}$ , verifying the inverse point relation for the series shunt.

### 3.4 Multi-mode damping

When only a subset  $n_p \leq N_p$  of the piezoelectric absorbers in Figure 3.2 are calibrated with respect to target mode  $r$ , the single mode tuning presented in the previous section may not be optimal. This is primarily due to the resistance tuning, which is inversely and directly proportional to the effective EMCC for the parallel and the series shunts, respectively. The inductance tuning on the other hand is only affected by the minor frequency shift occurring due to the effect of the piezoelectric absorbers not tuned to the target mode  $r$ . This may be accounted for by considering these non-resonant absorbers in the SC or OC condition corresponding to, respectively, releasing and blocking the absorbers in Figure 3.2(b). Two methods for the multi-mode tuning have been suggested in [P3], one which only considers the change of the resistance tuning due to the lower electromechanical coupling for the target mode  $r$  and another that considers the influence on both the inductance and resistance tuning from the SC or OC non-resonant piezoelectric absorbers.

#### Modified single-mode calibration

By assuming that the frequency shift caused by the non-resonant absorbers is negligible, the single-mode tuning of the shunt inductances is still considered to provide the optimum absorber frequency tuning. However, when fewer piezoelectric ab-

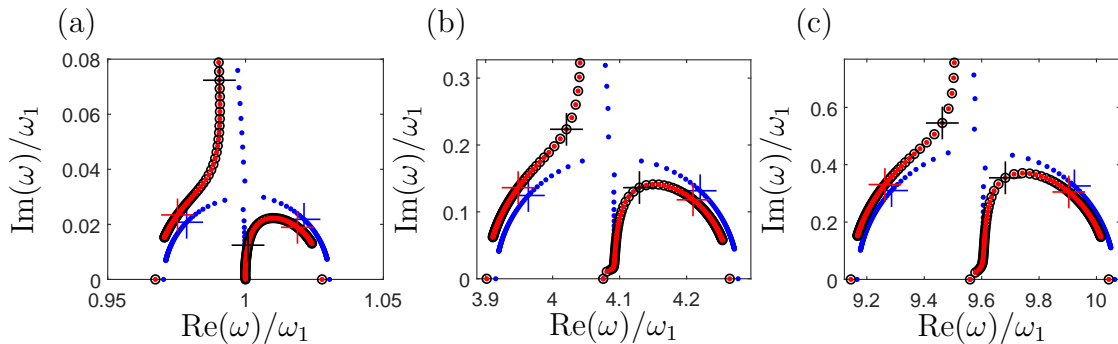


Figure 3.6. Root-locus diagram for simultaneous three mode damping of a simple supported beam, plotted around mode 1 (a), 2 (b) and 3 (c), for the single- ( $\circ, +$ ), modified single- ( $\bullet, +$ ) and multi-mode ( $\bullet, +$ ) calibrations with varying and optimum resistance, [P3].

sorbers contribute to the overall effective electromechanical coupling this will be reduced and cause less energy to enter the individual absorber shunt. Thereby, either higher and lower resistances are required for the parallel (3.27b) and series (3.30b) shunts, respectively. A modified effective EMCC  $\tilde{\kappa}_r^2$ , which only considers the coupling contribution from the absorbers tuned to mode  $r$  should therefore be used for the resistance tuning. This modified effective EMCC may be determined directly from (3.19) as

$$\tilde{\kappa}_r^2 = - \sum_{i=1}^{n_p} \frac{(Q_r)_i(\hat{V}_r)_i}{\tilde{m}_r \omega_r^2} = \sum_{i=1}^{n_p} \frac{(Q_r)_i(\hat{V}_r)_i}{\{Q_r\}^t \{\hat{V}_r\}} \kappa_r^2 \quad (3.31)$$

whereby it depends on variables already available from the solution to the SC and OC eigenvalue problems used in the single-mode tuning. The new optimum resistance tuning for the case where  $n_p$  piezoelectric absorbers are tuned to mode  $r$  may thereby be determined by the same tuning formulas for the parallel (3.27) and series (3.30) shunts where the effective EMCC  $\kappa_r^2$  is replaced by the modified effective EMCC  $\tilde{\kappa}_r^2$ .

In Figure 3.6 the single- (black) and the modified single-mode (red) calibrations are compared in a root-locus diagram for the simultaneous damping of the three lowest simple supported beam vibration modes in [P3], for varying (dots) an optimum (crosses) resistance. It is here seen that the root trajectories do not follow a perfect semi-circle in the complex plane due the frequency shift caused by the non-resonant absorbers. Furthermore, it can be seen that the single-mode tuning causes a corresponding root (black cross) in Figure 3.6 to be lightly damped, while for the modified single-mode tuning the two roots (red crosses) in Figure 3.6 have almost equal damping.

### Multi-mode calibration

In Figure 3.6 it has been seen that the root trajectories for the single- and modified single-mode calibrations do not follow the optimum semicircle into the complex plane because of the frequency shift caused by the non-resonant piezoelectric absorbers. This frequency shift is now estimated by including the SC or OC contribution from the piezoelectric absorbers tuned to other target modes  $j \neq r$ . Both the parallel (3.27) and series (3.30) shunt tuning are inversely proportional to the SC (or OC) frequency. This means that for lower modes  $j \ll r$  the optimum shunt components are large, while for higher modes  $j \gg r$  they appear small. The resulting absolute value of the parallel (3.25) and series (3.28) shunt impedances may therefore be described as

$$\begin{aligned} |Z_i^p(\omega_r)|, |Z_i^s(\omega_r)| &\rightarrow \infty \text{ for } \omega_j \ll \omega_r \\ |Z_i^p(\omega_r)|, |Z_i^s(\omega_r)| &\rightarrow 0 \text{ for } \omega_j \gg \omega_r \end{aligned} \quad (3.32)$$

for target modes  $j$  below and above the target mode  $r$ . Hereby, it can be seen that absorbers tuned to modes below the target mode  $\omega_j < \omega_r$  approximately contribute to the structural response around  $\omega_r$  by their OC stiffness, whereby the

corresponding mechanical absorbers in Figure 3.2(b) are considered locked. Oppositely, absorbers tuned to target modes  $\omega_j > \omega_r$  may be considered to contribute to the response only by their SC stiffness, whereby the absorbers in Figure 3.2(b) are released.

A new SC and OC eigenvalue problem for each target mode  $r$  may thereby be established, considering the SC or OC contributions from the non-resonant absorbers. The new SC eigenvalue problem may thus be written as

$$\begin{aligned} ([K^E] + [k_{me}^E]_{j<r}[C_p]_{j<r}^{-1}[k_{me}^E]_{j<r}^t - \underline{\omega}_r^2[M]) \{\underline{U}_r\} &= \{0\}, \\ \{\underline{Q}_r\} &= -[k_{me}^E]_r^t \{\underline{U}_r\} \end{aligned} \quad (3.33)$$

in which the original SC stiffness is increased by the OC stiffness contribution from the piezoelectric absorbers tuned to modes below the target mode  $\omega_j < \omega_r$ . The new OC eigenvalue problem similarly follows by

$$\begin{aligned} ([K^E] + [k_{me}^E][C_p]^{-1}[k_{me}^E]^t - [k_{me}^E]_{j>r}[C_p]_{j>r}^{-1}[k_{me}^E]_{j>r}^t - \hat{\omega}_r^2[M]) \{\hat{\underline{U}}_r\} &= \{0\}, \\ \{\hat{\underline{V}}_r\} &= [C_p]_r^{-1}[k_{me}^E]_r^t \{\hat{\underline{U}}_r\} \end{aligned} \quad (3.34)$$

where the original OC stiffness is reduced by the piezoelectric absorbers tuned to higher target modes  $\omega_j > \omega_r$ . Finally, the same parallel (3.27) and series (3.30) shunt tuning can be used by replacing the original frequencies and the effective modal capacitances by the new SC  $\underline{\omega}_r$  and OC  $\hat{\omega}_r$  frequencies and effective modal capacitances determined from the new modal charges  $\{\underline{Q}_r\}$  and voltages  $\{\hat{\underline{V}}_r\}$ .

The multi-mode tuning method (blue) is compared to the single- (black) and modified single-mode (red) calibrations by the root-locus diagram in Figure 3.6 for varying (dots) an optimum (crosses) resistance [P3]. It is here seen that the root trajectories for the multi-mode shunt tuning method (blue dots) in Figure 3.6 approximately follows the semicircle into the complex plane for each vibration mode, indicating that a near optimal tuning has been achieved, when the specific SC and OC stiffness contributions from the non-resonant absorbers have been considered.

### 3.5 Numerical examples

The presented shunt tuning methods are now considered for the numerical examples introduced in chapter 2, concerning a free beam and free plate with four piezoelectric absorbers. In chapter 2 the SC and OC eigenvalue problems have been evaluated by the plate-piezo and the 3D ANSYS models. They determine the modal SC charges and OC voltages and the corresponding frequencies. In the following these tuning parameters are used to evaluate the effective modal capacitances (3.20) and optimum series shunt tuning (3.30) for the OP-SW piezoelectric absorbers, which has been considered experimentally in [P4] and chapter 4.

### Free Beam

The effective modal capacitances  $(C_r)_i$  of the OP-SW piezoelectric absorbers bonded to the free beam are evaluated from the modal charges and voltages in Figure 2.8 and shown in Figure 3.7(a) for the plate-piezo (red bars) and 3D ANSYS (blue bars) models. It is noted that the effective modal capacitances become exactly four times larger when using the SP-PW absorbers. The dark red and blue lines in Figure 3.7(a) further represent the blocked  $\bar{C}_p^S$ , static  $C_p^0$  and free  $\bar{C}_p^T$  capacitances. It can then be seen that the effective modal capacitances are in between the blocked and the free capacitance, while the static capacitance is slightly larger than the effective modal capacitances. This agrees with the findings in [42, 13, 7] where the dynamic capacitance is stated to equal the static capacitance in the static limit, while it for increasing frequency approaches the original blocked capacitance. In the present case this is indicated by the general decrease of the effective modal capacitances for the higher target modes.

As previously described the single-mode representation of the electromechanical structure leads to a shunt tuning directly dependent on the blocked capacitance  $\bar{C}_p^S$  instead of the effective modal capacitances  $(C_r)_i$  in (3.27) and (3.30). When applying this assumption, the relative error on the corresponding shunt tuning is in the present case about 30% as seen by the light red and blue bars in Figure 3.7(b). However, the blocked capacitance is not always used for the subsequent experimental validation of the proposed shunt tuning methods. Instead, the static capacitance of the piezoelectric absorber is measured and used in the final shunt tuning [38, 42, 13, 33, 8]. The static capacitance provides in most cases a much more reliable shunt tuning, particularly for low-frequency target modes, as seen in the present example, where the relative errors on the shunt tuning based on the static capacitance (dark blue and red bars) in Figure 3.7(b) are much lower than for the tuning based on the blocked capacitance. The exact series shunt tuning for the OP-SW piezoelectric

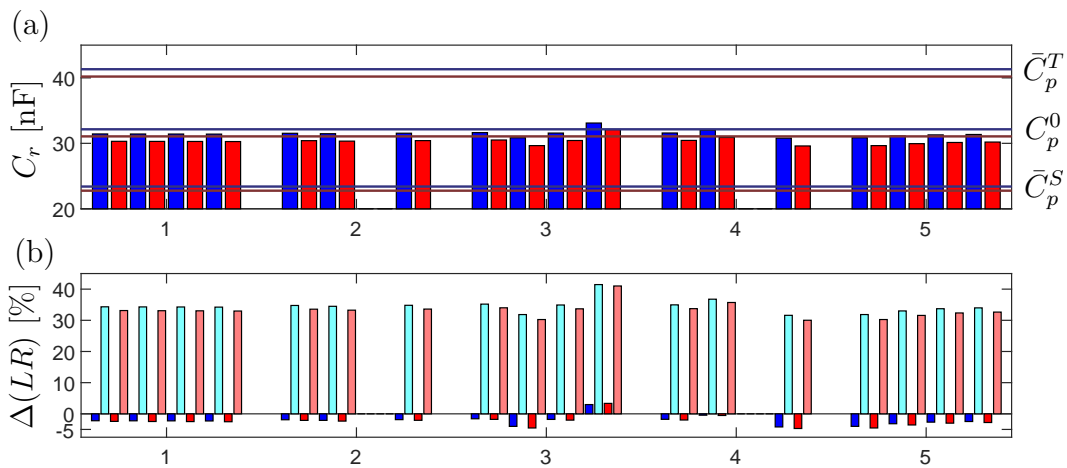


Figure 3.7. In (a) the effective modal (OP-SW) capacitance for beam mode 1-5 for the plate-piezo (red) and 3D ANSYS (blue) models, and (b) the relative deviation on the shunt tuning based on the static (dark colors) and blocked (light colors) capacitances.

Table 3.1. Series single mode tuning for free beam mode 1 to 5 by 3D ANSYS model.

Mode		1		2		3		4		5	
		$L$ [H]	$R$ [ $\Omega$ ]								
Absorber	1	29.9	6550	4.01	2260	1.07	1070	0.396	660	0.179	604
	2	29.9	6550	4.02	2270	1.09	1100	0.391	651	0.177	599
	3	29.9	6550	-	-	1.07	1070	-	-	0.176	596
	4	29.9	6560	4.01	2260	1.01	1020	0.406	676	0.176	595

absorbers based on the 3D ANSYS model are provided in Table 3.1 for the first five flexural beam vibration modes. The corresponding tuning of the SP-PW piezoelectric absorbers has not been provided, but is exactly four times lower than the OP-SW tuning. This means that the SP-PW piezoelectric absorber is often preferred as it requires a lower inductance value. Unfortunately this configuration may be impractical as the electrodes glued to the structure must be accessed.

The frequency response (FRF) to a modal load (Figure 3.8(a,b)) and an electromechanical point load (Figure 3.8(c,d)), imposed by the 5th piezoceramic patch pair in Figure 2.6, are now considered for the free beam with the piezoelectric absorbers all tuned to mode 2. From the FRF for the tip beam displacements to the modal load in Figure 3.8(a) it is seen that the optimum  $LR$ -shunt damping (solid red curve) causes a near flat plateau at the level of the DAF (horizontal dashed line) around the target mode 2. Furthermore, it is seen that the corresponding accumulated absorber voltage response (solid curves) in Figure 3.8(b) exactly retains a unit flat plateau. In the case of the electromechanical point load the absorber voltage response (solid curves) in Figure 3.8(d) inclines slightly, while a near flat plateau is still obtained for the tip beam displacements (red curve) in Figure 3.8(c). The FRFs for an absorber tuning based on the blocked capacitance  $\bar{C}_p^S$  has further

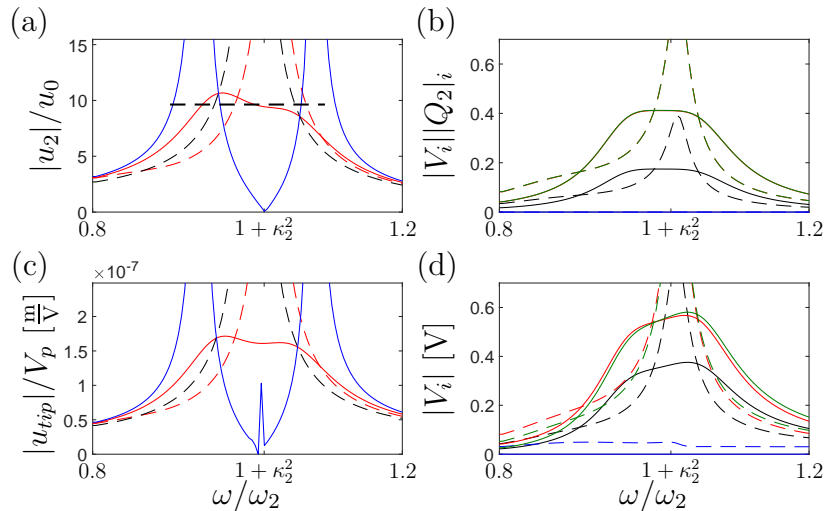


Figure 3.8. FRF to a (a,b) modal and (c,d) electromechanical point load, for the OC (---),  $L$  (—) and  $LR$ -shunted (—) piezoelectric absorbers and the tuning based on the blocked capacitance  $\bar{C}_p^S$  (---), and in (b,d) the voltage of absorber 1 (—), 2 (—), 3 (—), 4 (—).

Table 3.2. Optimum series single-, modified single- and multi-mode tuning for simultaneous damping of beam modes 2 to 5 based on the 3D ANSYS model in chapter 2.

Mode 2-5	$L_1$ [H]	$R_1$ [ $\Omega$ ]	$L_2$ [H]	$R_2$ [ $\Omega$ ]	$L_3$ [H]	$R_3$ [ $\Omega$ ]	$L_4$ [H]	$R_4$ [ $\Omega$ ]
Single	0.396	660	4.02	2270	1.07	1070	0.176	595
Modified	0.400	493	4.07	1480	1.08	741	0.180	305
Multi	0.398	487	4.07	1467	1.08	739	0.179	300

been provided (red dashed curves) in Figure 3.8, which is seen to cause a significant reduction in the shunt damping performance.

Finally, multi-mode damping is considered for the simultaneous damping of the beam flexural vibration modes 2 to 5. This is achieved by tuning the four absorbers to modes 4, 2, 3 and 5, respectively, for which the individual absorbers have significant modal charge and voltage in Figure 2.8. The corresponding optimum shunt calibrations based on the single-, modified single- and multi-mode tuning methods are provided in Table 3.2.

It is seen that the shunt inductances in Table 3.2 are almost identical for the three methods as the effect of the frequency shift caused by the non-resonant absorbers is insignificant. The resistances however are seen to vary significantly as less energy can be dissipated when only a single absorber is tuned to the specific target mode. The corresponding FRFs for the beam tip displacements and the absorber voltage response to the electromechanical point load are shown in Figure 3.9. It is seen that near flat plateaus around the four target modes in Figure 3.9(a) are obtained with the modified single- (red dashed curve) and multi-mode (solid black curve) shunt tuning methods. For the single-mode shunt tuning (red dash-dotted curve) the maximum amplitudes are seen to increase significantly, which indicates the importance of modifying the effective EMCC (3.31) according to the absorbers

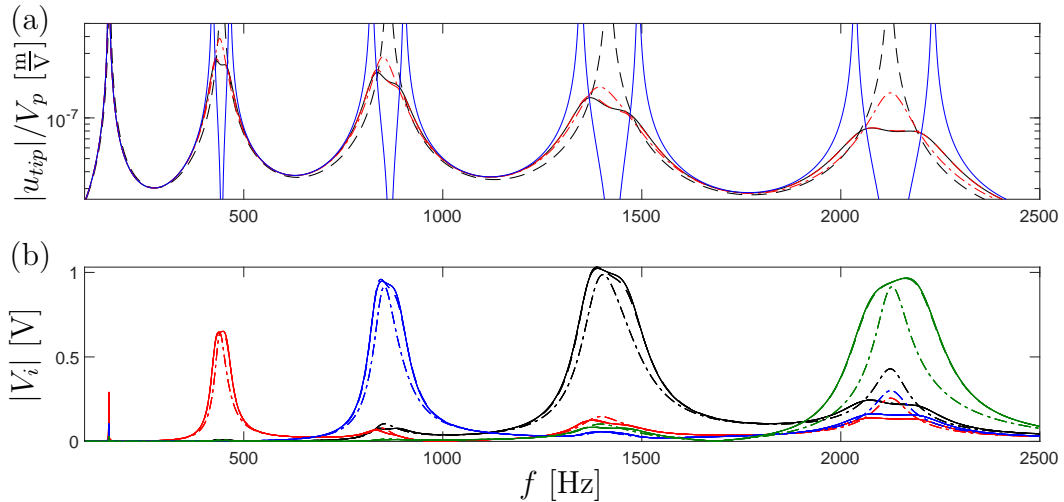


Figure 3.9. FRF for (a) tip beam displacements with OC (---), multi-mode tuned  $L$  (—) and  $LR$ -shunted (—) piezoelectric absorbers and for the single- (---) and modified single-mode (---) tuning, and (b) the voltage of absorber 1 (—), 2 (—), 3 (—), 4 (—).

tuned to the specific target mode. Furthermore, it is seen that the absorber voltage amplitudes in Figure 3.9(b) are significant only around the respective target modes.

### Free Plate

The effective modal capacitances  $(C_r)_i$  in (3.20) for the four OP-SW piezoelectric absorbers bonded to the free plate in Figure 2.9 are determined from the modal charges and voltages in chapter 2 and provided in Figure 3.10(a) for the plate-piezo (red bars) and the 3D ANSYS (blue bars) models. As it has been observed for the free beam example, the effective modal capacitances in Figure 3.10(a) are seen to be in between the blocked  $\bar{C}_p^S$  and free  $\bar{C}_p^T$  capacitances, while the static capacitance  $C_p^0$  is a bit larger than the effective capacitances. The tendency of slightly decreasing effective capacitances for the higher target modes are further seen, which causes the resonant shunt tuning based on the static capacitance to be less accurate for the higher modes (dark red and blue bars) in Figure 3.10(b). For the considered target modes the tuning based on the blocked capacitance (light red and blue bars) in Figure 3.10(b) is seen to cause significant relative deviations to the optimum tuning with residual modes contribution.

The optimum series shunt tuning, based on the 3D ANSYS model, is provided in Table 2.2 for the target vibration modes 2, 3, 4 and 6 of the free plate in Figure 2.9. The red colored values in Table 3.3 indicate the absorbers suitable for vibration mitigation of the specific target mode, based on the corresponding modal charges and voltages in Figure 2.11(c,d).

The consequence of using the static capacitance  $C_p^0$  for the shunt tuning to target mode 6 is now analyzed by the FRFs for the free plate exposed to a modal (Figure 3.11(a,b)) and an electromechanical point (Figure 3.11(c,d)) load, respectively. Again, it can be seen that the modal displacements for the optimally tuned

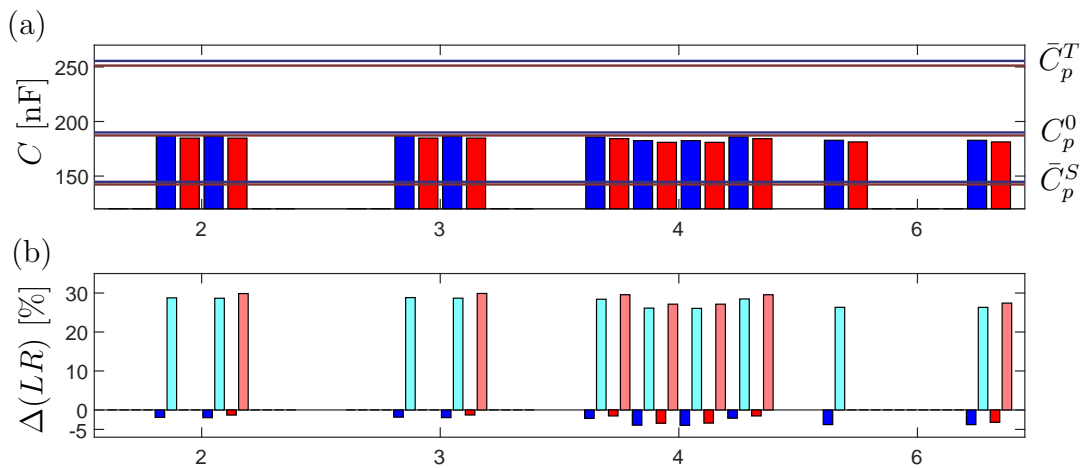


Figure 3.10. In (a) the effective modal (OP-SW) capacitance for plate mode 2, 3, 4, 6 for the plate-piezo (red) and ANSYS (blue) models, and (b) the relative deviation on the shunt tuning based on the static (dark colors) and blocked (light colors) capacitances.

Table 3.3. Series single mode tuning for free plate mode 2, 3, 4, 6 by 3D ANSYS model.

Mode		2		3		4		6	
		$L$ [H]	$R$ [ $\Omega$ ]						
Absorber	1	6.35	1210	0.842	307	0.912	517	0.509	422
	2	5.42	1030	1.16	424	0.928	527	0.516	428
	3	5.42	1030	1.16	424	0.929	527	0.836	693
	4	6.35	1210	1.15	418	0.911	517	0.509	422

absorbers (solid red curve) in Figure 3.11(a) have a near flat plateau at the level of the DAF (dashed horizontal line) and that the corresponding accumulated absorber voltage amplitudes exactly retain a unit flat plateau. For the electromechanical point load the plateaus around the target mode 6 incline slightly, while the 5th plate vibration mode also becomes visible in the FRF for the plate corner (cor) displacements and absorber voltage amplitudes in Figure 3.11(c,d). Considering the FRF for the tuning based on the static capacitance (red dashed curves) in Figure 3.11 it is seen that the shunt damping performance is slightly reduced for both the modal and electromechanical load cases. The static capacitance provides in the present case a proper shunt tuning. However, as the effective modal capacitances decrease for higher target modes, this may lead to an inaccurate shunt tuning based on the static capacitance for higher target modes.

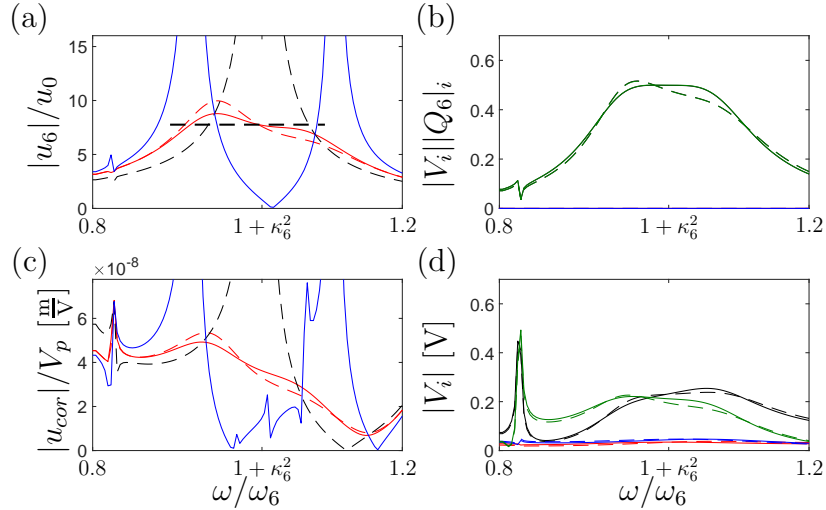


Figure 3.11. FRF to a (a,b) modal and (c,d) electromechanical point load, for the OC (---),  $L$  (—) and  $LR$ -shunted (—) piezoelectric absorbers and for the tuning based on the static capacitance  $\bar{C}_p^0$  (---), and the voltage (b,d) of absorber 1 (—), 2 (—), 3 (—), 4 (—).

## 4. EXPERIMENTAL VALIDATION

In the present chapter the experimental validation of the numerical FE-models presented in chapter 2 and implementation of the shunt tuning methods proposed in chapter 3 are considered. A good correlation between experiments and numerical FE-models is often challenged by the difficulties associated with the description of the exact structural boundary conditions, which in most cases leads to numerical overestimation of the resonance frequencies [20, 48, 50]. This may be solved by replacing the numerical supports by springs with stiffness that are updated according to the experimental results [21] or by eliminating the effect of the boundary conditions by considering unsupported structures. The latter is used in [P4], where a beam and a plate are supported by rubber bands in order to obtain free boundary conditions. Both structures are then equipped with five pairs of piezoceramic patches, where four are connected to resonant shunts in order to damp the structural vibrations excited by the remaining piezoceramic patch pair, see Figure 2.6 and 2.9. The experimental setup in Figure 4.1 contains a multimeter used to measure the electric response of the piezoelectric absorbers 1 to 4, a Power Amplifier controlling the 5th piezoceramic patch pair and a Laser Doppler Vibrometer used to measure the structural response.

The experimental implementation and validation of piezoelectric shunt tuning methods have traditionally been challenged by the manufacturing of passive inductors with high inductance required for low frequency vibrations [39] and the precise evaluation of the effective EMCC [50, 49]. The challenge of obtaining a high inductance has usually been solved by using the so-called synthetic inductor [16], which is also used in [C2] for the vibration mitigation of free beam vibrations. The synthetic inductor enables simple adjustments of the emulated inductance but consists of an active electric circuit, which requires a constant power source. The pure passive inductor is therefore desired and may be realized by winding a copper wire around a closed magnetic core as it was recently proposed in [33]. This permits the design of pure passive resonant shunts as demonstrated in [P4], while the precise prior inductance tuning including the effect of non-resonant vibration modes becomes compulsory for the determination of the exact number of required coil wire turns.

The second obstacle towards a practical implementation of piezoelectric shunt damping is to obtain a precise effective EMCC for the actual structure. As it was shown in the numerical examples of chapter 2 small deviations on the SC and OC frequencies may cause significant errors on the corresponding squared effective

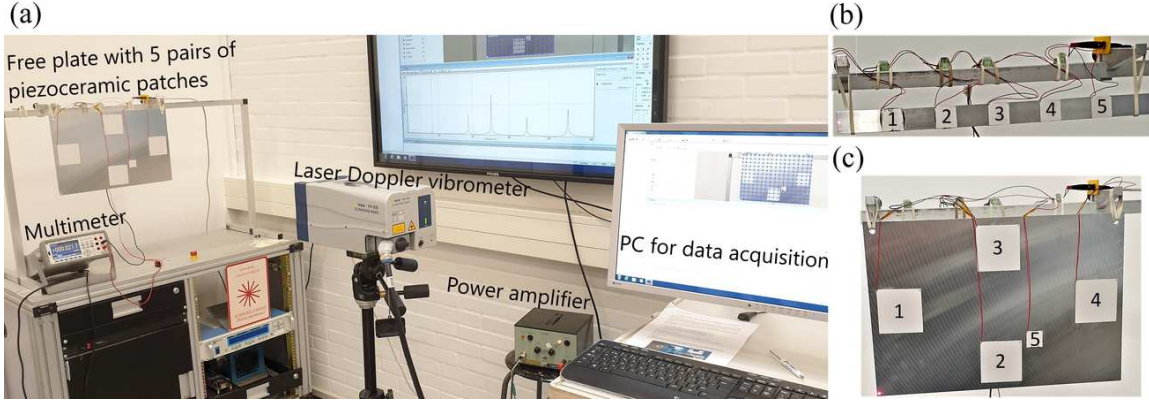


Figure 4.1. Experimental setup (a) and close-up of the tested free (b) beam and (c) plate with five pairs of co-located piezoceramic patches. From [P4].

EMCC (2.32). This makes the shunt tuning methods presented in [P1] and [P2] unsuitable for experimental implementation as the corresponding inductance tuning is directly dependent on the effective EMCC. However, the inductance tuning presented in [P3] becomes independent of the effective EMCC, by instead using the modal charge and voltage amplitudes, which may be determined accurately from experimental measurements as demonstrated in [P4].

In the following the steps of the experimental calibration procedure in [P4], based on the shunt tuning methods proposed in [P3], are explained by taking the free beam and free plate experiments from [P4] as examples, which were also analyzed numerically in chapters 2 and 3.

#### 4.1 Current and voltage response

The shunt tuning method proposed in [P3] requires the evaluation of four tuning parameters, given by the modal SC charge and OC voltage and the corresponding frequencies. Experimentally these parameters may be obtained by imposing a dynamic load to the analyzed structure, while the electric SC current and OC voltage absorber response is measured, as proposed in [P4]. In the present work the fifth piezoceramic patch pair in Figure 4.1(b,c) is used to excite pseudo-random structural vibrations generated by the power amplifier in Figure 4.1(a). Simultaneously the absorber response is measured with a 34465A Keysight Digital Multimeter, supporting high-resolution acquisition of the direct current and voltage time histories. Two FRFs are then obtained from the electric current and voltage time histories, by use of the build-in spectrum generator *pspectrum* in Matlab. The time derivatives of the electric charge equals electric current, whereby a FRF for the charge may be obtained in the frequency domain, by dividing the FRF for the electric current with the frequency  $\omega$ .

The FRFs for the SC charge and OC voltage of the four OP-SW piezoelectric absorbers bonded to the free beam in Figure 4.1(b) and the free plate in Figure 4.1(c) are shown in Figure 4.2 and 4.3, respectively.

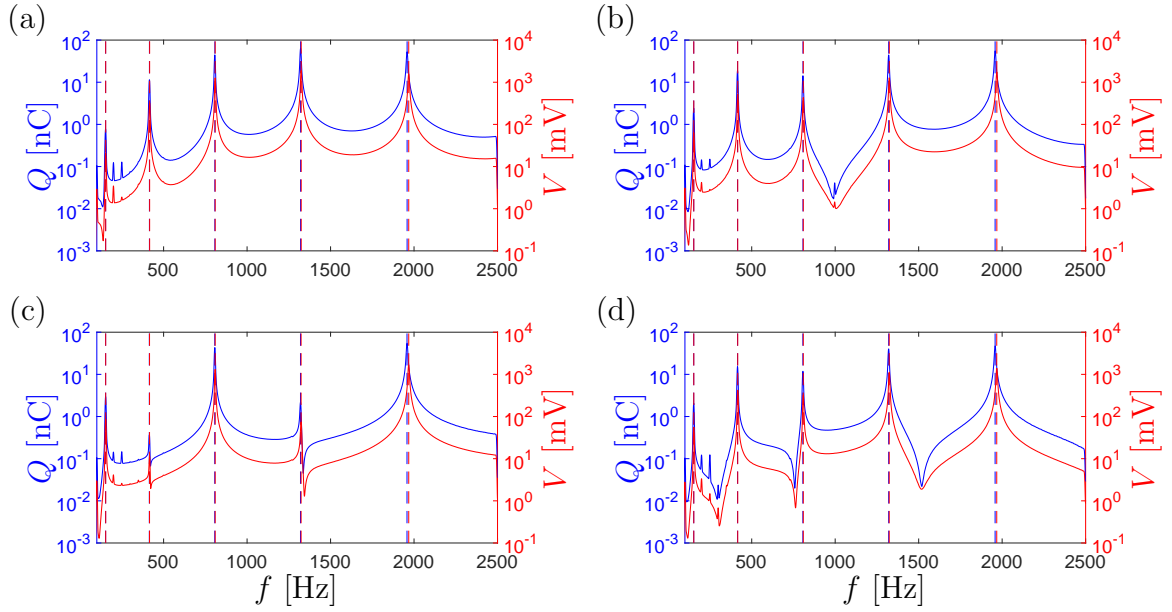


Figure 4.2. FRF for measured SC charge (—) and OC voltage (—) for piezoelectric absorber 1-4 (a-d) bonded to the free beam in Figure 4.1(b). From [P4].

The FRFs for the electric charge and voltage in Figure 4.2 for the free beam and in Figure 4.3 for the free plate provide all the information required for the evaluation of the shunt tuning to any target vibration mode represented in the analyzed frequency interval. The modal SC charge and OC voltage are determined by the peak resonance

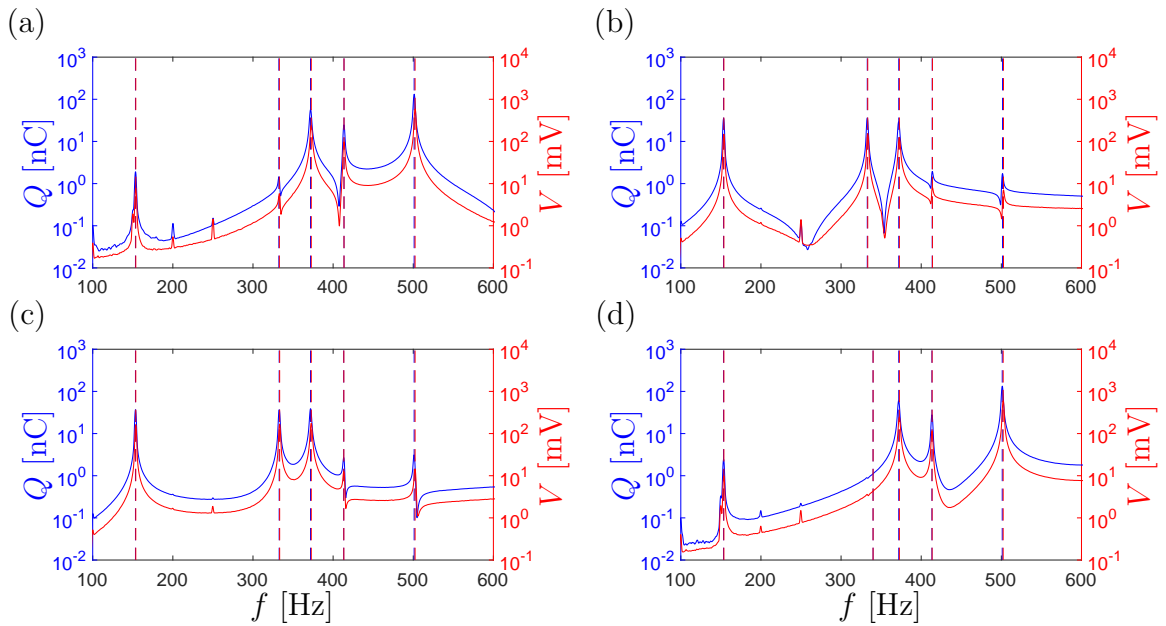


Figure 4.3. FRF for measured SC charge (—) and OC voltage (—) for piezoelectric absorber 1-4 (a-d) bonded to the free plate in Figure 4.1(c). From [P4].

values, as indicated in Figure 4.2 and 4.3 by the vertical dashed lines, while the SC and OC frequencies follows by the intersections of these dashed lines with the frequency axis. It is hereby immediately seen that five free beam modes and also five free plate modes may be targeted in the analyzed frequency intervals. Furthermore, The magnitude of the charge and voltage amplitudes provides information about which absorbers may be used to damp the individual resonant vibration modes. It is thus seen that the third absorber for the free beam in Figure 4.2(c) may not be used to damp modes 2 and 3 and that absorbers 1, 4 in Figure 4.3(a,d) and 2, 3 in Figure 4.3(b,c) for the free plate are not applicable for damping of modes 2, 3 and 5, 6, respectively. Similar observations could have been made from the corresponding free beam and plate mode shapes provided in [P4] and shown for the 3D ANSYS model in chapter 2.

## 4.2 Shunt tuning

The next step is to determine effective modal capacitances by (3.20) for each piezoelectric absorber, which are provided for the free beam in Figure 4.4(a) and for the free plate in Figure 4.5(a). Furthermore, the blocked  $\bar{C}_p^S$ , static  $C_p^0$  and free  $\bar{C}_p^T$  capacitances are shown by the horizontal lines, where the static capacitances are measured at low frequency for the piezoelectric absorbers 1 (black), 2 (red), 3 (blue) and 4 (green). It can be seen that the the effective capacitances in general are in between the blocked and the individual static capacitances, which were also observed numerically in chapter 3. The blocked capacitances are determined from the free capacitances, provided by the piezo manufacturer, with a standard deviation of 2.11 nF and 5.51 nF for the small and large piezoceramic patches, respectively.

The actual effective capacitances of the piezoceramic patches are seen to be larger

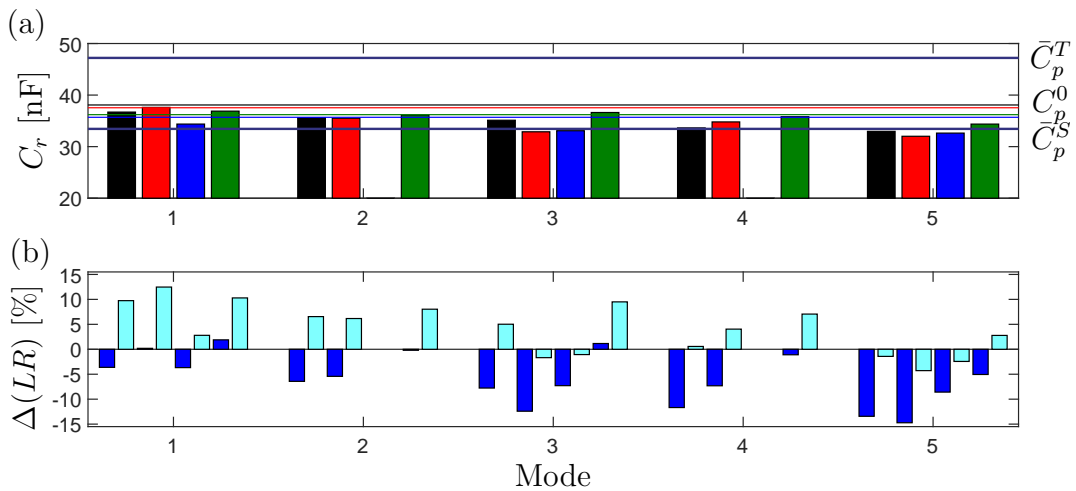


Figure 4.4. In (a) the effective modal capacitance for absorber 1 (—), 2 (—), 3 (—), 4 (—) for beam mode 1 to 5 and (b) the relative deviation on the shunt tuning based on the static (dark colors) and blocked (light colors) capacitances.

Table 4.1. Series single mode tuning for free beam mode 1 to 5 based on experiments.

Mode	1		2		3		4		5		
$f_j$ [Hz]	152.63		414.99		806.78		1320.4		1958.03		
$\tilde{f}_j$ [Hz]	153.24		416.21		808.91		1323.9		1968.10		
$\kappa_j^2$ [%]	0.80		0.59		0.53		0.53		1.03		
	$L$ [H]	$R$ [ $\Omega$ ]									
Absorber	1	29.2	3555	4.08	1158	1.10	532	0.427	375	0.196	343
	2	28.5	3469	4.09	1162	1.17	568	0.413	362	0.202	364
	3	31.1	3795	—	—	1.16	651	—	—	0.198	358
	4	29.0	3537	4.02	1142	1.05	588	0.402	322	0.188	330

than those obtained by the numerical models in chapter 2. Particularly, the blocked, static and effective modal capacitances are larger than their corresponding numerical values, since the plane piezoelectric coupling coefficients for the provided piezoceramic material 3265HD are notoriously lower than in theory. This also implies that the effective EMCCs are expected to be reduced compared to the numerical values. Furthermore, it can be seen that the static capacitances for the piezoelectric absorbers bonded to the free plate are generally closer to the free than the blocked capacitances, which indicates that the piezoceramic patches are poorly bonded to the structure [P4]. The effective modal capacitances are seen to be close to the static values for the low frequency target modes, while they slowly approach the blocked capacitance for the higher target modes, as for the numerical results in chapter 3. This implies that the shunt tuning based on the static capacitances (dark blue bars) in Figure 4.4(b) and 4.5(b) is close to the optimum tuning for low frequency target modes, while the blocked capacitance (light blue bars) in Figure 4.4(b) and 4.5(b) may be better for the tuning to higher target modes.

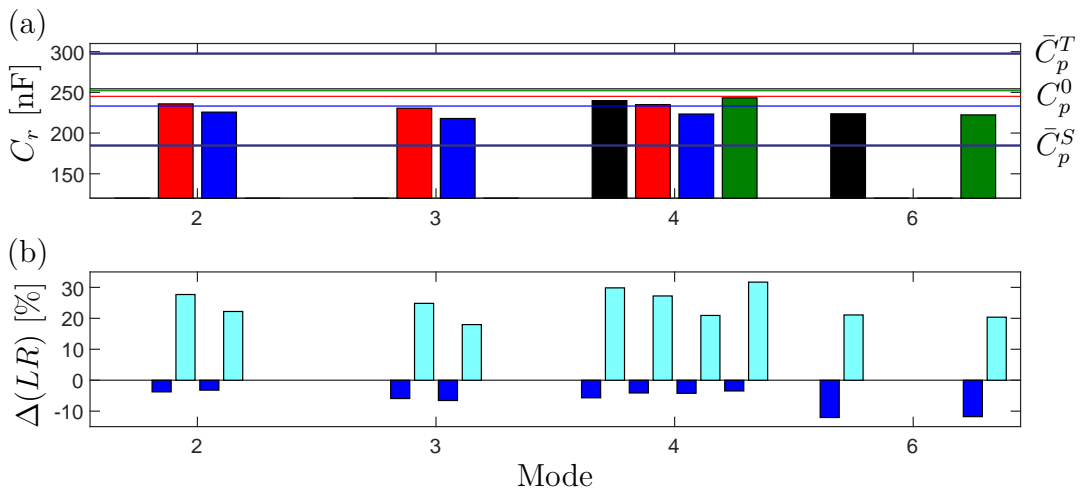


Figure 4.5. In (a) the effective modal capacitance for absorber 1 (—), 2 (—), 3 (—), 4 (—) for plate mode 2, 3, 4 and 6, and (b) the relative deviation on the shunt tuning based on the static (dark colors) and blocked (light colors) capacitances.

Table 4.2. Series single mode tuning for free plate mode 2, 3, 4, 6 based on experiments.

Mode		2		3		4		6	
$f_j$ [Hz]		153.36		332.70		371.87		501.10	
$\hat{f}_j$ [Hz]		153.75		333.28		372.75		502.27	
$\kappa_j^2$ [%]		0.51		0.35		0.47		0.47	
		$L$ [H]	$R$ [ $\Omega$ ]	$L$ [H]	$R$ [ $\Omega$ ]	$L$ [H]	$R$ [ $\Omega$ ]	$L$ [H]	$R$ [ $\Omega$ ]
Absorber	1	4.38	427	0.907	159	<b>0.756</b>	<b>172</b>	<b>0.446</b>	<b>137</b>
	2	<b>4.52</b>	<b>441</b>	<b>0.985</b>	<b>173</b>	<b>0.771</b>	<b>175</b>	0.408	125
	3	<b>4.73</b>	<b>461</b>	<b>1.04</b>	<b>183</b>	<b>0.812</b>	<b>184</b>	0.462	141
	3	4.32	421	0.876	151	<b>0.745</b>	<b>169</b>	<b>0.449</b>	<b>138</b>

The optimum series shunt tuning (3.30) is then determined from the effective modal capacitances in Figure 4.4(a) and 4.5(a) and provided in Table 4.1 and 4.2 together with the SC and OC frequencies and the effective EMCCs. The values in red indicate the absorber configurations suitable for vibration mitigation of the specific target modes. Relatively good correlation between the numerical results in chapter 2 and 3 and the present experimental results can be seen. The experimental SC and OC frequencies are a bit lower than the numerical frequencies, which is mainly due to the larger piezoelectric capacitances and because an ideal kinematic coupling between the piezoceramic patches and the aluminum beam and plate has not been achieved. Hence, the numerical model could be updated by reducing the electromechanical coupling through the kinematic relations and by implementing the experimental capacitances [6]. The optimum shunt tuning in Table 4.1 and 4.2 are seen to be close to the numerical tuning for the free beam, while the deviations are larger for the free plate, because of the poor bonding of the piezoceramic patches.

### 4.3 Inductance

The main challenge of the practical implementation of the resonant shunt is the design of the shunt inductance. Particularly, inductors with high inductance values (larger than 1 H), required for the damping of low frequency vibrations, have been considered impractical to obtain passively [17]. Instead, the so-called synthetic inductor [16] has traditionally been used for resonant piezoelectric shunt damping and it is also used in [C2] for the vibration mitigation of free beam vibrations. The synthetic inductor in Figure 4.6 is designed to emulate the effect of an inductance in an electric circuit defined as the ratio of the voltage to the time derivative of the current, which in the frequency domain can be described as

$$L = \frac{|V|}{\omega|I|} \quad (4.1)$$

The task is thereby to keep this voltage-current relation constant for any frequency  $\omega$ . This is obtained with the Antoniou circuit [2], which consists of two operational amplifiers, three resistors and a capacitance, as seen in Figure 4.6(a). The circuit is then connected to a variable resistance  $R_L$ , which governs the emulated inductance

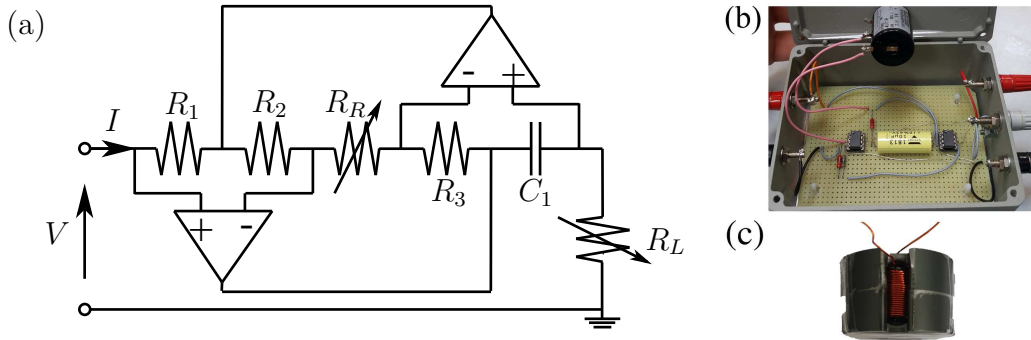


Figure 4.6. Synthetic inductor, circuit diagram (a) and prototype (b), from [C2] and (c) passive inductor, from [P4].

by the relation

$$L = \frac{C_1 R_1 R_3}{R_2} R_L \quad (4.2)$$

The other variable resistance  $R_R$  in Figure 4.6(a) is introduced to permit the addition of negative resistance to compensate for eventual parasitic losses [51].

The emulated inductance for different values of  $R_L$  is analyzed in [C2] by imposing a pseudo-random voltage between the circuit terminals, while acquiring the corresponding electric current time history. A spectrum generator is then used to determine the FRF for the input voltage and output current, which in Figure 4.7(a) is shown for four different  $R_L$  values. The corresponding emulated inductances are then obtained from the voltage-current relation (4.1) and shown in Figure 4.7(b).

It can be seen from the emulated inductances in Figure 4.7(b) that the theoretical inductance values are exactly obtained in the analyzed frequency interval, when the resistors  $R_1$ ,  $R_2$  and  $R_3$  and capacitor  $C_1$  results in a constant inductance factor of 20 H/(k $\Omega$ ) in (4.2). This demonstrates the reliability and simple adjustments of the emulated inductance with the synthetic inductor, which makes it highly attractive for use in shunt damping applications. However, because of the operational amplifiers, the synthetic inductor requires a constant power source, thereby making it an active electronic component, which may be undesirable. The interest for the pure passive resonant shunt has therefore been maintained and in [33] high inductance

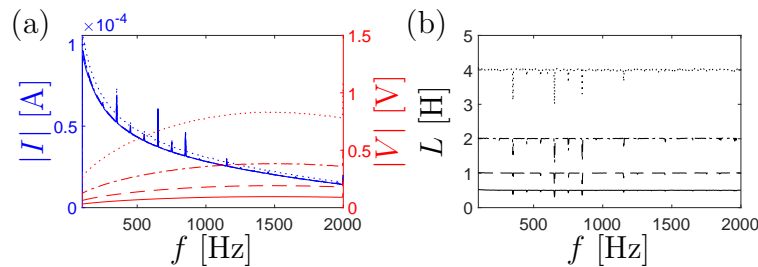


Figure 4.7. Synthetic inductor, (a) FRF for voltage input (—) and current response (—) and (b) emulated inductance, for  $R_L = 25\Omega$ (—),  $50\Omega$ (- -),  $100\Omega$ (- ·),  $200\Omega$  (··). From [C2].

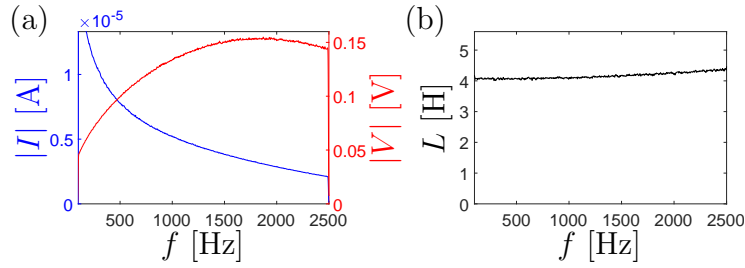


Figure 4.8. Passive inductor, (a) voltage input (—) and current response (—) and (b) effective inductance as function of the excitation frequency. From [P4].

were obtained passively by winding a copper wire around a closed magnetic core. This has subsequently been used for the design of a passive electrical analogue for a plate in [34], while non-linearity and temperature dependency have been considered in [35, 12]. In [P4] the passive inductor is used in the design of the optimum resonant shunts in Table 4.1 and 4.2 for the damping of free beam and plate vibrations.

Similarly to the synthetic inductor, the passive inductor in Figure 4.6(c) is designed to obtain the constant voltage-current relation (4.1). This is realized by considering the voltage  $V = n\omega\varphi I$ , which follows from the magnetic flux  $\varphi = n\mu(A_e/l_e)$  that goes through  $n$  turns in the magnetic coil with the specific permeability  $\mu$ , magnetic cross section  $A_e$  and path length  $l_e$ . Combining these expressions, the inductance becomes proportional to the square of the  $n$  coil turns,

$$L = \frac{\mu A_e}{l_e} n^2 = A_L n^2 \quad (4.3)$$

while  $A_L$  is the permeance or the constant inductance factor.

The passive inductor is tested similarly to the synthetic inductor by imposing a pseudo-random voltage between the circuit terminals, while the electric current time history is acquired. The FRF for the input voltage and output current are shown in Figure 4.8(a) for a magnetic RM-core T38 with properties reported in [P4] and  $n = 400$  wire turns, while the corresponding inductance is shown in Figure 4.8(b).

It can be seen in Figure 4.8(b) that the inductance is almost constant in the analyzed frequency interval. However, the theoretical inductance factor for the RM-core T38 of  $A_L = 28\mu\text{H}$  is not achieved. Instead, the attainable inductance factor has been estimated to be  $A_L \simeq 25\mu\text{H}$ , which is used in [P4] to determine the number of wire turns required for the specific inductance tuning.

#### 4.4 Frequency response analysis

The performance of the shunt tuning method based on experimental measurements is now analyzed by the same FRF analysis considered for the numerical examples in chapter 3. Initially, the effect of using the optimum tuning based on the blocked and static capacitances are considered for the damping of the second free beam

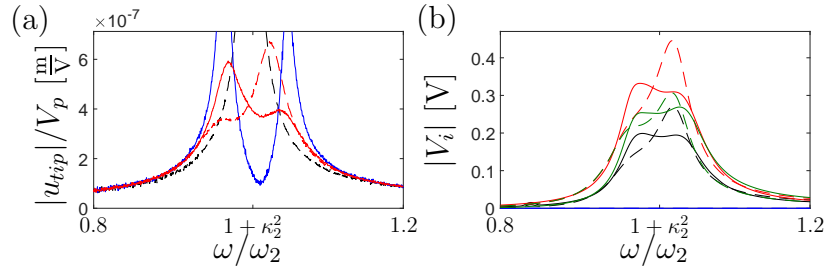


Figure 4.9. FRF for (a) the beam tip displacements with OC (---),  $L$  (—) and  $LR$ -shunted (—) piezoelectric absorbers and for the tuning based on the blocked capacitance  $\bar{C}_p^S$  (---), and (b) the voltage of absorber 1 (—), 2 (—), 3 (—), 4 (—).

mode and the sixth free plate mode, while multi-mode damping of the free beam is considered subsequently.

Three passive inductors with  $n = 400$  turns has been designed to obtain the optimal inductance tuning for the second free beam mode in Table 4.1. The obtained inductance values are respectively  $L_1 = 4.09\text{H}$ ,  $L_2 = 4.07\text{H}$  and  $L_4 = 4.02\text{H}$ , whereby they in average are 0.1% below the optimum tuning. By implementing the pure  $L$ -shunt, the corresponding FRF for the beam tip displacements (blue curve) in Figure 4.9(a) shows two split mode resonances around the original OC response (black dashed curve). Furthermore, it can be seen that the passive inductor has some internal resistance since the anti-resonance point at  $\omega = \omega_r^2(1 + \kappa_r^2)$  is not entirely obtained. This further implies that the implemented resistances are smaller than the tuning values in Table 4.1 as described in [P4]. Three resistors with the resistances  $R_1 = R_2 = R_4 = 750\Omega$  are thus connected in series with the passive inductors, whereby the FRF for the beam tip displacements are given by the red solid curve in Figure 4.9(a) while the corresponding absorber voltage response is provided (solid curves) in Figure 4.9(b). It is seen that the plateau around the target mode 2 (red curve) in Figure 4.9(a) is not entirely flat but is slightly inclined, which may be explained by the small deviation on the passive inductors. However, almost completely flat plateaus are obtained for the corresponding absorber response (solid curves) in Figure 4.9, which indicates that the optimum shunt tuning has been obtained. Oppositely it can be seen by the dashed curves in Figure 4.9 that the shunt is detuned when using the classic shunt tuning based on the blocked capacitance. In the present case this detuning causes a minor increase of the maximum tip beam amplitudes, as seen (red dashed curve) in Figure 4.9.

For the damping of the sixth free plate mode two passive inductors with  $n = 125, 127$  turns and corresponding inductances  $L_1 = 0.444\text{H}$  and  $L_4 = 0.446\text{H}$  have been used, whereby the corresponding FRF for the plate corner displacement (blue curve) in Figure 4.10 is obtained. It is again seen that the passive inductor introduces some resistance, whereby the implemented resistances of  $R_1 = R_4 = 250\Omega$  are less than the optimum tuning values in Table 4.2. The corresponding FRF for the plate corner displacements are shown by the solid red curve in Figure 4.10(a), which exhibits a fairly flat plateau around the target mode. The corresponding absorber

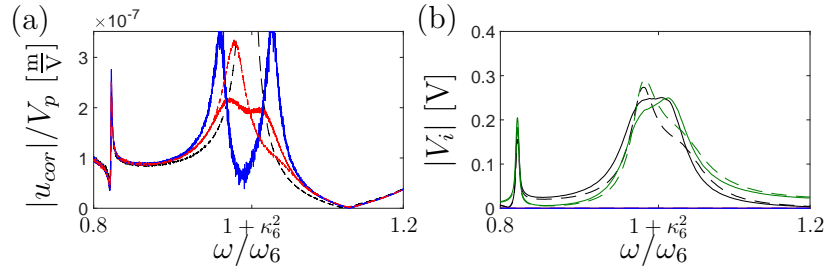


Figure 4.10. FRF for (a) the plate corner displacements with OC (---),  $L$  (—) and  $LR$ -shunted (—) piezoelectric absorbers and for the tuning based on the static capacitance  $\bar{C}_p^0$  (---), and (b) the voltage of absorber 1 (—), 2 (—), 3 (—), 4 (—).

reponse (solid curves) in Figure 4.10(b) is almost completely flat, demonstrating optimum shunt tuning. In this case, the performance of the shunt tuning based on the static capacitance is analyzed as this tuning generally becomes less accurate for higher target modes. It is clearly seen that the tuning based on the static capacitance is not optimal in the present case as the corresponding FRF for the plate corner (cor) displacements (red dashed curves) and absorber response (dashed curves) in Figure 4.10 are inclined significantly.

Finally, multi-mode damping of the free beam modes 2, 3, 4 and 5 has been tested experimentally. The modified single-mode tuning is considered, whereby the single-mode inductance tuning provided in Table 4.1 has been designed by passive inductors with the inductances  $L_1 = 0.760\text{H}$ ,  $L_2 = 4.53\text{H}$ ,  $L_3 = 1.05\text{H}$  and  $L_4 = 0.446\text{H}$ , targeting mode 4, 2, 3 and 5, respectively. The corresponding FRF for the tip beam displacements are seen (blue curves) in Figure 4.11. The optimum resistances are then reduced according to the modified effective EMCC in (3.31) and to account for the inherent resistance of the passive inductors, whereby the

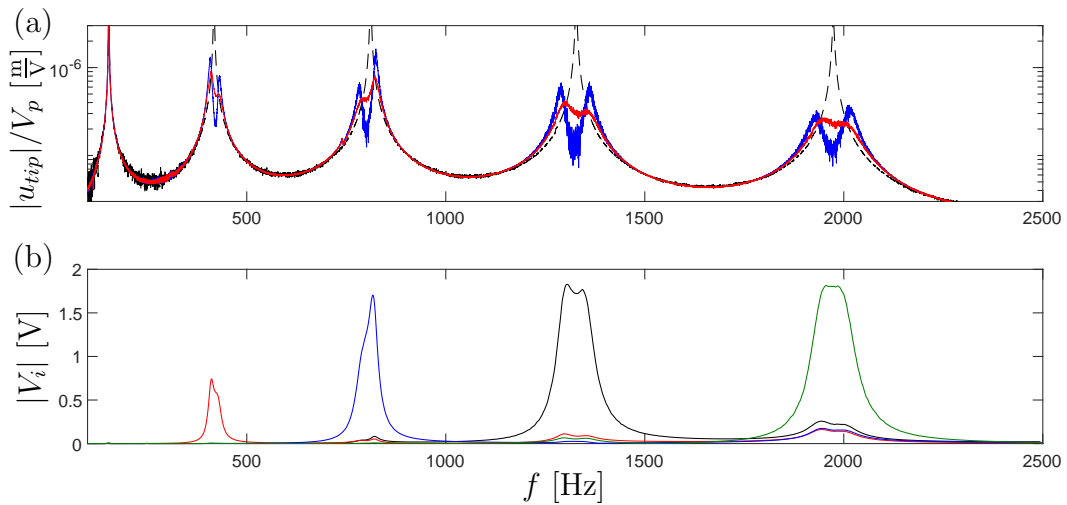


Figure 4.11. FRF for (a) tip beam displacements with OC (---),  $L$  (—) and  $LR$ -shunted (—) piezoelectric absorbers, and (b) the voltage of absorber 1 (—), 2 (—), 3 (—), 4 (—).

used resistances are  $R_1 = 140\Omega$ ,  $R_2 = 375\Omega$ ,  $R_3 = 200\Omega$  and  $R_4 = 70\Omega$ . The FRF for the beam tip displacements and the voltage response of the optimally  $LR$ -shunted piezoelectric absorbers are seen by the red solid and the four solid curves in Figure 4.11(a and b), respectively. The voltage absorber response in Figure 4.11(b) is seen to have almost flat plateaus around the respective target modes for each absorber, indicating an optimum shunt tuning. Furthermore, the FRF for the tip displacements (red curve) in Figure 4.11(a) are seen to have almost flat plateaus around the target modes, whereby vibrations are mitigated over a wide frequency spectrum. Multi-mode damping of the free plate is additionally considered in [P4].



## 5. CONCLUSIONS

The main topic of the present thesis is the development of a precise resonant piezoelectric shunt calibration procedure, which is practical in terms of numerical and experimental implementation. Additionally, it is the aim to achieve a good correlation between the numerical and experimental analysis, which requires an accurate numerical model, that includes the specific piezoelectric material properties and interaction with the considered vibrating structure.

In [P1] a numerical model was developed to describe shunted and electrically wired piezoceramic patches bonded to plate-like structures. When the piezoceramic patch is bonded to one of the major surfaces of a vibrating plate this mainly causes energy conversion through the electromechanical coupling between in-plane strains and the transverse electric field. A plane stress-assumption has therefore been used in [P1] to reduce the full 3D properties of the piezoceramic patch. The coupling between the plate and the piezoceramic patch is then enforced by considering the corresponding kinematic relations, where the plate bending moments are restricted by the in-plane electric forcing from the piezoceramic patch. Piezoceramic patches are conveniently placed in pairs on both sides of a vibrating plate, whereby more energy may be dissipated if the patches are either oppositely poled and series wired or have the same polarization and are parallel wired to the resonant shunt. In [P1] it is demonstrated how the specific wiring and polarization of the piezoceramic patch pair may be modeled numerically and results in a resulting piezoelectric coupling and capacitance for each patch pair configuration. It is thus found that the same poled and parallel wired patch pair has a resulting piezoelectric coupling coefficient and blocked capacitance which are, respectively, two and four times larger than for the oppositely poled and series wired patch pair. This results in a shunt tuning, which are four times lower for the same poled and series wired patch pair, which is beneficial for the practical shunt design.

A shunt tuning method with flexibility and inertia correction terms for the non-resonant vibration modes has been used in the developed numerical model in [P1] to calculate and verify the optimum resonant shunt tuning for a benchmark beam and plate structure. The method requires modifications of the system mass and stiffness matrices and may therefore be inconvenient to use in commercial FE-software. A new shunt tuning method based on the analysis of an SC, OC and a third eigenvalue problem associated with pure inductive shunts is therefore proposed in [P1]. In

[C1] and [P2] this new shunt tuning method is implemented in commercial FE-software and used to verify the developed numerical model in [P1]. In [P2] the exact evaluation of the non-resonant inertia correction term is demonstrated, while in [C1] it is shown that the shunt damping performance for most practical applications is insignificantly deteriorated by neglecting the specific non-resonant inertia correction. The new shunt tuning method is therefore conveniently evaluated exclusively from the analysis of the SC and OC eigenvalue problems.

The extension of the new shunt tuning method to cover the tuning of multiple piezoelectric absorbers and multi-mode damping is presented in [P3]. It is here shown how an effective modal capacitance, containing the inherent blocked capacitance and the influence from non-resonant vibration modes, is obtained by a modal SC charge to OC voltage ratio for each piezoelectric absorber. The effective modal capacitance then substitutes the blocked capacitance in traditional tuning formulas based on the pure single-mode truncation of the structural dynamics. Hereby the shunt tuning is readily obtained both numerically or from experimental measurements. Numerically the modal SC charge and OC voltage are available as electric reaction forces and displacements in the solutions to the SC and OC eigenvalue problems [P3]. In experiments the electric SC current and OC voltage time histories may instead be acquired for each absorber, while the structure is excited by pseudo-random vibrations, as demonstrated in [P4]. Hereby the FRFs for the SC electric charge, which is obtained from the current time history, and the OC voltage are calculated, while the peak amplitudes provides the modal SC charges and OC voltages and corresponding resonant frequencies. The method may also be used for multi-mode damping, either by neglecting the frequency shift caused by the non-resonant absorbers, whereby the shunt tuning is only altered by a new modified effective EMCC that excludes the contribution from the non-resonant absorbers. Otherwise, the frequency shift is considered by including the SC or OC contributions from the non-resonant absorbers depending on their individual target modes. It is demonstrated in [P3] that the influence on the damping performance from the frequency shift is insignificant and the first method based on a modified effective EMCC is therefore preferable as it does not require the evaluation of additional eigenvalue problems of new experimental measurements.

In [P4] experiments on a free beam and plate with four piezoelectric absorbers were used to verify the numerical models and the proposed shunt tuning methods. Good agreement between the numerical and experimental results were demonstrated and almost fully flat absorber response around the target vibration modes were obtained, which agrees with the principle of equal modal damping used for the proposed shunt tuning methods. Finally, the piezoelectric shunt damping is achieved by means of pure passive electronic components, where the passive inductor requires a precise prior tuning. Hereby, the traditional tuning based on the blocked or static capacitances has been demonstrated to be insufficient in many cases and to cause significant reductions in the corresponding attainable damping.

## REFERENCES

- [1] Anderson, E.H., Hagood, N.W., Simultaneous piezoelectric sensing/actuation: Analysis and application to controlled structures, *Journal of Sound and Vibration*, **174**(5) (1994) 617-639.
- [2] Antoniou, A., Realization of Gytrators Using Operational Amplifiers, and their Use in RC-Active-Network Synthesis, *In Proceedings of IEEE*, **116** (1969) 1838-1850.
- [3] Benjeddou, A., Advances in piezoelectric finite element modeling of adaptive structural elements: a survey, *Computers and Structures*, **76** (2000) 347-363.
- [4] Benjeddou, A., Ranger, J.A., Use of shunted shear-mode piezoceramics for structural vibration passive damping, *Computers and Structures*, **84** (2006) 1415-1425.
- [5] Benjeddou, A., Modal effective electromechanical coupling approximate evaluations and simplified analyses: numerical and experimental assessments, *Acta Mechanica*, **225** (2014) 2721-2742.
- [6] Benjeddou, A., Hamdi, M., Robust inverse identification of the effective three-dimensional elastic behaviour of a piezoceramic patch bonded to a multilayer unidirectional fibre composite, *Journal of Sound and Vibration*, **151**(2016) 58-69
- [7] Berardengo M., Thomas O., Giraud-Audine C., Manzoni S., Improved resistive shunt by means of negative capacitance: new circuit, performances and multi-mode control, *Smart Materials and Structures*, **25** (2016) 075033(23pp).
- [8] Berardengo M., Manzoni S., Thomas O., Vanali M., Piezoelectric resonant shunt enhancement by negative capacitances: Optimisation, performance and resonance cancellation, *Journal of Intelligent Material Systems and Structures*, **29**(12) (2018) 2581-2606.
- [9] Bisegna, P., Caruso, G., On the use of negative capacitances for vibration damping of piezoactuated structures, *Proceedings of SPIE*, **5760** (2005).

- [10] Caruso, G., A critical analysis of electric shunt circuits employed in piezoelectric passive vibration damping, *Smart Materials and Structures*, **10** (2001) 1059-1068.
- [11] Chevallier, G., Ghorbel, S., Benjeddou, A., Piezoceramic shunted damping concept: testing, modelling and correlation, *Mécanique and Industries*, **10**(5) (2009) 397-411.
- [12] Darleux R., Lossouarn B., Deü J.-F. Passive self-tuning inductor for piezoelectric shunt damping considering temperature variations, *Journal of Sound and Vibration*, **432** (2018) 105-118
- [13] de Marneffe, B., Preumont, A., Vibration damping with negative capacitance shunts: theory and experiments, *Smart Materials and Structures*, **17** (2008) 035015 (9pp).
- [14] Ducarne J., Thomas O., Deü J. F., Structural Vibration Reduction by Switch Shunting of Piezoelectric Elements: Modeling and Optimization, *Journal of Intelligent Material Systems and Structures*, **21** (2010) 797-816.
- [15] Ducarne, J., Thomas, O., Deü, J.-F., Placement and dimension optimization of shunted piezoelectric patches for vibration reduction, *Journal of Sound and Vibration*, **331** (2012) 3286-3303.
- [16] Fleming, A.J., Behrens, S., Moheimani, S.O.R., Synthetic impedance for implementation of piezoelectric shunt-damping circuits, *Electronics Letters*, **36** (2000) 1525-1526.
- [17] Fleming, A.J., Behrens, S., Moheimani, S.O.R., Reducing the inductance requirements of piezoelectric shunt damping systems, *Smart Materials and Structures*, **12** (2003) 57-64.
- [18] Forward, R.L., Electronic damping of vibrations in optical structures, *Applied Optics*, **18** (1979) 690-697.
- [19] Gardonio, P., Casagrande, D., Shunted piezoelectric patch vibration absorber on two-dimensional thin structure: Tuning considerations, *Journal of Sound and Vibration*, **395** (2017) 26-47.
- [20] Hagood, N.W., von Flotow, A., Damping of structural vibrations with piezoelectric materials and passive electrical networks, *Journal of Sound and Vibration*, **146** (1991) 243-268.
- [21] Hamdi, M., Ghanmi, S., Benjeddou, A., Nasri, R., Robust electromechanical finite element updating for piezoelectric structures effective coupling prediction, *Journal of Intelligent Material Systems and Structures*, **25**(2) (2014) 137-154.

- [22] Høgsberg, J., Krenk, S., Balanced calibration of resonant shunt circuits for piezoelectric vibration control, *Journal of Intelligent Material Systems and Structures*, **23** (2012) 1937-1948.
- [23] Høgsberg, J., Krenk, S., Balanced calibration of resonant piezoelectric RL shunts with quasi-static background flexibility correction, *Journal of Sound and Vibration*, **341** (2015) 16-30.
- [24] Høgsberg, J., Krenk, S., Calibration of piezoelectric RL shunts with explicit residual mode correction, *Journal of Sound and Vibration*, **386** (2017) 65-81
- [25] Hollkamp, J.J., Multimodal Passive Vibration Suppression with Piezoelectric Materials and Resonant Shunts, *Journal of Intelligent Material Systems and Structures*, **5**,(1994) 49-57.
- [26] IEEE Inc. (1988) *Standards on piezoelectricity* ANS/IEEE Std 176-1987 USA.
- [27] Kim, S.-M., Wang, S., Brennan, M.J., Dynamic analysis and optimal design of a passive and an active piezoelectrical dynamic vibration absorber, *Journal of Sound and Vibration*, **330** (2011) 603-614.
- [28] Kozłowski, M.V., Cole, D.G., Clark, R.L., A comprehensive study of the RL series resonant shunted piezoelectric: a feedback controls perspective, *Journal of Vibration and Acoustics*, **133** (2011) 011012 (10pp).
- [29] Krenk, S., Frequency analysis of the tuned mass damper, *Journal of Applied Mechanics*, **72** (2005) 936-942.
- [30] Krenk, S., Høgsberg, J., Equal modal damping design for a family of resonant vibration control formats, *Journal of Vibration and Control*, **19** (2013) 1294-1315.
- [31] Krenk, S., Høgsberg, J., Tuned resonant mass or inerter based absorbers: Unified calibration with quasi-dynamic flexibility and inertia correction, *Proceedings of the Royal Society A: Mathematical, Physical and Engineering Sciences*, **472** (2016) pp. 20150718 (23 pp.)
- [32] Lammering, R., Mesecke-Rischmann, S., Multi-field variational formulations and related finite elements for piezoelectric shells, *Smart Materials and Structures*, **12**(6) (2003) 904-913.
- [33] Lossouarn B., Aucejo M., Deü J.-F., Multon B., Design of inductors with high inductance values for resonant piezoelectric damping, *Sensors and Actuators A: Physical*, **259** (2017) 68-76.
- [34] Lossouarn, B., Aucejo, M., Deü, J.-F., Cunefare, K. A., Design of a passive electrical analogue for piezoelectric damping of a plate, *Journal of Intelligent Material Systems and Structures*, **29**(7) (2018) 1301-1314.

- [35] Lossouarn B., Deü J.-F., Kerschen G., A fully passive nonlinear piezoelectric vibration absorber, *Philosophical Transactions of the Royal Society A: Mathematical, Physical and Engineering Sciences*, **376** (2018) pp. 20170142.
- [36] Manzoni, S., Moschini, S., Redaelli, M., Vanali, M., Vibration attenuation by means of piezoelectric transducer shunted to synthetic negative capacitance, *Journal of Sound and Vibration*, **331** (2012) 4644-4657.
- [37] Ogden, J.W., Grandhi, R.V., Optimal placement of a piezoelectric patch on plate structures for vibration suppression, *Proceedings of SPIE*, **3321** (1996) 170-184.
- [38] Park, C.H., Inman, D.J., A uniform model for series R-L and parallel R-L shunt circuits and power consumption, *Proceedings of SPIE*, **3668** (1999) 797-804.
- [39] Park, C.H., Inman, D.J., Enhanced Piezoelectric Shunt Design, *Shock and Vibration*, **10**(2) (2003) 127-133.
- [40] Park, C.H., Kim, Y.H., Park, H.C., Dynamic Formulations of Plates with Shunted Piezoelectric Materials, *Journal of Intelligent Material Systems and Structures*, **16** (2005) 971-976.
- [41] Piefort, V., Henriouille, K., Modelling of Smart Structures with Colocated Piezoelectric Actuator/Sensor Pairs: Influence of the In-Plane Components, *Identification, Control and Optimisation of Engineering Structures*, (2000) 47-57.
- [42] Porfiri, M., Maurini, C., Pouget, J., Identification of electromechanical modal parameters of linear piezoelectric structures, *Smart Materials and Structures*, **16** (2007) 323-331.
- [43] Preumont, A., *Vibration Control of Active Structures. An Introduction*, 3rd edition, Springer, Heidelberg, 2011.
- [44] Preumont, A., de Marneffe, B., Deraemaeker, A., Bossens, F., The damping of a truss structure with a piezoelectric transducer, *Computers and Structures*, **86** (2008) 227-239.
- [45] Soltani, P., Kerschen, G., Tondreau, G., Deraemaeker, A., Piezoelectric vibration damping using resonant shunt circuits: an exact solution, *Smart Materials and Structures*, **23** (2014) 125014 (11pp).
- [46] Soltani, P., Kerschen, G., Tondreau, G., Deraemaeker, A., Tuning of a piezoelectric vibration absorber attached to a damped structure, *Journal of Intelligent Material Systems and Structures*, **28**(9) (2017) 1115-1129.
- [47] Soltani, P., Kerschen, G., The nonlinear piezoelectric tuned vibration absorber, *Smart Materials and Structures*, **24** (2015) 075015 (13pp).

- [48] Thomas, O., Deü, J.-F., Ducarne, J., Vibrations of an elastic structure with shunted piezoelectric patches: efficient finite element formulation and electromechanical coupling coefficients, *International Journal for Numerical Methods in Engineering*, **80** (2009) 235-268
- [49] Thomas, O., Ducarne, J., Deü, J.-F., Performance of piezoelectric shunts for vibration reduction, *Smart Materials and Structures*, **21** (2012) 015008 (16pp).
- [50] Trindade M., Benjeddou A., Effective electromechanical coupling coefficients of piezoelectric adaptive structures: critical evaluation and optimization, *Mechanics of Advanced Materials and Structures*, **16** (2009) 210-223.
- [51] Von Wangeheim, L., Modification of the classical GIC structure and its application to RC-oscillators, *Electronic letters*, **32**(1) (1996) 6-8
- [52] Wu, S.Y., Bicos, A. S., Structural vibration damping experiments using improved piezoelectric shunts, *Proceedings of SPIE*, **3045** (1997) 40-50.
- [53] Wu, S.Y., Piezoelectric shunts with a parallel R-L circuit for structural damping and vibration control, *Proceedings of SPIE*, **2720** (1996) 259-269.
- [54] Wu, S.Y., Method for Multiple Mode Shunt Damping of Structural Vibration Using a Single PZT Transducer, *Proceedings of SPIE*, **3327**(1) (1998) 159-168.
- [55] Yamada, K., Matsuhisa, H., Utsuno, H., Sawada, K., Optimum tuning of series and parallel LR circuits for passive vibration suppression using piezoelectric elements, *Journal of Sound and Vibration*, **329** (2010) 5036-5057.



P1

Optimal piezoelectric resistive-inductive shunt damping of plates  
with residual mode correction

Johan Frederik Toftekær, Ayeche Benjeddou, Jan Høgsberg  
and Steen Krenk

*Journal of Intelligent Material Systems and Structures*

Vol **29**:3346–3370, 2018.



# Optimal piezoelectric resistive–inductive shunt damping of plates with residual mode correction

Journal of Intelligent Material Systems and Structures  
2018, Vol. 29(16) 3346–3370  
© The Author(s) 2018  
Article reuse guidelines:  
sagepub.com/journals-permissions  
DOI: 10.1177/1045389X18798953  
journals.sagepub.com/home/jim  


Johan F Toftekær<sup>1</sup> , Ayech Benjeddou<sup>2,3</sup>, Jan Høgsberg<sup>1</sup>   
and Steen Krenk<sup>1</sup>

## Abstract

This work concerns vibration suppression of plates and plate-like structures by resonant piezoelectric damping, introduced by resistive–inductive shunts. The performance of this type of shunt damping relies on the precise calibration of the shunt frequency, where an important aspect is the ability to account for the energy spill-over from the non-resonant modes, not taken into account by most available calibration methods. A newly proposed calibration procedure includes this residual mode contribution by a quasi-dynamic modal correction, taking both flexibility and inertia effects of the non-resonant modes into account. In this work, this procedure is implemented in a finite element model combining Kirchhoff plate bending kinematics for the host structure and a plane stress assumption for a pair of bonded piezoceramic patches. The established model is verified by comparison with shunt calibrations from benchmark examples in the literature. As demonstrated by frequency response plots and the obtained damping ratios, the resistive–inductive shunt tuning is influenced by the effect of the non-resonant modes and omission may yield a significant detuning of the shunt circuit. Finally, an alternative method for precise evaluation of the effective (or generalized) electromechanical coupling coefficient is derived from the modal electromechanical equations of motion. This results in a new shunt tuning method, based on the effective electromechanical coupling coefficient obtained by the short- and open-circuit frequencies of the coupled piezo-plate structure.

## Keywords

Shunt piezoelectric damping, resonant shunt calibration, quasi-dynamic residual mode correction, effective modal electromechanical coupling coefficient, plates

## Introduction

This article concerns the suppression of plate vibrations by means of resonant piezoelectric shunt damping. Piezoceramic patches, bonded to vibrating plates, have the ability to convert mechanical energy into electrical energy that can then be dissipated in supplemental resonant shunts. The amount of converted energy is governed by the squared effective (or generalized) electromechanical coupling coefficient (EMCC), which depends on the properties of the piezoceramic patches and their placement on the host structure. Furthermore, the EMCC is a key parameter for the performance and tuning of a shunt, traditionally composed of an inductor ( $L$ ), calibrated such that the shunted piezoelectric device works in resonance with the host structure, and a resistor ( $R$ ), dissipating the converted mechanical energy into heat via the Joule effect. However, alternative passive and semi-active resonant ( $RL$ ) shunts have been proposed, for instance,

by the addition of a negative capacitance (Berardengo et al., 2016; De Marneffe and Preumont, 2008) or by the use of switch damping (Ducarne et al., 2010). The motivation behind most of these alternative resonant shunts is the difficulty in generating the large inductance required in shunt damping of (low-frequency) structural vibrations. The problem is commonly solved by the introduction of synthetic inductors (Thomas et al., 2012), which are active components that emulate

<sup>1</sup>Department of Mechanical Engineering, Technical University of Denmark, Kgs. Lyngby, Denmark

<sup>2</sup>Sorbonne Universités and Université de Technologie de Compiègne, CNRS, FRE 2012 ROBERVAL, Compiègne, France

<sup>3</sup>Supmeca, Saint Ouen, France

### Corresponding author:

Johan F Toftekær, Department of Mechanical Engineering, Technical University of Denmark, Nils Koppels Allé, Building 404, 2800 Kgs. Lyngby, Denmark.

Email: jotof@mek.dtu.dk

the inductive behavior in the desired frequency range. Nonetheless, high inductance values have recently been obtained and demonstrated for pure passive inductors with windings around a magnetic coil (Lossouarn et al., 2017), allowing an unconditionally stable resistive–inductive ( $RL$ ) shunt with large damping potential if a precise shunt tuning can be obtained already in the structural design phase. This can be realized using a consistent calibration procedure that explicitly takes into account the dynamic effects of the full flexible structure, as this work shall demonstrate.

Piezoelectric vibration damping by resonant  $RL$  shunts was originally suggested by Forward (1979) and further developed by Hagood and Von Flotow (1991), who proposed two calibration procedures for a series shunt based on minimization of the response amplitudes and maximization of the damping characteristics. A calibration procedure for the parallel  $RL$  shunt was subsequently proposed by Wu (1996), arguing that the series shunt would be inappropriate for large resistances. The series and parallel shunts have been compared by Park and Inman (1999), revealing a larger attainable energy dissipation using the parallel configuration, while a critical analysis of the calibration methods has been provided by Caruso (2001). Methods for multi-modal piezoelectric shunt damping have been proposed by Hollkamp (1994) and Wu (1998). In the later years, several alternative procedures have been proposed for the detailed tuning of  $RL$  shunts, for example, based on an  $H_\infty$ -norm of the response amplitude (Soltani et al., 2014) or a balanced calibration procedure based on the principle of equal modal damping (Høgsberg and Krenk, 2012), originally developed for the mechanical tuned mass damper (Krenk, 2005). The balanced calibration procedure has recently been extended to include the effects from non-resonant structural modes, first by a quasi-static correction (Krenk and Høgsberg, 2014) and then by a more general quasi-dynamic correction with both flexibility and inertia terms (Krenk and Høgsberg, 2016).

An important part of all calibration methods is the accurate determination of the squared EMCC, which governs both the attainable damping and the shunt tuning. Commonly, the squared EMCC is estimated from a single-mode representation of the electromechanical structure (Thomas et al., 2009), while improved accuracy has been demonstrated by including quasi-static effects from higher non-resonant vibration modes (Berardengo et al., 2016). In other cases, the tuning is based directly on the squared effective EMCC determined either from experiments (Delperro et al., 2012; Porfiri et al., 2007) or by numerical analysis (Benjeddou, 2014; Trindade and Benjeddou, 2009). However, inherent inconsistencies between the squared modal and effective EMCC often lead to discrepancies in the tuning formulas, because the influence from non-resonant modes is neglected in the modal

representation of the electromechanical structure. This motivates the present derivation of a new and consistent  $RL$  shunt tuning procedure based on the effective EMCC.

The proposed shunt calibration relies on the procedure with residual mode correction, introduced by Krenk and Høgsberg (2016) for mechanical absorbers and subsequently extended to piezoelectric shunt damping in Høgsberg and Krenk (2017). It is applied to the optimal calibration of  $RL$  shunted piezoceramic patches, bonded symmetrically to plate elements and structures for which the tuning is influenced by vibration modes and frequencies that are closely grouped both spectrally and spatially. It is the aim to account for the influence from the non-resonant modes on the shunt calibration and discuss the errors associated with the pure single-mode representation of the electromechanical structure, by considering both the squared modal and effective EMCC. A new modal EMCC is presented that accounts for the spill-over from non-resonant modes, whereby it becomes identical to the effective EMCC. Thus, a consistent relation is established between the modal equations of motion and the corresponding short-circuit (SC) and open-circuit (OC) frequencies of the coupled electromechanical structure. Consequently, this enables the derivation of a shunt tuning procedure based on the effective EMCC, as demonstrated in the third section of this article.

The first section of this article presents a finite element (FE) model for plates with a symmetrically bonded pair of piezoceramic patches in order to facilitate the subsequent analysis and assessment of the proposed  $RL$  shunt tuning procedures. The plate displacements are approximated using Kirchhoff plate bending kinematics, whereas only the in-plane displacements are considered for the piezoceramic patch. Equipotential conditions are imposed to all continuous patch electrodes, reducing the number of electric variables to two for the discretized piezoceramic patch. Subsequently, the coupling between a pair of piezoceramic patches and a plate is established by transforming the electric forcing from the patches to the equivalent moment loads in the plate model. In this work, a symmetric pair of identical piezoceramic patches is considered. The patches are either same-poled and parallel-wired (SP-PW) or opposite-poled and series-wired (OP-SW), whereby they operate out of phase. The number of variables in the electric domain can hereby be reduced to the voltage over the supplemental shunt by the introduction of the resulting capacitance and the plane stress-reduced piezoelectric coupling coefficient for the specific patches electric connection. A thorough review of FE techniques for the modeling of piezoelectric structural elements was provided by Benjeddou (2000).

The second section conducts a modal analysis of the SC electromechanical structure. For a specific vibration mode, the consistent modal truncation in Krenk and Høgsberg (2016) reduces the system to a single

mechanical equation, in which the piezoceramic patches are represented by their resulting displacement. Hereby, the optimal tuning for both parallel and series shunt circuits (Høgsberg and Krenk, 2017) can be derived for the targeted mode of the electromechanical FE model.

In the third section, a new shunt tuning procedure is developed based on the effective EMCC, where a simple format of the shunt tuning formulas is obtained.

In the fourth section, it is demonstrated and justified that the influence from the residual modes can be directly identified from the squared modal EMCC, both with and without residual mode correction. Furthermore, the influence on the shunt tuning when having either an SP-PW or an OP-SW pair of piezoceramic patches can be seen from the new tuning formulas.

In the fifth section, the established FE model and implementation of the calibration procedures with residual mode corrections is compared with *RL* shunt tuning results from the previously proposed calibration methods for benchmark examples with a cantilever beam (Thomas et al., 2009) and a simply supported plate (Gardonio and Casagrande, 2017). For the cantilever, the available experimental data are used for comparison with the proposed FE-based tuning methods. Both examples analyze the ability to achieve optimal damping by the proposed calibration procedures and validate the equality between the squared effective EMCC, and the squared modal EMCC with residual mode correction.

As a closure of this introduction, it is worth emphasizing the originality of this work with regard to the related earlier publications (Høgsberg and Krenk, 2012, 2015, 2017). In previous works, the balanced shunt tuning has been considered with and without residual mode correction for beam structures. Thus, the present implementation for plates and two-dimensional (2D) piezoceramic patches is a novel extension that relies on the derived FE model. Furthermore, optimal tuning formulas have here been derived directly from the underlying electric equations. Besides, a new methodology for the precise evaluation of the effective EMCC is proposed. It is based on the corresponding modal EMCC with residual mode correction. Following the accurate evaluation of the effective EMCC, an alternative tuning procedure based on the latter is proposed in the third section which, as well, is a new contribution. Finally, the present shunt tuning procedures with residual mode corrections are assessed by comparison with benchmark examples for beam and plate structures.

### Electromechanical piezo-plate model

This first section is devoted to the derivation of an FE model for the coupled piezo-plate structure. Initially, the variational formulations are obtained for the host plate structure and the piezoceramic patch separately, by considering the respective kinematic and constitutive

relations. Subsequently, the coupling is established by transforming the electric forcing from a considered pair of piezoceramic patches to the equivalent moment loads in the plate model. Alternatively, a layer model could have been established by the use of sandwich theory (Benjeddou, 2002).

### Host elastic plate

The host elastic structure is considered to cover the three-dimensional (3D) domain  $\Omega$ , subjected to prescribed displacements  $\bar{u}_i$  on part of the boundary  $\Gamma_u$ , and prescribed surface tractions  $F_i$  on the remaining part of the domain boundary  $\Gamma_F$ , such that  $\partial\Omega = \Gamma_u \cup \Gamma_F$  and  $\Gamma_u \cap \Gamma_F = \emptyset$ . Hereby, the dynamic equilibrium, under free-body loads, and boundary equations can be written as

$$\sigma_{ij,j} = \rho\ddot{u}_i \text{ in } \Omega \quad (1)$$

$$\sigma_{ij}n_j = F_i \text{ on } \Gamma_F \quad (2)$$

$$u_i = \bar{u}_i \text{ on } \Gamma_u \quad (3)$$

where  $i, j$  denote the 3D vector and tensor components, with repeated subscripts implying summation. Partial differentiation with respect to a space coordinate is denoted by comma and time differentiation by a dot. The material density of the plate is denoted  $\rho$ , and  $n_j$  are the components of the outward unit normal to  $\Omega$ .

The variational formulation is established using the weighted residual method by multiplying the equation of motion (equation (1)) with the virtual displacement  $\delta u_i$ , followed by an integration over the structural domain

$$\int_{\Omega} \delta u_i (\sigma_{ij,j} - \rho\ddot{u}_i) d\Omega = 0 \quad (4)$$

Integration by parts then, using the kinematically admissible boundary conditions, gives the weak variational formulation

$$\int_{\Omega} \delta \varepsilon_{ij} \sigma_{ij} d\Omega + \int_{\Omega} \delta u_i \rho \ddot{u}_i d\Omega = \int_{\Gamma_F} \delta u_i F_i d\Gamma \quad (5)$$

where the displacement has to satisfy the essential boundary condition (equation (3)).

In this work, plates and plate-like structures with thickness  $t_0$  significantly smaller than the in-plane dimensions of the surface area  $A$  are considered. Thus, a good representation of the structural behavior is obtained by Kirchhoff plate theory. The latter considers a plane stress state, whereby the constitutive relation between the strains and stresses is reduced to the relation between the in-plane components. For an isotropic material

$$\boldsymbol{\sigma} = \frac{E}{1 - \nu} \mathbf{D}_p \boldsymbol{\varepsilon} \quad (6)$$

with Young's modulus  $E$ , Poisson's ratio  $\nu$ , and the stress and strain vectors and constitutive matrix defined as

$$\boldsymbol{\sigma} = \begin{bmatrix} \sigma_{xx} \\ \sigma_{yy} \\ \sigma_{xy} \end{bmatrix}, \boldsymbol{\varepsilon} = \begin{bmatrix} \varepsilon_{xx} \\ \varepsilon_{yy} \\ 2\varepsilon_{xy} \end{bmatrix}, \mathbf{D}_p = \frac{1}{1 + \nu} \begin{bmatrix} 1 & \nu & 0 \\ \nu & 1 & 0 \\ 0 & 0 & \frac{1 - \nu}{2} \end{bmatrix} \quad (7)$$

The particular form of  $\mathbf{D}_p$  becomes convenient in the subsequent derivations. Considering bending only, the in-plane strains are determined from the transverse coordinate  $z$  and vertical displacement  $w$  as

$$\boldsymbol{\varepsilon} = \mathbf{z}\boldsymbol{\kappa} = -z\Delta w \quad (8)$$

where  $\Delta$  is a 2D Laplace-like operator, defined as

$$\Delta = \nabla_p \nabla = \begin{bmatrix} \frac{\partial}{\partial x} & 0 \\ 0 & \frac{\partial}{\partial y} \\ \frac{\partial}{\partial y} & \frac{\partial}{\partial x} \end{bmatrix} \begin{bmatrix} \frac{\partial}{\partial x} \\ \frac{\partial}{\partial y} \end{bmatrix} = \begin{bmatrix} \frac{\partial^2}{\partial x^2} \\ \frac{\partial^2}{\partial y^2} \\ 2\frac{\partial^2}{\partial x \partial y} \end{bmatrix} \quad (9)$$

Using the constitutive relation (equation (6)), the strain definition (equation (8)), and the Laplace-like operator (equation (9)), the variational formulation (5) can be written as

$$\int_A \delta w (\Delta^T \mathbf{D} \Delta - \omega^2 \rho t_0) w dA = \int_{A_F} \delta w F_w dA \quad (10)$$

where harmonic solutions  $w = w \exp(i\omega t)$  of circular frequency  $\omega$  are assumed, and the boundary forces are given only by the vertical surface traction  $F_w$  on  $\Gamma_F = A_F$ . In equation (10), the constitutive matrix for the isotropic plate is

$$\mathbf{D} = \frac{Et_0^3}{12(1 - \nu)} \mathbf{D}_p \quad (11)$$

The FE formulation is now obtained from the variational formulation (10) by discretizing the amplitude of the displacement field as

$$w(x, y) = \mathbf{N}(x, y) \mathbf{u}^e \quad (12)$$

where the shape functions in  $\mathbf{N}$  and nodal degrees of freedom (dofs) in the harmonic amplitude vector  $\mathbf{u}^e$  for element  $e$  are

$$\mathbf{N} = [N_w^1 \quad N_\phi^1 \quad N_\psi^1 \quad \cdots \quad N_w^4 \quad N_\phi^4 \quad N_\psi^4] \\ \mathbf{u}^e = [w_1 \quad \phi_1 \quad \psi_1 \quad \cdots \quad w_4 \quad \phi_4 \quad \psi_4]^T \quad (13)$$

The numerical index  $1, \dots, 4$  denotes the node number in the considered rectangular plate element. The shape functions  $N_w^i, N_\phi^i$ , and  $N_\psi^i$  are derived for the nodal vertical displacement  $w_i$  and the associated nodal rotations  $\phi_i$  and  $\psi_i$  about the  $x$ - and  $y$ -axis, respectively, corresponding to a cubic Hermitian interpolation of the vertical displacement field.

By substitution of equation (12) into the variational equation (10), followed by summation over the number of elements  $n$ , the equation of motion for the discretized plate can be written as

$$\sum_{e=1}^n (\delta \mathbf{u}^e)^T \{ (\mathbf{K}_0^e - \omega^2 \mathbf{M}_0^e) \mathbf{u}^e - \mathbf{f}^e \} = 0 \quad (14)$$

where the element mass and stiffness matrices have been introduced as

$$\mathbf{M}_0^e = \int_{A^e} \mathbf{N}^T \rho t_0 \mathbf{N} dA^e \\ \mathbf{K}_0^e = \int_{A^e} (\Delta \mathbf{N})^T \mathbf{D} (\Delta \mathbf{N}) dA^e \quad (15)$$

and the external element force vector as

$$\mathbf{f}^e = \int_{A_F^e} \mathbf{N}^T F_w dA^e \quad (16)$$

It is noted that four-point Gauss integration is sufficient to integrate the highest polynomial order exactly.

The global mass and stiffness matrices  $\mathbf{M}_0$  and  $\mathbf{K}_0$ , and the force  $\mathbf{f}$  and displacement  $\mathbf{u}$  vectors are then assembled using a standard finite element method (FEM) assembly procedure, adding each mass, stiffness, and force component to a defined global nodal order, whereby the full discretized equation of motion can be written as

$$(\mathbf{K}_0 - \omega^2 \mathbf{M}_0) \mathbf{u} = \mathbf{f} \quad (17)$$

which represents a system of  $3N$  linear equations of motion, where  $N$  is the number of FE model nodes.

### Piezoceramic patch

In the following, the variational formulation for a piezoceramic patch with continuous top and bottom electrodes is derived and an FE model established, which will later be coupled to the FE model of the host plate structure.

The mechanical dynamic equilibrium of the piezoceramic patch is described similarly to equations (1) to (3) as

$$\sigma_{ij,j}^p = \rho_p \ddot{u}_i^p \text{ in } \Omega_p \quad (18)$$

$$\sigma_{ij}^p n_j^p = F_i^p \text{ on } \Gamma_F^p \quad (19)$$

$$u_i^p = \bar{u}_i^p \text{ on } \Gamma_u^p \quad (20)$$

with  $\Omega_p$  being the patch domain of boundary  $\partial\Omega_p = \Gamma_F^p \cup \Gamma_u^p$  and  $\Gamma_F^p \cap \Gamma_u^p = \emptyset$ , and  $\rho_p$  being the mass density of the piezoceramic patch. Again, it is assumed that no body loads act on the patch domain. In addition, the electric quasi-static equilibrium and boundary conditions for the piezoceramic patch are as follows

$$D_{i,i} = 0 \text{ in } \Omega_p \quad (21)$$

$$D_i n_i = -Q \text{ on } \Gamma_Q \quad (22)$$

$$\varphi = \bar{\varphi} \text{ on } \Gamma_\varphi \quad (23)$$

with the electric displacement  $D_i$ , surface charge density  $Q$  on  $\Gamma_Q$ , electric potential  $\varphi$ , and prescribed potential  $\bar{\varphi}$  on  $\Gamma_\varphi$ . Here, the total patch boundary is as follows:  $\partial\Omega_p = \Gamma_Q \cup \Gamma_\varphi$  and  $\Gamma_Q \cap \Gamma_\varphi = \emptyset$ .

Again, the weighted residual method is used to obtain the variational formulations, by multiplying the mechanical and electric equilibrium equations (18) and (21) with the virtual displacements  $\delta u_i^p$  and potential  $\delta\varphi$ , respectively, followed by integration over the patch domain

$$\begin{aligned} \int_{\Omega_p} (\sigma_{ij,j}^p - \rho_p \ddot{u}_i^p) \delta u_i^p d\Omega_p &= 0 \\ \int_{\Omega_p} D_{i,i} \delta\varphi d\Omega_p &= 0 \end{aligned} \quad (24)$$

The weak variational formulations follow by integration by parts and substitution of the mechanical and electrical kinematically admissible boundary conditions (equations (19) and (22))

$$\begin{aligned} \int_{\Omega_p} \delta \varepsilon_{ij}^p \sigma_{ij}^p d\Omega_p + \int_{\Omega_p} \delta u_i^p \rho_p \ddot{u}_i^p d\Omega_p &= \sum_{i_c=1}^{n_c} \delta u_\alpha^p(x_{i_c}, y_{i_c}) (F_\alpha^p)_{i_c} \\ \int_{\Omega_p} \delta E_i D_i d\Omega_p &= \int_{\Gamma_Q} \delta\varphi Q d\Gamma_Q \end{aligned} \quad (25)$$

where the fields have to satisfy the corresponding mechanical and electrical essential boundary conditions (equations (20) and (23)). It is noted that the boundary loads will be considered only as concentrated loads at  $n_c$  points of the coordinates  $(x_{i_c}, y_{i_c})$ , while  $\alpha = 1, 2$  with summation over the repeated indices.

By assuming that the piezoceramic patch is thin and bonded to either of the major plate surfaces, the effect from the patch on the plate approximately reduces to the in-plane electric forces, whereby a plane stress constitutive behavior, similar to equation (6), can be used for the patch. This implies that the bending stiffness and associated transverse inertia effects of the patch are not considered. However, when the patch is thin, the bending stiffness of the patch becomes insignificant,

while the omission of the transverse inertia effects can be accounted for by lumping the mass of the patch at the relevant dofs in the system mass matrix, which will be discussed in the benchmark examples.

Regarding the electric domain, it is assumed that no electric field is generated from bending of the piezoceramic patch and the electric field is considered to be non-vanishing only in the transverse (poling) direction 3. Hereby, the reduced electromechanical constitutive equations can be written as

$$\begin{bmatrix} \boldsymbol{\sigma}_p \\ D_3 \end{bmatrix} = \begin{bmatrix} \frac{E_p}{1-\nu_p} \mathbf{D}_p & -\mathbf{e}_3 \\ \mathbf{e}_3^T & \epsilon_{33}^p \end{bmatrix} \begin{bmatrix} \boldsymbol{\varepsilon}_p \\ E_3 \end{bmatrix} \quad (26)$$

They represent the relations between the mechanical in-plane stresses  $\boldsymbol{\sigma}_p$  and transverse electric displacement  $D_3$ , and the associated in-plane strains  $\boldsymbol{\varepsilon}_p$  and transverse electric field  $E_3$ . The pure mechanical behavior is recovered by SC patch electrodes, while the pure electric behavior is represented by the dielectric constant at constant (nil) strains  $\epsilon_{33}^p$ . The electromechanical coupling is governed by the piezoelectric constants in the vector  $\mathbf{e}_3$ , defined for a piezoceramic patch as

$$\mathbf{e}_3 = d_{31} \frac{E_p}{1-\nu_p} \mathbf{D}_p \mathbf{b} = e_{31} \mathbf{b} \quad (27)$$

where  $E_p$  is the Young's modulus of the piezoceramic material,  $\nu_p$  is the corresponding Poisson's ratio, and  $d_{31} \mathbf{b} = d_{31} [1 \ 1 \ 0]^T$  represents the isotropic plane electromechanical coupling with the strength governed by the piezoelectric strain coefficient  $d_{31} = d_{32}$ . It is noted that there is no inherent coupling with the in-plane shear strain for piezoceramic materials, which is the reason for the zero component in the last entry of  $\mathbf{b}$ . Because  $1 - \nu_p$  is contained explicitly in equation (27), the remaining SC constitutive matrix  $\mathbf{D}_p$  can be written as in equation (7) with  $\nu_p$  instead of  $\nu$ . It is readily shown that  $\mathbf{D}_p \mathbf{b} = \mathbf{b}$ , whereby the scalar plane stress-reduced piezoelectric coupling coefficient in equation (27) is identified as

$$e_{31} = d_{31} \frac{E_p}{1-\nu_p} \quad (28)$$

It recovers the stress piezoelectric coupling coefficient resulting from the one-dimensional (1D) transverse mode constitutive equation when  $\nu_p = 0$ .

The in-plane strains can here be represented by

$$\boldsymbol{\varepsilon}_p = \nabla_p \mathbf{v}_p \quad (29)$$

where the in-plane displacements  $u$  and  $v$  are arranged in the displacement vector  $\mathbf{v}_p = [u \ v]^T$  and the 2D derivation operator  $\nabla_p$  is as in equation (9). As for the host plate, the frequency domain representation of the weak variational formulations (25) of the patch is

reached by assuming harmonic loads and solutions  $\mathbf{v}_p = \mathbf{v}_p \exp(i\omega t)$ .

The patch thickness  $t_p$  is assumed significantly smaller than a characteristic in-plane dimension of the patch surface. Hereby, the electric field  $E_3$  is approximately constant through the patch thickness and can thus be determined by the difference between the electric potentials on the top  $\varphi_+$  and bottom  $\varphi_-$  electrodes by

$$E_3 = -\nabla_\varphi \varphi = -\left[1/t_p \quad -1/t_p\right] \begin{bmatrix} \varphi_+ \\ \varphi_- \end{bmatrix} \quad (30)$$

Thus, in this notation, the symbol  $\nabla_\varphi$  denotes the row vector  $[1 \quad -1]/t_p$ . By substituting equations (26), (27), (29), and (30) into (25), the variational weak formulations for the patch (equation (25)) can be written in the frequency domain as

$$\int_{A_p} \delta \mathbf{v}_p^T \left( \nabla_p^T \frac{E_p t_p}{1 - \nu_p} \mathbf{D}_p \nabla_p \mathbf{v}_p + \nabla_p^T e_{31} t_p \mathbf{b} \nabla_\varphi \varphi - \omega^2 \rho_p t_p \mathbf{v}_p \right) dA_p = \sum_{i_c=1}^{n_c} \delta u_\alpha^p(x_{i_c}, y_{i_c}) (F_\alpha^p)_{i_c} \quad (31)$$

for the mechanical relation and as

$$\int_{A_p} \delta \varphi^T \nabla_\varphi^T (-e_{31} t_p \mathbf{b}^T \nabla_p \mathbf{v}_p + \epsilon_{33}^p t_p \nabla_\varphi \varphi) dA_p = \int_{A_Q} \delta \varphi^T \mathbf{Q} dA_Q \quad (32)$$

for the corresponding electrical relation. In both relations, the integration over the constant patch thickness  $t_p$  has been conducted. From equation (32), it is seen that the surface charge densities in  $\mathbf{Q} = [Q_+, Q_-]^T$  are distributed on the top and bottom electrodes with identical surface areas  $A_Q$ , while zero surface charges are assumed on the lateral parts of the patch boundaries.

The FE formulation for the piezoceramic patch is then established by introducing a rectangular four-node element with two uniform electric potential surface dofs for the top and bottom electrodes

$$\varphi = \varphi^e = [\varphi_+ \quad \varphi_-]^T \quad (33)$$

and two nodal dofs representing the in-plane displacements  $u_i$  and  $v_i$ , as shown in Figure 1. The harmonic amplitudes  $\mathbf{v}_p$  can therefore be represented by

$$\mathbf{v}_p^e(x, y) = \mathbf{N}_p(x, y) \mathbf{u}_p^e = \begin{bmatrix} N_1 & 0 & \cdots & N_4 & 0 \\ 0 & N_1 & \cdots & 0 & N_4 \end{bmatrix} \begin{bmatrix} u_1^e \\ v_1^e \\ \vdots \\ u_4^e \\ v_4^e \end{bmatrix} \quad (34)$$

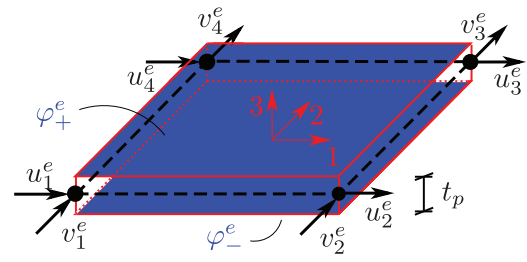


Figure 1. Piezoceramic patch element with eight mechanical and two electric dofs.

where  $\mathbf{N}_p$  contains the shape functions  $N_i$ ,  $\mathbf{u}_p^e$  the nodal displacements, while the subscript 4 again represents the number of element nodes.

The discretized equations of motion are obtained next by substituting equations (33) and (34) into both equations (31) and (32), followed by summation over the number of patch elements  $n_p$  as

$$\sum_{e=1}^{n_p} \begin{bmatrix} \delta \mathbf{u}_p^e \\ \delta \varphi^e \end{bmatrix}^T \left\{ \begin{bmatrix} \mathbf{K}_p^e - \omega^2 \mathbf{M}_p^e & \mathbf{K}_c^e \\ -(\mathbf{K}_c^e)^T & (\mathbf{C}_p^e)^e \end{bmatrix} \begin{bmatrix} \mathbf{u}_p^e \\ \varphi^e \end{bmatrix} - \begin{bmatrix} \mathbf{f}_p^e \\ \mathbf{Q}^e \end{bmatrix} \right\} = 0 \quad (35)$$

In this expression, the element mass, SC stiffness, and electromechanical coupling matrices are determined as

$$\begin{aligned} \mathbf{M}_p^e &= \int_{A_p^e} \mathbf{N}_p^T \rho_p t_p \mathbf{I}_2 \mathbf{N}_p dA_p^e \\ \mathbf{K}_p^e &= \int_{A_p^e} (\nabla_p \mathbf{N}_p)^T \frac{E_p t_p}{1 - \nu_p} \mathbf{D}_p (\nabla_p \mathbf{N}_p) dA_p^e \\ \mathbf{K}_c^e &= \int_{A_p^e} (\nabla_p \mathbf{N}_p)^T \mathbf{b} e_{31} t_p \nabla_\varphi dA_p^e \end{aligned} \quad (36)$$

where  $\mathbf{I}_2$  is the two-by-two identity matrix and the element nodal force and surface charge vectors are defined as

$$\begin{aligned} \mathbf{f}_p^e &= \sum_{i_c=1}^{n_c} \mathbf{N}(x_{i_c}, y_{i_c}) \mathbf{f}_{i_c}^p \\ \mathbf{Q}^e &= \int_{A_Q^e} \mathbf{Q} dA_p^e \end{aligned} \quad (37)$$

with the concentrated force vector  $\mathbf{f}_{i_c}^p = [F_x^p \quad F_y^p]^T_{i_c}$ . Furthermore, the blocked capacitance matrix in (35) is given by

$$(\mathbf{C}_p^e)^e = \int_{A_Q^e} \nabla_\varphi^T \epsilon_{33}^p t_p \nabla_\varphi dA_p^e = C_p^e \begin{bmatrix} 1 & -1 \\ -1 & 1 \end{bmatrix} \quad (38)$$

where

$$C_p^e = \frac{\epsilon_{33}^p A_p}{t_p} \quad (39)$$

is the scalar blocked capacitance.

The global coupled FE equations for a piezoceramic patch discretized by  $n_p$  elements are then established by assembly of the element matrices and vectors to the global nodal order, following a rearrangement of the full system matrices and vectors such that the final format of the global FE equations can be written as

$$\begin{bmatrix} \mathbf{K}_p - \omega^2 \mathbf{M}_p & \mathbf{K}_c \\ -\mathbf{K}_c^T & \mathbf{C}_p^{e_p} \end{bmatrix} \begin{bmatrix} \mathbf{u}_p \\ \boldsymbol{\varphi}_p \end{bmatrix} = \begin{bmatrix} \mathbf{f}_p \\ \mathbf{Q} \end{bmatrix} \quad (40)$$

where the mechanical and electric equations are arranged, respectively, as the first  $2N_p$  and last  $N_{pe}$  coupled equations of motions,  $N_p$  is the number of element nodes, and  $N_{pe} = 2n_p$  is the number of electrical dofs.

The equipotential condition is then applied to the potentials of the piezoceramic elements forming a continuous surface of an electrode. In the present case, only a single piezoceramic patch is considered with one top and one bottom electrode, whereby

$$\varphi_+^1 = \varphi_+^2 = \dots = \varphi_+^{n_p}, \quad \varphi_-^1 = \varphi_-^2 = \dots = \varphi_-^{n_p} \quad (41)$$

The equipotential conditions (equation (41)) can be imposed by defining a boolean matrix  $\mathbf{P}$  that determines the relation between the element potentials in  $\boldsymbol{\varphi}_p$  and the full surface potentials of the top or bottom electrodes as

$$\boldsymbol{\varphi}_p = \mathbf{P} \boldsymbol{\varphi}_\pm = \begin{bmatrix} 1 & 0 & \dots & 1 & 0 \\ 0 & 1 & \dots & 0 & 1 \end{bmatrix}^T \begin{bmatrix} \varphi_+ \\ \varphi_- \end{bmatrix} \quad (42)$$

The coupled FE equations for the discretized piezoceramic patch with consideration of the equipotential condition can thereby be written as

$$\begin{bmatrix} \mathbf{K}_p - \omega^2 \mathbf{M}_p & \mathbf{K}_c \mathbf{P} \\ -\mathbf{P}^T \mathbf{K}_c^T & \mathbf{P}^T \mathbf{C}_p^{e_p} \mathbf{P} \end{bmatrix} \begin{bmatrix} \mathbf{u}_p \\ \boldsymbol{\varphi}_\pm \end{bmatrix} = \begin{bmatrix} \mathbf{f}_p \\ \mathbf{Q}_\pm \end{bmatrix} \quad (43)$$

which consists of  $2N_p + 2$  equations of motion, where the charges at the top and bottom electrodes are defined similarly to equation (42) by

$$\mathbf{Q} = \mathbf{P} \mathbf{Q}_\pm, \quad \mathbf{Q}_\pm = [\mathbf{Q}_+ \quad \mathbf{Q}_-]^T \quad (44)$$

The introduction of the equipotential conditions results in pure edge coupling between the electric and mechanical domains. The coupling between the equations of motion of the plate (equation (17)) and the patch (equation (43)) is obtained next by transforming the electric forcing from the patch elements to the equivalent moment loads for the plate elements.

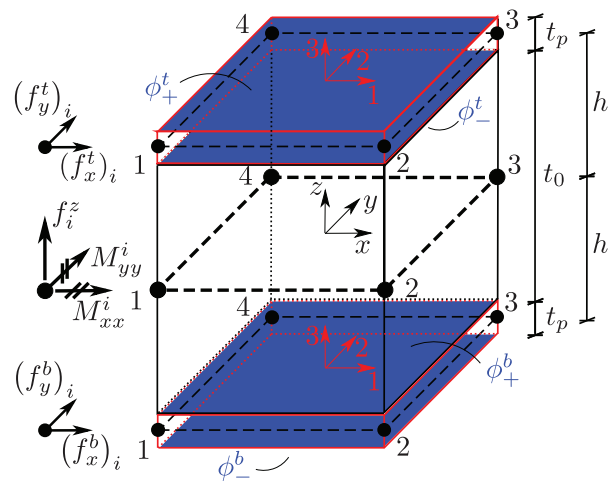


Figure 2. Moment equilibrium of plate and piezoceramic patch elements; the superscript e is omitted in the figure notations.

### Coupled piezo-plate structure

Piezoceramic patches are often placed symmetrically on the host structure. This is beneficial as the neutral axes of the composite and host structure hereby coincide and higher electromechanical coupling can be achieved, when the piezoceramic patches are poled and wired correctly. In the later benchmark examples, only pairs of identical and symmetrically positioned piezoceramic patches are considered. Therefore, a single pair of piezoceramic patches, bonded symmetrically to the upper and lower plate surfaces, is considered in the following. It is assumed that the discretization of the piezoceramic patches coincides with the discretization of the underlying part of the plate, whereby the coupling between each (top and bottom) patch and plate element can be described as shown in Figure 2. It is now considered that the generated electric forcing from the piezoceramic patches acts as external moment loads on the host plate structure, whereby the former force vector  $\mathbf{f}$  in equation (17) can be written as a sum

$$\mathbf{f} = \mathbf{f}_e + \mathbf{f}_p^r \quad (45)$$

of the external mechanical loads  $\mathbf{f}_e$  and the resulting transformed electric forcing from the patches  $\mathbf{f}_p^r$ . It is seen from Figure 2 that the in-plane forces  $f_x^t, f_y^t$  and  $f_x^b, f_y^b$  of the top and bottom piezoceramic patch elements, respectively, couple with the associated moments  $M_{xx}$  and  $M_{yy}$  of the plate, through the distance  $h$  between the mid-planes of the plate and the patches. The moment loads to the plate from the patches's in-plane forces can thus be obtained as

$$\begin{aligned} M_{xx} &= -hf_y^t + hf_x^b \\ M_{yy} &= hf_x^t - hf_y^b \end{aligned} \quad (46)$$

Hereby, the resulting electric forcing from the piezoceramic patches  $\mathbf{f}_p^r$  on the plate can be written as

$$\mathbf{f}_p^r = \mathbf{W}\mathbf{f}_p^t - \mathbf{W}\mathbf{f}_p^b \quad (47)$$

where  $\mathbf{f}_p^t$  and  $\mathbf{f}_p^b$  are, respectively, the in-plane forces from equation (43) of the top and bottom piezoceramic patches transformed through equation (46) by the connectivity matrix

$$\mathbf{W} = \begin{bmatrix} \mathbf{0} & \mathbf{0} & \mathbf{0} \\ \mathbf{W}_1 & \mathbf{0} & \mathbf{0} \\ \mathbf{0} & \ddots & \mathbf{0} \\ \mathbf{0} & \mathbf{0} & \mathbf{W}_{N_p} \\ \mathbf{0} & \mathbf{0} & \mathbf{0} \end{bmatrix}, \quad \mathbf{W}_i = \begin{bmatrix} 0 & 0 \\ 0 & -h \\ h & 0 \end{bmatrix} \quad (48)$$

for the top patch, while forcing from the bottom patch is determined by  $-\mathbf{W}$ , as in equation (47). The nodal connectivity array  $\mathbf{W}_i$  of the patch node  $i$  is placed at the rows and columns of  $\mathbf{W}$  that correspond to the dofs shared by the plate and patches, respectively. Thus, there are as many nodal arrays as there are nodes ( $N_p$ ) in the piezoceramic patch.

By use of equation (45), the equation of motion (equation (17)) for the plate structure, augmented by the electric forcing from the pair of piezoceramic patches, can then be written as

$$(\mathbf{K}_0 - \omega^2\mathbf{M}_0)\mathbf{u} - \mathbf{f}_p^r = \mathbf{f}_e \quad (49)$$

The coupled FE equations then follow from eliminating the piezoelectric forces  $\mathbf{f}_p^r$  in equation (49) by equations (47) and (43), whereby they can be written as

$$\begin{bmatrix} \mathbf{K} - \omega^2\mathbf{M} & -\mathbf{W}\mathbf{K}_c\mathbf{P} & \mathbf{W}\mathbf{K}_c\mathbf{P} \\ (\mathbf{W}\mathbf{K}_c\mathbf{P})^T & \mathbf{P}^T\mathbf{C}_p^{e_p}\mathbf{P} & \mathbf{0} \\ -(\mathbf{W}\mathbf{K}_c\mathbf{P})^T & \mathbf{0} & \mathbf{P}^T\mathbf{C}_p^{e_p}\mathbf{P} \end{bmatrix} \begin{bmatrix} \mathbf{u} \\ \boldsymbol{\varphi}_+^t \\ \boldsymbol{\varphi}_+^b \end{bmatrix} = \begin{bmatrix} \mathbf{f}_e \\ \mathbf{Q}_+^t \\ \mathbf{Q}_+^b \end{bmatrix} \quad (50)$$

which consists of the full set of  $3N$  mechanical equations and four electric equations for the pair of piezoceramic patches. The mass and stiffness matrices of the piezoceramic patches further provide additional terms in the system matrices

$$\mathbf{K} = \mathbf{K}_0 + 2\mathbf{W}\mathbf{K}_p\mathbf{W}^T, \quad \mathbf{M} = \mathbf{M}_0 + 2\mathbf{W}\mathbf{M}_p\mathbf{W}^T \quad (51)$$

where the multiplication with the connectivity matrix  $\mathbf{W}$  ensures that the mass and stiffness effects of the patches are transferred to the correct nodes of the plate structure.

It is now the aim to reduce the number of electric equations by considering the pair of patches being

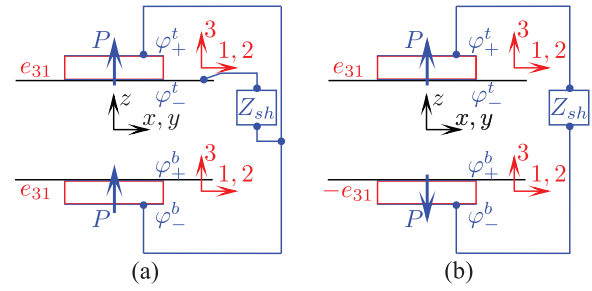


**Figure 3.** Conducting plate structure with a pair of patches wired to a shunt circuit according to poling configurations: (a) SP-PW and (b) OP-SW.

configured as either SP-PW or OP-SW and connected to a shunt circuit with an impedance  $Z_{sh}(\omega)$  (Figure 3).

**SP-PW pair of patches.** For the SP-PW shunted pair of piezoceramic patches, the following relations between the electrode potentials can be deduced from Figure 3(a) as

$$\varphi_-^t = \varphi_+^b, \quad \varphi_+^t = \varphi_-^b, \quad V = \varphi_+^t - \varphi_-^t \quad (52)$$

These relations are now used to eliminate some potentials and to introduce the voltage  $V$  over the electric shunt by establishing the matrix  $\mathbf{P}_\varphi$  as follows

$$\begin{bmatrix} \varphi_+^t \\ \varphi_-^t \\ \varphi_+^b \\ \varphi_-^b \end{bmatrix} = \mathbf{P}_\varphi \begin{bmatrix} V \\ \varphi_-^t \\ \varphi_+^b \end{bmatrix}, \quad \mathbf{P}_\varphi = \begin{bmatrix} 1 & 1 & 0 & 0 \\ 0 & 1 & 0 & 0 \\ 0 & 1 & 0 & 0 \\ 1 & 1 & 0 & 0 \end{bmatrix} \quad (53)$$

Introducing equation (53) in equation (50), the coupling and capacitance matrices are altered by  $\mathbf{P}_\varphi$ , such that

$$\begin{aligned} \mathbf{P}_\varphi^T \begin{bmatrix} \mathbf{P}^T\mathbf{C}_p^{e_p}\mathbf{P} & \mathbf{0} \\ \mathbf{0} & \mathbf{P}^T\mathbf{C}_p^{e_p}\mathbf{P} \end{bmatrix} \mathbf{P}_\varphi &= 2\mathbf{C}_p^{e_p} \begin{bmatrix} 1 \\ \mathbf{0} \end{bmatrix} \begin{bmatrix} 1 & \mathbf{0} \end{bmatrix} \\ \mathbf{W}[-\mathbf{K}_c\mathbf{P} & \mathbf{K}_c\mathbf{P}]\mathbf{P}_\varphi &= -\mathbf{W}\mathbf{k}_c 2e_{31} \begin{bmatrix} 1 & \mathbf{0} \end{bmatrix} \end{aligned} \quad (54)$$

Thus, the capacitance is determined by a scalar  $2\mathbf{C}_p^{e_p}$  for the parallel-wired pair of patches and the coupling by a vector  $\mathbf{W}\mathbf{k}_c 2e_{31}$  as the rows and arrays associated with the remaining potentials contain zeroes only. It is noted that the blocked capacitance  $\mathbf{C}_p^{e_p}$  is given in equation (39) and the coupling vector  $\mathbf{k}_c$  is defined as

$$\mathbf{k}_c = \mathbf{K}_c\mathbf{P} \begin{bmatrix} 1 \\ -1 \end{bmatrix} \frac{1}{2e_{31}} \quad (55)$$

By defining a resulting capacitance  $\bar{\mathbf{C}}_p^{e_p}$  and plane stress-reduced piezoelectric coupling coefficient  $\bar{e}_{31}$  as

$$\bar{\mathbf{C}}_p^{e_p} = 2\mathbf{C}_p^{e_p}, \quad \bar{e}_{31} = 2e_{31} \quad (56)$$

the coupled FE equations (50) can be reduced to

$$\begin{bmatrix} \mathbf{K} - \omega^2 \mathbf{M} & -\mathbf{Wk}_c \bar{e}_{31} \\ (\mathbf{Wk}_c \bar{e}_{31})^T & \bar{C}_p^{ep} \end{bmatrix} \begin{bmatrix} \mathbf{u} \\ V \end{bmatrix} = \begin{bmatrix} \mathbf{f}_e \\ Q \end{bmatrix} \quad (57)$$

where the number of electric equations is reduced to one with the voltage as a variable, while the resulting charge

$$Q = Q_+^t + Q_-^b \quad (58)$$

is obtained after multiplication of the surface charges in equation (50) with  $\mathbf{P}_\varphi^T$ .

The resulting charge  $Q$  can be linked to the voltage  $V$  through the shunt impedance  $Z(\omega)$  via Ohm's law

$$V = -i\omega Z_{sh}(\omega)Q \quad (59)$$

Therefore, the coupled FE equations for the plate with a pair of SP-PW shunted piezoceramic patches can be written as

$$\begin{bmatrix} \mathbf{K} - \omega^2 \mathbf{M} & -\mathbf{Wk}_c \bar{e}_{31} \\ (\mathbf{Wk}_c \bar{e}_{31})^T & \bar{C}_p^{ep} + \frac{1}{i\omega Z_{sh}(\omega)} \end{bmatrix} \begin{bmatrix} \mathbf{u} \\ V \end{bmatrix} = \begin{bmatrix} \mathbf{f}_e \\ 0 \end{bmatrix} \quad (60)$$

where the inverse of the shunt impedance enters in the last diagonal term of the system matrix after the substitution of equation (59) into equation (57) leading to the zero on the right-hand side of equation (60).

**OP-SW pair of patches.** For the OP-SW shunted pair of patches in Figure 3(b), the relations between the potentials can be defined as

$$\varphi_-^t = \varphi_+^b, \quad V = \varphi_+^t - \varphi_-^b \quad (61)$$

and, furthermore, as the patches are considered identical and symmetrically positioned on the host structure, the individual differences in patches' potentials are equal

$$\varphi_+^t - \varphi_-^t = \varphi_+^b - \varphi_-^b \quad (62)$$

These relations are now defined by the matrix  $\mathbf{P}_\varphi$  as

$$\begin{bmatrix} \varphi_+^t \\ \varphi_-^t \\ \varphi_+^b \\ \varphi_-^b \end{bmatrix} = \mathbf{P}_\varphi \begin{bmatrix} V \\ \varphi_+^t \\ \varphi_-^t \\ \varphi_+^b \\ \varphi_-^b \end{bmatrix}, \quad \mathbf{P}_\varphi = \begin{bmatrix} 1/2 & 1 & 0 & 0 \\ 0 & 1 & 0 & 0 \\ 0 & 1 & 0 & 0 \\ -1/2 & 1 & 0 & 0 \end{bmatrix} \quad (63)$$

whereby the capacitance and coupling matrices are altered by the substitution of equation (63) into equation (50)

$$\mathbf{P}_\varphi^T \begin{bmatrix} \mathbf{P}^T \mathbf{C}_p^{ep} \mathbf{P} & \mathbf{0} \\ \mathbf{0} & \mathbf{P}^T \mathbf{C}_p^{ep} \mathbf{P} \end{bmatrix} \mathbf{P}_\varphi = \frac{1}{2} \mathbf{C}_p^{ep} \begin{bmatrix} 1 \\ \mathbf{0} \end{bmatrix} \begin{bmatrix} 1 & \mathbf{0} \end{bmatrix} \quad (64)$$

$$\mathbf{W}[-\mathbf{K}_c \mathbf{P} \quad -\mathbf{K}_c \mathbf{P}] \mathbf{P}_\varphi = -\mathbf{Wk}_c e_{31} \begin{bmatrix} 1 & \mathbf{0} \end{bmatrix}$$

As for the SP-PW pair of patches, the number of electric equations can be reduced to one with the voltage as a variable, whereby equation (50) can be written as equation (60), now with the resulting capacitance and plane stress-reduced piezoelectric coupling coefficient defined for the OP-SW pair of patches as

$$\bar{C}_p^{ep} = \frac{1}{2} C_p^{ep}, \quad \bar{e}_{31} = e_{31} \quad (65)$$

It is seen that the resulting capacitances for the SP-PW and OP-SW pairs of piezoceramic patches correspond to the resulting capacitances of two capacitors connected, respectively, in parallel and series; see Chevallier et al. (2009). For both configurations of the pairs of piezoceramic patches, the vector

$$\mathbf{w} = \mathbf{Wk}_c \quad (66)$$

defines a resulting scalar measure of displacement  $u_p$  of the pair of patches as

$$u_p = \mathbf{w}^T \mathbf{u} \quad (67)$$

used in the following.

### Shunt circuit

In the coupled FE equations (60), the voltage  $V$  is governed by the relation between the resulting blocked capacitance  $\bar{C}_p^{ep}$  and plane stress-reduced piezoelectric coupling coefficient  $\bar{e}_{31}$  and the shunt circuit impedance  $Z_{sh}(\omega)$ . The former can be obtained from the material properties, electrode configuration, and wiring of the pair of piezoceramic patches, while the shunt circuit impedance depends on the configuration and tuning of the connected shunt electronic components.

The solution to equation (60) is bounded by two limits associated with SC and OC patch electrodes. The corresponding SC and OC eigenvalue problems can be deduced from equation (57), with, respectively,  $V = 0$  and  $Q = 0$ . The SC eigenvalue problem hereby follows as

$$[\mathbf{K} - \omega_j^2 \mathbf{M}] \mathbf{u}_j = \mathbf{0} \quad (68)$$

with SC frequencies  $\omega_j$  and mode shapes  $\mathbf{u}_j$ , while the additional sensor equation provides the modal charge

$$Q_j = -\bar{e}_{31} \mathbf{w}^T \mathbf{u}_j \quad (69)$$

In the opposite OC limit, the stiffness is augmented by the voltage stiffening contribution which, for  $Q = 0$ , can be determined as

$$V = \frac{\bar{e}_{31}}{C_p^{ep}} \mathbf{w}^T \mathbf{u} \quad (70)$$

Inserting this relation into the former mechanical equations of equation (57), the OC eigenvalue problem is determined as

$$\left[ \left( \mathbf{K} + \frac{\bar{e}_{31}^2}{\bar{C}_p^{e_p}} \mathbf{w}\mathbf{w}^T \right) - \hat{\omega}_j^2 \mathbf{M} \right] \hat{\mathbf{u}}_j = \mathbf{0} \quad (71)$$

Thus, the OC circular frequencies  $\hat{\omega}_j \geq \omega_j$  because of the piezoelectric effect, where the equality might occur due to charge cancellation effects.

The relative difference between the squared OC and SC frequencies provides the so-called squared effective EMCC

$$\kappa_e^2 = \frac{\hat{\omega}_j^2 - \omega_j^2}{\omega_j^2} \quad (72)$$

which determines the authority of the pair of patches on mode  $j$  and consequently the associated attainable modal damping from the supplemental shunt. Therefore, the latter increases with the separation of the two limiting natural frequencies  $\omega_j$  and  $\hat{\omega}_j$ .

For  $RL$  shunts, the inductance  $L$  is calibrated in order for the circuit frequency to work in resonance with the vibrating structure, while the resistance  $R$  is tuned in order to maximize the dissipation of electrical energy. The  $RL$  network can be established by placing the inductance and resistance either in parallel or in series, as shown in Figure 4. It is noted that these networks are idealized in the sense that any resistance associated with either synthetic or purely passive inductors is neglected, which may have an effect on the tuning of the shunt resistance. Furthermore, it can be seen from Figure 4 that the capacitance is the stress-free capacitance  $C_p^{\sigma_p}$ , which can be found by the relation to the blocked capacitance for the transverse response mode as

$$C_p^{e_p} = C_p^{\sigma_p} (1 - k_{31}^2) \quad , \quad k_{31}^2 = 2 \frac{d_{31}e_{31}}{\epsilon_{33}\sigma_p} \quad (73)$$

where  $k_{31}$  is the piezoceramic material plane stress-reduced electromechanical coupling factor.

For the parallel shunt configuration in Figure 4(b), the impedance  $Z_{sh}(\omega)$  is conveniently expressed in terms of reciprocal values as

$$\frac{1}{Z_{sh}(\omega)} = \frac{1}{R} + \frac{1}{i\omega L} \quad (74)$$

Substitution of the previous impedance function into equation (60) gives the parallel coupled FE equations

$$\left[ \begin{array}{c} \mathbf{K} - \omega^2 \mathbf{M} \\ \bar{e}_{31} \mathbf{w}^T \end{array} \quad \bar{C}_p^{e_p} + \left( \frac{1}{i\omega R} - \frac{1}{\omega^2 L} \right) \right] \begin{bmatrix} \mathbf{u} \\ V \end{bmatrix} = \begin{bmatrix} \mathbf{f}_e \\ 0 \end{bmatrix} \quad (75)$$

with the inverse impedance terms appearing directly in the system matrix.

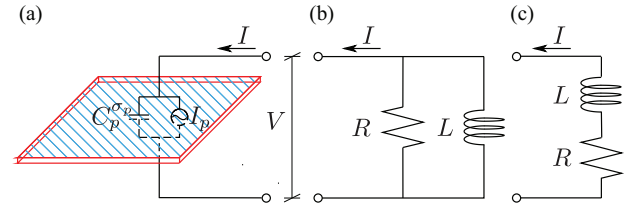


**Figure 4.** Electric model for (a) piezoceramic patch, with (b) parallel and (c) series  $RL$  shunts, where  $I$  is the electric current and  $C_p^{\sigma_p}$  is the constant stress (free) capacitance.

For the series network in Figure 4(c), the impedance function is given as

$$Z_{sh}(\omega) = R + i\omega L \quad (76)$$

whereby the series coupled FE matrix equation takes the form

$$\left[ \begin{array}{c} \mathbf{K} - \omega^2 \mathbf{M} \\ \bar{e}_{31} \mathbf{w}^T \end{array} \quad \bar{C}_p^{e_p} + \frac{-\mathbf{w}\bar{e}_{31}}{i\omega R - \omega^2 L} \right] \begin{bmatrix} \mathbf{u} \\ V \end{bmatrix} = \begin{bmatrix} \mathbf{f}_e \\ 0 \end{bmatrix} \quad (77)$$

For both shunt circuit configurations, the mechanical equivalence is presented in, for example, Høgsberg and Krenk (2017), where the inerter (inductance) and the damper (resistance) are connected in series for the parallel  $RL$  shunt, while they are connected in parallel for the series shunt. However, in this work the electric notation is kept, whereby the existing shunt calibration formulas can be directly applied based on the derived electric analogies.

### Shunt tuning based on balanced modal calibration

In this second section, the coupled FE equations (75) and (77) for the parallel and series shunt circuits are analyzed in order to determine the particular shunt tuning that maximizes the damping of a targeted resonant vibration mode  $j = r$ . In order to apply analytical calibration methods, the full complex eigenvalue problem is reduced to a representative system of only two coupled equations, governing the structural response of the target mode  $r$  and the associated electric loading from the pair of piezoceramic patches.

The mechanical equations in equations (75) and (77) can be decoupled in terms of the mode shapes  $\mathbf{u}_j$  from the SC eigenvalue problem in equation (68). For this purpose, the displacement vector  $\mathbf{u}$  is represented by a linear combination of the normalized mode shape vectors  $\mathbf{u}_j/(\mathbf{w}^T \mathbf{u}_j)$ , whereafter the pre-multiplication of equations (75) and (77), with the transpose of the normalized mode shape vector, gives the scalar equation of motion

$$(k_j - \omega^2 m_j) u_j - \bar{e}_{31} V = f_j \quad (78)$$

where the normalized modal mass, stiffness, and loads are defined as

$$m_j = \frac{\mathbf{u}_j^T \mathbf{M} \mathbf{u}_j}{(\mathbf{w}^T \mathbf{u}_j)(\mathbf{u}_j^T \mathbf{w})}, k_j = \frac{\mathbf{u}_j^T \mathbf{K} \mathbf{u}_j}{(\mathbf{w}^T \mathbf{u}_j)(\mathbf{u}_j^T \mathbf{w})}, f_j = \frac{\mathbf{u}_j^T \mathbf{f}_e}{\mathbf{w}^T \mathbf{u}_j} \quad (79)$$

The resulting displacement  $u_p$  (equation (67)) of the pair of patches is, because of the normalization, given by the sum of the modal displacements  $u_j$  obtained by solving the  $3N$  scalar equations (78).

The aim is to derive the optimal shunt tuning for a specific resonant vibration mode  $j = r$ , which can be approximated by the single dynamic term  $j = r$  and two supplemental terms, accounting for the flexibility and inertia effects from the non-resonant modes  $j \neq r$  (Krenk and Høgsberg, 2016). This modal correction approach is based on a two-term representation of the response contribution from non-resonant modes and enables the derivation of explicit expressions for the optimal shunt tuning. This is briefly reviewed in the following and expressed in terms of representative electro-mechanical components.

The resulting plane stress-reduced piezoelectric coupling coefficient  $\bar{e}_{31}$  translates displacement in the mechanical domain to charge  $Q$  in the electric domain by equation (69). This is now used to eliminate  $u_j$  in the modal equations of motion (equation (78)), which by considering free vibrations can be written as

$$-\left(\frac{k_j}{\bar{e}_{31}^2} - \omega^2 \frac{m_j}{\bar{e}_{31}^2}\right) Q_j = V \quad (80)$$

The sum of the modal charge components  $Q_j$  determines the magnitude of the resulting charge  $Q$ .

For resonant damping, the charge  $Q$  is specifically determined at the resonant frequency of mode  $r$ , taking into account the influence from the other residual modes by including the flexibility and inertia correction terms as presented in Krenk and Høgsberg (2016) and transferred to the equivalent electric corrections by multiplication with  $\bar{e}_{31}^2$

$$C_{r'} = \bar{e}_{31}^2 \mathbf{w}^T \mathbf{K}_r^{-1} \mathbf{K} \mathbf{K}_r^{-1} \mathbf{w} - \frac{\bar{e}_{31}^2}{k_r} \quad (81)$$

$$\frac{\omega_r^2}{L_{r'}} = \bar{e}_{31}^2 \mathbf{w}^T \mathbf{K}_r^{-1} \mathbf{K} \mathbf{K}_r^{-1} \mathbf{w} - \bar{e}_{31}^2 \mathbf{w}^T \mathbf{K}_r^{-1} \mathbf{w}$$

The modified stiffness and mass matrices correspond to removing the mass contribution from the resonant mode and making a frequency shift of the stiffness matrix. They are given as (Krenk and Høgsberg, 2016)

$$\mathbf{K}_r = \mathbf{K} - \omega_r^2 \mathbf{M}_r, \quad \mathbf{M}_r = \mathbf{M} - \frac{(\mathbf{M} \mathbf{u}_r)(\mathbf{M} \mathbf{u}_r)^T}{\mathbf{u}_r^T \mathbf{M} \mathbf{u}_r} \quad (82)$$

with  $\mathbf{K}_r = \mathbf{K}$  for the case of a pure quasi-static residual mode correction. The flexibility and inertia corrections for the non-resonant modes, due to the presence of the electric shunt, can thus be represented by the modal capacitance  $C_{r'}$  and inductance  $L_{r'}$  in equation (81), respectively. Hereby, the charge  $Q$  is truncated consistently for mode  $r$  as

$$Q \simeq Q_r - \left(C_{r'} - \frac{1}{\omega^2 L_{r'}}\right) V \quad (83)$$

where the modal charge for the resonant mode  $r$  is determined from equation (80) by the dynamic equation

$$Q_r = -\frac{\omega_r^2}{\omega_r^2 - \omega^2} \frac{\bar{e}_{31}^2}{k_r} V \quad (84)$$

Substitution of the modal electric representation (equation (83)) into the last equation of (equation (60)) gives the homogeneous equation

$$\left(\frac{\omega_r^2}{\omega_r^2 - \omega^2} \frac{\bar{e}_{31}^2}{k_r} + C_r - \frac{1}{\omega^2 L_{r'}} + \frac{1}{i\omega Z_{sh}(\omega)}\right) V = 0 \quad (85)$$

when the modal charge  $Q_r$  has been eliminated by equation (84), while the modal capacitance

$$C_r = \bar{C}_p^{e_p} + C_{r'} \quad (86)$$

is conveniently represented as the sum of the resulting blocked capacitance  $\bar{C}_p^{e_p}$  and modal capacitance  $C_{r'}$  in equation (81).

Non-trivial solutions require the expression inside the parenthesis in equation (85) to vanish, constituting the characteristic equation of the system. In common calibration methods, based on single-mode representations of the mechanical structure, division with the blocked capacitance  $\bar{C}_p^{e_p}$  introduces the so-called squared modal EMCC

$$\kappa_0^2 = \frac{\bar{e}_{31}^2}{\bar{C}_p^{e_p} k_r} \quad (87)$$

see, for instance, Thomas et al. (2012). In the present case, the introduced residual mode corrections in equation (81) modify the effective capacitance of the pair of piezoceramic patches by a constant flexibility and a frequency-dependent inertia contribution from the non-resonant modes. This means that the effective capacitance varies with the frequency as discussed in Berardengo et al. (2016). At resonance in mode  $r$ , the effective capacitance can thus be determined as

$$C_L = C_r - \frac{1}{\omega_r^2 L_{r'}} \quad (88)$$

whereby the residual mode-corrected squared modal EMCC can be defined as

$$\kappa_L^2 = \frac{\bar{e}_{31}^2}{C_L k_r} \quad (89)$$

As demonstrated in the later benchmark examples, this residual mode–corrected modal EMCC approximately equals the effective EMCC in equation (72), with a minor deviation due to the approximation of the non-resonant mode representation in Krenk and Høgsberg (2016). However, for the derivation of the shunt tuning formulas, it is convenient to introduce the frequency-independent squared modal EMCC

$$\kappa_r^2 = \frac{\bar{e}_{31}^2}{C_r k_r} \quad (90)$$

which is only modified by the flexibility correction for the non-resonant modes, by the modified capacitance in equation (86). Hereby, the characteristic equation for equation (85) can be written as

$$\frac{\omega_r^2}{\omega_r^2 - \omega^2} \kappa_r^2 + \frac{1}{i\omega Z_r(\omega) C_r} + 1 = 0 \quad (91)$$

where the modal shunt circuit impedance

$$\frac{1}{Z_r(\omega)} = \frac{1}{Z_{sh}(\omega)} + \frac{1}{i\omega L_r} \quad (92)$$

is explicitly modified by the modal inductance  $L_r$  in equation (81).

### Parallel shunt

For the parallel shunt circuit, the impedance function  $Z_{sh}(\omega)$  in equation (74) is substituted into equation (92), whereby the modal impedance function can be written as

$$\frac{1}{Z_r(\omega)} = \frac{1}{R_r} + \frac{1}{i\omega L_r} \quad (93)$$

introducing the modal inductance and resistance as

$$\frac{1}{L_r} = \frac{1}{L} + \frac{1}{L_r'} \quad , \quad R_r = R \quad (94)$$

Any preferred calibration procedure can now be used to determine the modal inductance  $L_r$  and resistance  $R_r$ . In the present case, the modal shunt components are determined by the balanced calibration method (Høgsberg and Krenk, 2017), based on the equal modal damping calibration for the tuned mass damper (Krenk, 2005). The electric components of the modal shunt circuit are therefore determined according to Høgsberg and Krenk (2012) by the two calibration formulas

$$L_r C_r \omega_r^2 = 1 \quad , \quad R_r C_r \omega_r = \sqrt{\frac{1}{2\kappa_r^2}} \quad (95)$$

where  $\omega_r$  is the natural frequency of the targeted mode with SC electrodes,  $C_r$  is the modal capacitance in equation (86), while  $\kappa_r$  has been defined in equation (90).

The actual shunt inductance  $L$  follows from equation (94) and is conveniently written as in equation (95)

$$L C_L \omega_r^2 = 1 \quad (96)$$

with the effective modal capacitance defined in equation (88). Hereby, the resistance in equation (95) and the inductance in equation (96) are determined by expressions similar to those for an idealized single-mode structure (Høgsberg and Krenk, 2012), but with modified capacitances  $C_r$  and  $C_L$ , respectively.

The calibration formulas for  $L_r$ ,  $R_r$  with only flexibility correction and for  $L$ ,  $R$  with the full flexibility–inertia residual mode correction are listed in the second column of Table 1. Furthermore, the table provides the commonly used single-mode calibration ( $L_0$ ,  $R_0$ ) determined by the squared modal EMCC in equation (87) and the resulting blocked capacitance  $\bar{C}_p^{cp}$  of the pair of piezoceramic patches.

### Series shunt

For the series shunt circuit, the modal impedance  $Z_r(\omega)$  is obtained by the substitution of equation (76) into equation (92)

$$Z_r(\omega) = \frac{i\omega L_r'(R + i\omega L)}{i\omega L_r' + (R + i\omega L)} \quad (97)$$

As for the parallel shunt, this modal function is approximated by the format

**Table 1.** Balanced calibration procedure for parallel and series shunt circuits, without  $L_0$ ,  $R_0$ , with flexibility  $L_r$ ,  $R_r$ , and with flexibility–inertia  $L$ ,  $R$  residual mode corrections.

Parameter	Parallel	Series
$L_0$	$\frac{1}{\bar{C}_p^{cp} \omega_r^2}$	$\frac{1}{\bar{C}_p^{cp} (1 + \kappa_0^2)^2 \omega_r^2}$
$R_0$	$\frac{1}{\bar{C}_p^{cp} \omega_r} \sqrt{\frac{1}{2\kappa_0^2}}$	$\frac{1}{\bar{C}_p^{cp} \omega_r} \sqrt{\frac{2\kappa_0^2}{(1 + \kappa_0^2)^3}}$
$L_r$	$\frac{1}{C_r \omega_r^2}$	$\frac{1}{C_r (1 + \kappa_r^2)^2 \omega_r^2}$
$R_r$	$\frac{1}{C_r \omega_r} \sqrt{\frac{1}{2\kappa_r^2}}$	$\frac{1}{C_r \omega_r} \sqrt{\frac{2\kappa_r^2}{(1 + \kappa_r^2)^3}}$
$L$	$\frac{1}{C_L \omega_r^2}$	$\frac{1}{C_L (1 + \kappa_L^2)^2 \omega_r^2}$
$R$	$R_r$	$R_r (L/L_r)^2$

$$Z_r(\omega) = R_r + i\omega L_r \quad (98)$$

similar to the actual shunt in equation (76). The modal impedance in equation (97) is separated into its real and imaginary parts, whereby the frequency-independent  $R_r$  and  $L_r$  are obtained by omitting the terms containing  $R^2$ . The electrical components of the modal shunt impedance are then obtained as

$$\frac{1}{L_r} = \frac{1}{L} + \frac{1}{L_r'} \quad , \quad R_r = \frac{R}{\left(1 + \frac{L}{L_r'}\right)^2} \quad (99)$$

where the inductance  $L_r$  is defined as for the parallel shunt in equation (94), while the modal resistance  $R_r$  is additionally affected by the modal inductance correction  $L_r'$ . Again, the balanced calibration in Høgsberg and Krenk (2012) is applied, which in the present notation gives the following calibration formulas for the modal components of the series shunt

$$L_r C_r \omega_r^2 = \frac{1}{(1 + \kappa_r^2)^2} \quad , \quad R_r C_r \omega_r = \sqrt{\frac{2\kappa_r^2}{(1 + \kappa_r^2)^3}} \quad (100)$$

The actual shunt tuning then follows by considering equations (88), (89), (99), and (100)

$$L C_L \omega_r^2 = \frac{1}{(1 + \kappa_r^2)^2 + \kappa_L^2 \xi} \quad , \quad R = R_r \left(\frac{L}{L_r}\right)^2 \quad (101)$$

which is seen to depend on the residual mode-corrected squared modal EMCC, while the parameter  $\xi$ , in the inductance tuning formula, represents the difference between  $\kappa_r^2$  and  $\kappa_L^2$

$$\xi = \kappa_r^2 - \kappa_L^2 = \kappa_r^2 \frac{1}{1 - \omega_r^2 L_r' C_r} \quad (102)$$

The parameter  $\xi$  depends on the difference between unity and the ratio of the modal capacitance  $C_r$  to the inertia correction  $1/(\omega_r^2 L_r')$ , and therefore  $\xi \rightarrow 0$  when the inertia correction becomes small relative to the modal capacitance. As  $\xi$  in equation (101) is further multiplied by  $\kappa_L^2$ , the term is negligible and can be omitted in the tuning of the series-connected inductance. The optimal calibration formulas both with and without the flexibility and flexibility-inertia residual mode corrections are summarized in the last column of Table 1.

### Shunt tuning based on the effective EMCC

The squared effective EMCC  $\kappa_e^2$  defined in equation (72) is commonly used as the governing parameter in the calibration of resonant shunt circuits. It is a

convenient parameter, as it can be determined experimentally by simple dynamic tests in the SC and OC limits and thereby takes actual device imperfections into account. However, the squared effective EMCC is typically represented by the squared modal EMCC  $\kappa_0^2$  in equation (87), evaluated for a single-mode of the structure without any residual mode correction. As demonstrated in the later analysis of two benchmark examples, the approximation  $\kappa_0^2 \simeq \kappa_e^2$  becomes rather inaccurate when the contribution from non-resonant modes is substantial. In particular, the flexibility contribution from the residual modes can be shown to have a significant effect on the evaluated squared modal EMCC  $\kappa_r^2$  in equation (90), as also discussed by Berardengo et al. (2016). An even more accurate evaluation of the squared effective EMCC is however obtained by the squared modal EMCC  $\kappa_L^2$  in equation (89), where the modified capacitance  $C_L$  in equation (88) contains both the flexibility correction by  $C_r$  in equation (86) and the inertia correction directly by  $L_r'$ . The only approximation associated with this coupling coefficient is the truncation introduced in the derivation of the residual mode components in equation (81); see details in Krenk and Høgsberg (2016). Thus, it is investigated in the next section by two benchmark examples how accurately the representation of the squared effective EMCC by

$$\kappa_L^2 \simeq \kappa_e^2 \quad (103)$$

captures the influence from residual vibration modes. Assuming  $\kappa_L^2 = \kappa_e^2$ , an alternative calibration procedure based on the SC and OC frequencies of the structure can then be established, as demonstrated in the following.

The characteristic equation resulting from equation (85) is now expressed in terms of the squared effective EMCC  $\kappa_e^2$  and the modified capacitance  $C_L$  via the elimination of  $e_{31}^2/k_r$  by equations (89) and (103) and of  $L_r'$  by equation (88). Hereby, the characteristic equation can be written as

$$\frac{\kappa_e^2 \omega_r^2 \omega^2}{\omega_r^2 - \omega^2} + \omega_r^2 - \frac{C_r}{C_L} (\omega_r^2 - \omega^2) + \frac{\omega^2}{i\omega Z_{sh}(\omega) C_L} = 0 \quad (104)$$

The optimal shunt inductance is now based on the squared effective EMCC  $\kappa_e^2$ , while the resistance is subsequently derived from the squared modal EMCC  $\kappa_r^2$ . Thus, the present calibration procedure depends on two effective coupling coefficients:  $\kappa_e^2$  and  $\kappa_r^2$ .

### Parallel shunt

For the parallel shunt circuit, the inductance  $L$  is determined by equation (96). When the modified capacitance  $C_L$  is eliminated in terms of the squared effective EMCC  $\kappa_e^2$  by equations (89) and (103), with the

normalized modal stiffness expressed as  $k_r = m_r \omega_r^2$ , the shunt inductance can be represented as

$$L = \kappa_e^2 \frac{m_r}{\bar{e}_{31}^2} \quad (105)$$

In this expression, the normalized modal mass  $m_r$  may often be estimated quite accurately from the vibration form of the structure, while the squared effective EMCC  $\kappa_e^2$  is determined by equation (72). The resulting plane stress–reduced piezoelectric coupling coefficient  $\bar{e}_{31}^2$  is further specified for the particular piezoceramic patches through equation (28) and wiring by equations (56) and (65) for, respectively, the SP-PW and OP-SW pairs of patches.

Once the inductance  $L$  has been determined, a pure  $L$  shunt is constructed, as indicated in Figure 4(b) with  $R = 0$ . Hereby, two new resonant frequencies  $\omega_+^2$  and  $\omega_-^2$  emerge around the original SC frequency  $\omega_r^2$ . Expressions for these two frequencies can be determined by inserting the expression for the inductance (equation (96)) into the characteristic equation (104) and considering the expressions for the residual mode–corrected modal EMCCs (equations (89) and (90)), whereby the following quadratic equation in  $\omega^2$  is obtained

$$\omega^4 - (2 + \kappa_r^2)\omega_r^2\omega^2 + \omega_r^4 = 0 \quad (106)$$

The product and sum of the solutions  $\omega_+^2$  and  $\omega_-^2$  can be written as

$$\omega_+^2 \omega_-^2 = \omega_r^4, \quad \omega_+^2 + \omega_-^2 = (2 + \kappa_r^2)\omega_r^2 \quad (107)$$

and the elimination of  $\omega_r^2$  between these relations gives the modal EMCC  $\kappa_r^2$  as

$$\kappa_r^2 = \frac{(\omega_+ - \omega_-)^2}{\omega_+ \omega_-} \quad (108)$$

The shunt resistance then follows from equation (95) as

$$R = \kappa_r^2 \frac{m_r \omega_r}{\bar{e}_{31}^2} \sqrt{\frac{1}{2\kappa_r^2}} \quad (109)$$

where  $C_r$  has been eliminated by equation (90) and  $k_r = \omega_r^2 m_r$  has again been used. As for the inductance  $L$  in equation (105), the resistance  $R$  is determined by the normalized modal mass and the resulting plane stress–reduced piezoelectric coupling coefficient  $\bar{e}_{31}^2$ , while  $\kappa_r^2$  should be used for  $R$  instead of  $\kappa_e^2$ . The tuning formulas for the optimal parallel-connected inductance and resistance based on the effective EMCC are summarized in the second column of Table 2.

### Series shunt

For the series shunt circuit, the same approach is used. The inductance  $L$  is calibrated by the expression in

**Table 2.** Tuning procedure based on the effective EMCC for parallel and series shunt circuits.

Parameter	Parallel	Series
$L$	$\kappa_e^2 \frac{m_r}{\bar{e}_{31}^2}$	$\kappa_e^2 \frac{m_r}{(1 + \kappa_e^2)^2 \bar{e}_{31}^2}$
$R$	$\kappa_r^2 \frac{m_r \omega_r}{\bar{e}_{31}^2} \sqrt{\frac{1}{2\kappa_r^2}}$	$\kappa_r^2 \frac{m_r \omega_r}{\bar{e}_{31}^2} \sqrt{\frac{2\kappa_r^2}{(1 + \kappa_r^2)^3}}$
Initial step	$\kappa_e^2 = \frac{\hat{\omega}^2 - \omega^2}{\omega^2}, L = \kappa_e^2 \frac{m_r}{\bar{e}_{31}^2}$	
Determine	$\omega_+, \omega_-, \kappa_r^2 = \frac{(\omega_+ - \omega_-)^2}{\omega_+ \omega_-}$	

EMCC: electromechanical coupling coefficient.

equation (101), where the assumption  $\kappa_L^2 \xi \ll 1$  yields the simplified expression

$$L = \kappa_e^2 \frac{m_r}{(1 + \kappa_e^2)^2 \bar{e}_{31}^2} \quad (110)$$

which only contains the squared effective EMCC  $\kappa_e^2$  from equation (103), the normalized modal mass  $m_r$ , and the squared resulting plane stress–reduced piezoelectric coupling coefficient  $\bar{e}_{31}^2$ , while  $C_L$  is eliminated by equations (89) and (103) and  $k_r = \omega_r^2 m_r$ . Again, the pure  $L$  shunt with  $R = 0$  in Figure 4(b) is constructed and the two natural frequencies  $\omega_+$  and  $\omega_-$  are determined numerically or experimentally. The shunt resistance is given by the expression in equation (101), in which the modal resistance  $R_r$  from equation (100) is scaled by the apparent inductance ratio  $L/L_r$ , where the modal inductance in equation (100a) can alternatively be written as

$$L_r = \kappa_r^2 \frac{m_r}{(1 + \kappa_r^2)^2 \bar{e}_{31}^2} \quad (111)$$

when introducing equations (89) and (103) and  $k_r = \omega_r^2 m_r$ . Thus, the shunt resistance can be obtained by the expression

$$R = \kappa_r^2 \frac{m_r \omega_r}{\bar{e}_{31}^2} \sqrt{\frac{2\kappa_r^2}{(1 + \kappa_r^2)^3}} \left(\frac{L}{L_r}\right)^2 \quad (112)$$

which, besides the normalized modal mass  $m_r$ , the resulting plane stress–reduced piezoelectric coupling coefficient  $\bar{e}_{31}^2$ , and the squared modal EMCC  $\kappa_r^2$ , also depends on the squared effective EMCC  $\kappa_e^2$  through the ratio  $L/L_r$ . However, while the calibration of the inductance must be calibrated rather precisely because it governs the shunt frequency, the corresponding shunt resistance may subsequently be approximated by assuming  $L_r/L \simeq 1$ , as the shunt performance is less sensitive to deviations in the resistance. The

approximated tuning formulas for the series-connected resistance and the corresponding expression for the inductance are listed in the last column of Table 2.

For both the parallel and series shunt circuits, accurate calibration of the inductance and resistance can be achieved from the effective EMCC only, when the inertia correction is significantly smaller than the flexibility correction  $1/(\omega_r^2 L_r) \ll C_r$ , whereby  $\kappa_r \simeq \kappa_e$ . This is often the case for the lower and well-separated vibration modes, while the influence of the inertia correction may increase for the higher and closely spaced modes. It is beneficial to base the shunt tuning on the effective EMCC only, as one avoids the evaluation of an additional eigenvalue problem or experiments with the pure  $L$  shunt, which can be difficult to produce due to the inherent resistance in both synthetic and purely passive inductors.

### Error estimate

The error arising from the use of either a single-mode representation  $\kappa_0^2$  or the method with pure quasi-static corrections  $\kappa_r^2$  for the shunt circuit calibration can for the parallel shunt be represented by the ratio  $\kappa^2/\kappa_e^2$ , which is unity when the residual mode correction is insignificant. For the series shunt, this ratio provides a good estimate of the error, although it is not entirely unity because of the truncations introduced for this shunt. Thus, the necessity of including both the flexibility and the inertia contributions from the non-resonant modes can be evaluated by comparing the different squared modal EMCCs:  $\kappa_0^2$ ,  $\kappa_r^2$ , and  $\kappa_L^2$  with the squared effective EMCC  $\kappa_e^2$ , as demonstrated in the following benchmark examples.

In the shunt tuning formulas in Table 2, the effect of having, respectively, an SP-PW or an OP-SW configured pair of piezoceramic patches is directly seen to be governed by the corresponding resulting plane stress-reduced piezoelectric coupling coefficient  $\bar{e}_{31}^2$ . The SC and OC frequencies and thereby the squared effective EMCC will be the same for the structure with, respectively, a pair of patches in SP-PW and OP-SW configurations. Consequently, the squared modal EMCC  $\kappa_r^2$  will as well be identical for the two configurations. Finally, since the normalized modal mass  $m_r$  is also independent of the poling and wiring of the pair of piezoceramic patches, it is found that both the optimal inductance and resistance for the OP-SW pair of patches are four times as large as the corresponding values for the SP-PW patch configuration. This is because the resulting plane stress-reduced piezoelectric coupling coefficients for the SP-PW and OP-SW pairs of patches are, respectively,  $2e_{31}$  and  $e_{31}$  (see equations (56) and (65)). Hence, as  $\bar{e}_{31}$  is squared in the denominator of the tuning formulas in Table 2, a factor of four occurs between the shunt tunings of the two respective

pairs of patches' configurations. In Thomas et al. (2009) and Lossouarn et al. (2017), the same cantilever beam with a single pair of, respectively, OP-SW and SP-PW piezoceramic patches is analyzed. Considering the corresponding optimal shunt tunings based on experiments, it is approximately found that the OP-SW configured patches cause four times larger optimal inductance and resistance values compared to the SP-PW configuration.

### Benchmark examples

In this section, the balanced calibration procedures based on the modal and effective EMCC, respectively, are analyzed. It is noted that only one shunt tuning will be provided in the examples as the two methods give almost the same tuning values. The small deviations are only due to the approximation (equation (103)).

The implemented FE model enables comparison with shunt tuning methods from benchmark examples in the literature concerning optimal  $RL$  shunt tuning. The two examples of this section consider a cantilever beam, analyzed by both Thomas et al. (2009, 2012) and Ducarne et al. (2012), and a plate analyzed by Gardonio and Casagrande (2017). In both cases, the structure is equipped with a single pair of piezoceramic patches, configured either as OP-SW or as SP-PW. The present examples apply the particular configurations from the benchmark cases, although the SP-PW configuration is seemingly adequate, as it leads to four times smaller inductances and resistances than for OP-SW.

As the experimental results are available for the cantilever beam example, it can be used to verify the established numerical model as well as assess the effect of using beam instead of plate elements for the modeling of plate-like beam structures. For the subsequent plate benchmark presented by Gardonio and Casagrande (2017), the influence of the non-resonant modes is investigated by a thorough parametric study. Therefore, this example constitutes a good opportunity to compare the benchmark results with the present calibration procedures, in which the presence of the non-resonant modes is accounted for explicitly.

#### Cantilever beam

The first example concerns the cantilever beam with a single pair of OP-SW piezoceramic patches, for which the SC and OC frequencies and the associated modal EMCC are determined both numerically and experimentally by Thomas et al. (2009). The optimal tuning of the electronic components for both  $R$  and  $RL$  shunts is provided in Thomas et al. (2012), while the optimal design and placement of the piezoceramic patches are analyzed by Ducarne et al. (2012). The geometry of the cantilever beam can be seen in Figure 5. The single pair of ideally bonded OP piezoceramic patches (red color) is placed in series with a shunt circuit (blue color) with

**Table 3.** Dimensions and material properties for cantilever beam and piezoceramic patches.

	Beam		Piezoceramic	
Length (mm)	$l$	170	$l_p$	25
Width (mm)	$b$	20	$b$	20
Thickness (mm)	$t_0$	2	$t_p$	0.5
Density ( $\text{kg/m}^3$ )	$\rho$	2800	$\rho_p$	8500
Young's modulus (GPa)	$E$	72	$E_p$	66.7
Poisson's ratio (-)	$\nu$	0	$\nu_p$	0
Piezoelectric coefficient ( $10^{-12}$ m/V)			$d_{31}$	-210
Blocked dielectric coefficient (F/m)			$\epsilon_{33}^{ep}$	2068 $\epsilon_0$

$\epsilon_0 = 8.854 \times 10^{-12}$  F/m; see IEEE (1988).

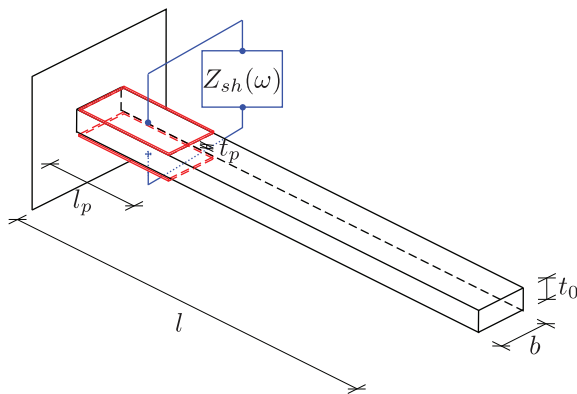


**Figure 5.** Geometry of cantilever beam, with one pair of OP, surface-bonded, and SWV piezoceramic patches.

impedance  $Z_{sh}(\omega)$ . The beam is conductive and a conductive adhesive is used for the bonding of the piezoceramic patches, whereby the two inner electrodes of the patches are connected. The pair of patches is modeled as described in the first section, where the resulting capacitance and plane stress-reduced piezoelectric coupling coefficient can be determined by equation (65).

The dimensions and material properties of the beam and the piezoceramic patches are given in Table 3. A vanishing Poisson's ratio is assumed for both patch and beam, whereby the present results can be compared to the numerical results for the beam model in Thomas et al. (2009). In the original experimental design, an additional tip mass  $m_{ex} = 4.2$  g is added for excitation purpose. This mass is therefore also added to the diagonal element of the mass matrix for the transverse dof of the center node at the free end of the beam. Finally, the pair of piezoceramic patches is placed with a horizontal offset of  $x_p = 0.5$  mm relative to the fixed support.

The cantilever beam is discretized by  $41 \times 2$  plate elements, while the piezoelectric patches are each represented by  $5 \times 2$  patch elements. The corresponding beam model (Høgsberg and Krenk, 2015) with 41 Bernoulli beam elements and 5 (1D) patch elements is used for comparison. It corresponds to the model in Thomas et al. (2009) with 41 beam elements, with 5

elements containing the electromechanical coupling to the pair of patches, and it reproduces the first two vibration modes with sufficient accuracy.

In order to verify the current electromechanical piezo-plate model, the first two SC and OC frequencies are determined. They are summarized in Table 4, which also contains the experimental and numerical frequencies for the first bending modes reported in Thomas et al. (2009).

The optimum series and parallel shunt tuning of the pair of piezoceramic patches, based on the present piezo-plate model, is now determined with and without residual mode contribution. The results are shown in the first rows of Table 4 for modes 1 and 2. The table also contains the optimal series shunt tuning with residual mode correction for the simple beam model. For comparison, Table 4 also presents the optimal experimental shunt tuning (Thomas et al., 2012) (superscript 2), the theoretical tuning based on the tuning formulas without correction (Thomas et al., 2012) (superscript 1), and the numerical beam model described in Thomas et al. (2009). Finally, the modal EMCCs  $\kappa$ , in Table 4, are calculated, respectively, with (equation (89)) and without (equation (87)) the residual mode correction, while  $\kappa$  values provided for the experiment are the effective EMCC (equation (72)).

The reported numerical results based on the tuning formulas in Thomas et al. (2012) are obtained by the numerical beam model described in Thomas et al. (2009). They are observed to be in good agreement with the frequencies determined by the beam model in Høgsberg and Krenk (2015). The reason for the slightly lower frequencies is mainly due to the omission of the patches' bending contribution in the present model. A good agreement is observed also for the determined SC and OC frequencies for the plate model, where the small decrease of the OC frequency occurs because of plate effects at the supports, which is not captured by the simpler beam model. The experimentally obtained SC and OC frequencies (Thomas et al., 2012) are slightly larger for the first mode, while the mode 2 frequencies are in very good

**Table 4.** SC and OC frequencies, modal EMCC, and shunt circuit calibration for modes 1 and 2 of a cantilever beam, using a beam and a plate model.

	Model shunt	$f$ (Hz)	$\hat{f}$ (Hz)	$\kappa$	$L$ (H)	$R$ (k $\Omega$ )
Mode 1	<b>Plate</b>					
	Parallel*	48.93	49.36	0.13	991.0	1619
	Series*				957.0	55.85
	Parallel <sup>0</sup>	48.93	49.36	0.14	1156	1749
	Series <sup>0</sup>				1110	70.00
	<b>Beam</b>					
	Series*	48.93	49.39	0.14	1021	61.69
	Series <sup>1</sup>	48.96	49.42	0.14	1131	61.56
Mode 2	<b>Experiment</b>					
	Series <sup>2</sup>	51.64	52.17	0.14	1020 <sup>3</sup>	58.6 <sup>3</sup>
	<b>Plate</b>					
	Parallel*	337.0	340.3	0.14	21.26	226.2
	Series*				20.45	8.702
	Parallel <sup>0</sup>	337.0	340.3	0.15	24.36	242.5
	Series <sup>0</sup>				23.29	10.61
	<b>Beam</b>					
Series*	337.1	340.7	0.15	21.84	9.63	
Series <sup>1</sup>	337.1	340.7	0.15	23.81	9.37	
<b>Experiment</b>						
Series <sup>2</sup>	337.0	340.2	0.14	23.9 <sup>3</sup>	8.65 <sup>3</sup>	

SC: short-circuit; OC: open-circuit; EMCC: electromechanical coupling coefficient.

\*Present model with residual mode correction ( $\kappa_L$ ).

<sup>0</sup>Present model without residual mode correction ( $\kappa_0$ ).

<sup>1</sup>Tuning based on theory in Thomas et al. (2012)( $\kappa_0$ ).

<sup>2</sup>Experimental results from Thomas et al. (2012)( $\kappa_e$ ).

<sup>3</sup>Final values not measured in Thomas et al. (2012).

agreement with the numerical results. Significant differences are found between the modal EMCCs  $\kappa_L$  and  $\kappa_0$  with and without residual mode correction, respectively. Furthermore, the corrected modal EMCC  $\kappa_L$  from the beam model is seen to deviate from the corresponding EMCC determined by the plate model, demonstrating that the influence from the residual modes depends on the model accuracy. The effective EMCC based on the experimental data is expected to correspond well with the modal EMCC  $\kappa_L$ . However, it is seen to be larger for the first vibration mode, due to differences between the associated SC and OC frequencies. For the second vibration mode, the SC and OC frequencies are in better agreement, whereby the effective EMCC determined by equation (72) is more accurately represented by  $\kappa_L$ .

Comparison of the values of the shunt resistances and inductances in Table 4 shows that the spill-over from the non-resonant residual vibration modes has a significant effect on the calibration. For both vibration modes, the relative deviation is approximately 15% on the shunt inductance between the calibration with and without residual mode correction for both series and parallel shunts. Because of this deviation in inductance, substantial changes in the corresponding resistance are also observed. It is noted that the final electronic components based on experiments are not measured, but merely stated in Thomas et al. (2012) to be close to the

theoretical values. This indicates that a precise shunt tuning has not been obtained prior to the experiments.

The effective EMCCs for the first two beam vibration modes are provided in the first column of Table 5. Furthermore, the ratios between the squared modal EMCCs and the squared effective EMCCs are compared in the second to the last column of Table 5. It is found that the ratio between  $\kappa_0^2$  (without correction) and the squared effective EMCC  $\kappa_e^2$  exactly accounts for the observed error in the inductance for the parallel shunt, while it accounts approximately for the error for the series shunt; see Table 5. It follows from the last two columns of Table 5 that the residual mode-corrected squared modal EMCC  $\kappa_L^2$  almost exactly recovers the squared effective EMCC  $\kappa_e^2$ . When  $\kappa_L^2$  is determined by the beam model, the deviation is around 7%, while it exactly matches  $\kappa_e^2$  for the plate model. This shows that the accuracy of the numerical model also influences the residual mode correction and thus the subsequent shunt tuning.

The effect of including the residual mode contributions in the shunt tuning is now illustrated by the frequency response plots in Figure 6, for the cantilever beam exposed to a harmonic tip load with excitation frequencies around the first and second resonant frequencies. The response is determined by solving the full system of equations for the parallel (equation (75)) and series (equation (77)) shunts with optimal components in Table 4.

**Table 5.** The effective EMCC ( $\kappa_e$ ) and the ratio between this squared and the squared modal EMCC, with ( $\kappa_0^2$ ) and without ( $\kappa_L^2$ ) residual mode correction.

Mode	$\kappa_e$	$\kappa_0^2/\kappa_e^2$	$(\kappa_L^2/\kappa_e^2)^1$	$\kappa_L^2/\kappa_e^2$
1	0.1330	1.1661	1.0694	1.0000
2	0.1405	1.1457	1.0682	1.0001

EMCC: electromechanical coupling coefficient.  
<sup>1</sup> $\kappa_L$  from the beam model.

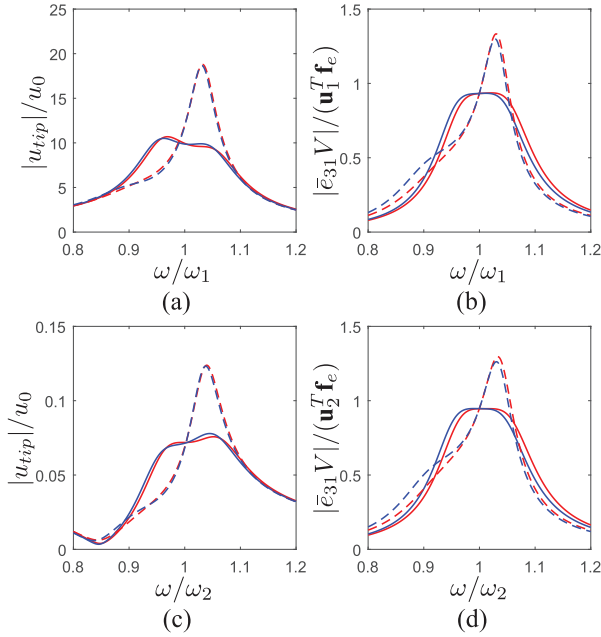


**Figure 6.** Frequency response around modes 1 and 2 of a cantilever beam exposed to a harmonic tip load: (a), (c) tip displacement and (b), (d) voltage response. Blue lines indicate the parallel shunts and red lines the series shunts, tuned, respectively, with (solid) and without (dashed) residual mode correction.

It can be seen from Figure 6 that the calibrations without residual mode correction (dashed lines) cause significantly larger maximum amplification of both tip displacement and voltage, compared to the tuning including the contribution from the non-resonant modes (solid lines). In particular, for the voltage amplification, an almost flat plateau around both resonant modes is seen for the calibration with the residual mode correction. The small deviations from a completely flat plateau are caused by the inclusion of structural damping in the model and from the fact that we do not have an ideal modal load, which is not accounted for by the calibration method. The structural damping is represented by Rayleigh damping with the damping ratios  $\zeta_1 = 0.34\%$  and  $\zeta_2 = 0.28\%$  for the first two vibration modes (Thomas et al., 2009). The damping introduced by the shunted piezoceramic patches can be assessed either directly by the obtained damping ratios or from the reduction in vibration amplitude, as summarized in

Table 6. The damping ratios are determined by solving the full complex eigenvalue problems for the parallel (equation (75)) and series (equation (77)) shunt circuits. The table contains the two damping ratios for each mode, associated with the two resonant frequencies emerging around the original resonant frequency when introducing the resonant shunt circuit. It is noted that the two damping ratios in Table 6 are ordered according to the magnitude of their associated natural frequencies. The amplitude reduction is obtained as the logarithm to the ratio of the maximum amplification of the structure with SC patch electrodes to that with optimally shunted pair of piezoceramic patches

$$A_{dB} = 20 \log \left( \frac{A_{SC}}{A_{opt}} \right) \quad (113)$$

It can be seen from the attained damping ratios and amplitude reductions in Table 6 that the inclusion of the non-resonant modes significantly improves the shunt calibration. The amplitude reduction is found to decrease about 35% from the best to the worst shunt calibration. It can also be seen that equal modal damping of the emerging resonant modes is obtained exactly for the parallel shunt with residual mode correction, while almost insignificant deviations occur for the corresponding series shunt, due to approximations made to simplify the tuning formulas. These results illustrate the potential improvement in common calibration methods, when taking into account the influence from non-resonant vibration modes. However, small discrepancies occur when the simplified beam model is used to obtain the desired level of damping or vibration mitigation. This illustrates the importance of having a sufficiently accurate numerical model for the dynamic structure, in order to obtain a precise shunt tuning. For the beam-based shunt tuning without residual mode contribution, the damping ratios and amplitude reductions are identical to those obtained from the plate model. This is because the more substantial residual mode correction in the plate model is now omitted, while the corresponding vibration modes are almost identical.

### Simply supported plate

The second example concerns a simply supported plate analyzed by Gardonio and Casagrande (2017), with a

**Table 6.** Damping ratios and amplitude reductions of cantilever beam with optimally calibrated parallel and series shunted piezoceramic patches, for resonant modes 1 and 2.

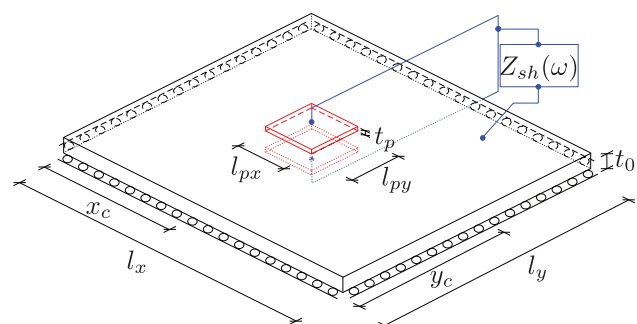
Model	Shunt	Corrected		Non-corrected		
		$\zeta_d$ (%)	$A_{dB}$	$\zeta_d^0$ (%)	$A_{dB}^0$	
Mode 1	<b>Plate</b>					
	Parallel	4.88	4.88	22.86	7.39	17.86
	Series	4.91	4.85	22.70	8.90	17.80
	<b>Beam</b>					
Mode 2	Parallel	6.28	3.48	20.98	7.39	17.86
	Series	6.83	3.57	21.04	8.90	17.80
	<b>Plate</b>					
	Parallel	5.10	5.10	24.26	7.49	20.28
Series	5.13	5.07	24.50	8.85	20.23	
<b>Beam</b>						
Parallel	6.55	3.66	22.33	7.49	20.28	
Series	7.14	3.77	22.38	8.85	20.23	

<sup>0</sup>Without residual mode correction.

**Table 7.** Dimensions and material properties for the plate and piezoceramic patches.

	Plate		Piezoceramic	
Length (mm)	$l_x$	414	$l_{px}$	82.8
Width (mm)	$l_y$	314	$l_{py}$	62.8
Thickness (mm)	$t_0$	1	$t_p$	0.5
Center patch along the x-axis (mm)			$x_c$	$\frac{13}{28}x$
Center patch along y-axis (mm)			$y_c$	$\frac{15}{28}y$
Density ( $\text{kg/m}^3$ )	$\rho$	2700	$\rho_p$	7600
Young's modulus (GPa)	$E$	70	$E_p$	50
Poisson's ratio (-)	$\nu$	0.33	$\nu_p$	0.35
Piezoelectric coefficient ( $10^{-12}$ m/V)			$d_{31}$	-150
Free dielectric coefficient ( $10^{-9}$ F/m)			$\epsilon_{33}^0$	29.2

single SP-PW shunted pair of piezoceramic patches placed with a small offset of  $(1/28l_x, -1/28l_y)$  to the plate center. The plate geometry and the geometry and position of the pair of piezoceramic patches are shown in Figure 7, while the dimensions and material properties are provided in Table 7. It is noted that the plate is conductive and that a conductive adhesive is used for the bonding of the piezoceramic patches, whereby the inner electrodes are connected. The structural damping is assumed to be  $\zeta_s = 0.2\%$ , and side lengths of the pair of patches are 1/5th of the corresponding lengths of the plate ( $l_{px,py} = l_{x,y}/5$ ). As the piezoceramic patches in the present example are relatively thick and placed far from the boundary simple supports, the omission of the patches' bending stiffness and transverse inertia becomes significant. Thus, the additional mass from the pair of piezoceramic patches is lumped and included at the relevant dofs in the system mass matrix. Hereby, the present results are comparable to those in Gardonio and Casagrande (2017).

**Figure 7.** Geometry of a simply supported plate with one pair of SP-PW piezoceramic patches.

In Gardonio and Casagrande (2017), the optimal calibration of the parallel  $RL$  shunts electronic components is determined for a particular load case, described as a rain-on-the-roof load scenario. The solution is evaluated using a mode shape expansion, with a gradually increasing number of modes. The solution is

**Table 8.** Fundamental frequencies of simply supported plate with ( $f$ ) and without ( $f_0$ ) short-circuit piezoceramic patches, modal EMCC, and optimal shunt tuning.

Shunt	$f_0$ (Hz)	$f$ (Hz)	$\kappa$	$L$ (H)	$R$ (k $\Omega$ )
Parallel*	39.05	35.73	0.070	33.87	76.89
Parallel <sup>0</sup>			0.074	36.92	80.31
Parallel <sup>1</sup>	$\approx 39.1$	$\approx 37.2$	–	$\approx 34$	$\approx 160$

EMCC: electromechanical coupling coefficient.

\*With residual mode correction ( $\kappa_L$ ).

<sup>0</sup>Without residual mode correction ( $\kappa_0$ ).

<sup>1</sup>Results from Gardonio and Casagrande (2017).

seemingly converged when 150 modes are included. The bottom row of Table 8 provides the fundamental frequencies of the plate, both with and without SC patches, and the optimal tuning components from Gardonio and Casagrande (2017). The two top rows of the table summarize the corresponding results obtained by the present balanced calibration procedure, with and without residual mode correction. The present FE model consists of  $28 \times 28$  plate elements and  $6 \times 6$  patch elements, whereby the relative errors on the first eight SC frequencies of the coupled piezo-plate structure are below 1%, as demonstrated by the convergence curves in Figure 8 with the reference values obtained by a fine mesh with  $112 \times 112$  plate and  $24 \times 24$  patch elements. Furthermore, the straight lines in the logarithmic scale of Figure 8 indicate quadratic convergence. The SP-PW pair of piezoceramic patches is modeled according to the piezo-plate coupling subsection in the first section, with the resulting capacitance and plane stress-reduced piezoelectric coupling coefficient determined from equation (56). The blocked dielectric constant

$$\epsilon_{33}^p = \epsilon_{33}^{\sigma p} - 2d_{31}\bar{e}_{31} \quad (114)$$

is determined from the free dielectric constant  $\epsilon_{33}^{\sigma p}$  in Table 7.

A good agreement between the base plate frequencies ( $f_0$ ) can be observed in Table 8, while the SC frequency of the piezo-plate structure ( $f$ ) is seen to be lower using the present FE model. This discrepancy occurs because of the omission of the patches' bending stiffness. Therefore, the presently determined SC frequencies will all be lower than the actual frequencies (Gardonio and Casagrande, 2017). The present tuning of the inductance  $L$  with residual mode correction is seen to be in good agreement with the tuning obtained by Gardonio and Casagrande (2017), while a significant deviation can be seen for the shunt resistance  $R$ . This agrees well with the fact that the present tuning formula for the inductance is identical to that in Gardonio and Casagrande (2017), while the present resistance is  $\sqrt{2}$  smaller than in the previous study. The slightly smaller inductance is due to the differences in the SC

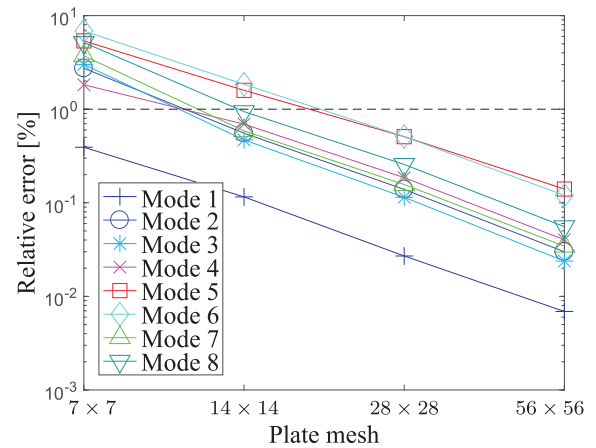


**Figure 8.** Relative error on the first eight SC frequencies of piezo-plate structure (reference, refined mesh  $112 \times 112$ ).

frequencies, while the deviation in the resistance is dominated by the different tuning formulas based on the free vibration properties in the present procedure and a specific forcing in Gardonio and Casagrande (2017). In Table 8, the calibration without residual mode contribution ( $L_0$ ,  $R_0$ ) deviates about 9% for the inductance and 4.5% for the resistance, which is slightly less than in the previous beam example. This is because the patches in the present plate example have reduced authority, whereas the larger capacitance of the present SP-PW patches' configuration is equalled by the correspondingly larger plane stress-reduced piezoelectric coupling coefficient (see equations (56) and (65)).

The magnitude of structural authority by the piezoceramic patches is determined by the relation between stiffness, mass, and dimensions for the host structure and the patches in SC conditions. In the present case, the low authority is caused by the small patch-to-plate area ratio, whereby the contribution from non-resonant modes becomes less pronounced than in the previous beam example. However, as it will be shown subsequently, the low structural authority causes the shunt performance to be more sensitive to deviations from the optimum shunt tuning. The low structural authority implies reduced effective EMCCs, as the separation of

the SC and OC frequencies in equation (72) is governed by the term  $(\bar{e}_{31}^2/\bar{C}_p^{6p})\mathbf{w}\mathbf{w}^T$  in equation (71). A significant effective EMCC and thereby large damping are attainable in the present plate example, when the pair of patches is placed optimally with respect to the deformation pattern of the concerned vibration mode. Figures 9(a) to (h) show the first eight vibration modes of the base plate and Figures 9(i) to (p) show those of the plate with the SC patches. It is seen that the pair of patches is placed optimally for the first vibration mode (Figures 9(a) and (i)), while the authority is reduced for the second mode (Figures 9(b) and (j)). To realize a desired level of damping by an indirectly placed pair of patches requires either larger patch dimensions or improved electromechanical coupling, in which case the influence from residual modes will increase as well. Thus, it is important in these cases to include the influence from residual vibration modes in the shunt calibration. This is illustrated in Figure 10, which shows the dynamic amplification curve for harmonic distributed transverse load with constant spatial intensity. The figure shows the resonance peaks for the base plate (black dashed) and the plate with the SC pair of patches (green dash-dotted), and the curves obtained by shunt with (blue) and without residual mode correction (red). It is seen that the dynamic amplification is doubled, when neglecting the residual mode correction compared to the calibration with correction. In the beam example, a factor of two can also be observed between the dynamic amplifications associated with the shunt tunings with and without residual mode correction (see Figure 6(a)). However, in the beam example the relative deviation in shunt tuning is significantly larger than that in the plate example. This indicates that the shunt tuning is more sensitive to deviations, when the piezoceramic patches have less structural authority. It should also be noted that the frequency response plots are produced by dynamic point load and distributed load, respectively, in the beam and plate examples, which influence the responses as well.

Optimum calibration for the parallel shunt circuit with and without residual mode correction is now determined for the first eight vibration modes with the corresponding mode shapes shown in Figures 9(i) to (p) for SC patch electrodes. The results are summarized in Table 9, where the provided modal EMCCs are  $\kappa = \kappa_L$  in equation (89) with residual mode correction and  $\kappa = \kappa_0$  in equation (87) without correction. The last columns of the table show the two damping ratios for the targeted vibration mode, determined from the full complex eigenvalue problem in equation (75).

The results in Table 9 indicate that considerable damping is realized only for modes 1, 4, and 7. This is due to the low structural authority of the pair of piezoceramic patches and its indirect location with respect to the deformation form of the five remaining vibration

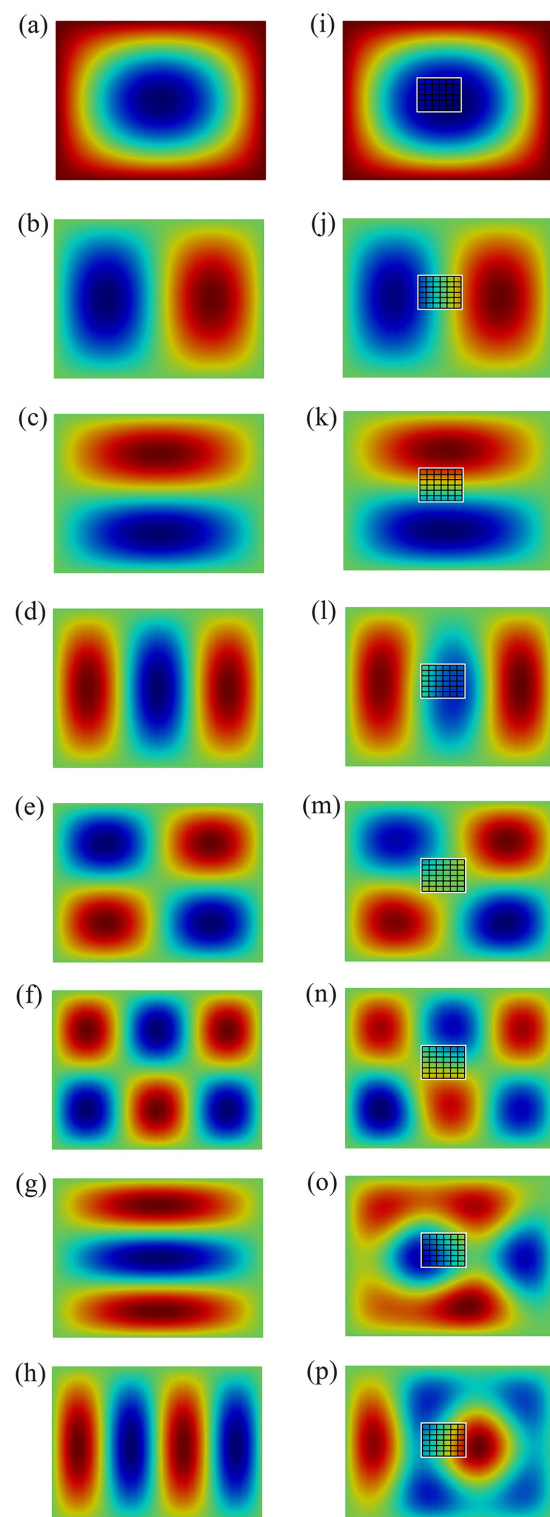


**Figure 9.** Plate modes 1–8 for (a)–(h) a bare plate and (i)–(p) a plate with an SC pair of piezoceramic patches.

modes in Figure 9. Some of the vibration modes in Figure 9 are very sensitive to the actuation by the pair of patches. For example, in modes 5 (Figures 9(e) and (m)) and 6 (Figures 9(f) and (n)), the symmetry in the pattern is slightly altered by the presence of the patch,

**Table 9.** Optimum parallel shunt tuning and attained damping ratios, with and without residual mode correction, for the first eight vibration modes of simply supported plate.

Mode		$f$ (Hz)	$\kappa$	$L$ (H)	$R$ (k $\Omega$ )	$\zeta$ (%)	
1	w	35.73	0.070	33.87	76.89	2.57	2.57
	wo		0.073	36.92	80.31	3.95	1.19
2	w	80.03	0.016	6.740	152.9	0.66	0.66
	wo		0.016	7.358	160.3	1.08	0.23
3	w	111.0	0.017	3.488	99.29	0.71	0.71
	wo		0.018	3.827	104.9	1.18	0.23
4	w	153.4	0.074	1.840	16.74	2.72	2.71
	wo		0.078	2.003	17.59	1.31	0.21
5	w	163.1	0.007	1.698	153.5	0.33	0.33
	wo		0.007	1.772	185.1	0.37	0.21
6	w	227.8	0.007	0.801	90.90	0.36	0.35
	wo		0.008	0.908	116.8	0.50	0.20
7	w	239.9	0.070	0.756	11.34	2.55	2.55
	wo		0.073	0.819	11.99	1.24	0.21
8	w	247.3	0.005	0.772	107.8	0.27	0.27
	wo		0.005	0.771	169.8	0.23	0.24

w—with residual mode correction ( $\kappa_L$ ).  
 wo—without residual mode correction ( $\kappa_0$ ).

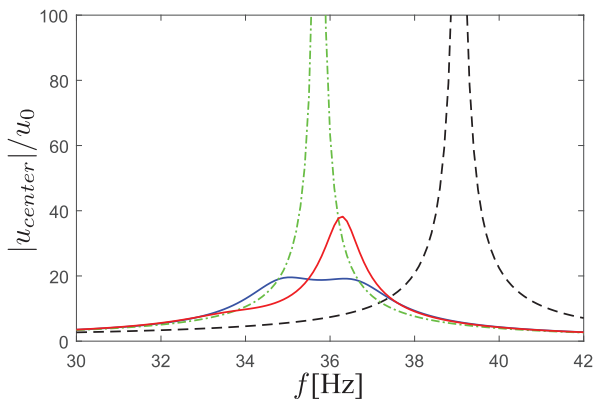


**Figure 10.** Frequency response around mode 1 for a plate (dashed black line) with an SC (green dot-dashed line) and parallel shunted pair of patches, optimally tuned with (blue line) and without (red line) residual mode correction.

while for modes 7 (Figures 9(g) and (o)) and 8 (Figures 9(h) and (p)) the shape is more drastically changed. As it was observed for the damping of the first vibration modes, the deviation in the shunt calibration, when neglecting the residual modes, leads to significant detuning and thereby smaller minimum damping ratios of the first eight vibration modes (see Table 9). There also seems to be a connection between the magnitude of the modal EMCC and the deviations observed for shunt tuning without residual mode correction. This supports the previous conclusion that the effect of the residual mode correction is governed by the apparent structural authority of the piezoceramic patches.

The influence of using the flexibility and flexibility–inertia corrections, respectively, for the shunt tuning can be analyzed by looking at the relative errors on the squared modal EMCC, without  $\kappa_0^2$  and with flexibility  $\kappa_r^2$  and flexibility–inertia  $\kappa_L^2$  residual mode corrections, with respect to the squared effective EMCC  $\kappa_e^2$ , provided in Table 10. It follows from Table 10 that the squared effective EMCC ( $\kappa_e^2$ ) is determined very accurately by the squared modal EMCC ( $\kappa_L^2$ ) with residual mode correction. Also, the squared modal EMCC with pure flexibility correction ( $\kappa_r^2$ ) recovers the effective values rather precisely, in particular for the first four modes. For modes 5–8, the importance of using the more accurate flexibility–inertia corrections increases, especially for modes 5, 6, and 8, where the errors on the squared modal EMCCs ( $\kappa_r^2$ ) are significant. The latter may be due to the indirect placement of the pair of patches with respect to these modes. Generally, the importance of using the more substantial flexibility–inertia corrections for the non-resonant modes increases for resonant shunt damping of higher and closely spaced vibration modes with indirectly placed patches. The ratio between the squared modal and effective EMCCs seems to correlate with the relative errors observed for the (parallel) shunt inductance. It is, for instance, noted in Table 10 that  $\kappa_0^2/\kappa_e^2$  indicates a 9% relative error on the inductance, while for the first vibration mode the same order of error has been observed between  $L$  and  $L_0$ . The error associated with the pure flexibility correction for the non-resonant modes observed for modes 5–8 is now analyzed by

**Table 10.** The squared effective EMCC and the ratio between this and the squared modal EMCC with flexibility, flexibility–inertia, and no residual mode correction.

Mode	$\kappa_e$	$\kappa_0^2/\kappa_e^2$	$\kappa_r^2/\kappa_e^2$	$\kappa_L^2/\kappa_e^2$
1	0.0699	1.0899	1.0007	1.0000
2	0.0156	1.0917	0.9976	1.0000
3	0.0172	1.0974	1.0029	1.0000
4	0.0744	1.0891	1.0006	1.0001
5	0.0068	1.0442	0.9540	1.0000
6	0.0074	1.1343	1.0364	1.0000
7	0.0699	1.0826	0.9939	1.0002
8	0.0050	0.9985	0.9123	1.0000

EMCC: electromechanical coupling coefficient.

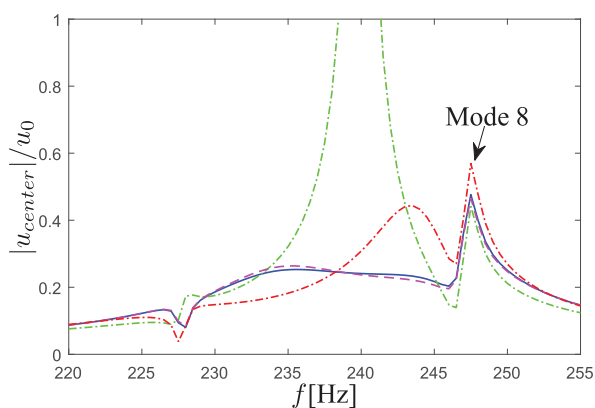


**Figure 11.** Frequency response around the seventh resonant frequency of a plate with a pair of piezoceramic patches; SC (green dot-dashed line) and shunted optimally with flexibility–inertia (blue line), flexibility (dashed magenta line), and without (dot-dashed red line) residual mode corrections.

considering the frequency response to a harmonic uniformly distributed load around the seventh resonant frequency shown in Figure 11.

It can be seen from Figure 11 that the calibration without residual mode correction (red dot-dashed) causes significantly larger maximum amplifications compared to the tuning with flexibility–inertia residual mode correction (blue solid). The tuning with pure flexibility correction (magenta dashed) yields a small off-calibration, which shows that it may be important to use the precise flexibility–inertia compensation for the dynamic residual mode effects. In this example, larger levels of attainable damping could have been achieved for the five lightly damped modes (2, 3, 5, 6, and 8) either by placing the pair of piezoceramic patches more appropriately, according to the deformation pattern of the respective modes, or by applying several interconnected pairs of patches. The same position with larger patches or lower resulting capacitance could also have been realized, whereby the effects of including the non-resonant modes in the calibration would have been more pronounced. However, the design, optimization,

and application of several pairs of patches are outside the main scope of this work.

## Conclusion and future work

An FE model for coupled piezo-plate structures was established, by considering the constitutive relations and dynamic equilibrium equations of the plate, described by Kirchhoff theory, in which the patch was represented by a plane stress assumption and its electromechanical interaction. The coupling between the plate and a pair of either SP-PW or OP-SW piezoceramic patches was considered through the transformation of the electric forcing from the two patches to the equivalent moment loads on the plate. The wiring and poling are subsequently implemented by considering the relations between the patch electrodes' potentials and the voltage over the connected shunt. This reduces the number of electric equations to one, by the introduction of a resulting capacitance and a plane stress–reduced piezoelectric coupling coefficient. Hereby, the voltage across the shunt becomes the governing electric variable in the equations of motion.

A recently proposed balanced calibration procedure for *RL* shunted piezoelectric transducers, with quasi-dynamic residual mode correction, is implemented for the shunted pair of piezoceramic patches bonded symmetrically to the plate. This calibration procedure enables precise and effective calibration of the electronic shunt components, as demonstrated by two benchmark examples concerning beam and plate vibrations.

A new calibration procedure based on the effective EMCC has also been proposed and used in the two benchmark examples. The method was derived from a new modal EMCC corrected by the spill-over from the non-resonant modes. In the benchmark examples, it is illustrated that this modal EMCC precisely retains the effective EMCC, hereby providing an explicit connection between the SC and OC frequencies of the coupled structure and the modal shunt tuning based on the numerical FE model. It is further shown that the ratio between the squared modal EMCC with and without

residual mode correction and the corresponding squared effective EMCC provides the deviation in the corresponding shunt tuning. A simple format of the tuning formulas was obtained for the new calibration procedure. It showed that the difference in the shunt calibration of, respectively, an SP-PW or an OP-SW pair of patches is simply determined by the reciprocal value of the squared resulting plane stress–reduced piezoelectric coupling coefficient. In the present case, this corresponds to four times higher shunt tuning values for the OP-SW pair of patches for a given level of attainable damping. Thus, it is often preferable to use this SP-PW configuration, as it is notoriously difficult to achieve the large inductances associated with damping of low-frequency structural vibrations.

The considered benchmark examples represent a cantilever beam and a simply supported plate, both equipped with a single pair of shunted piezoceramic patches configured in OP-SW and SP-PW, respectively. For the cantilever beam, optimum shunt tuning for vibration suppression of the first two resonant modes was determined and compared to the calibration results reported in the literature (Thomas et al., 2012). It was found that the omission of the residual mode correction leads to significant deviations in the shunt circuit electronic components. The latter is directly related to the ratio between the modal EMCC with and without residual mode correction. The deviation in the shunt tuning when neglecting the non-resonant modes leads to a further reduction in attainable damping. This was demonstrated directly by the damping ratios and by the amplitude reduction from the frequency response curves for a particular harmonic load.

For the second benchmark example with a simply supported plate and a single pair of SP-PW piezoceramic patches, the effect of the non-resonant modes on the shunt tuning was found to be less pronounced. This is due to a smaller structural authority by the piezoceramic patches. However, notable influence by the residual mode correction is still observed on the frequency response curves and the damping ratios, verifying that the residual mode correction may be important in shunt tuning. It was found for the lower vibration modes that the residual mode corrections are sufficiently determined by the pure flexibility contribution, while the importance of using the flexibility–inertia corrections increases for higher and closely spaced vibration modes. This was illustrated by the frequency response curves at the first and the seventh vibration modes and the evaluation of the modal EMCC, both with flexibility and flexibility–inertia residual mode corrections. Finally, it was shown that the deviation in the shunt inductances can be determined by the ratio between the squared modal EMCC with and without residual mode correction and the corresponding squared effective EMCC. It was demonstrated here that the newly proposed residual mode–corrected modal EMCC precisely retains

the effective EMCC, which suggests that this coefficient should be used in shunt calibration based on modal analysis.

It is worth mentioning that the two proposed calibration methods give approximately the same shunt tuning as the corrected modal EMCC precisely retains the effective EMCC. The choice of method thus depends on whether the tuning is based on experiments or a numerical model and the associated computational costs. For the first balanced modal calibration procedure, the SC eigenvalue problem of the electromechanical structure has to be solved and a modified stiffness matrix has to be inverted in order to determine the residual mode correction terms. For the calibration based on the effective EMCC, both the SC and OC and an additional third eigenvalue problem, after the determination of the optimal inductance, have to be evaluated. However, in many cases the inversion of the modified stiffness matrix will be associated with significant computational costs, and thus the new calibration procedure, based on the effective EMCC, will in many cases be superior, also in regards to the experimental calibration.

In future works, the proposed calibration procedures will be implemented in more sophisticated numerical models, allowing for even more accurate modeling of an experimental set-up or an industrial application. It is expected that the new procedure with the corrected modal EMCC will result in a good agreement between optimum numerical and experimental shunt tuning.

### Declaration of conflicting interests

The author(s) declared no potential conflicts of interest with respect to the research, authorship, and/or publication of this article.

### Funding

The author(s) disclosed receipt of the following financial support for the research, authorship, and/or publication of this article: This research has been supported by the Danish Council for Independent Research via the project “Resonant Piezoelectric Shunt Damping of Structures.”

### ORCID iDs

Johan F Toftekær  <https://orcid.org/0000-0003-1809-5063>  
Jan Høgsberg  <https://orcid.org/0000-0002-1098-3245>

### References

- Benjeddou A (2000) Advances in piezoelectric finite element modeling of adaptive structural elements: a survey. *Computers and Structures* 76: 347–363.
- Benjeddou A (2002) Modelling of piezoelectric adaptive beam, plate and shell structures: some developments and results. In: *Proceedings of the sixth international conference on computational structures technology*. Available at: <http://www.ctresources.info/ccp/download/ccp.5245.pdf>

- Benjeddou A (2014) Modal effective electromechanical coupling approximate evaluations and simplified analyses: numerical and experimental assessments. *Acta Mechanica* 225: 2721–2742.
- Berardengo M, Thomas O, Giraud-Audine C, et al. (2016) Improved resistive shunt by means of negative capacitance: new circuit, performances and multi-mode control. *Smart Materials and Structures* 25: 075033.
- Caruso G (2001) A critical analysis of electric shunt circuits employed in piezoelectric passive vibration damping. *Smart Materials and Structures* 10: 1059–1068.
- Chevallier G, Ghorbel S and Benjeddou A (2009) Piezoceramic shunted damping concept: testing, modelling and correlation. *Mechanics and Industry* 5: 397–411.
- De Marneffe B and Preumont A (2008) Vibration damping with negative capacitance shunts: theory and experiment. *Smart Materials and Structures* 17: 035015.
- Delperro T, Bergamini AE and Ermanni P (2012) Identification of electromechanical parameters in piezoelectric shunt damping and loss factor prediction. *Journal of Intelligent Material Systems and Structures* 24: 287–298.
- Ducarne J, Thomas O and Deü J-F (2010) Structural vibration reduction by switch shunting of piezoelectric elements: modeling and optimization. *Journal of Intelligent Material Systems and Structures* 21: 797–816.
- Ducarne J, Thomas O and Deü J-F (2012) Placement and dimension optimization of shunted piezoelectric patches for vibration reduction. *Journal of Sound and Vibration* 331: 3286–3303.
- Forward RL (1979) Electronic damping of vibrations in optical structures. *Applied Optics* 18: 690–697.
- Gardonio P and Casagrande D (2017) Shunted piezoelectric patch vibration absorber on two-dimensional thin structure: tuning considerations. *Journal of Sound and Vibration* 395: 26–47.
- Hagood NW and Von Flotow A (1991) Damping of structural vibrations with piezoelectric materials and passive electrical networks. *Journal of Sound and Vibration* 146: 243–268.
- Høgsberg J and Krenk S (2012) Balanced calibration of resonant shunt circuits for piezoelectric vibration control. *Journal of Intelligent Material Systems and Structures* 23: 1937–1948.
- Høgsberg J and Krenk S (2015) Balanced calibration of resonant piezoelectric RL shunts with quasi-static background flexibility correction. *Journal of Sound and Vibration* 341: 16–30.
- Høgsberg J and Krenk S (2017) Calibration of piezoelectric RL shunts with explicit residual mode correction. *Journal of Sound and Vibration* 386: 65–81.
- Hollkamp JJ (1994) Multimodal passive vibration suppression with piezoelectric materials and resonant shunts. *Journal of Intelligent Material Systems and Structures* 5: 49–57.
- IEEE (1988) *Standards on Piezoelectricity* (ANS/IEEE Std 176-1987). New York: IEEE.
- Krenk S (2005) Frequency analysis of the tuned mass damper. *Journal of Applied Mechanics* 72: 936–942.
- Krenk S and Høgsberg J (2014) Tuned mass absorber on a flexible structure. *Journal of Sound and Vibration* 333: 1577–1595.
- Krenk S and Høgsberg J (2016) Tuned resonant mass or inerter-based absorbers: unified calibration with quasi-dynamic flexibility and inertia correction. *Proceedings of the Royal Society A: Mathematical, Physical and Engineering Sciences* 472: 20150718 (23 pp.).
- Lossouarn B, Aucejo M, Deü J-F, et al. (2017) Design of inductors with high inductance values for resonant piezoelectric damping. *Sensors and Actuators A: Physical* 259: 68–76.
- Park CH and Inman DJ (1999) A uniform model for series R-L and parallel R-L shunt circuits and power consumption. *SPIE Proceedings* 3668: 797–804.
- Porfiri M, Maurini C and Pouget J (2007) Identification of electromechanical modal parameters of linear piezoelectric structures. *Smart Materials and Structures* 16: 323–331.
- Soltani P, Kerschen G, Tondreau G, et al. (2014) A Piezoelectric vibration damping using resonant shunt circuits: an exact solution. *Smart Materials and Structures* 23: 125014.
- Thomas O, Deü J-F and Ducarne J (2009) Vibration of an elastic structure with shunted piezoelectric patches: efficient finite element formulation and electromechanical coupling coefficients. *International Journal for Numerical Methods in Engineering* 80: 235–268.
- Thomas O, Ducarne J and Deü J-F (2012) Performance of piezoelectric shunts for vibration reduction. *Smart Materials and Structures* 21: 015008.
- Trindade MA and Benjeddou A (2009) Effective electromechanical coupling coefficients of piezoelectric adaptive structures: critical evaluation and optimization. *Mechanics of Advanced Materials and Structures* 16: 210–223.
- Wu SY (1996) Piezoelectric shunts with a parallel R-L circuit for structural damping and vibration control. *SPIE Proceedings* 2720: 259–269.
- Wu SY (1998) Method for multiple mode piezoelectric shunting with single PZT transducer for vibration control. *Journal of Intelligent Material Systems and Structures* 12: 991–998.



## P2

General numerical implementation of a new piezoelectric shunt tuning method based on the effective electromechanical coupling coefficient

Johan Frederik Toftækær, Aych Benjeddou and Jan Høgsberg

*Mechanics of Advanced Materials and Structures*

First published online: January 25, 2019,  
<https://doi.org/10.1080/15376494.2018.1549297>.



# General numerical implementation of a new piezoelectric shunt tuning method based on the effective electromechanical coupling coefficient

Johan Frederik Toftekær<sup>a</sup> , Ayech Benjeddou<sup>b,c</sup> , and Jan Høgsberg<sup>a</sup> 

<sup>a</sup>Department of Mechanical Engineering, Technical University of Denmark, Lyngby, Denmark; <sup>b</sup>Université de Technologie de Compiègne, CNRS, ROBERVAL, Compiègne, France; <sup>c</sup>SUPMECA, Saint Ouen, France

## ABSTRACT

A recently proposed tuning method for resistive-inductive (RL) shunts is implemented in a commercial finite element (FE) code (ANSYS®). A main result of the paper is therefore the consistent formulation of the tuning method in terms of variables directly available as solutions in any commercial FE code: The two natural frequencies associated with short- and open-circuit (SC and OC) electrodes and a modal charge obtained as the electrical SC reaction force. An alternative method is based on quasi-static solutions with SC and OC electrodes, convenient for both numerical analysis and experiments. The proposed shunt tuning method is suitable for implementation in any commercial FE software supporting electromechanical analysis and ANSYS® has been used to assess its accuracy for a piezoelectric smart plate benchmark problem. The method is finally extended to multiple piezoceramic patches, placed symmetrically on the structure and shunted to a single RL network, whereby more vibration modes can be effectively controlled for the specific plate problem.

## ARTICLE HISTORY

Received 26 September 2018  
Accepted 26 September 2018

## KEYWORDS

Shunt piezoelectric damping; resonant shunt calibration; residual mode correction; effective electromechanical coupling coefficient; ANSYS® finite element code; plates

## 1. Introduction

Piezoelectric transducers attached locally to a host structure enable dissipation of converted mechanical energy into heat by a supplemental resonant shunt. The latter is often designed as a series or parallel connection of a resistance ( $R$ ) and an inductance ( $L$ ), whereby the effect on the host structure from the electromechanical transducer corresponds to an inerter-based absorber [1]. The  $RL$ -shunt circuit was first suggested and experimentally demonstrated by Forward [2]. Actual calibration procedures were subsequently derived first for the series [3] and since for the parallel shunt circuit [4]. Both calibration methods are based on a single mode representation of the vibrating host structure and are governed by the resonant frequency of a targeted vibration form and the capacitive properties of the piezoelectric transducer(s).

Recently, the modal coupling introduced by the presence of a supplemental absorber on the structure has been represented in [5] via the dynamic characteristics of the other nonresonant modes around the targeted resonant frequency. It demonstrated the ability of two consistent correction terms to accurately account for both the flexibility and inertia effects from residual modes and to adjust the absorber tuning to retain a desired flat plateau in the frequency response curves. The initial analysis for mechanical tuned mass- and inerter-based absorbers [5] has recently been extended to  $RL$ -shunted piezoelectric transducers [1].

The performance of a piezoelectric transducer is inherently limited by its capacitive property, which is inversely proportional to the stiffness of an equivalent mechanical absorber. A key factor in the electromechanical absorber tuning has therefore been the accurate representation and maximization of the effective (or generalized) electromechanical coupling coefficient (EMCC). The latter represents the apparent electromechanical to modal stiffness ratio and thus the relation between the inherent capacitance, electromechanical coupling and structural resonance. In [6], a piezoelectric shunt tuning procedure has been derived on the basis of the effective EMCC, demonstrating its direct equivalence to a modal EMCC with residual corrections from nonresonant modes. The effective EMCC is therefore a key parameter for electromechanical structures; it is commonly defined by the relative difference between (the square of) the associated short circuit (SC) and open circuit (OC) frequencies [7]. Consequently, it is a measure for the level of attainable damping and has therefore been the objective for the design and optimization of piezoelectric transducer systems [8]. It is possible to increase the effective EMCC—and thereby the attainable damping—by the application of a negative capacitance in the electric shunt circuit [9]. Unfortunately, this increases the required shunt inductance, which is usually so large that it must already be realized by active electronic shunt components. Thus, the absorber realization is often limited by the magnitude of the shunt inductance instead of the inherent transducer capacitance.

However, it has recently been demonstrated that even large inductances can be obtained by simply winding a copper wire around a magnetic core [10], which substantially improves the feasibility of genuine passive shunts [11]. The present work concerns pure passive vibration control, in which case the attainable damping is governed by the magnitude of the transducer capacitance with the magnitude of the EMCC as a limiting factor in the design of the transducer and the corresponding shunt tuning procedure.

In the present work, a recently proposed shunt tuning method, based on the effective EMCC, is implemented in the commercial finite element (FE) code ANSYS<sup>®</sup> [12]. Correction terms, that represent the interaction with nonresonant modes, are consistently derived from the natural frequencies obtained by the three eigenvalue problems associated with piezoelectric SC and OC electrodes and a pure inductive shunt. However, as demonstrated in [13], the solution for the pure inductive shunt is only needed when the effective EMCC is almost vanishing because of a very indirect location of the transducer(s). Therefore, in most practical problems, the tuning formulae only rely on the two natural frequencies from the SC and OC limits and a modal charge that appears as a supplemental reaction force associated with SC electrodes. This tuning procedure is simply and very directly implemented in a commercial FE code. The present tuning method is implemented in ANSYS<sup>®</sup>, which supports three-dimensional (3D) coupled analysis of electromechanical structures, previously used for the assessment of both 2D and 3D evaluations of the effective EMCCs [14]. Furthermore, a full 3D analysis of a CD-ROM drive base with shunted piezoelectric patches has previously been analyzed in ANSYS<sup>®</sup> [15], while the possibility of exporting system matrices and vectors has been further utilized in [16] to determine optimal shunt calibration and in [17] for optimal patch positioning by optimization functions written in Matlab. Presently, the implementation of the new shunt calibration method in ANSYS<sup>®</sup> is used to perform full 3D analysis of a benchmark problem concerning a simply supported plate presented in [6] with a single pair of piezoceramic patches and subsequently with multiple pairs placed symmetrically with respect to the targeted vibration forms. The aim of the paper is to introduce an adapted calibration procedure that is suitable for use and implementation in commercial FE software and consistently incorporates the effective EMCC to accurately represent the effects from nonresonant modes in a flexible structure.

## 2. FE formulation

This section is devoted to the notations and general structure of commercial codes with electromechanical packages, such as the ANSYS<sup>®</sup> 3D FE model, and is presented to clarify and support the theory behind the proposed shunt calibration procedure in [6] based on a consistent use of the effective EMCC.

### 2.1. Constitutive equations

The constitutive relations for piezoelectric materials can be written in four different forms, depending on the choice of

independent variables. The most commonly implemented form in commercial software, such as ANSYS<sup>®</sup>, is the so-called  $e$ -form,

$$\{T\} = [C^E]\{S\} - [e]\{E\} \quad (1)$$

$$\{D\} = [e]^t\{S\} + [\epsilon^S]\{E\} \quad (2)$$

where superscript  $t$  denotes the transpose operation. For a full 3D representation, the six engineering stresses in  $\{T\}$  and three electric displacements in  $\{D\}$  are expressed in terms of the energy conjugated strains in  $\{S\}$  and electric fields in  $\{E\}$  through the SC elastic stiffness matrix  $[C^E]$ , piezoelectric (stress) coupling coefficients matrix  $[e]$ , and dielectric blocked constants matrix  $[\epsilon^S]$ . Details about the coupled constitutive relations in Eqs. (1) and (2) can be found in [14].

### 2.2. Eigenvalue equations

In the following, mechanically unloaded harmonic vibrations are considered by implying general harmonic solutions of the form  $\{\dots\} = \{\dots\}e^{i\omega t}$ , where  $\omega$  is the representative angular frequency when  $t$  represents time. Thus, the variational formulation for the combined electromechanical structure can be written as

$$\begin{aligned} & \int_{\Omega} \{\delta S\}^t \{T\} d\Omega - \omega^2 \int_{\Omega} \{\delta u\}^t \rho \{u\} d\Omega - \int_{\Omega} \{\delta E\}^t \{D\} d\Omega \\ & = \int_{\Gamma_q} \delta \phi q d\Gamma_q \end{aligned} \quad (3)$$

where the  $\delta$  indicates the variational function. In Eq. (3),  $\rho$  denotes the material mass density,  $\phi$  the electric potential,  $q$  the corresponding surface charge density,  $\Omega$  the material volume, and  $\Gamma_q$  the area of the electrode where the charge  $q$  is applied or measured.

Upon substitution of the constitutive relations in Eqs. (1) and (2) into the variational equation (3), the stresses  $\{T\}$  and electric displacements  $\{D\}$  no longer appear explicitly in the variational equation (3). In the coupled FE formulation, the 3D displacements in the vector  $\{u\}$  are then approximated by their nodal displacements in  $\{U\}$  via appropriate shape functions, while a similar interpolation is used to represent the electric potential  $\phi$  by the corresponding nodal values in  $\{\varphi\}$ . The corresponding mechanical strains in  $\{S\}$  and electric fields in  $\{E\}$  are then obtained by consistent differentiation of the shape functions associated with  $\{U\}$  and  $\{\varphi\}$ , respectively. In the discrete representation by the nodal degrees of freedom (dofs), the variational equation (3) contains two coupled equations with system matrices obtained by performing the volume integration over  $\Omega$  on the left-hand side of Eq. (3) and the integral across the electrode area  $\Gamma_q$  on the right-hand side. Hereby, the discrete vibrational problem can be represented by this coupled set of equations

$$\left( \begin{bmatrix} K_U^E & K_{U\varphi}^E \\ (K_{U\varphi}^E)^t & -K_{\varphi}^{\epsilon^S} \end{bmatrix} - \omega^2 \begin{bmatrix} M & 0 \\ 0 & 0 \end{bmatrix} \right) \begin{Bmatrix} U \\ \varphi \end{Bmatrix} = \begin{Bmatrix} 0 \\ -Q_{\varphi} \end{Bmatrix} \quad (4)$$

where  $[K_{UV}^E]$ ,  $[K_{U\phi}^E]$ , and  $[K_{\phi}^{\epsilon^s}]$  contain the stiffness components associated with the mechanical displacements, electromechanical coupling, and electric potentials, while  $M$  contains the physical mass associated with the vibrational inertia of the host structure and piezoelectric patches. Finally, the vector  $\{Q_{\phi}\}$  contains the applied electric charges from, for example, an external power source or a supplemental shunt.

When modeling a piezoelectric patch in an FE code, some dofs constitute the patch electrode, while other dofs describe the pure electromechanical material. A continuous electrode distributed on the patch is represented by a scalar electric potential via an equipotential condition, which in the present case is introduced for thin piezoceramic patches with two in-plane electrodes. In the case of a single patch or a single system of connected patches, only a single electric potential dof remains unconstrained once a non-wired (interface) electrode is grounded. Appendix A presents the extension to several independent pairs of symmetrically placed piezoceramic patches. When introducing the equipotential condition, the discrete vibrational problem (Eq. 4) can be decomposed into

$$\left( \begin{bmatrix} K_{UV}^E & \bar{K}_{U\phi}^E & K_{UV}^E \\ (\bar{K}_{U\phi}^E)^t & -\bar{K}_{\phi}^{\epsilon^s} & -K_{\phi V}^{\epsilon^s} \\ (K_{UV}^E)^t & -(K_{\phi V}^{\epsilon^s})^t & -C_p^{\epsilon^s} \end{bmatrix} - \omega^2 \begin{bmatrix} M & 0 & 0 \\ 0 & 0 & 0 \\ 0 & 0 & 0 \end{bmatrix} \right) \begin{Bmatrix} U \\ \phi \\ V \end{Bmatrix} = \begin{Bmatrix} 0 \\ 0 \\ -Q \end{Bmatrix} \quad (5)$$

While  $[\bar{K}_{U\phi}^E]$  and  $[\bar{K}_{\phi}^{\epsilon^s}]$  contain contributions associated with the electric potential dofs that are not part of an electrode, the coupling matrix  $\{K_{UV}^E\}$  represents the apparent stiffness associated with the dofs representing the patch electrode and  $C_p^{\epsilon^s}$  is the effective capacitance of the single network of piezoceramic patches. Thus, the electric potential on the ungrounded non-wired electrode defines the difference in electric potential or voltage  $V$ , while  $Q$  is the corresponding charge. Finally,  $\{K_{\phi V}^{\epsilon^s}\}$  describes the coupling between the non-electroded and the electroded dofs. The vibrational problem (Eq. 5) may therefore be written in the collapsed format

$$\left( \begin{bmatrix} K^E & k_{me}^E \\ (k_{me}^E)^t & -\bar{C}_p^{\epsilon^s} \end{bmatrix} - \omega^2 \begin{bmatrix} M & 0 \\ 0 & 0 \end{bmatrix} \right) \begin{Bmatrix} U \\ V \end{Bmatrix} = \begin{Bmatrix} 0 \\ -Q \end{Bmatrix} \quad (6)$$

obtained by eliminating  $\{\phi\}$  from the second set of equations in Eq. (5). Hereby, the resulting system matrices and resulting modified capacitance follow as:

$$\begin{aligned} [K^E] &= [K_{UV}^E] + [\bar{K}_{U\phi}^E] [\bar{K}_{\phi}^{\epsilon^s}]^{-1} [\bar{K}_{U\phi}^E]^t, \\ \bar{C}_p^{\epsilon^s} &= C_p^{\epsilon^s} - \{K_{\phi V}^{\epsilon^s}\}^t [\bar{K}_{\phi}^{\epsilon^s}]^{-1} \{K_{\phi V}^{\epsilon^s}\} \end{aligned} \quad (7)$$

while the coupling between the mechanical and electric domains is computed as

$$\{k_{me}^E\} = \{K_{UV}^E\} - [\bar{K}_{U\phi}^E] [\bar{K}_{\phi}^{\epsilon^s}]^{-1} \{K_{\phi V}^{\epsilon^s}\} \quad (8)$$

It is found that the compact form of the equations of motion in Eq. (6) is equivalent to the system previously derived in [6] with a slightly different notations for the electromechanical coupling.

### 3. Electromechanical coupling coefficients

The vibrational problem (Eq. 6) constitutes the governing equation used in the subsequent analysis and derivations, in which the mechanical and electric stiffnesses are governed by the stiffness matrix  $[K^E]$  and the resulting capacitance in Eq. (7), while the coupling between the system of mechanical equations and the single electric equation is governed by the electromechanical coupling vector  $\{k_{me}^E\}$  in Eq. (8). For a specific vibration mode of the structure, the magnitude of the electromechanical coupling is conveniently represented by the effective EMCC, basically describing the modal ratio between electrical and mechanical stiffnesses. In this section, the effective EMCC and its quasi-static approximation are derived and then subsequently used to calibrate resonant RL shunt circuits for optimal piezoelectric vibration damping.

#### 3.1. Effective EMCC

The effective EMCC may be defined as the rate of converted energy by the piezoelectric material and therefore described by the difference between the modal strain energies associated with SC and OC patch electrodes. The modal strain energies are proportional to the eigenvalues from the SC and OC eigenvalue problems [14], obtained from Eq. (6) with  $V=0$  and  $Q=0$ , respectively. For vanishing voltage, the SC eigenvalue problem can be directly written as

$$([K^E] - \omega_j^2[M])\{U\}_j = \{0\} \quad (9)$$

for a particular vibration mode  $j$  with circular frequency  $\omega_j$ . In the SC limit, the bottom equation in Eq. (6) provides the (sensed) modal charge

$$Q_j = -\{k_{me}^E\}^t \{U\}_j \quad (10)$$

as a reaction force securing  $V=0$ . This modal charge is easily extracted from a FE solution and therefore conveniently used to determine the effective EMCC. The SC eigenvalue problem (Eq. 9) conveniently constitutes the foundation of a dynamic analysis, with the mode shape vectors  $\{U\}_j$  normalized to unit modal mass,

$$\{U\}_j^t [M] \{U\}_j = 1, \quad \{U\}_j^t [K^E] \{U\}_j = \omega_j^2 \quad (11)$$

while  $\omega_j^2$  then determines the corresponding modal stiffness.

The opposite OC eigenvalue problem follows from Eq. (6) for vanishing charge ( $Q=0$ ), conveniently formulated as

$$\left( [K^E] + \frac{1}{\bar{C}_p^{\epsilon^s}} \{k_{me}^E\} \{k_{me}^E\}^t - \hat{\omega}_j^2 [M] \right) \{\hat{U}\}_j = \{0\} \quad (12)$$

to secure a nonvanishing determinant of the resulting mass matrix. In the corresponding stiffness matrix, the SC contribution  $[K^E]$  is then increased by the quadratic projection of the coupling vector  $\{k_{me}^E\}$  on the modified capacitance  $\bar{C}_p^{\epsilon^s}$  such that the OC circular frequency  $\hat{\omega}_j \geq \omega_j$ . In the following the  $(\hat{\cdot})$ -symbol denotes solutions for the OC configuration.

The calibration procedure is derived for a specific target mode  $j=r$  with circular SC and OC frequencies  $\omega_r$  and  $\hat{\omega}_r$ , respectively. The effective EMCC for this mode is referred

to as  $\kappa_e^2$ , representing the ability to convert between mechanical and electrical energy and therefore the damping attainable by the supplemental shunt. The effective EMCC is presently defined by the relative difference between the SC and OC circular frequencies squared,

$$\kappa_e^2 = \frac{\hat{\omega}_r^2 - \omega_r^2}{\omega_r^2} \quad (13)$$

Pre-multiplying Eq. (9) with  $\{\hat{U}\}_r^t$  and oppositely Eq. (12) with  $\{U\}_r^t$ , the terms involving  $[K^E]$  may be eliminated so that the effective EMCC for the target mode  $r$  can be expressed as

$$\kappa_e^2 = \frac{\{U\}_r^t \{k_{me}^E\} \{k_{me}^E\}^t \{\hat{U}\}_r}{\omega_r^2 \bar{C}_p^{\epsilon_s} \{U\}_r^t [M] \{\hat{U}\}_r} \quad (14)$$

A simpler expression is obtained by assuming  $\{\hat{U}\}_r \simeq \{U\}_r$ , which is commonly used in the literature [9]. Thus, the effective EMCC can be estimated as

$$\kappa_0^2 = \frac{Q_r^2}{\omega_r^2 \bar{C}_p^{\epsilon_s}} \quad (15)$$

whereby evaluation of the OC eigenvalue problem in Eq. (12) can be avoided.

### 3.2. Quasi-static EMCC

The approximation in Eq. (15) of the effective EMCC in Eq. (13) has in [6] been demonstrated to be rather imprecise for flexible host structures. However, a more accurate approximation can quite simply be obtained by considering two static problems associated with SC and OC patch electrodes, obtained from Eq. (6) when  $[M] = [0]$  and a mechanical load  $\{f\}$  is applied. As for the approximative solution in Eq. (15), this quasi-static approach avoids solving the OC eigenvalue problem in Eq. (12). When applying any external load to the electromechanical structure with SC patch electrodes the quasi-static solution to the measured charge is found as

$$Q_s = -\{k_{me}^E\}^t [K^E]^{-1} \{f\} \quad (16)$$

with subscript  $s$  referring to a sufficiently static limit where the inertia can be neglected. As the same external load  $\{f\}$  is applied to the structure with OC electrodes, the deflection is slightly altered due to the electromechanical stiffening. This gives the following solution for the difference in electric potential between the patch electrodes for the quasi-static behavior,

$$V_s = \frac{\{k_{me}^E\}^t [K^E]^{-1} / \bar{C}_p^{\epsilon_s}}{1 + \{k_{me}^E\}^t [K^E]^{-1} \{k_{me}^E\} / \bar{C}_p^{\epsilon_s}} \{f\} \quad (17)$$

Note that the inverse of the SC stiffness matrix is obtained explicitly by the Sherman–Morrison relation [18]. Both the quasi-static solution to the measured charge  $Q_s$  and the difference in electric potential  $V_s$  are easily accessible reaction and response outputs in any electromechanical FE analysis, from which the quasi-static capacitance of the piezoceramic patches can be evaluated as

$$C_s = -\frac{Q_s}{V_s} = \bar{C}_p^{\epsilon_s} + \{k_{me}^E\}^t [K^E]^{-1} \{k_{me}^E\} \quad (18)$$

This quasi-static capacitance  $C_s$  is more precise than the modified capacitance  $\bar{C}_p^{\epsilon_s}$  since it includes the (static) interaction with the specific host structure by the last term in Eq. (18). This further implies an improved approximation of the effective EMCC ( $\kappa_e^2 \simeq \kappa_s^2$ ) by an expression similar to Eq. (15)

$$\kappa_s^2 = \frac{Q_r^2}{C_s \omega_r^2} \quad (19)$$

where  $\bar{C}_p^{\epsilon_s}$  has been replaced by  $C_s$ . The use of the quasi-static EMCC in Eq. (19) might be a suitable alternative in both practical applications and experiments when the SC and OC natural frequencies are almost indistinguishable. Furthermore, for large and complex FE models this method may require less computational effort than solving the dynamic eigenvalue problems.

## 4. Modal reduced equations

A reduced-order model for the vibrating structure is effectively introduced by a modal representation in terms of the most energetic vibration form. In this section, the representative modal equations are derived in order to obtain an accurate shunt tuning method that is suitable for implementation in a commercial FE-software. The structural part of Eq. (6) is effectively described by the mode shapes  $\{U\}_j$  from the SC limit, collected as columns in the modal matrix  $[U]$ . Hereby, the structural response  $\{U\}$  in Eq. (6) can be represented as

$$\{U\} = [U] \{v\} \quad (20)$$

where the vector  $\{v\}$  contains the modal coordinates. When substituting Eq. (20) into Eq. (6) and then pre-multiplying the structural equation with the vibration form  $\{U\}_r^t$  of the resonant mode  $j=r$ , the coupled set of modal equations can be written as

$$(\omega_r^2 - \omega^2) v_r = Q_r V \quad (21)$$

$$\bar{C}_p^{\epsilon_s} V - Q = -\{Q\}^t \{v\} \quad (22)$$

where the vector  $\{Q\}^t = \langle Q_1, Q_2, \dots \rangle$  contains the modal sensed charges  $Q_j$  defined in Eq. (10). Thus, the right-hand side of Eq. (22) contains contribution from both the resonant mode through the modal charge  $Q_r$  as well as residual contributions from the nonresonant modes due to the non-vanishing  $Q_j$  for  $j \neq r$ . The residual terms ( $j \neq r$ ) are now represented by two supplemental terms that are proportional to the electrical forcing  $V$  and describe corrections to the system impedances. Thus, the right-hand side of Eq. (22) is approximated as

$$\{Q\}^t \{v\} = Q_r v_r + \left( C_r' - \frac{1}{\omega^2 L_r'} \right) V \quad (23)$$

where  $C_r'$  and  $L_r'$  are artificial capacitance and inductance, respectively, taking into account the influence from the non-resonant structural modes ( $j \neq r$ ). The two correction terms

can be calculated explicitly and elegantly based on the system matrices [5]. However, next, the correction terms are instead calibrated by solving three eigenvalue problems associated with SC and OC patch electrodes and a pure inductive shunt with an optimally tuned inductance from the preferred calibration formulae without residual mode corrections. Elimination of  $Q_r v_r$  between Eqs. (21)–(23) gives the governing equation

$$\left[ \left( \bar{C}_p^{\epsilon_s} + C'_r - \frac{1}{\omega^2 L'_r} \right) (\omega_r^2 - \omega^2) + Q_r^2 \right] V = Q (\omega_r^2 - \omega^2) \quad (24)$$

where the relation between charge  $Q$  and voltage  $V$  depends on the particular shunt impedance.

#### 4.1. SC and OC electrodes

The SC condition corresponds to  $V=0$ , in which case the nontrivial solution to Eq. (24) is readily obtained as  $\omega = \omega_r$ , exactly recovering the solution to the SC eigenvalue problem in Eq. (9). The corresponding OC condition follows when  $Q=0$  and the associated circular frequency  $\hat{\omega}_r$  may be obtained numerically from Eq. (12) or experimentally by measurements. The relative difference between the SC and OC frequencies defines the effective EMCC by the relation in Eq. (13). Thus, substituting the OC frequency  $\omega = \hat{\omega}_r$  into Eq. (24) and then imposing  $Q=0$ , the former becomes

$$\left[ \left( C_r - \frac{1}{\hat{\omega}_r^2 L'_r} \right) (\omega_r^2 - \hat{\omega}_r^2) + Q_r^2 \right] V = 0 \quad (25)$$

after introducing

$$C_r = \bar{C}_p^{\epsilon_s} + C'_r \quad (26)$$

as a modal capacitance, modified by the quasi-static correction term  $C'_r$  introduced in Eq. (23).

Solving for nontrivial solutions with  $V \neq 0$ , the problem in Eq. (25) constitutes a quadratic equation in  $\hat{\omega}_r^2$ . The effective EMCC  $\kappa_e^2$  can thereby be obtained from the solution to this quadratic equation, see details in Appendix B, as

$$\kappa_e^2 = \frac{\hat{\omega}_r^2 - \omega_r^2}{\omega_r^2} = \kappa_r^2 + \frac{1}{2} (1 + \kappa_r^2 - \lambda'_r \kappa_r^2) \left( \sqrt{1 + \frac{4(\kappa_r^2)^2 \lambda'_r}{(1 + \kappa_r^2 - \lambda'_r \kappa_r^2)^2}} - 1 \right) \quad (27)$$

in which the inertia correction from the residual modes is represented by

$$\lambda'_r = \frac{1}{Q_r^2 L'_r} \quad (28)$$

while the flexibility correction in  $C_r$  is contained in a modified EMCC (see Eqs. (15) and (26))

$$\kappa_r^2 = \frac{Q_r^2}{C_r \omega_r^2} \quad (29)$$

It follows from Eq. (27) that for vanishing inertia correction from the residual modes ( $\lambda'_r = 0$ ), the modified EMCC is  $\kappa_e^2 = \kappa_r^2$ . And if furthermore the flexibility correction is

ignored ( $C'_r = 0$ ), the modal capacitance  $C_r = \bar{C}_p^{\epsilon_s}$  and the EMCC  $\kappa_e^2 = \kappa_0^2$  from Eq. (15).

An improved estimate is achieved for finite  $\lambda'_r \ll 1$ , whereby a Taylor expansion of first order can be applied on the square root in Eq. (27). This gives

$$\kappa_e^2 = \kappa_r^2 \frac{1 + \kappa_r^2}{1 + \kappa_r^2 - \lambda'_r \kappa_r^2} = \frac{Q_r^2}{C_L \omega_r^2} \quad (30)$$

where the latter equality defines an actual modal capacitance  $C_L$  of the piezoelectric patches around the targeted resonance  $j=r$ ,

$$C_L = C_r \left( 1 - \frac{\lambda'_r \kappa_r^2}{1 + \kappa_r^2} \right) \quad (31)$$

It is found that for vanishing  $\lambda'_r$  the inertia reduced capacitance  $C_r$  recovers the actual capacitance  $C_L$  associated with  $\kappa_e^2$ .

It follows from Eq. (30) that the effective EMCC is the ratio between the apparent electrical absorber stiffness  $Q_r^2/C_L$  and the modal stiffness  $\omega_r^2$ . The expression in Eq. (30) can furthermore be used to determine the artificial inductance  $L'_r$  as

$$\frac{1}{(1 + \kappa_r^2) \omega_r^2 L'_r} = \left( 1 - \frac{\kappa_r^2}{\kappa_e^2} \right) \frac{Q_r^2}{\kappa_r^2 \omega_r^2} \quad (32)$$

using Eqs. (28) and (31). By elimination of  $L'_r$ , using Eqs. (32), (26), and (29), the governing modal equation (24) can be expressed as

$$\left\{ \left[ \frac{\omega^2}{\omega_r^2} - (1 + \kappa_r^2) \left( 1 - \frac{\kappa_r^2}{\kappa_e^2} \right) \right] \left( 1 - \frac{\omega^2}{\omega_r^2} \right) + \kappa_r^2 \frac{\omega^2}{\omega_r^2} \right\} V = \frac{Q}{Q_r^2} \kappa_r^2 \omega^2 \left( 1 - \frac{\omega^2}{\omega_r^2} \right) \quad (33)$$

containing both the effective EMCC  $\kappa_e^2$  and the modified EMCC  $\kappa_r^2$ .

As mentioned above, a simplified representation can be obtained by assuming that  $L'_r \rightarrow \infty$ , whereby the last (inertia) correction term in Eq. (23) vanishes, leaving only the former flexibility term proportional to  $C'_r$ . For this approximation, it follows directly from Eq. (27) that  $\kappa_r^2 = \kappa_e^2$ , obtained directly from Eq. (13). The validity and accuracy of  $\kappa_r^2 = \kappa_e^2$  is verified by the numerical results obtained in Section 7 and the tuning formulae presented in Section 5 which are therefore expressed directly in terms of  $\kappa_e^2$ . However, for a non-negligible residual mode inertance, represented by  $L'_r$ , a supplemental condition is then needed to separate the individual correction effects from  $C'_r$  and  $L'_r$ . This separation is conveniently achieved by introducing a pure inductive (L) shunt that creates a supplemental resonance. For completeness, this improved  $L$ -shunt calibration is now summarized, although its influence is limited for most flexible structures, as illustrated in [6].

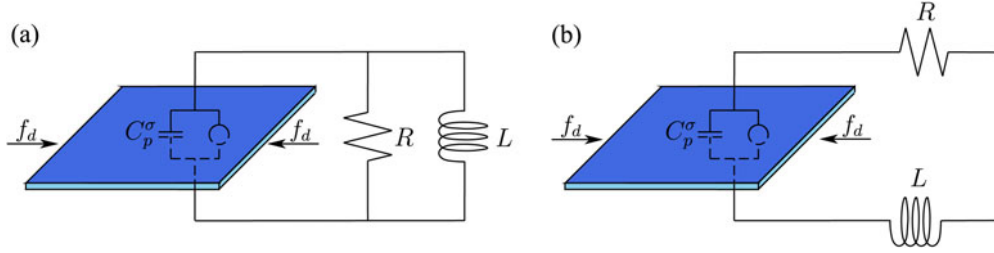


Figure 1. (a) Parallel and (b) series shunted piezoceramic patch with inherent capacitance  $C_p^\sigma$ .

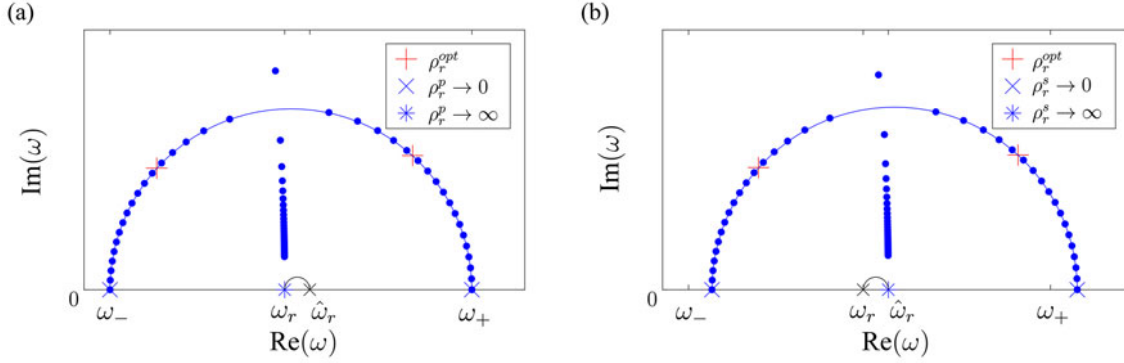


Figure 2. Root-Locus diagram for (a) parallel Eq. (46) and (b) series Eq. (52) shunt circuits.

#### 4.2. Pure L-shunt

In the OC limit, the effective EMCC  $\kappa_e^2$  in Eq. (27) or Eq. (30) depends on both the flexibility correcting capacitance  $C_r'$  in  $\kappa_r^2$  and the inertia correcting inductance  $L_r'$  in  $\lambda_r'$ . In order to distinguish these two nonresonant modal corrections, a supplemental condition must be introduced. By introducing a pure inductive (L) shunt, an expression for  $\kappa_r^2$  can be determined by solving the corresponding quadratic characteristic equation, as detailed subsequently.

For a pure L-shunt, the impedance relation between charge and voltage can be written as

$$V = \omega^2 L Q \quad (34)$$

Hereby, the charge  $Q$  can be eliminated, after using Eq. (34), in Eq. (33), whereby the characteristic equation associated with  $V \neq 0$  can be written as

$$\left(\frac{\omega}{\omega_r}\right)^4 - \left[1 + \kappa_r^2 + (1 + \kappa_r^2) \left(1 - \frac{\kappa_r^2}{\kappa_e^2}\right) + \lambda_r \kappa_r^2\right] \left(\frac{\omega}{\omega_r}\right)^2 + (1 + \kappa_r^2) \left(1 - \frac{\kappa_r^2}{\kappa_e^2}\right) + \lambda_r \kappa_r^2 = 0 \quad (35)$$

representing the shunt inductance  $L$  in normalized form as

$$\lambda_r = \frac{1}{Q_r^2 L} \quad (36)$$

similar to Eq. (28) for the correction inductance  $L_r'$ . It is noted that the form of  $\lambda_r$  in Eq. (36) is due to the present normalization of the SC mode shapes to unit modal masses in Eq. (11).

Because of the inclusion of the inductance  $L$ , the quadratic characteristic equation (35) governs two roots  $\omega_-^2$  and  $\omega_+^2$ ,

with the corresponding circular frequencies  $\omega_-$  and  $\omega_+$  being smaller and larger than the SC circular frequency  $\omega_r$ , respectively. The two circular frequencies associated with the L-shunt can be found experimentally or numerically by solving the eigenvalue problem Eq. (6) with  $Q$  eliminated by Eq. (34),

$$\left( \begin{bmatrix} K^E & k_{me}^E \\ 0 & 1 \end{bmatrix} - \omega^2 \begin{bmatrix} M & 0 \\ -(k_{me}^E)^t L & \bar{C}_p^{\epsilon^3} L \end{bmatrix} \right) \begin{Bmatrix} U \\ V/L \end{Bmatrix} = \begin{Bmatrix} 0 \\ 0 \end{Bmatrix} \quad (37)$$

The product of the two roots must be equal to the constant term in (35), which gives the condition

$$\left(\frac{\omega_+}{\omega_r}\right)^2 \left(\frac{\omega_-}{\omega_r}\right)^2 = \lambda_r^* \kappa_r^2 \quad (38)$$

where

$$\lambda_r^* = \frac{1 + \kappa_r^2}{\kappa_r^2} \left(1 - \frac{\kappa_r^2}{\kappa_e^2}\right) + \lambda_r \quad (39)$$

represents the  $\kappa_r^2$  factored out constant term in the characteristic equation Eq. (35). It may be noted, considering the first relation of Eq. (30), that  $\lambda_r^* = \lambda_r' + \lambda_r$  represents the combined inductance from shunt, Eq. (36) and residual modes Eq. (28).

The sum of roots must further equal the coefficient to the linear term in Eq. (35) with opposite sign, which results in

$$\left(\frac{\omega_+}{\omega_r}\right)^2 + \left(\frac{\omega_-}{\omega_r}\right)^2 = 1 + \kappa_r^2 (1 + \lambda_r^*) \quad (40)$$

Subtracting Eq. (38) from Eq. (40) gives the modified EMCC as

$$\kappa_r^2 = \left(1 - \frac{\omega^2}{\omega_r^2}\right) \left(\frac{\omega_+^2}{\omega_r^2} - 1\right) \quad (41)$$

Once  $\kappa_r^2$  is determined, the modal capacitance  $C_r$  is obtained from Eq. (29), whereby the quasi-static correction capacitance  $C'_r$  subsequently follows from Eq. (26) after using Eq. (15), as

$$C'_r = C_r - \bar{C}_p^{\epsilon^s} = \left(1 - \frac{\kappa_r^2}{\kappa_0^2}\right) \frac{Q_r^2}{\kappa_r^2 \omega_r^2} \quad (42)$$

The corresponding inductive correction term  $L'_r$  is determined by the previously derived expression in Eq. (32).

The introduction of the pure  $L$ -shunt enables the individual determination of the two correction terms in Eq. (23) with the artificial modal capacitance  $C'_r$  and inductance  $L'_r$ . However, in the following, the modified EMCC  $\kappa_r^2$  is replaced by the effective EMCC  $\kappa_e^2$ , which is readily available from an FE analysis when using the definition in Eq. (14). As demonstrated in the present section, this estimate of  $\kappa_e^2$  is valid for vanishing  $\lambda'_r$ .

## 5. Resonant shunt tuning

The resonant shunt circuit consists of an inductance  $L$  and a resistance  $R$  connected either in parallel or in series, as shown in Figure 1. For both circuit connections, the charge  $Q$  on the right-hand side of Eq. (33) can be eliminated by the generalized Ohm's law

$$V = -i\omega Z_{sh}(\omega)Q \quad (43)$$

where  $Z_{sh}(\omega)$  is the impedance of the supplemental shunt.

Upon elimination, by Eq. (43), of  $Q$  in Eq. (33), the corresponding characteristic equation can be written as

$$\left[\frac{\omega^2}{\omega_r^2} - (1 + \kappa_r^2) \left(1 - \frac{\kappa_r^2}{\kappa_e^2}\right) - i\omega \frac{1}{Z_{sh}(\omega)Q_r^2} \kappa_r^2\right] \left(1 - \frac{\omega^2}{\omega_r^2}\right) + \kappa_r^2 \frac{\omega^2}{\omega_r^2} = 0 \quad (44)$$

Next, the calibration principle for the parallel and series  $RL$  resonant shunt circuits are considered, in which the tuning expressions are subsequently simplified by assuming  $\kappa_r^2 \simeq \kappa_e^2$ .

### 5.1. Parallel shunt circuit

The schematics of a parallel shunted piezoceramic patch is shown in Figure 1(a). Because of its inductive property it operates as a vibration absorber on the host structure and details about its equivalent mechanical properties are provided in [1]. The impedance  $Z_{sh}(\omega)$  is for the parallel shunt circuit given as

$$\frac{1}{Z_{sh}(\omega)} = \frac{1}{R} + \frac{1}{i\omega L} \quad (45)$$

and, by substituting the latter into Eq. (44), the characteristic equation can be written as

**Table 1.** Tuning procedure based on the effective EMCC for parallel and series shunt circuits with  $\kappa_r^2 \simeq \kappa_e^2$ .

Parallel	Series
$L = \frac{\kappa_e^2}{Q_r^2}, R = \frac{\kappa_e^2 \omega_r}{Q_r^2} \sqrt{\frac{1}{2\kappa_e^2}}$	$L = \frac{\kappa_e^2}{Q_r^2 (1 + \kappa_e^2)^2}, R = \frac{\kappa_e^2 \omega_r}{Q_r^2} \sqrt{\frac{2\kappa_e^2}{(1 + \kappa_e^2)^3}}$

$$\left(\frac{\omega}{\omega_r}\right)^4 - (1 + \kappa_r^2 + \lambda_r^* \kappa_r^2) \left(\frac{\omega}{\omega_r}\right)^2 + \lambda_r^* \kappa_r^2 + i \left(\frac{\omega}{\omega_r}\right) \rho_r^p \kappa_r^2 \omega_r \left[1 - \left(\frac{\omega}{\omega_r}\right)^2\right] = 0 \quad (46)$$

where the electric damping parameter (superscript  $p$  refers to *parallel*)

$$\rho_r^p = \frac{1}{RQ_r^2} \quad (47)$$

is inversely proportional to the shunt resistance  $R$ . Furthermore, the shunt inductance  $L$  is contained in  $\lambda_r^*$  as defined in Eq. (39), with the normalized shunt inductance  $\lambda_r$  introduced in Eq. (36).

When introducing the estimate  $\kappa_r^2 \simeq \kappa_e^2$ , the characteristic equation (46) reduces to

$$\left(\frac{\omega}{\omega_r}\right)^4 - (1 + \kappa_e^2 + \lambda_r \kappa_e^2) \left(\frac{\omega}{\omega_r}\right)^2 + \lambda_r \kappa_e^2 + i \left(\frac{\omega}{\omega_r}\right) \rho_r^p \kappa_e^2 \omega_r \left[1 - \left(\frac{\omega}{\omega_r}\right)^2\right] = 0 \quad (48)$$

where  $\lambda_r$  then directly replaces  $\lambda_r^*$  from Eq. (39). In the following Eq. (48) constitutes the basis of the shunt tuning.

Initially, the tuning of the inductance  $L$  in  $\lambda_r$  must secure that the electric shunt reacts properly in resonance with the targeted mode  $j=r$ . For this, the principle of equal modal damping is applied; initially, the latter was introduced for the mechanical tuned mass damper in [19] and subsequently proposed for pole placement calibration of a resonant series  $RL$  shunt [1]. The principle states that the two complex roots must meet at a bifurcation point, whereby they have equal damping up to the point of bifurcation because the roots follow semicircular trajectories for increasing  $\rho_r^p$ . It, furthermore, implies that equal damping can be secured for a pure  $L$ -shunt in the limit  $\rho_r^p \rightarrow 0$ , at which the real-valued roots  $\omega_-$  and  $\omega_+$  must be inverse points with respect to the circular frequency  $\omega_r$  in the opposite (SC) limit  $\rho_r^p \rightarrow \infty$ . For  $\rho_r^p \rightarrow 0$ , the characteristic equation (46) recovers Eq. (35) for the pure  $L$ -shunt. The inverse point condition can therefore be directly represented by the relation  $\lambda_r \kappa_e^2 = 1$ , see Eq. (48). Hereby, the inductance calibration follows readily from Eq. (36) as

$$L = \frac{\kappa_e^2}{Q_r^2} \quad (49)$$

It is important to observe that the optimal inductance is given by the effective EMCC  $\kappa_e^2$  relative to the square of the modal charge  $Q_r$  in Eq. (10), obtained directly from an FE analysis as a reaction force associated with the SC eigenvalue problem.

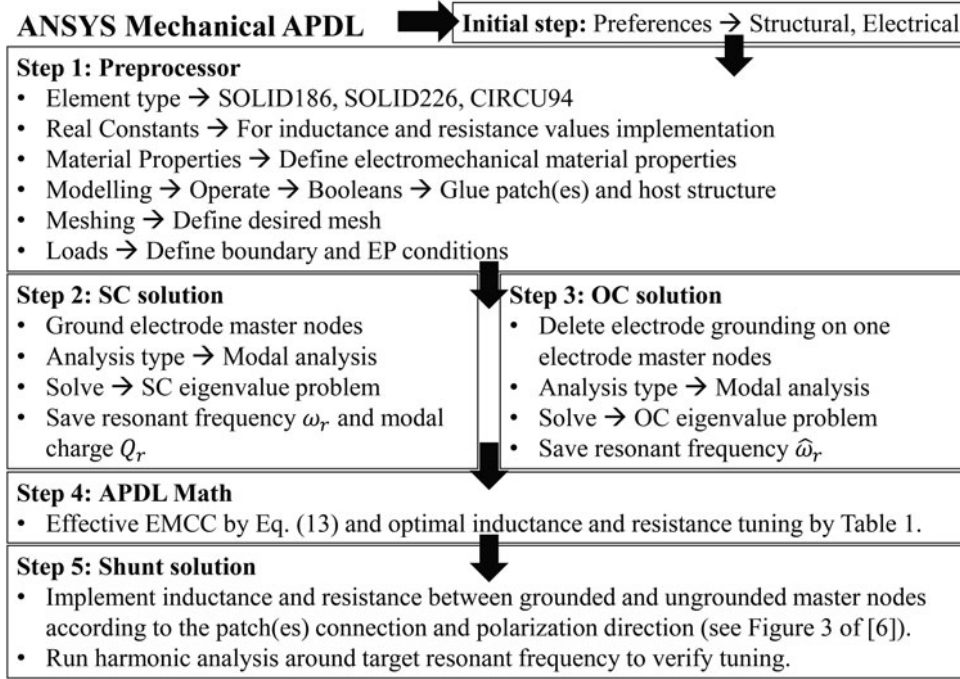


Figure 3. Flow chart illustrating ANSYS® implementation of the proposed optimum shunt tuning procedure.

In Figure 2(a), the blue trajectories represent the path of the complex roots in the first quadrant, obtained by solving the characteristic equation (46) with respect to  $\rho_r^p$  as gain. For infinite resistance ( $\rho_r^p \rightarrow 0$ ), the roots recover  $\omega_-$  and  $\omega_+$  below and above  $\omega_r$ . When increasing  $\rho_r^p$  (or decreasing the resistance), the two roots move into the complex plane along semicircular paths until they meet at the bifurcation point, hereafter one root becomes heavily damped when approaching the imaginary axis along a quarter circle, while the other root becomes undamped when terminating at the SC solution  $\omega_r$  for  $\rho_r^p \rightarrow \infty$ . Thus, the reference frequency for the parallel  $RL$  shunt is associated with the SC configuration.

The shunt resistance is now tuned to secure a reasonably flat plateau in the frequency response curve. Several expressions have been proposed for this calibration [3], [4], and [8] and in the present case the resistance tuning in [1], [13], [19], and [20]. By comparing the generic equation (33) in [20] with the characteristic equation (48), this gives the optimum resistance tuning as

$$R = \frac{\kappa_e^2 \omega_r}{Q_r^2} \sqrt{\frac{1}{2\kappa_e^2}} \quad (50)$$

when the approximation  $\kappa_r^2 \simeq \kappa_e^2$  has been introduced. The tuning in Eq. (50) provides a reasonable compromise between large modal damping and effective response mitigation, and furthermore it gives a flat plateau in the amplitude curve for the shunt loading  $V$ . The complex roots obtained by Eq. (50) are indicated by the red crosses in Figure 2(a).

As demonstrated in [13], it is numerically advantageous and, for most actual problems, sufficiently accurate to base the tuning of the resistance on the effective EMCC, whereby  $\kappa_r^2 \simeq \kappa_e^2$  is used in the calibration formulae for both  $L$  and  $R$ . Thus, the subsequent implementation of the shunt tuning

method only involves the use of modal parameters  $\omega_r$ ,  $Q_r$  and  $\kappa_e^2$  for the SC and OC configurations, while avoiding the pure  $L$ -shunt and its supplemental eigenvalue problem in Eq. (37). The tuning formulae for the parallel shunt are summarized in Table 1.

## 5.2. Series shunt circuit

The series shunted piezoceramic patch is shown in Figure 2(b). This configuration implies that the residual mode corrections and shunt components are not additive, whereby optimal calibration is associated with an iterative procedure, unless the assumption  $\kappa_r^2 \simeq \kappa_e^2$  is conveniently introduced, as demonstrated subsequently.

The series shunt impedance is introduced as

$$Z_{sh}(\omega) = R + i\omega L \quad (51)$$

whereby substitution into Eq. (44) gives this characteristic equation (see Appendix C for its derivation)

$$\left(\frac{\omega}{\hat{\omega}_r}\right)^4 - \left(\frac{1+\kappa_r^2}{1+\kappa_e^2} + \frac{\lambda_r^* \kappa_r^2}{1+\kappa_e^2}\right) \left(\frac{\omega}{\hat{\omega}_r}\right)^2 + \frac{\lambda_r^* \kappa_r^2}{(1+\kappa_e^2)^2} + i \left(\frac{\omega}{\hat{\omega}_r}\right) \rho_r^s \frac{\lambda_r}{\hat{\omega}_r} \left\{ \frac{1+\kappa_r^2}{1+\kappa_e^2} - \left(\frac{\omega}{\hat{\omega}_r}\right)^2 + \frac{1+\kappa_r^2}{1+\kappa_e^2} \left(1 - \frac{\kappa_r^2}{\kappa_e^2}\right) \left[\left(\frac{\omega_r}{\omega}\right)^2 - 1\right] \right\} = 0 \quad (52)$$

conveniently given in terms of the OC frequency  $\hat{\omega}_r$  and introduction of an electric damping parameter (superscript  $s$  refers to series)

$$\rho_r^s = RQ_r^2 \quad (53)$$

that becomes proportional to the shunt resistance  $R$ .

In Eq. (52), the characteristic equation is actually quintic, due to the presence of the frequency ratio  $\omega_r^2/\omega^2$  in the final

**Table 2.** Dimensions of simply supported plate with a single pair of piezoceramic patches.

Plate				Center patch	Piezoceramic PZT 5H
Dimensions $l_x \times l_y \times t$ [mm <sup>3</sup> ]	Density [kg/m <sup>3</sup> ]	Young's modulus [GPa]	Poisson's ratio [-]	$x, y$ [mm]	Dimensions $l_{px} \times l_{py} \times t_p$ [mm <sup>3</sup> ]
$414 \times 314 \times 1$	2700	70	0.33	$\frac{13}{28}l_x, \frac{15}{28}l_y$	$82.8 \times 62.8 \times 0.5$

term. However, by applying the estimate  $\kappa_r^2 \simeq \kappa_e^2$  the last term inside the latter curled brackets vanishes and Eq. (52) reduces, after Eq. (39), to

$$\left(\frac{\omega}{\hat{\omega}_r}\right)^4 - \left(1 + \frac{\lambda_r \kappa_e^2}{1 + \kappa_e^2}\right) \left(\frac{\omega}{\hat{\omega}_r}\right)^2 + \frac{\lambda_r \kappa_e^2}{(1 + \kappa_e^2)^2} + i \left(\frac{\omega}{\hat{\omega}_r}\right) \rho_r^s \frac{\lambda_r}{\hat{\omega}_r} \left[1 - \left(\frac{\omega}{\hat{\omega}_r}\right)^2\right] = 0 \quad (54)$$

For this reduced equation, the desired inverse point relation is secured by  $\lambda_r \kappa_e^2 = (1 + \kappa_e^2)^2$ , corresponding to the roots  $\omega_-$  and  $\omega_+$  for vanishing  $\rho_r^s$  being inverse points with respect to the OC natural frequency  $\hat{\omega}_r$ . The optimal inductance is then determined from Eq. (36) as

$$L = \frac{\kappa_e^2}{Q_r^2 (1 + \kappa_e^2)^2} \quad (55)$$

For the inductance tuning in Eq. (55), the complex roots obtained by solving Eq. (52) are plotted in Figure 2(b) for increasing  $\rho_r^s$ . The root locus diagram verifies that  $\omega_-$  and  $\omega_+$  are in fact inverse points on the real axis with respect to  $\hat{\omega}_r$ , whereby the OC natural frequency is the apparent reference frequency for the series  $RL$  shunt, as also observed by [11].

It can be seen from Figure 2(b) that the roots to Eq. (52) approximately follow a semicircle in the complex plane up to a bifurcation point. However, due to the approximations associated with the inverse point relation, the bifurcation point is not perfectly met. The optimal resistance tuning indicated by red crosses in Figure 2(b) is again found by the balanced calibration devised in [20] by comparing its generic equation (33) with Eq. (54), which results in the resistance formula

$$R = \frac{\kappa_e^2 \hat{\omega}_r}{Q_r^2 (1 + \kappa_e^2)^2} \sqrt{2\kappa_e^2} = \frac{\kappa_e^2 \omega_r}{Q_r^2} \sqrt{\frac{2\kappa_e^2}{(1 + \kappa_e^2)^3}} \quad (56)$$

expressed in terms of  $\kappa_r^2 \simeq \kappa_e^2$ . Thus, the optimum piezoelectric shunt tuning for both the parallel and series  $RL$  shunts are now consistently derived with respect to the SC modal charge  $Q_r$ , the SC circular frequency  $\omega_r$  and the effective EMCC  $\kappa_e^2$  obtained by the classical expression in Eq. (13). The calibration formulae used in the following numerical analysis are summarized in the second column of Table 1 for the series shunt connection.

## 6. Numerical implementation in ANSYS®

The modeling of the electromechanical structure in ANSYS®, evaluations of the SC and OC eigenvalue problems and implementation of the proposed shunt tuning method

are summarized in the flow-chart shown in Figure 3, and briefly explained in the following. Initially, “Structural” and “Electrical” analyses have to be chosen. The first step then follows by defining the geometry, material properties, element types and mesh partitions of the analyzed electromechanical structure. In the present work, SOLID186 and SOLID226 3D 20 node elements are used for the discretization of the host structure and piezoceramic patch(es), respectively. Next, the boundary conditions and equipotential (EP) conditions for all continuous electrodes are imposed to the discretized model. For each continuous electrode, the EP condition is defined in a master node which is saved for later use. In the second step, zero electric potential is applied to the master nodes to obtain SC piezoceramic patch(es). A modal analysis is then conducted to determine the targeted SC resonant frequency  $\omega_r$  and modal charge  $Q_r$ , with the latter being a reaction force of the modal analysis. The third step deletes the zero electric potential constraint on one of the master nodes to obtain OC piezoceramic patch(es). A modal analysis is then conducted to determine the target OC resonant frequency  $\hat{\omega}_r^2$ . The fourth step then determines the effective EMCC  $\kappa_e^2$  using Eq. (13), whereby the optimum inductance and resistance values can be determined according to Table 1 for either the parallel or series shunt circuit. The fifth and final step implements the optimum inductance and resistance between the grounded and ungrounded master nodes according to the patch(es) connection and polarization directions, see [6]. The inductance and resistance are implemented using CIRC94 elements with specific key options and real constants. The shunt tuning can then be validated by performing a harmonic analysis around the target resonant frequency.

If the alternative tuning method based on the quasi-static EMCC  $\kappa_s^2$  is preferred, the evaluation of the OC eigenvalue problem can be omitted, while two static problems associated with SC and OC patch electrodes must instead be solved. Finally, for single mode tuning with the effective EMCC approximated by the modal EMCC  $\kappa_0^2$  in Eq. (15), the resulting modified capacitance is determined by Eq. (7b). In the following the performance of these three tuning methods are analyzed for the smart plate benchmark [6] with either a single pair or four pairs of piezoceramic patches.

## 7. Benchmark examples

In the present section, the smart plate benchmark analyzed in [6] is modeled with 3D FEs in ANSYS® with the aim of determining the optimum parallel and series shunt tuning and demonstrate the simplicity of the proposed tuning

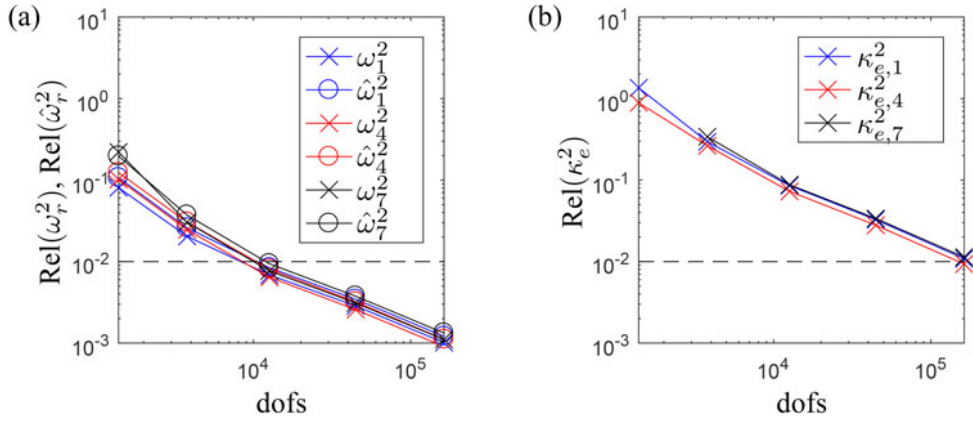


Figure 4. Convergence of (a) SC and OC frequencies and (b) effective EMCC for modes 1, 4 and 7, determined by  $\text{Rel}(X) = (X_{\text{approx}} - X_{\text{ref}}) / X_{\text{ref}}$ .

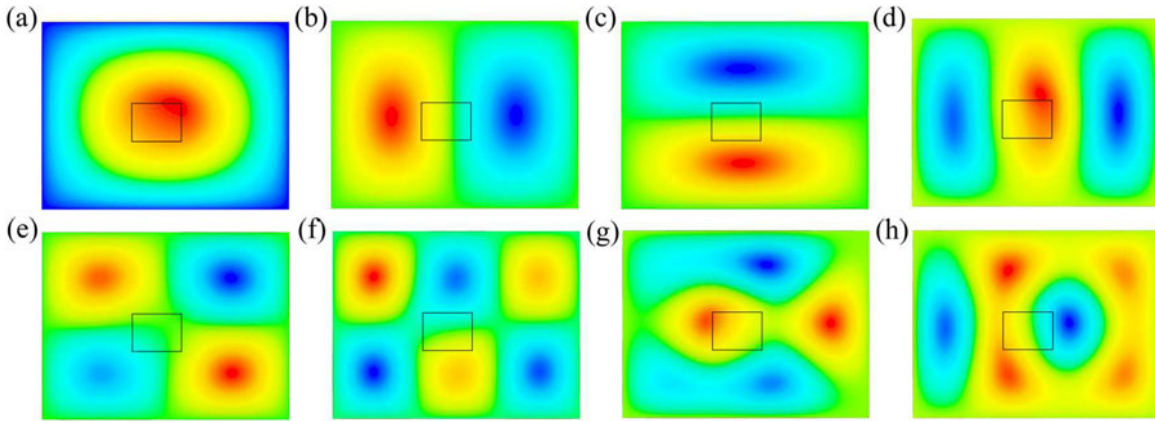


Figure 5. Mode shapes of a simply supported plate with a single SC patch pair.

method based on  $\omega_r$ ,  $Q_r$  and  $\kappa_e^2$ . Details about the dimensions of the simply supported plate and the single pair of piezoceramic patches as well as the location of the latter are provided in Table 2, along with the material properties of the plate. In the present work, it is chosen to use the piezoceramic material PZT 5H, for which the material properties can be accessed through the “eFunda portal” [21].

### 7.1. Simply supported plate with a single pair of patches

The first example concerns optimum shunt tuning to the first eight vibration modes of the simply supported plate described in [6] with a single pair of piezoceramic patches. Initially, a short convergence study is carried out in order to justify the chosen discretization. It is first of all noted that increasing the number of elements in thickness direction only slightly alters the numerical results. The convergence study is thus carried out for an increasing number of elements along the two in-plane axes. The convergence of the squared SC and OC frequencies and effective EMCC for three of the first eight vibration modes is shown in Figure 4. The three modes 1, 4, and 7 are of particular interest because they possess significant electromechanical coupling, as indicated by large  $\kappa_e^2$  in the following. The relative errors are obtained by comparing the approximate (approx.) results to the reference (ref) ones obtained with a very fine mesh consisting of 23,104 elements and 633,064 dofs.

It can be seen from Figure 4(a) that the squared SC and OC frequencies converge rapidly and have relative errors below 1% (dashed black line) when using a model with approximately  $10^4$  dofs. Furthermore, a nearly linear tendency of the convergence on the double logarithmic scale can be observed, indicating quadratic convergence. From Figure 4(b) it can be seen that the convergence of the squared effective EMCC is slower than that for the SC and OC frequencies. This is because  $\kappa_e^2$  is determined as the relative difference between  $\hat{\omega}_r^2$  and  $\omega_r^2$ , where the SC frequency simply converges faster than the OC one. It is seen that the relative error on the effective EMCC is around 1% (dashed black line) when using a model with approximately  $1.5 \times 10^5$  dofs. This discretization is therefore used in the present analysis. The relative error on the effective EMCC for the remaining five vibration modes might be larger since the convergence rate is proportional to the magnitude of  $\kappa_e^2$ , as demonstrated in [14].

The first eight vibration modes for the simply supported plate with a single SC pair of piezoceramic patches are shown in Figure 5, with the location of the patch pair indicated by the black rectangle. It can be seen from Figure 5(a, d, g) that the pair of piezoceramic patches is favorably positioned targeting vibration modes 1, 4 and 7, as their large curvatures over the patch area give large in-plane patch deformation. For the remaining five vibration modes, the pairs are positioned close to nodal points, whereby the EP condition results in cancellation of the charge across the patch area.

**Table 3.** SC and OC frequencies, effective EMCC, normalized modal charge and optimum  $RL$ -shunt tunings, for simply supported plate with a pair of same poled and parallel wired piezoceramic patches.

Mode (type)	$f$ [Hz]	$\hat{f}$ [Hz]	$\kappa_e^2$ [%]	$Q_r^2/\omega_r^2 \left[ \mu \left( \frac{C_s}{C_{rad}} \right)^2 \right]$	$L_p$ [H]	$R_p$ [k $\Omega$ ]	$L_s$ [H]	$R_s$ [k $\Omega$ ]
<b>1 (1,1)</b>	<b>35.89</b>	<b>36.22</b>	<b>1.86</b>	<b>1.013</b>	<b>36.03</b>	<b>42.16</b>	<b>34.73</b>	<b>1.523</b>
2 (2,1)	80.73	80.77	0.10	0.054	7.071	80.96	7.057	0.159
3 (1,2)	111.9	112.0	0.12	0.066	3.604	52.32	3.592	0.122
<b>4 (3,1)</b>	<b>154.7</b>	<b>156.5</b>	<b>2.30</b>	<b>1.252</b>	<b>1.943</b>	<b>8.810</b>	<b>1.857</b>	<b>0.392</b>
5 (2,2)	165.7	165.7	0.02	0.008	1.999	1.115	1.998	0.038
6 (3,2)	230.6	230.7	0.04	0.027	0.744	37.31	0.744	0.031
<b>7 (1,3)</b>	<b>242.3</b>	<b>244.8</b>	<b>2.01</b>	<b>1.067</b>	<b>0.814</b>	<b>6.176</b>	<b>0.782</b>	<b>0.241</b>
8 (4,1)	252.3	252.3	0.00	0.000	0.976	24.17	0.976	0.010

Table 3 provides the SC and OC frequencies, the effective EMCC, the normalized modal charge and the optimum parallel ( $p$ ) and series ( $s$ ) shunt tunings for modes 1 to 8. It can be seen for the present piezoceramic patch design that damping with the present patch pair location and dimensions is attainable for modes 1, 4, and 7, denoted in bold face in Table 3. The squared effective EMCCs are for these three modes around 2%, yielding a damping ratio of approximately  $\zeta_{1,4,7} = \sqrt{\frac{1}{8} \kappa_e^2} \approx 5\%$ , see [1]. It is seen that the normalized modal charge  $Q_r$  is seemingly proportional to the level of attainable damping. Finally, it is noted in Table 3 that the parallel and series optimum inductances have the same order of magnitude, while much lower resistance values are required for the series shunt configuration.

The tuning of the electronic components could as well have been based on the quasi-static (Eq. 19) or the modal (Eq. 15) EMCC, whereby evaluation of the OC eigenvalue is avoided. For the quasi-static EMCC, the two static Eqs. (16) and (17) must instead be computed, whereby the quasi-static capacitance can be determined by Eq. (18). In the present example, this is found to be  $C_s = 554.6\text{nF}$ . The quasi-static EMCC  $\kappa_s^2$  then follows by multiplying the inverse of  $C_s$  with  $Q_r^2/\omega_r^2$  in Table 3. Using the single mode approximation, the resulting modified capacitance  $\bar{C}_p^e$  can be determined by Eq. (7) by mapping the corresponding entries in the system stiffness matrix in ANSYS<sup>®</sup>. However, mapping the correct entries in the stiffness matrix is a heavy and rather complicated task in ANSYS<sup>®</sup>, which uses three different layers of ordering. Therefore, it may be advantageous simply to solve the two static problems, associated to Eqs. (16) and (17) in order to get  $Q_s$  and  $V_s$ , and to determine the quasi-static capacitance  $C_s$ . In the present case, the resulting modified capacitance is found to be  $\bar{C}_p^e = 616.2\text{nF}$ , from which the modal EMCC  $\kappa_0^2$  (Eq. 15) follows by multiplication of its inverse with  $Q_r^2/\omega_r^2$  in Table 3.

The performance of the tuning methods based on the effective, quasi-static and modal EMCC is now analyzed by considering the frequency response plot (FRP) around the first and fourth resonant frequencies, which are shown in Figure 6. It can be seen from Figure 6 that the tuning based on the effective EMCC (solid line) gives an optimum response around the resonant frequencies with a flat (unit) plateau for the shunt voltage response. The latter is observed when an idealized harmonic modal load is used for producing the FRP. This modal load is determined from the mass matrix, the SC mode shape and the modal charge as  $\{F\}_r = [M]\{U\}_r Q_r$ . The tuning based on the quasi-static EMCC (dashed line in Figure 6) is also seen to perform

relatively well (with small deviations to the optimum shunt tuning). However, the tuning based on the modal EMCC (dashed-dotted line) is seen to be very poor in the given example causing large dynamic amplification around the original SC resonance frequency. Hence, an accurate description of the electromechanical structure, accounting for the nonresonant modes, is apparently of great importance as it furthermore results in a relatively simple tuning procedure.

## 7.2. Simply supported plate with four pairs of patches

It may be of general interest to place piezoelectric patches at decentralized location on the host structure, while maintaining the same level of supplemental modal damping. This can be realized by the application of several interacting piezoelectric patches, which further may have the potential of increasing the number of vibration modes with attainable damping, as investigated in the following for the simply supported plate. The second example thus concerns the same simply supported plate but with four pairs of piezoceramic patches placed symmetrically in the quarter points of the plate. The pairs are only a quarter of the size of the former single pair, whereby the piezoceramic volume is unchanged. The aim of the present example is to demonstrate the performance of the piezoelectric shunt damping when having several patches and to investigate the difference between having an individual patch and a network of wired patches.

As in the first example, the first eight vibration modes are exploited and shown in Figure 7 with the position of the piezoceramic SC patches indicated by the black rectangles. It can be seen from the mode shapes in Figure 7, compared to those in Figure 5, that modes 4 and 5 have interchanged. Also, the piezoceramic patches are in the present case seen to alter the vibration modes less compared to the first example, in particular for modes 7 and 8.

The SC and OC frequencies, effective EMCC, squared normalized modal charge, and parallel ( $p$ ) and series ( $s$ ) shunt tunings are now determined for the plate with four individually shunted pairs of patches and provided in Table 4. As the pairs of patches are symmetrically (or anti-symmetrically) positioned with respect to the deformation pattern of the first eight vibration modes, see Figure 7, the optimum tuning of each pair of patches will be identical and determined according to Appendix A. In Table 4, the provided modal charge and shunt tunings are thus for a single patch pair. It can be seen from Table 4 that damping is attainable for the first seven vibration modes given in bold-face. This is a considerable improvement

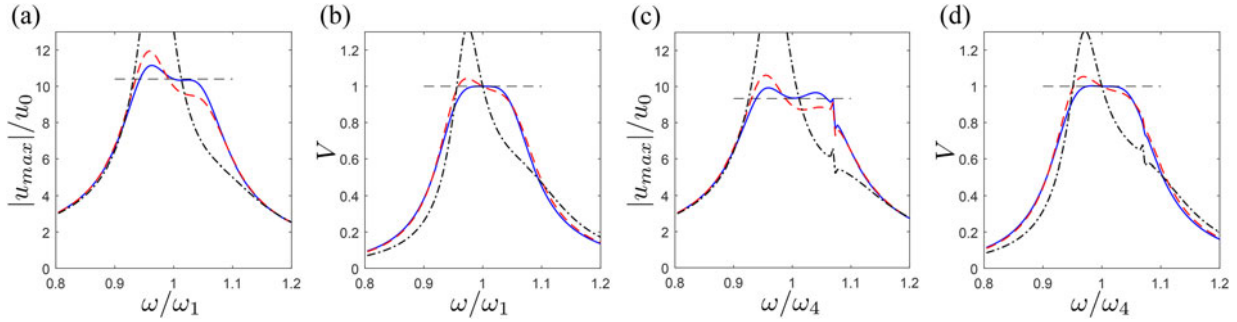


**Figure 6.** FRP for displacement and voltage around the (a)+(b) first and (c)+(d) fourth resonant frequency for parallel shunt tuning based on the effective Eq. (13) (solid line), quasi-static Eq. (19) (dashed line) and modal Eq. (15) (dashed-dotted line) EMCC in respect to mode  $r$ .

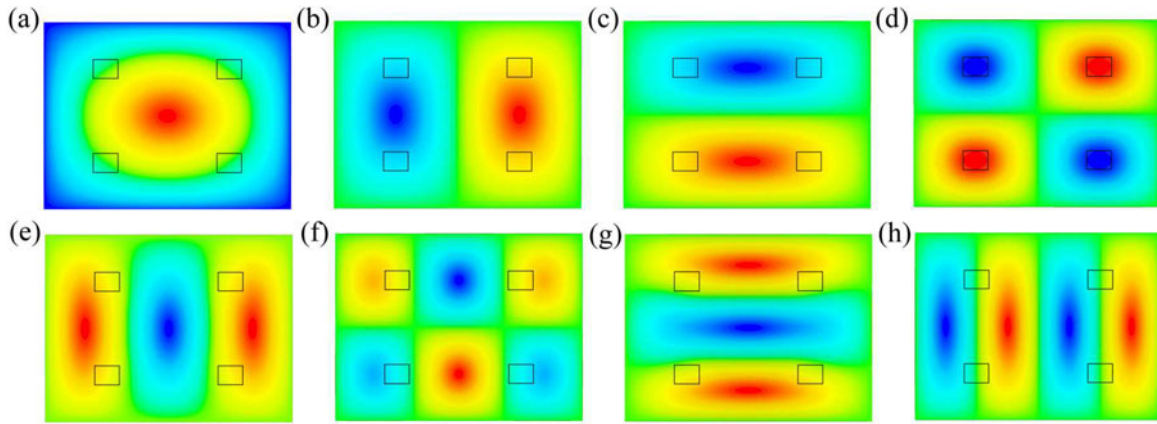


**Figure 7.** Mode shapes of a simply supported plate with four pairs of SC patches.

**Table 4.** SC and OC frequencies, effective EMCC, normalized modal charge and optimum  $RL$ -shunt tunings for each individual shunted pair of piezoceramic patches, for the simply supported plate with four pairs of same poled and parallel wired piezoceramic patches.

Mode (type)	$f$ [Hz]	$\hat{f}$ [Hz]	$\kappa_e^2$ [%]	$Q_r^2 / \omega_r^2 \left[ \eta \left( \frac{c_s}{rad} \right)^2 \right]$	$L_p$ [H]	$R_p$ [k $\Omega$ ]	$L_s$ [H]	$R_s$ [k $\Omega$ ]
1 (1,1)	38.58	38.66	0.41	0.141	123.1	330.8	122.1	2.678
2 (2,1)	78.24	78.64	1.01	0.348	30.09	104.0	29.49	2.073
3 (1,2)	109.3	109.8	0.93	0.321	15.36	77.36	15.08	1.420
4 (2,2)	143.3	144.7	1.90	0.648	9.049	41.77	8.714	1.545
5 (3,1)	153.0	153.5	0.62	0.216	7.821	67.28	7.725	0.833
6 (3,2)	219.8	220.9	0.98	0.334	3.840	37.92	3.766	0.731
7 (1,3)	236.3	236.9	0.52	0.178	3.295	48.06	3.261	0.494
8 (4,1)	254.6	254.6	0.00	0.000	3.253	–	3.253	–

compared to the three modes with substantial damping in the first example (Section 7.1). Vibration mode 8 is again seen to have vanishing attainable damping since the patches locations in Figure 7(h) are at nodal points. The effective EMCC is seen to be lower for modes 1, 5 (4 in first example) and 7 compared to the first example, which is therefore superior for these specific modes. Furthermore, it is seen that the magnitude of the optimum electronic components are considerably larger compared to the tuning in the first example. This is mainly due to the much lower modal charges caused by the smaller individual patch volumes with less conversion into electrical energy. However, this can be changed by connecting the four pairs of patches to a single common shunt. This causes the squared modal charges to increase by a factor sixteen, while the optimum tuning values for the electronic components will be a quarter of the values provided in Table 4. The attainable damping will remain unchanged, since the SC and OC frequencies and thus the effective EMCC are the same. However,

attention has to be paid to the connection of the four pairs of patches as the particular configuration depends on the shape of the vibration mode to be damped. For example, for the first vibration mode, the interface (top and bottom) electrodes and the inner electrodes should be connected, respectively, and wired in parallel to the shunt circuit. This is because the in-plane strains of all the patches have equal sign. However, this is not the case for modes 2, 3, 4 and 6, for which the in-plane strains have opposite signs. These signs, and thereby the wiring of the four pairs of patches, can be determined by considering the signs of the individual modal charges. For instance, in mode 2, the modal charges of the two pairs of patches to the left are positive while they are negative for the pairs to the right, see Figure 7(b). This implies that the interface electrodes of the left patch pairs should be connected to the inner electrodes of the corresponding right patch pairs and vice versa. When the wiring of the patches is done correctly, it is apparently beneficial to connect the four pairs of

patches in a single network, requiring smaller optimum shunt components.

## 8. Summary and conclusions

In the present work, a newly proposed *RL* shunt calibration procedure based on the effective EMCC is generalized and demonstrated suitable for implementation in the commercial ANSYS® FE code. The calibration procedure includes the effects of the nonresonant vibration modes, which are assumed to contribute by flexibility and inertia effects. These nonresonant effects can be determined by solving three eigenvalue problems associated with SC and OC piezoceramic patch electrodes and when a shunt circuit consisting of an inductance is introduced. However, the latter eigenvalue problem is found unnecessary to evaluate in all desired cases where the effective EMCC, and thereby the attainable damping, is significant. An alternative method based on a quasi-static EMCC is also proposed which may be of interest for a tuning based on experiments and also when computational costs are a limiting factor in the numerical analysis. The optimum tuning formulae for parallel and series shunt circuits are based on a balanced calibration principle, where the roots in the pure inductive limit appear as inverse points with respect to the SC and OC frequencies, respectively.

In the numerical examples, a smart plate benchmark is analyzed for two patch pairs configurations, consisting of either a single centralized pair of piezoelectric patches or four decentralized, but symmetrically placed, patch pairs. A convergence study has been carried out, for the former configuration, to demonstrate that a precise numerical model is important in order to accurately determine the effective EMCC. The first eight vibration modes have then been analyzed with both patch designs and the optimum shunt circuit calibrations were determined for each individual mode. For the single patch pair design, nonvanishing damping was observed for three of the first eight vibration modes, while this increased to seven modes for the second design with four symmetric pairs. It has been demonstrated that the optimum shunt tuning causes a nearly flat plateau in the frequency response around the target resonant mode, when applying a representative modal harmonic load. Furthermore, the voltage response is found to have a completely flat (unit) plateau as dictated by the principle of equal modal damping. Finally, it was found that larger tuning values are required for the plate with four patch pairs shunted individually. However, by connecting the four pairs of patches in a single network, these tuning values can be reduced by a factor four since the modal charge increases by a factor sixteen. It is noted that close attention has to be given to the particular wiring of the patch pairs electrodes, according to the signs of the individual modal charges.

## Acknowledgment

This research has been supported by the Danish Council for Independent Research (Det Frie Forskningsråd) via the project "Resonant Piezoelectric Shunt Damping of Structures." The authors gratefully acknowledge this support.

## ORCID

Johan Frederik Toftekær  <http://orcid.org/0000-0003-1809-5063>

Ayech Benjeddou  <https://orcid.org/0000-0002-4760-4800>

Jan Høgsberg  <https://orcid.org/0000-0002-1098-3245>

## References

- [1] J. Høgsberg, and S. Krenk, "Calibration of piezoelectric RL shunts with explicit residual mode correction," *J. Sound Vib.*, vol. 386, pp. 65–81, 2017.
- [2] R. L. Forward, "Electronic damping of vibrations in optical structures," *Appl. Opt.*, vol. 18, no. 5, pp. 690–697, 1979.
- [3] N. W. Hagood, and A. von Flotow, "Damping of structural vibrations with piezoelectric materials and passive electrical networks," *J. Sound Vib.*, vol. 146, no. 2, pp. 243–268, 1991.
- [4] S. Y. Wu, "Piezoelectric shunts with a parallel R-L circuit for structural damping and vibration control," In *Proc. SPIE*, vol. 2720, pp. 259–269, 1996.
- [5] S. Krenk, and J. Høgsberg, "Tuned resonant mass or inerter-based absorbers: Unified calibration with quasi-dynamic flexibility and inertia correction," *Proc. Roy. Soc. A*, vol. 472, pp. 23 2016. Paper no. 20150718.
- [6] J. F. Toftekær, A. Benjeddou, J. Høgsberg, and S. Krenk, "Optimal piezoelectric RL shunt damping of plates with residual mode correction," *J. Intell. Mater. Syst. Struct.*, vol. 29, no. 16, pp. 3346–3370, 2018.
- [7] M. Trindade, and A. Benjeddou, "Effective electromechanical coupling coefficients of piezoelectric adaptive structures: critical evaluation and optimization," *Mech. Adv. Mat. Struct.*, vol. 16, no. 3, pp. 210–223, 2009.
- [8] A. Belloli, and P. Ermanni, "Optimum placement of piezoelectric ceramic modules for vibration suppression of highly constrained structures," *Smart Mater. Struct.*, vol. 16, no. 5, pp. 1662–1671, 2007.
- [9] M. Berardengo, O. Thomas, C. Giraud-Audine, and S. Manzoni, "Improved resistive shunt by means of negative capacitance: new circuit, performances and multi-mode control," *Smart Mater. Struct.*, vol. 25, pp. 23 2016. Paper no. 075033(23pp).
- [10] B. Lossouarn, M. Aucejo, J.-F. Deü, and B. Multon, "Design of inductors with high inductance values for resonant piezoelectric damping," *Sens. Act. A: Phys.*, vol. 259, pp. 68–76, 2017.
- [11] B. Lossouarn, J.-F. Deü, and G. Kerschen, "A fully passive nonlinear piezoelectric vibration absorber," *Phil. Trans. Roy. Soc. A*, vol. 376, 2018. Paper no. 2017014268 (16pp).
- [12] ANSYS 18.0 Documentation. ANSYS, Inc. Canonsburg, Pennsylvania, USA (2017)
- [13] J. F. Toftekær, A. Benjeddou, and J. Høgsberg, New piezoelectric shunt tuning method based on the effective electromechanical coupling coefficient: validation and 3D implementation. in *Proc. 7th Int. Symp. Aircraft Mater.*, A. Benjeddou and Z. Aboura, Eds., pp. 351–362, 2018.
- [14] A. Benjeddou, "Modal effective electromechanical coupling approximate evaluations and simplified analyses: numerical and experimental assessments," *Acta Mech.*, vol. 225, no. 10, pp. 2721–2742, 2014.
- [15] S. B. Choi, H. S. Kim, and J. S. Park, "Multi-mode vibration reduction of a CD-ROM drive base using a piezoelectric shunt circuit," *J. Sound Vib.*, vol. 300, no. 1-2, pp. 160–175, 2007.
- [16] B. Seba, J. Ni, and B. Ni Lohmann, "Vibration attenuation using a piezoelectric shunt circuit based on finite element method analysis," *Smart Mater. Struct.*, vol. 15, no. 2, pp. 509–517, 2006.
- [17] F. Bachmann, A. E. Bergamini, and P. Ermanni, "Optimum piezoelectric patch positioning: A strain energy-based finite element approach," *J. Intell. Mater. Syst. Struct.*, vol. 23, no. 14, pp. 1575–1591, 2012.

- [18] G. H. Golub, and C. F. van Loan, *Matrix Computations*. 2nd ed. Baltimore, MD: The Johns Hopkins University Press, 1989.
- [19] S. Krenk, "Frequency analysis of the tuned mass damper," *J. Appl. Mech.*, vol. 72, no. 6, pp. 936–942, 2005.
- [20] J. Høgsberg, and S. Krenk, "Balanced calibration of resonant shunt circuits for piezoelectric vibration control," *J. Intell. Mater. Syst. Struct.*, vol. 23, no. 17, pp. 1937–1948, 2012.
- [21] eFunda Portal *Lead Zirconate Titanate (PZT-5H)* (2017) (available: [http://www.efunda.com/materials/piezo/material\\_data/mat\\_data\\_output.cfm?Material\\_ID=PZT-5H](http://www.efunda.com/materials/piezo/material_data/mat_data_output.cfm?Material_ID=PZT-5H)).

## Appendix A. Identical and symmetrically placed pairs of piezoceramic patches

The proposed shunt tuning procedure and its implementation in ANSYS® for a single pair of patches are here extended to the case of several identical and symmetrically placed pairs of piezoceramic patches, whereby the optimum shunt tuning is the same for each pair of patches. The coupling vector  $\{k_{me}^E\}$  in Eq. (6) becomes a coupling matrix  $[k_{me}^E]$  with columns equal to the number of individually shunted patch pairs, while the scalar quantity  $C_p^E$  becomes a diagonal matrix  $\bar{C}_p^E [I_n]$  containing the identical capacitive properties. At last, the variables  $V$  and  $Q$  become vectors  $\{V\}$  and  $\{Q\}$  with entries equal to the number of shunted patch pairs. The SC eigenvalue problem is the same as for the single piezoceramic patch pair (Eq. 9), while the sensor equation is given as

$$\{Q_j\} = -[k_{me}^E]^t \{U\}_j \quad (\text{A1})$$

It is seen that the modal charge becomes a vector containing the individual modal charges for each shunted patch pair, which are now collected in the modal charge matrix

$$[Q]^t = [\{Q_1\} \quad \{Q_2\} \quad \cdots \quad \{Q_n\}] \quad (\text{A2})$$

The modal equations (21) and (22) are then, for  $n$  shunted pairs of patches and the  $r$ th mode, given as

$$(\omega_r^2 - \omega^2) v_r = \{Q_r\}^t \{V\} \quad (\text{A3})$$

$$\bar{C}_p^E [I_n] \{V\} - \{Q\} = -[Q]^t \{v\} \quad (\text{A4})$$

The right-hand side of Eq. (A4) is approximated similarly to Eq. (23) as

$$[Q]^t \{v\} = \{Q_r\} v_r + \left( C_r' - \frac{1}{\omega^2 L_r'} \right) [I_n] \{V\} \quad (\text{A5})$$

whereby the governing equation follows by eliminating  $\{Q_r\} v_r$  between Eqs. (A3) and (A5)

$$\left[ \left( \bar{C}_p^E + C_r' - \frac{1}{\omega^2 L_r'} \right) (\omega_r^2 - \omega^2) [I_n] + \{Q_r\} \{Q_r\}^t \right] \{V\} = \{Q\} (\omega_r^2 - \omega^2) \quad (\text{A6})$$

For identical and symmetrically placed patches, with respect to the deformation pattern of the target vibration mode, Eq. (A6) represents the number of shunt circuits  $n$  redundant equations given as

$$\left[ \left( \bar{C}_p^E + C_r' - \frac{1}{\omega^2 L_r'} \right) (\omega_r^2 - \omega^2) + n Q_r^2 \right] V = Q (\omega_r^2 - \omega^2) \quad (\text{A7})$$

in which  $Q_r^2$  is the common squared modal charge, while  $Q$  and  $V$  are the common circuit charges and electric potentials, respectively.

Finally, use of Ohm's law in Eq. (43) gives the characteristic equation

$$\left[ \frac{\omega^2}{\omega_r^2} - (1 + \kappa_r^2) \left( 1 - \frac{\kappa_r^2}{\kappa_e^2} \right) - i \omega \frac{1}{Z_{sh}(\omega) n Q_r^2} \kappa_r^2 \right] \left( 1 - \frac{\omega^2}{\omega_r^2} \right) + \kappa_r^2 \frac{\omega^2}{\omega_r^2} = 0 \quad (\text{A8})$$

which is similar to Eq. (44) but with  $n Q_r^2$  instead of  $Q_r^2$ . The effect on the individual shunt tunings is thus the factor  $n$  on the modal

charge  $Q_r^2$ , whereby the optimum shunt tunings are given as listed in Table 5.

## Appendix B. Determination of $\kappa_e^2$ from quadratic equation (25)

Initially, Eq. (25) is multiplied with  $-\hat{\omega}_r^2/C_r$ , whereby one obtains the quadratic equation

$$\left( -\hat{\omega}_r^2 + \frac{1}{C_r L_r'} \right) (\omega_r^2 - \hat{\omega}_r^2) - \hat{\omega}_r^2 \frac{Q_r^2}{C_r} = 0 \quad (\text{A9})$$

Division with  $\omega_r^4$  and using Eqs. (28)–(29), and (A9) transform above relation to

$$\left[ -\left( \frac{\hat{\omega}_r}{\omega_r} \right)^2 + \kappa_r^2 \lambda_r' \right] \left[ 1 - \left( \frac{\hat{\omega}_r}{\omega_r} \right)^2 \right] - \left( \frac{\hat{\omega}_r}{\omega_r} \right)^2 \kappa_r^2 = 0 \quad (\text{A10})$$

Now, after using Eq. (13), the characteristic equation is obtained in terms of the effective EMCC as

$$(1 + \kappa_e^2 - \kappa_r^2 \lambda_r') \kappa_e^2 - \kappa_r^2 (1 + \kappa_e^2) = 0 \quad (\text{A11})$$

Which can be written in a quadratic form as

$$(\kappa_e^2)^2 + (1 - \kappa_r^2 - \lambda_r' \kappa_r^2) \kappa_e^2 - \kappa_r^2 = 0 \quad (\text{A12})$$

This is a quadratic equation in  $\kappa_e^2$  that can be solved in order to find  $\kappa_e^2$  when both correction terms are included. However, it is of interest to find a solution that can be truncated for  $\lambda_r' \simeq 0$ . Thus, instead, Eq. (A12) is solved with respect to  $\Delta \kappa^2 = \kappa_e^2 - \kappa_r^2 \rightarrow 0$  for  $\lambda_r' \rightarrow 0$ . Using the former relation, the following holds

$$(\kappa_e^2)^2 = (\Delta \kappa^2 + \kappa_r^2)^2 = (\Delta \kappa^2)^2 + 2 \kappa_r^2 \Delta \kappa^2 + (\kappa_r^2)^2 \quad (\text{A13})$$

Then, elimination of  $\kappa_e^2$  between Eqs. (A12) and (A13) gives

$$(\Delta \kappa^2)^2 + (1 + \kappa_r^2 - \lambda_r' \kappa_r^2) \Delta \kappa^2 - (\kappa_r^2)^2 \lambda_r' = 0 \quad (\text{A14})$$

For  $\lambda_r' \rightarrow 0$ , Eq. (A14) reduces to

$$\Delta \kappa^2 = -(1 + \kappa_r^2) \quad \text{or} \quad \Delta \kappa^2 = 0 \quad (\text{A15})$$

while the full solution can be found as

$$\Delta \kappa^2 = \frac{1}{2} (1 + \kappa_r^2 - \lambda_r' \kappa_r^2) \left[ \sqrt{1 + \frac{4(\kappa_r^2)^2 \lambda_r'}{(1 + \kappa_r^2 - \lambda_r' \kappa_r^2)^2}} - 1 \right] \quad (\text{A16})$$

whereby the effective EMCC  $\kappa_e^2$  follows by Eq. (27).

## Appendix C. Derivation of characteristic equation (52) for series shunt connection

Initially, the series shunt circuit impedance  $Z_{sh}(\omega)$  in Eq. (51) is inserted in the characteristic equation (44), followed by the elimination of the inductance and resistance through the normalized inductance in Eq. (36) and electric damping parameter in Eq. (53). Thus, the characteristic equation (44) can hereby be written as

$$\left[ \left( \frac{\omega}{\omega_r} \right)^2 - (1 + \kappa_r^2) \left( 1 - \frac{\kappa_r^2}{\kappa_e^2} \right) + \omega^2 \frac{\lambda_r \kappa_r^2}{i \omega \rho_r^2 \lambda_r - \omega^2} \right] \left[ 1 - \left( \frac{\omega}{\omega_r} \right)^2 \right] + \kappa_r^2 \left( \frac{\omega}{\omega_r} \right)^2 = 0 \quad (\text{A17})$$

**Table 5.** Parallel and series shunt tuning for identical and symmetrically placed pairs of piezoceramic patches.

Parallel		Series	
$L = \frac{\kappa_e^2}{n Q_r^2}$	$R = \frac{\kappa_e^2 \omega_r}{n Q_r^2} \sqrt{\frac{1}{2 \kappa_e^2}}$	$L = \frac{\kappa_e^2}{n Q_r^2 (1 + \kappa_e^2)}$	$R = \frac{\kappa_e^2 \omega_r}{n Q_r^2} \sqrt{\frac{2 \kappa_e^2}{(1 + \kappa_e^2)^3}}$

The characteristic equation (A17) is now multiplied by  $(i\omega\rho_r^s\lambda_r - \omega^2)/\omega^2$  whereby the former, after using Eq. (39), can be written as

$$\left\{ i\left(\frac{\omega}{\omega_r}\right)\rho_r^s\frac{\lambda_r}{\omega_r}\left[1 - \left(\frac{\omega_r}{\omega}\right)^2(1 + \kappa_r^2)\left(1 - \frac{\kappa_r^2}{\kappa_g^2}\right)\right] + \lambda_r^*\kappa_r^2 - \left(\frac{\omega}{\omega_r}\right)^2 \right\} \left[1 - \left(\frac{\omega}{\omega_r}\right)^2\right] + i\left(\frac{\omega}{\omega_r}\right)\rho_r^s\frac{\lambda_r}{\omega_r}\kappa_r^2 - \kappa_r^2\left(\frac{\omega}{\omega_r}\right)^2 = 0 \quad (\text{A18})$$

Finally, the products in Eq. (A18) are expanded and this characteristic equation can be written as

$$\left(\frac{\omega}{\omega_r}\right)^4 - (1 + \kappa_r^2 + \lambda_r^*\kappa_r^2)\left(\frac{\omega}{\omega_r}\right)^2 + \lambda_r^*\kappa_r^2 + i\left(\frac{\omega}{\omega_r}\right)\rho_r^s\frac{\lambda_r}{\omega_r}\left[1 + \kappa_r^2 - \left(\frac{\omega}{\omega_r}\right)^2 - (1 + \kappa_r^2)\left(1 - \frac{\kappa_r^2}{\kappa_g^2}\right)\left(\frac{\omega_r^2}{\omega^2} - 1\right)\right] = 0 \quad (\text{A19})$$

In order to identify the inverse points relation, it is convenient to multiply Eq. (A19) by  $1/(1 + \kappa_g^2)^2$  and use the relation  $1/(1 + \kappa_g^2) = (\omega_r/\hat{\omega}_r)^2$  from Eq. (13). Hereby, the characteristic Eq. (A19) can be written as in Eq. (52).



P3

Multi-mode piezoelectric shunt damping with residual mode  
correction by evaluation of modal charge and voltage

Johan Frederik Toftekær and Jan Høgsberg

*Journal of Intelligent Material Systems and Structures*

Accepted, JIM-19-319



# Multi-Mode Piezoelectric Shunt Damping with Residual Mode Correction by Evaluation of Modal Charge and Voltage

Journal Title  
XX(X):1-15  
©The Author(s) 2016  
Reprints and permission:  
sagepub.co.uk/journalsPermissions.nav  
DOI: 10.1177/ToBeAssigned  
www.sagepub.com/

SAGE

Johan Frederik Toftekær<sup>1</sup> and Jan Høgsberg<sup>1</sup>

## Abstract

A resonant piezoelectric shunt tuning procedure is based on the limiting eigenvalue problems associated with short and open circuiting (SC and OC) of the piezoelectric domains attached to a vibrating structure. Whereas SC and OC frequencies are directly obtained from the eigenvalues, the associated electrical equation further determines a modal charge as an SC reaction force and a new modal voltage from the electric deflection in the OC limit. By a modal representation with SC mode shapes the structural equation fully decomposes, while the inherent contributions from non-resonant vibration modes in the corresponding electrical equation consistently define an effective modal capacitance, conveniently estimated by the modal charge to voltage ratio. The shunt tuning is obtained from the governing characteristic equation for the targeted vibration mode, in which the residual mode correction is explicitly represented by the effective modal capacitance. The tuning procedure with an effective modal capacitance is generalized to multiple piezoelectric domains with independent shunts for simultaneous damping of multiple vibration modes. The accuracy of the proposed shunt tuning methods is demonstrated by a numerical beam example with three piezoceramic patch pairs and independent resistive-inductive shunts. The analysis is carried out in a commercial finite element program, in which the required modal frequencies, charge and voltage are readily available as output to the SC and OC eigenvalue problems.

## Keywords

Piezoelectric shunt damping, resonant shunt calibration, residual mode correction, effective electromechanical coupling coefficient

## Introduction

Piezoelectric materials are characterized by their ability to couple mechanical strains and stresses with electrical fields and displacements. This property may be exploited for vibration mitigation of structures, by attaching piezoelectric transducers to the structure, whereby a fraction of the vibrational energy can be converted into electrical energy by the piezoelectric material and dissipated in an electric circuit or shunt wired between the two transducer electrodes.

A piezoelectric shunt may be composed in various designs by either passive (Hagood and von Flotow, 1991; Hollkamp, 1994; Wu, 1996, 1998), semi-active (de Marneffe and Preumont, 2008; Ducarne et al., 2010; Berardengo et al., 2016, 2018) or active (Anderson and Hagood, 1994; Preumont, 2011) electric circuits. The entirely passive piezoelectric shunt is attractive because of its independence of external power and unconditional stability. The simplest passive ( $R$ ) shunt is pure resistive, whereby the shunted piezoelectric material has viscoelastic properties (Hagood and von Flotow, 1991). The resonant shunt is obtained by adding an inductance ( $L$ ), designed to resonate with the inherent piezoelectric capacitance, as initially suggested and experimentally demonstrated by Forward (1979). A tuning procedure based on a single-mode approximation of the electromechanical structure has been derived for the series  $LR$ -shunt by Hagood and von Flotow (1991), with tuning formulas that explicitly depend on the inherent piezoelectric

capacitance. The optimal tuning for the corresponding parallel shunt is subsequently proposed by Wu (1996), while the series and parallel shunts have been compared in Park and Inman (1999) and Caruso (2001). Alternative methods for the optimum series and parallel shunt tuning has been suggested in Thomas et al. (2012); Yamada et al. (2010); Høgsberg and Krenk (2012); Soltani et al. (2014), all relying on modal truncation, whereby the inherent piezoelectric capacitance appears as a direct tuning parameter.

The main issue with the practical implementation of passive resonant shunt has traditionally been to obtain the high inductance values required for the damping of low-frequency vibrations. For experimental verification of shunt tuning methods, a so-called synthetic inductor therefore commonly emulates high inductance values (Fleming et al., 2000). A benefit of the synthetic inductor is that the emulated inductance is adjustable, whereby an exact prior inductance tuning is of less important.

<sup>1</sup>Department of Mechanical Engineering  
Technical University of Denmark  
Nils Koppels Allé, Building 404, DK-2800 Kgs. Lyngby, Denmark

## Corresponding author:

Johan F. Toftekær, Department of Mechanical Engineering  
Technical University of Denmark, Nils Koppels Allé, Building 404, DK-2800 Kgs. Lyngby, Denmark  
Email: jotof@mek.dtu.dk

A major drawback of the synthetic inductor is the use of operational amplifiers, requiring constant power sources. Because resonant shunts are often realized by such semi-active circuits with operational amplifiers, further active or semi-active improvements of the shunts has naturally been suggested, for instance by the design of a negative capacitance (de Marneffe and Preumont, 2008; Berardengo et al., 2016, 2018) or the use of switch damping (Ducarne et al., 2010). However, recently high inductance values have been obtained passively by winding a copper wire around a closed magnetic coil (Lossouarn et al., 2017), permitting the construction of pure passive resonant shunts and electrical circuit analogies (Lossouarn et al., 2018). Contrary to a synthetic inductor, this passive component requires a precise prior tuning to determine the exact number of wire winds, whereby it may be necessary to include the effect of non-resonant vibration modes to obtain a sufficiently accurate shunt tuning.

Recently, the inaccuracy associated with the traditional use of the inherent piezoelectric capacitance as a direct tuning parameter has been recognized. In Berardengo et al. (2016) the inherent capacitance of the piezoelectric material has thus been modified by the influence from higher vibration modes, while a theoretical study of the influence from an increasing number of vibration modes on the shunt tuning was provided in Gardonio and Casagrande (2017) for a simply supported plate. A Common denominator for these approaches is the inclusion and evaluation of additional resonant frequencies and mode shapes. In Krenk and Høgsberg (2016) this is avoided through the derivation of explicit expressions for the supplemental flexibility and inertia effects from the non-resonant vibration modes, thus explicitly correcting the tuning of tuned mass- and inerter-based absorbers. The equivalence to resonant piezoelectric shunt damping has subsequently been considered in Høgsberg and Krenk (2017), with Toftekær et al. (2018) proposing an expression for the frequency dependent effective capacitance, which incorporates a consistent residual mode correction. As full system mass and stiffness matrices are not necessarily available in commercial finite element (FE) software, an alternative shunt tuning method in Toftekær et al. (2019) relies on the so-called effective electromechanical coupling coefficient (EMCC) (IEEE inc., 1988) at resonance, limited by the short and open circuit (SC and OC) conditions for the piezoelectric material. The proposed tuning formulas have thus been based on the effective EMCC and a modal charge in the SC limit, which are readily accessible quantities in any FE software supporting electromechanical coupled analysis. However, for shunt tuning based on experimental measurements the method proposed in Toftekær et al. (2019) is less evident, since the modal charge assumes a particular normalization and the effective EMCC may be difficult to evaluate to a sufficient accuracy. Instead, the present paper provides a deeper insight to the influence of the non-resonant vibration modes, demonstrating that the optimum shunt tuning with residual mode correction may be determined from a modal charge and a modal voltage, obtained from the eigenvalue problems in the SC and OC conditions, respectively. Hereby the shunt tuning becomes independent of modal normalization and it is therefore suitable for both numerical and experimental

implementation. The novelty of the present single mode calibration method, compared to the method proposed in Toftekær et al. (2019), specifically concerns the inclusion of the modal voltage as a shunt tuning parameter, which also allows the direct evaluation of an effective modal capacitance that inherently contains the influence from the non-resonant vibration modes. Furthermore, the present tuning method is derived for an arbitrary number of piezoelectric shunts, whereby the method is readily extended to multi-mode damping through the individual tuning of several shunted piezoelectric domains (absorbers).

The paper is structured in four main sections. In the section **Discrete vibration problem** the general electromechanical discrete vibration problem is presented, for which the SC and OC limits are considered. The OC resonant frequencies are inherently larger than the corresponding SC frequencies, due to the stiffening by the capacitance of the piezoelectric material. The traditional modal assumption states this stiffening effect to be inversely proportional to the inherent piezoelectric capacitance, while the exact stiffening, including non-resonant modal interaction, may be represented by an effective modal capacitance, evaluated directly from the stored modal charge in the SC condition and the modal voltage in the OC condition. Hereby, the governing characteristic equation for a representative 2-dof modal system of the full electromechanical structure is obtained and used in the section **Single-mode calibration** to determine the optimum single-mode calibration of multiple piezoelectric absorbers. In the section **Multi mode calibration** the effect of having piezoelectric absorbers tuned to simultaneously suppress several resonant vibrations is investigated and two methods for the optimum shunt calibration are proposed. The former considers the effect of the piezoelectric absorbers tuned to other vibration modes to be insignificant, whereby the optimum tuning to any resonant vibration mode may be evaluated from the same SC and OC eigenvalue problems and a modified effective EMCC. An enhanced method also includes the influence from the piezoelectric absorbers tuned to other vibration modes by considering them either in their SC or OC condition. Finally, in the section **Numerical example** the single-mode and two multi-mode shunt tuning methods are analyzed and compared by a numerical example concerning a simply supported beam with three pairs of shunted piezoceramic patches.

## Discrete vibration problem

In the present section, the coupled vibration problem considered in Toftekær et al. (2019) for a single piezoelectric absorber is generalized to a vibrating structure with  $i = 1, 2, \dots, N_p$  piezoelectric domains and independent shunts  $Z_i$ , see Figure 1. When discretized by finite elements (FE) the vibration problem may be written according to (Toftekær et al., 2019) as

$$\left( \begin{bmatrix} K^E & k_{me}^E \\ (k_{me}^E)^t & -C_p \end{bmatrix} - \omega^2 \begin{bmatrix} M & 0 \\ 0 & 0 \end{bmatrix} \right) \begin{Bmatrix} U \\ V \end{Bmatrix} = \begin{Bmatrix} 0 \\ -Q \end{Bmatrix} \quad (1)$$

Here  $[K^E]$  is the elastic stiffness matrix for the structure with SC piezoelectric electrodes ( $Z_i = 0$ ), while  $[M]$  is the mass matrix. The coupling between the mechanical and

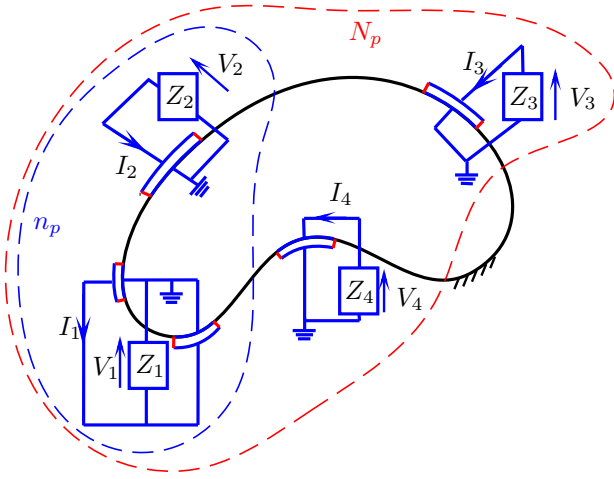


**Figure 1.** Vibrating structure with attached piezoelectric domains and  $N_p = 4$  independent shunts (red dashed).

the electrical domains is governed by the coupling matrix  $[k_{me}^E]$  with rows equal to the number of mechanical degrees of freedom (dofs) and columns equal to the number of independent piezoelectric shunts  $N_p$ , while  $(\dots)^t$  represents the transpose operation.

A piezoelectric shunt may be wired to several piezoelectric domains and act as a single resulting piezoelectric absorber, as long as two interface electrodes can be defined, where one is grounded for practical reasons, see Figure 1. The electrical domain is described by a diagonal matrix  $[C_p]$  containing the resulting modified blocked capacitance  $(\bar{C}_p^{\epsilon^s})_i$  for each piezoelectric absorber (Toftækær et al., 2019). The total number of dofs in the discrete system is given by the mechanical displacements in  $\{U\}$  and the voltages in  $\{V\}$  between each pair of grounded and non-grounded electrodes. Finally, the vector  $\{Q\}$  contains the stored electric charge on each of the non-grounded electrodes, while the corresponding time-derivative provides the flow of current represented in the frequency domain as

$$I_i = -i\omega Q_i \quad (2)$$

and shown in Figure 1 between each pair of grounded and non-grounded electrodes, with  $i = \sqrt{-1}$  denoting the imaginary unit.

### Electromechanical coupling

The influence of the piezoelectric absorbers on the vibrating structure is characterized by two limiting eigenvalue problems associated with SC and OC piezoelectric electrodes.

The SC condition is defined by zero voltage between the piezoelectric electrodes ( $Z_i = 0$ ), for which the current is free to flow. The corresponding eigenvalue problem thus follows from  $\{V\} = \{0\}$  in (1),

$$([K^E] - \omega_j^2[M])\{U_j\} = \{0\} \quad (3)$$

where  $\omega_j$  is the SC frequency and  $\{U_j\}$  the corresponding SC mode shape vector of vibration mode  $j$ . The second

equation in (1) provides a stored modal charge on each non-grounded electrode as

$$\{Q_j\} = -[k_{me}^E]^t\{U_j\} \quad (4)$$

which may be determined from (2) when the electric current is measured for the SC piezoelectric absorbers bonded to a structure vibrating in resonant mode  $j$ . Assuming harmonic oscillations with SC frequency  $\omega_j$ , the magnitude of the stored modal charge may alternatively be determined by the corresponding flow of current  $\{Q_j\} = \{I_j\}/(i\omega_j)$  from (2).

In the opposite OC condition, no current flows between the piezoelectric electrodes ( $Z_i \rightarrow \infty$  in Figure 1), equivalent to vanishing charge. The OC eigenvalue problem thus follows from (1) with  $\{Q\} = \{0\}$ , conveniently formulated as

$$\left([K^E] + [k_{me}^E][C_p]^{-1}[k_{me}^E]^t - \hat{\omega}_j^2[M]\right)\{\hat{U}_j\} = \{0\} \quad (5)$$

where  $\{V\}$  has been eliminated by the second equation in (1). In (5),  $\hat{\omega}_j$  and  $\{\hat{U}_j\}$  are respectively the OC frequency and mode shape of vibration mode  $j$ . The second equation of the discrete system in (1) determines the corresponding modal electric response, which in this case is given by a modal voltage between each pair of grounded and non-grounded electrodes

$$\{\hat{V}_j\} = [C_p]^{-1}[k_{me}^E]^t\{\hat{U}_j\} \quad (6)$$

This has not been considered previously for shunt tuning and may be directly measured over the OC piezoelectric absorbers bonded to a structure vibrating in resonant mode  $j$ .

In the remainder of the present paper, a similar normalization of the SC  $\{U_j\}$  and OC  $\{\hat{U}_j\}$  mode shape vectors is assumed, for instance by normalizing the mode shapes to unit modal mass.

The rate of convertible energy by the piezoelectric domains may now be determined for a resonant mode  $j$  by the effective EMCC, defined as the relative difference between the squared SC and OC frequencies,

$$\kappa_j^2 = \frac{\hat{\omega}_j^2 - \omega_j^2}{\omega_j^2} \quad (7)$$

It is noted that  $\hat{\omega}_j^2 \geq \omega_j^2$  due to the quadratic projection of the coupling matrix  $[k_{me}^E]$  on the capacitance matrix  $[C_p]$  in (5). Thus, the effective EMCC is also a measure of the relative stiffness increase by the OC piezoelectric domains on the vibrating structure. The effective EMCC may alternatively be determined by considering the OC eigenvalue problem (5) multiplied with the SC mode shape  $\{U_j\}^t$ ,

$$\{U_j\}^t[K^E]\{\hat{U}_j\} + \{U_j\}^t[k_{me}^E][C_p]^{-1}[k_{me}^E]^t\{\hat{U}_j\} - \hat{\omega}_j^2\{U_j\}^t[M]\{\hat{U}_j\} = \{0\} \quad (8)$$

After division with an intermediate modal mass,

$$\tilde{m}_j = \{U_j\}^t[M]\{\hat{U}_j\} \quad (9)$$

and introduction of the SC modal charge (4) and the OC modal voltage (6), the equation (8) can be written as

$$\omega_j^2 - \frac{\{Q_j\}^t\{\hat{V}_j\}}{\tilde{m}_j} - \hat{\omega}_j^2 = 0 \quad (10)$$

Considering the relation between the SC and OC resonant frequencies defined by (7), it is found from (10) that the effective EMCC can alternatively be determined as

$$\kappa_j^2 = -\frac{\{Q_j\}^t \{\hat{V}_j\}}{\tilde{m}_j \omega_j^2} \quad (11)$$

This expression for the effective EMCC is conveniently used in the following, where a modal decomposition of the general vibration problem (1) is considered. It is noted that the combined modal projection used here is proposed as basis for a modal reduction technique in Larbi and Deü (2019), which is found to improve the response accuracy compared to traditional modal reduction methods. This result is in a agreement with the findings in the subsequent section **Modal equations**, in which the influence from the non-resonant vibration modes is included through the combined modal projection.

### Modal equations

The general vibration problem (1) may be decoupled by introducing a modal representation with the SC mode shapes of the mechanical vibrations  $\{U\} = [U]\{v\}$ , where the matrix  $[U]$  contains  $\{U_j\}$  as columns and  $\{v\}$  represents the  $N$  modal coordinates  $v_j$ . Introducing this modal representation into (1) and multiplying with the transpose of the SC mode shapes  $[U]^t$ , the vibration problem (1) can be written as

$$\begin{aligned} [U]^t ([K^E] - \omega^2 [M]) [U] \{v\} + [U]^t [k_{me}^E] \{V\} &= \{0\}, \\ [k_{me}^E]^t [U] \{v\} - [C_p] \{V\} &= -\{Q\} \end{aligned} \quad (12)$$

The top set of mechanical equations in (12) uncouple and may for vibration mode  $j$  be written as

$$(\omega_j^2 - \omega^2) v_j - \frac{\{Q_j\}^t}{m_j} \{V\} = 0, \quad j = 1, 2, \dots, N \quad (13)$$

where  $\{Q_j\}$  has been introduced as in (4). Each of the bottom  $N_p$  electric equations in (12) still depends on the full range of modal coordinates  $v_j$ ,

$$\sum_{j=1}^N \{Q_j\} v_j = \{Q\} - [C_p] \{V\} \quad (14)$$

It is inconvenient to evaluate the full range of modal coefficients and charge components. Thus, a modal approximation of the left hand-side in (14) is introduced. In order to maintain the accuracy of the model, the effect of the non-resonant modes is included and subsequently approximated around a target resonant mode  $j = r$  by e.g. a flexibility and an inertia correction term according to (Krenk and Høgsberg, 2016). In Toftekar et al. (2018), these flexibility and inertia effects have been demonstrated to correspond to a capacitance and an inductance, respectively, altering the resulting modified blocked capacitance  $\tilde{C}_p^{\epsilon^S}$  at resonance. In the present analysis, this additional capacitance from the non-resonant vibration modes is determined by considering the SC and OC limits.

It follows from the modal equation (13) that  $v_j$  is proportional to the voltage vector  $\{V\}$ , whereby the sum

over the non-resonant vibration modes in (14) contributes with an additional term to the blocked capacitance,

$$\begin{aligned} \{Q_r\} v_r &= \{Q\} - \left( [C_p] + \sum_{j \neq r}^N \frac{\{Q_j\} \{Q_j\}^t}{m_j \omega_j^2} \frac{\omega_j^2}{\omega_j^2 - \omega^2} \right) \{V\} \\ &= \{Q\} - [C_r] \{V\} \end{aligned} \quad (15)$$

in which the introduced matrix  $[C_r]$  is assumed diagonal, deliberately ignoring any coupling effects from the summation inside the parenthesis. Hereby the diagonal of  $[C_r]$  contains the effective modal capacitance around the target vibration mode  $r$ , for each piezoelectric absorber.

The modal coefficient for target mode  $r$  may be determined from (15) by multiplying with the modal voltage  $\{\hat{V}_r\}^t$  and then dividing with the scalar product  $\{\hat{V}_r\}^t \{Q_r\}$ ,

$$v_r = \frac{\{\hat{V}_r\}^t}{\{\hat{V}_r\}^t \{Q_r\}} \{Q\} - \frac{\{\hat{V}_r\}^t [C_r]}{\{\hat{V}_r\}^t \{Q_r\}} \{V\} \quad (16)$$

This target modal coordinate  $v_r$  may now be inserted into (13), whereby a governing modal equation is obtained as

$$\begin{aligned} (\omega_r^2 - \omega^2) \left( \frac{\{\hat{V}_r\}^t \{Q\}}{\{\hat{V}_r\}^t \{Q_r\}} - \frac{\{\hat{V}_r\}^t [C_r] \{V\}}{\{\hat{V}_r\}^t \{Q_r\}} \right) \\ - \frac{\{Q_r\}^t \{V\}}{m_r} = 0 \end{aligned} \quad (17)$$

The impedance relation for each shunt is then introduced as

$$\{V\} = -i\omega [Z(\omega)] \{Q\} \quad (18)$$

where  $[Z(\omega)]$  is a diagonal matrix containing the impedance  $Z_i(\omega)$  for shunt  $i$  in the diagonal. The impedance relation (18) is used in (17) to eliminate  $\{Q\}$ , whereby it can be written in homogeneous form,

$$\begin{aligned} (\omega_r^2 - \omega^2) \left( \frac{\{\hat{V}_r\}^t [Z(\omega)]^{-1} \{V\}}{i\omega \{\hat{V}_r\}^t \{Q_r\}} + \frac{\{\hat{V}_r\}^t [C_r] \{V\}}{\{\hat{V}_r\}^t \{Q_r\}} \right) \\ + \frac{\{Q_r\}^t \{V\}}{m_r} = 0 \end{aligned} \quad (19)$$

The expression inside the square brackets constitutes  $N_p$  independent characteristic equations, since both  $[Z(\omega)]$  and  $[C_r]$  are diagonal matrices. The independent equation for a piezoelectric shunt  $i$  may therefore be written as

$$\begin{aligned} (\omega_r^2 - \omega^2) \left( \frac{(\hat{V}_r)_i}{i\omega Z_i(\omega) \{\hat{V}_r\}^t \{Q_r\}} + \frac{(\hat{V}_r)_i (C_r)_i}{\{\hat{V}_r\}^t \{Q_r\}} \right) \\ + \frac{(Q_r)_i}{m_r} = 0 \end{aligned} \quad (20)$$

The effective capacitances  $(C_r)_i$  for the targeted resonant mode  $r$  may now be determined from (20) in the OC limit ( $Z_i(\omega) \rightarrow \infty$ ), at which it reduces to

$$(\omega_r^2 - \hat{\omega}_r^2) \frac{(\hat{V}_r)_i (C_r)_i}{\{\hat{V}_r\}^t \{Q_r\}} + \frac{(Q_r)_i}{m_r} = 0 \quad (21)$$

when  $\omega = \hat{\omega}_r$  has been introduced. The relation between the SC and OC resonant frequencies may then be introduced by the previous expression for the effective EMCCs in (7) or (11). Hereby, shunt  $i$ 's effective modal capacitance  $(C_r)_i$  for the targeted mode  $r$  is determined from (21) as

$$\begin{aligned} (C_r)_i &= \frac{\{\hat{V}_r\}^t \{Q_r\}}{m_r \omega_r^2} \frac{\omega_r^2}{\hat{\omega}_r^2 - \omega_r^2} \frac{(Q_r)_i}{(\hat{V}_r)_i} \\ &= -\frac{(Q_r)_i \tilde{m}_r}{(\hat{V}_r)_i m_r} \simeq -\frac{(Q_r)_i}{(\hat{V}_r)_i} \end{aligned} \quad (22)$$

where the last approximation  $\tilde{m}_r \simeq m_r$  is valid for most practical problems with limited electromechanical coupling. Furthermore, it should be noted that the minus in the effective capacitance expression requires that the distribution of negative and positive displacements of the SC and OC mode shapes is the same, whereby  $(Q_r)_i$  and  $(\hat{V}_r)_i$  always have opposite signs. This may be circumvented by simply introducing absolute values of both  $|Q_r|_i$  and  $|\hat{V}_r|_i$ , as applied later.

The effective capacitance, comprising both the resulting blocked capacitance and any contributions from non-resonant vibration modes, is found to be accurately approximated by the absolute value of the SC modal charge  $|Q_r|_i$  divided by the OC modal voltage  $|\hat{V}_r|_i$ . The effective capacitance (22) also implies an alternative definition of the effective EMCC, for the  $r$ -th mode, obtained by elimination of  $\{\hat{V}_j\}$  in (11),

$$\kappa_r^2 = \frac{\{Q_r\}^t [C_r]^{-1} \{Q_r\}}{m_r \omega_r^2} \quad (23)$$

This expression for the effective EMCC is similar to the often used modal EMCC (Park and Inman, 1999) without non-resonant mode contributions, where the resulting blocked capacitance  $[C_p]$  is here simply replaced by the effective capacitance  $[C_r]$ .

Finally, the characteristic equation for target mode  $r$ , represented by the square brackets in (19), may be rewritten, after using (23), by multiplication, from the right with  $[C_r]^{-1} \{Q_r\}$  and  $\omega^2/\omega_r^4$ ,

$$\begin{aligned} \left(1 - \frac{\omega^2}{\omega_r^2}\right) \left(\frac{\omega^2}{\omega_r^2} - i \frac{\omega}{\omega_r} \frac{\{\hat{V}_r\}^t [Z(\omega)]^{-1} [C_r]^{-1} \{Q_r\}}{\{\hat{V}_r\}^t \{Q_r\} \omega_r}\right) \\ + \kappa_r^2 \frac{\omega^2}{\omega_r^2} = 0 \end{aligned} \quad (24)$$

In the following sections, this characteristic equation (24) is used to obtain optimum single- and multi-mode shunt calibration by inserting the respective shunt impedances and compare the corresponding characteristic equations with the generic equation from (Krenk and Høgsberg, 2013),

$$\frac{\omega^4}{\omega_r^4} - (2 + 4\chi^2) \frac{\omega^2}{\omega_r^2} + 1 + 4i\lambda\chi \frac{\omega}{\omega_r} \left(1 - \frac{\omega^2}{\omega_r^2}\right) = 0 \quad (25)$$

This generic equation ensures equal modal damping through the tuning of the shunt inductance  $L$ , while the subsequent tuning of the shunt resistance  $R$  by  $\lambda = 1/\sqrt{2}$  balances large attainable damping and effective vibration amplitude mitigation. It finally follows from (Krenk and Høgsberg, 2013)

that the damping ratio for the target mode  $r$  can be estimated as

$$\zeta_r \simeq \lambda\chi = \sqrt{\frac{1}{2}\chi^2} \quad (26)$$

where  $\chi^2$  is proportional to the effective EMCC (Høgsberg and Krenk, 2012), as also demonstrated in the following.

### Single-mode calibration

This section presents the tuning of  $N_p$  independent piezoelectric absorbers to a single target vibration mode  $r$ . The corresponding characteristic equation is given by (24), in which the term depending on the impedance and capacitance may be replaced by a sum over the  $N_p$  absorbers tuned to mode  $r$ . When inserting the effective capacitances (22), the characteristic equation (24) can be written as

$$\begin{aligned} \left(1 - \frac{\omega^2}{\omega_r^2}\right) \left(\frac{\omega^2}{\omega_r^2} + i\omega \sum_{i=1}^{N_p} \frac{(\hat{V}_r)_i (Q_r)_i}{\{\hat{V}_r\}^t \{Q_r\}} \frac{(\hat{V}_r)_i}{Z_i(\omega) (Q_r)_i \omega_r^2}\right) \\ + \kappa_r^2 \frac{\omega^2}{\omega_r^2} = 0 \end{aligned} \quad (27)$$

The optimum tuning for the parallel and series shunts is then derived by introducing the corresponding impedances into (27) followed by comparison with the generic equation (25) to obtain the balanced calibration principle for resonant absorbers (Krenk and Høgsberg, 2013).

### Parallel shunt tuning

The parallel shunt impedance  $Z_i = Z_i^p$  is conveniently expressed in terms of the inverse shunt inductance and resistance for shunt  $i$  as (superscript  $p$  refers to parallel)

$$\frac{1}{Z_i^p(\omega)} = \frac{1}{R_i^p} + \frac{1}{i\omega L_i^p} \quad (28)$$

When inserting this parallel shunt impedance, the characteristic equation (27) can be written in accordance with the generic form (25) as

$$\begin{aligned} \frac{\omega^4}{\omega_r^4} - \left(1 + \kappa_r^2 - \sum_{i=1}^{N_p} \frac{(\hat{V}_r)_i (Q_r)_i}{\{\hat{V}_r\}^t \{Q_r\}} \frac{1}{L_i^p (Q_r)_i \omega_r^2}\right) \frac{\omega^2}{\omega_r^2} \\ - \sum_{i=1}^{N_p} \frac{(\hat{V}_r)_i (Q_r)_i}{\{\hat{V}_r\}^t \{Q_r\}} \frac{1}{L_i^p (Q_r)_i \omega_r^2} \\ - i \frac{\omega}{\omega_r} \sum_{i=1}^{N_p} \frac{(\hat{V}_r)_i (Q_r)_i}{\{\hat{V}_r\}^t \{Q_r\}} \frac{1}{R_i^p (Q_r)_i \omega_r} \left(1 - \frac{\omega^2}{\omega_r^2}\right) = 0 \end{aligned} \quad (29)$$

Comparison with (25) requires a unit constant term in (29), which is only secured by the inductance

$$L_i^p = -\frac{(\hat{V}_r)_i}{(Q_r)_i \omega_r^2} \quad (30)$$

since the first fraction inside the summation of the constant term in (29) sums to unity. It is seen that (30) corresponds

to the traditional modal inductance tuning  $L_i^p(C_r)_i\omega_r^2 = 1$  with the effective modal capacitance  $(C_r)_i$  replacing the inherent blocked capacitance  $C_p^{\epsilon_s}$ . The influence of using the new effective modal instead of the blocked capacitance for the optimum shunt tuning is analyzed in the section **Numerical example**.

When all  $N_p$  inductances are optimally tuned, the parameter  $\chi$  can be identified as  $\chi^2 = \kappa_r^2/4$  from comparison of the quadratic terms, whereafter the shunt resistances are determined by comparing the common factor to the odd-power terms in (25) and (29),

$$R_i^p = -\frac{(\hat{V}_r)_i}{(Q_r)_i\omega_r} \sqrt{\frac{1}{2\kappa_r^2}} \quad (31)$$

It is noted that the minus signs in the tuning formulas (30) and (31) appear because of the implied opposite signs between  $(Q_r)_i$  and  $(\hat{V}_r)_i$ , as discussed previously. This may be circumvented by simply using the corresponding absolute values, whereby the tuning formulas can be written as presented in the first row of **Table 1**.

### Series shunt tuning

The series impedance  $Z_i = Z_i^s$  for shunt  $i$  is given as (superscript  $s$  refers to series)

$$Z_i^s(\omega) = R_i^s + i\omega L_i^s \quad (32)$$

The impedances in the characteristic equation (27) are replaced by the series impedances (32) and the characteristic equation may then be written in accordance with the generic form (25),

$$\begin{aligned} \frac{\omega^4}{\hat{\omega}_r^4} - \left( 1 - \sum_{i=1}^{N_p} \frac{\{\hat{V}_r\}^t\{Q_r\}}{(\hat{V}_r)_i(Q_r)_i} \frac{1}{L_i^s} \frac{(\hat{V}_r)_i}{(Q_r)_i\hat{\omega}_r^2} \right) \frac{\omega^2}{\hat{\omega}_r^2} \\ - \sum_{i=1}^{N_p} \frac{\{\hat{V}_r\}^t\{Q_r\}}{(\hat{V}_r)_i(Q_r)_i} \frac{1}{L_i^s} \frac{(\hat{V}_r)_i}{(Q_r)_i\hat{\omega}_r^2(1+\kappa_r^2)} \\ + i\frac{\omega}{\hat{\omega}_r} \frac{\sum_{i=1}^{N_p} (Q_r)_i^2 R_i^s}{\sum_{i=1}^{N_p} (Q_r)_i^2 L_i^s \hat{\omega}_r} \left( 1 - \frac{\omega^2}{\hat{\omega}_r^2} \right) = 0 \end{aligned} \quad (33)$$

expressed relative to the OC resonance frequency  $\hat{\omega}_r$ . For a detailed derivation of (33), see **Appendix I**. As for the parallel shunt the characteristic equation (33) is now compared with the generic equation (25), whereby the optimum series inductance is determined as

$$L_i^s = -\frac{(\hat{V}_r)_i}{(Q_r)_i\hat{\omega}_r^2(1+\kappa_r^2)} = -\frac{(\hat{V}_r)_i}{(Q_r)_i\hat{\omega}_r^2} \frac{\omega_r^2}{\hat{\omega}_r^2} \quad (34)$$

ensuring that the constant term in (33) becomes unity.

The parameter  $\chi^2 = \kappa_r^2/4$  is the same as for the parallel shunt. The optimum tuning of the series resistance follows by inserting the series inductances (34) into (33) and then comparing the odd-term factors in (25) and (33), which gives

$$R_i^s = -\frac{(\hat{V}_r)_i}{(Q_r)_i\hat{\omega}_r(1+\kappa_r^2)} \sqrt{2\kappa_r^2} = -\frac{(\hat{V}_r)_i}{(Q_r)_i\hat{\omega}_r} \frac{\omega_r^2}{\hat{\omega}_r^2} \sqrt{2\kappa_r^2} \quad (35)$$

The optimum series shunt tuning is also summarized in the first row of **Table 1**, which also defines the effective EMCC and the attainable damping ratio  $\zeta_r$  from (26).

## Multi mode calibration

This section presents simultaneous damping of multiple vibration modes. Each piezoelectric absorber is still considered to be optimally tuned to a single target vibration mode. This implies that a reduced number of absorbers  $n_p$  is tuned to a specific target mode  $r$ , whereby  $n_p$  becomes a subset of the total number of absorbers  $N_p$ , as indicated by the blue dashed group in **Figure 1**.

### Modified single-mode calibration

When  $n_p \leq N_p$ , the single-mode calibration presented in the section **Single-mode calibration** will not provide the optimum resonant tuning with respect to mode  $r$ , mainly because the effective EMCC in (7) includes all  $N_p$  piezoelectric absorbers. The tuning of the shunt inductances (30) and (34) are both independent of the effective EMCC. Hence, the inaccuracy of the single-mode calibration used on a subset of the piezoelectric absorbers  $n_p$  mainly concerns the tuning of the shunt resistances in (31) and (35), which causes an apparent decrease in the attainable damping  $\zeta_r$ . By comparing the common factor to the odd-power terms in the characteristic equations (29) and (33) with the generic equation (25) it can be found that the damping ratio  $\zeta_r$  from (26) is reduced by  $\sum_{i=1}^{n_p} (\hat{V}_r)_i (Q_r)_i$  for the  $n_p$  absorbers relative to the total amount  $\{\hat{V}_r\}^t\{Q_r\}$  for all  $N_p$  absorbers,

$$\zeta_r = \sum_{i=1}^{n_p} \frac{(\hat{V}_r)_i (Q_r)_i}{\{\hat{V}_r\}^t\{Q_r\}} \sqrt{\frac{1}{8}\kappa_r^2} \quad (36)$$

This reduction in attainable damping may be circumvented without additional computational costs by instead evaluating a modified effective EMCC, which only includes the subset of piezoelectric absorbers  $n_p$  tuned to the target mode  $r$ . This modified effective EMCC  $\tilde{\kappa}_r^2$  follows from (11) as

$$\tilde{\kappa}_r^2 = -\sum_{i=1}^{n_p} \frac{(Q_r)_i (\hat{V}_r)_i}{\tilde{m}_r \omega_r^2} = \sum_{i=1}^{n_p} \frac{(Q_r)_i (\hat{V}_r)_i}{\{Q_r\}^t\{\hat{V}_r\}} \kappa_r^2 \quad (37)$$

which is the original effective EMCC scaled by the same factor that in (36) reduces the damping ratio. The tilde (...) will in the following refer to this modified single-mode calibration of the reduced  $n_p$  shunts. From this modified effective EMCC, an enhanced resistance tuning is then simply obtained by replacing the effective EMCC  $\kappa_r^2$  in (31) and (35) with its modified counter-part  $\tilde{\kappa}_r^2$ . The modified single-mode tuning formulas are provided in the second row of **Table 1** and used for multi-mode damping in the numerical example in the section **Numerical example**.

The single-mode and modified single-mode calibrations are now compared in a root-locus diagram obtained by evaluating the full eigenvalue problem (1), with  $\{Q\}$  eliminated by the parallel shunt impedances in (28), for the simply supported beam considered in the numerical example of the section **Numerical example**. The eigenvalue problems are established and evaluated using the in-house FE-code developed and described in **Toftekær et al. (2018)**. In **Figure 2**, the roots around the first three resonant frequencies of the simply supported beam are plotted for varying resistance values, when each shunt circuit is tuned to a single target mode, as outlined in

**Table 1.** Optimum parallel and series single-mode, modified single-mode and multi-mode calibration for shunt  $i$  tuned with respect to target mode  $r$  and the corresponding effective EMCCs and damping ratios.

Method	Inductance		Resistance		EMCC	Damping
	$L_i^p$	$L_i^s$	$R_i^p$	$R_i^s$	$\kappa_r^2$	$\zeta_r$
Single	$\frac{ \hat{V}_r _i}{ Q_r _i \omega_r^2}$	$\frac{ \hat{V}_r _i}{ Q_r _i \hat{\omega}_r^2} \frac{\omega_r^2}{\hat{\omega}_r^2}$	$\frac{ \hat{V}_r _i}{ Q_r _i \omega_r} \sqrt{\frac{1}{2\kappa_r^2}}$	$\frac{ \hat{V}_r _i}{ Q_r _i \hat{\omega}_r} \frac{\omega_r^2}{\hat{\omega}_r^2} \sqrt{2\kappa_r^2}$	$\frac{\hat{\omega}_r^2 - \omega_r^2}{\omega_r^2}$	$\sqrt{\frac{1}{8\kappa_r^2}}$
Modified	$\frac{ \hat{V}_r _i}{ Q_r _i \omega_r^2}$	$\frac{ \hat{V}_r _i}{ Q_r _i \hat{\omega}_r^2} \frac{\omega_r^2}{\hat{\omega}_r^2}$	$\frac{ \hat{V}_r _i}{ Q_r _i \omega_r} \sqrt{\frac{1}{2\kappa_r^2}}$	$\frac{ \hat{V}_r _i}{ Q_r _i \hat{\omega}_r} \frac{\omega_r^2}{\hat{\omega}_r^2} \sqrt{2\kappa_r^2}$	$\sum_{i=1}^{n_p} \frac{(Q_r)_i (\hat{V}_r)_i}{\{Q_r\}^t \{\hat{V}_r\}} \kappa_r^2$	$\sqrt{\frac{1}{8\kappa_r^2}}$
Multiple	$\frac{ \hat{V}_r _i}{ Q_r _i \omega_r^2}$	$\frac{ \hat{V}_r _i}{ Q_r _i \hat{\omega}_r^2} \frac{\omega_r^2}{\hat{\omega}_r^2}$	$\frac{ \hat{V}_r _i}{ Q_r _i \omega_r} \sqrt{\frac{1}{2\kappa_r^2}}$	$\frac{ \hat{V}_r _i}{ Q_r _i \hat{\omega}_r} \frac{\omega_r^2}{\hat{\omega}_r^2} \sqrt{2\kappa_r^2}$	$\frac{\hat{\omega}_r^2 - \omega_r^2}{\omega_r^2}$	$\sqrt{\frac{1}{8\kappa_r^2}}$

the section **Three-modes damping**. The single-mode and modified single-mode methods (black and red dots) are seen to follow the same root trajectories, which almost describe a semi-circle in the complex plane, indicating that the common inductance calibrations are close to optimum with equal modal damping. However, the optimum resistance tuning is seen to be off for the single-mode calibration (black crosses), as one of the two complex roots approaches the real axis along the right trajectory in **Figure 2**. The modified resistance tuning (red crosses) is however seen to be in better agreement with the balanced calibration principle (Krenk and Høgsberg, 2013), with roots approximately placed on  $\pm 45^\circ$  lines from the respective undamped SC frequencies.

Although the enhanced resistance tuning in many cases will provide an almost optimum resonant shunt tuning and a flat plateau in the frequency response curve around the target resonant frequency, it is not the exact optimum tuning, since the modal charge and voltage and the corresponding SC and OC frequencies are influenced by the effect of the piezoelectric absorbers not tuned with respect to target mode  $r$ , whereby the trajectories (with black and red dots) in **Figure 2** do not meet at a bifurcation point. This modal interaction is neglected when simply using the modified effective EMCC in (37). A more precise shunt tuning may thus be obtained by reevaluating the SC and OC eigenvalue problems, in which the piezoelectric absorbers not tuned to mode  $r$  are included either in their SC or OC state, depending on whether they are targeted to a mode  $j$  above or below  $r$ .

### Multi-mode calibration with non-resonant absorbers

In the modified single-mode calibration, the influence from the piezoelectric absorbers not tuned with respect to mode  $r$  is assumed negligible, whereby the governing SC and OC eigenvalue problems may be represented by (3) and (5) with all  $N_p$  piezoelectric domains jointly in SC and OC conditions, respectively. However, the influence from the piezoelectric absorbers not tuned with respect to mode  $r$  may instead be included by considering them in either SC or OC condition, depending on whether an individual shunt targets a mode below or above the present tuning mode  $r$ .

By inserting the optimum inductance and resistance tuning from the first row of **Table 1** into the respective parallel (28)

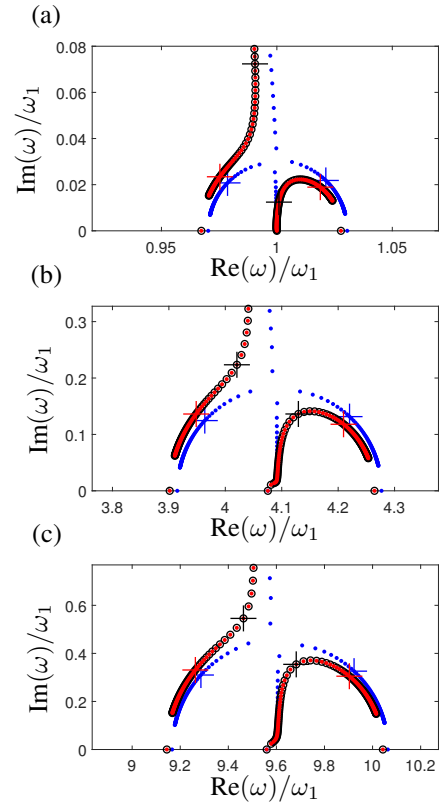


**Figure 2.** Root-locus diagram based on the numerical example in the section **Numerical example** and simultaneous three mode damping in **Three-modes damping**, plotted around mode 1 (a), 2 (b) and 3 (c) for the single-mode (•), modified single-mode (•) and multi-mode (•) calibration and varying resistance values. The roots to the corresponding optimum resistance tuning are indicated by (+), (+) and (+).

and series (32) shunt impedances, these can be written for the resonant mode  $r$  as

$$\begin{aligned} Z_i^p(\omega) &= \frac{1}{|\hat{V}_r|_i} \left( \sqrt{2\kappa_r^2} - i \frac{\omega_r}{\omega} \right), \\ Z_i^s(\omega) &= \frac{|\hat{V}_r|_i}{|Q_r|_i \hat{\omega}_r} \left( \sqrt{2\kappa_r^2} + i \frac{\omega}{\hat{\omega}_r} \right) \frac{\omega_r^2}{\hat{\omega}_r^2} \end{aligned} \quad (38)$$

Considering the shunt tuning to the target mode  $r$ , it can be seen from (38) that the absolute value of the parallel and series impedances of the piezoelectric absorbers tuned to a mode  $j \neq r$  can be described around the target mode  $r$  as

$$\begin{aligned} |Z_i^p(\omega_r)|, |Z_i^s(\omega_r)| &\rightarrow \infty \text{ for } \omega_j \ll \omega_r, \\ |Z_i^p(\omega_r)|, |Z_i^s(\omega_r)| &\rightarrow 0 \text{ for } \omega_j \gg \omega_r. \end{aligned} \quad (39)$$

An approximation of the influence from the piezoelectric absorbers not tuned with respect to mode  $r$  is therefore obtained by keeping the piezoelectric absorbers tuned with respect to mode  $j < r$  in the OC condition, while the absorbers tuned with respect to mode  $j > r$  are in the SC condition when evaluating the SC and OC eigenvalue problems for the present target mode  $r$ . The SC eigenvalue problem and corresponding modal charge may thus be determined as

$$\begin{aligned} ([K^E] + [k_{me}^E]_{j<r} [C_p]_{j<r}^{-1} [k_{me}^E]_{j<r}^t - \underline{\omega}_r^2 [M]) \{ \underline{U}_r \} &= \{ 0 \}, \\ \{ \underline{Q}_r \} &= -[k_{me}^E]_{j>r}^t \{ \underline{U}_r \} \end{aligned} \quad (40)$$

in which the OC stiffness contribution from the piezoelectric absorbers tuned to mode(s)  $j < r$  will increase the original SC frequency  $\underline{\omega}_r \geq \omega_r$ , while the modal charges are evaluated only for the piezoelectric absorbers tuned with respect to mode  $r$ .

The OC eigenvalue problem and corresponding modal voltages are further given as

$$\begin{aligned} \left( [K^E] + [k_{me}^E] [C_p]^{-1} [k_{me}^E]^t - [k_{me}^E]_{j>r} [C_p]_{j>r}^{-1} [k_{me}^E]_{j>r}^t \right. \\ \left. - \underline{\omega}_r^2 [M] \right) \{ \hat{\underline{U}}_r \} &= \{ 0 \}, \\ \{ \hat{\underline{V}}_r \} &= [C_p]_{j>r}^{-1} [k_{me}^E]_{j>r}^t \{ \hat{\underline{U}}_r \} \end{aligned} \quad (41)$$

in which the OC stiffness contribution from the piezoelectric absorbers tuned to mode(s)  $j > r$  is subtracted from the original OC stiffness matrix in (5), whereby the original OC frequency decreases  $\hat{\omega}_r \leq \omega_r$ . Furthermore, the modal voltages are now evaluated only for the piezoelectric absorbers tuned with respect to mode  $r$ .

After evaluation of the SC and OC eigenvalue problems (40) and (41), a new effective EMCC can further be determined for a target mode  $r$  as

$$\underline{k}_r^2 = \frac{\hat{\omega}_r^2 - \omega_r^2}{\omega_r^2} \quad (42)$$

The underbar will in the following denote the modal parameters for these new SC and OC eigenvalue problems with more advanced book keeping, including the state of the non-resonant shunts.

The optimum parallel and series shunt tunings then follow by the same tuning formulas proposed for the single-mode calibration, but with frequencies, modal charges and modal voltages based on the SC and OC eigenvalue problems in (40) and (41). The tuning formulas are provided in the third row of Table 1.

Using this shunt tuning, the root trajectories for varying resistance are seen to follow semi-circles around the targeted

resonant frequencies (blue dots) in Figure 2, while the optimum resistance tuning (blue crosses) appear on the  $\pm 45^\circ$  lines from the respective undamped SC frequencies, with a corresponding damping ratio that can be estimated accurately as

$$\zeta_r = \sqrt{\frac{1}{8} k_r^2} \quad (43)$$

The present multi-mode calibration method requires the evaluation of two eigenvalue problems for each target mode  $r$ , while tuning to any resonant mode may be determined by evaluating only two eigenvalue problems when using the single-mode calibration in the section **Single-mode calibration** and the modified single-mode calibration in **Modified single-mode calibration**. In the numerical example of the section **Numerical example**, it is thus investigated how well the previous single-mode and modified single-mode calibrations perform compared to the multi-mode calibration of this section for a simply supported beam with three pairs of shunted piezoceramic patches, simultaneously targeting modes 1 to 3.

## Numerical example

In the present section the calibration methods presented in the section **Single-mode calibration** and are demonstrated by the analysis of a simple numerical example. The example concerns a simply supported beam with three pairs of piezoceramic patches, which can be seen in Figure 3. All the piezoceramic patches have the same polarisations and are connected in parallel in pairs with a resonant shunt circuit  $Z_i^p$ . The dimensions of the beam are  $40 \times 3 \times 0.2$  cm<sup>3</sup>, while the piezoceramic patch pairs are placed with their respective centers in the quarter, half and three-quarter point locations along the beam. The dimensions of the piezoceramic patches are  $5 \times 3 \times 0.1$  cm<sup>3</sup>. The material properties of the beam are defined for aluminum by a Young's modulus  $E = 70$  GPa, a density  $\rho_b = 2700$  kg/m<sup>3</sup> and a Poisson's ratio  $\nu = 0.33$ . PZT 5H is the material considered for the piezoceramic patches with material properties that can be accessed through the "eFunda portal" (eFunda Portal, 2019). The beam and piezoceramic patches are discretized by respectively  $48 \times 4 \times 1$  and  $6 \times 4 \times 1$  20-node three dimensional solid elements in ANSYS®. The equipotential condition of the piezoelectric electrodes are enforced by a coupling constraint on the concerned electrical dofs, reducing the number of electrical dofs for each electrode to a single dof defined in a so-called master node (Toftekær et al., 2019). The master nodes of the top and bottom interface electrodes are coupled, while the inner interface electrodes are coupled and grounded, in order to model the parallel connection of each piezoceramic patch pair. In the following, each of the three parallel connected piezoceramic patch pairs will therefore act as a single combined piezoelectric absorber with shunt impedance  $Z_i^p$  ( $i = 1, 2$  or  $3$ ).

Optimum piezoelectric shunt tuning is considered for the first three resonant vibration modes of the simply supported beam in Figure 3. Firstly, the three piezoelectric absorbers are in turn tuned with respect to a single target mode. Secondly, simultaneous damping of modes 1 and 2 is considered and finally simultaneous damping of modes 1,

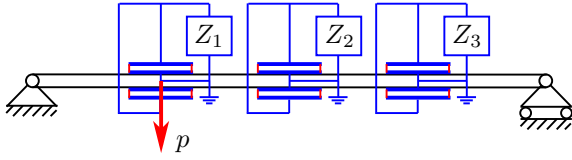


**Figure 3.** Simply supported beam with three pairs of shunted piezoceramic patches (absorbers) and position of a dynamic point load  $p$ .

**Table 2.** SC and OC frequencies and the effective EMCC of the simply supported beam with three piezoelectric absorbers.

Mode	$\omega_r/(2\pi)$ [Hz]	$\hat{\omega}_r/(2\pi)$ [Hz]	$\kappa_r^2$ [%]
1	25.18	25.35	1.41
2	102.8	103.5	1.53
3	242.0	244.2	1.79

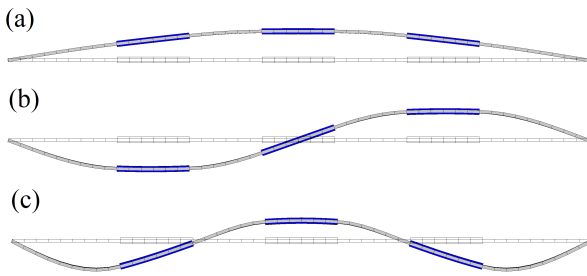


**Figure 4.** The first three mode shapes (a-c) of the simply supported beam with three pairs of SC piezoceramic patches.

2 and 3 is analyzed. Initially, the SC and OC eigenvalue problems are evaluated in order to determine the resonant frequencies, the effective EMCC and the corresponding mode shapes of the simply supported beam. The SC eigenvalue problem (3) is established by enforcing zero electric potential at all interface electrodes, while the OC eigenvalue problem (5) follows by deleting the zero potential constraints on the top/bottom interface electrodes of the three piezoelectric patch pairs. The first three SC and OC resonant frequencies and the corresponding effective EMCCs are provided in Table 2. The three mode shapes corresponding to the SC resonant frequencies in Table 2 can be seen in Figure 4, where the gray and blue colors indicate the beam and piezoelectric absorbers, respectively. It can be seen from Figure 4(a,c) that the second piezoelectric absorber ( $Z_2$ ) is placed optimally for vibration modes 1 and 3 (the location of maximum curvature), while the position of the first ( $Z_1$ ) and third ( $Z_3$ ) piezoelectric absorbers are optimally located for mode 2 in Figure 4(b). Moreover, it can be seen from Figure 4(b) that the second piezoelectric absorber ( $Z_2$ ) is positioned at a nodal point for the second mode shape, which means that this absorber is without electromechanical coupling for vibration mode 2, for which it can therefore not be applied.

### Single mode damping

The optimum piezoelectric shunt tuning is now considered for the case where all three piezoelectric shunts are

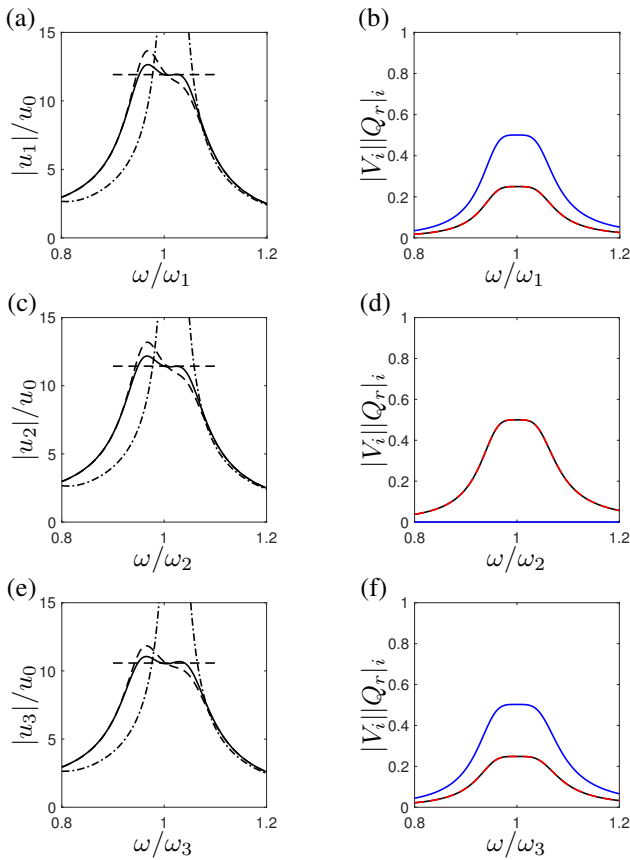
simultaneously tuned to the same target mode  $r$ . The single-mode calibration formulas, provided in the first row of Table 1, are thus used to determine the optimum parallel and series shunt tuning, given in Table 3. Furthermore, Table 3 also gives the modal charge (4) and voltage (6) found for each piezoelectric absorber from the ANSYS® model as an SC electric "reaction force" and an OC electric "displacement" in the master node of the top/bottom electrodes, respectively. It is noted that both the SC and OC mode shapes are scaled in order to obtain unit modal mass, which ensures that the (units) provided for modal charge and voltage are the mass normalized quantities.

The magnitude of the normalized modal charges and voltages in Table 3 determine the authority of the corresponding piezoelectric absorber on the targeted vibration mode. The largest modal charge and voltage are thus found for the second absorber ( $Z_2$ ) in mode 1 and 3 and for the first ( $Z_1$ ) and third ( $Z_3$ ) absorbers in mode 2. As expected, zero electric charge and voltage is observed for the second absorber ( $Z_2$ ) in mode 2. It can also be seen from Table 3 that the tuning of the three shunts is identical for both modes 1 and 3, while it is identical for the first ( $Z_1$ ) and third ( $Z_3$ ) absorbers for mode 2. This is because the three absorbers are positioned symmetrically and thus perform almost equally well for the first three vibration modes, except for the second absorber ( $Z_2$ ) in mode 2 with vanishing influence.

The amplitudes of the frequency response functions (FRF) around vibration modes 1, 2 and 3 are now determined in order to verify the obtained shunt tuning in Table 3. It is noted that the FRFs are only presented for the model with optimum parallel shunts, as the corresponding curves for the series shunts are almost identical. The FRFs are obtained by applying the modal load  $\{f_r\} = [M]\{U_r\}$  to the structure for which the three parallel shunts are tuned. The magnitude of the FRFs in the point of maximum modal deflection  $|u_1|$ ,  $|u_2|$  and  $|u_3|$  are in Figure 5(a,c,e) normalized by the corresponding static deflection  $u_0$ , while the corresponding voltage amplitudes  $|V_1|$ ,  $|V_2|$  and  $|V_3|$  are shown in Figure 5(b,d,f). The term FRF will in the remainder of the paper refer to the magnitude of the frequency response function, and specifically for the normalized structural amplitudes it denotes therefore the dynamic amplification factor (DAF). In Figure 5(a,c,e) the horizontal dashed line indicates the dynamic amplification factor  $DAF = 1/(2\zeta_r)$  at resonance  $\omega = \omega_r$ , with the damping ratios  $\zeta_r$  determined from Table 1. Furthermore, the FRFs corresponding to the tuning without residual modes correction is provided in Figure 5(a,c,e) by the dashed and dashed-dotted curves for, respectively, the tuning based on the static capacitance  $C_s = 82.2nF$  (Toftækær et al., 2019) and the traditional blocked capacitance  $C_p^s = 51.8nF$  (Toftækær et al., 2018). It can be seen that flat plateaus in  $DAF = |FRF|$  agree well with the estimated damping level and that the omission of the residual contribution modes (dashed and dashed-dotted curves) leads to a reduced damping performance, in particular for the tuning based on the blocked capacitance (dashed-dotted curves). Furthermore, it can be seen from Figure 5(b,d,f) that completely flat plateaus are obtained for the voltage response amplitudes  $|V_i|$  normalized by the corresponding modal charges  $|Q_r|_i$  around the resonance. For mode 1, the flat

**Table 3.** Modal charge and voltage and optimum parallel and series single-mode calibration for each piezoelectric absorber to the first three resonant vibration modes.

	Shunt	$ Q_r _i \left[ \frac{(mC)}{m\sqrt{kg}} \right]$	$ \hat{V}_r _i \left[ \frac{(kV)}{m\sqrt{kg}} \right]$	$L_i^p [H]$	$R_i^p [k\Omega]$	$L_i^s [H]$	$R_i^s [k\Omega]$
Mode 1	$Z_1$	2.670	32.94	493.0	464.7	479.4	12.81
	$Z_2$	3.781	46.64	493.0	464.7	479.4	12.81
	$Z_3$	2.670	32.94	493.0	464.7	479.4	12.81
Mode 2	$Z_1$	16.06	198.4	29.62	109.3	28.73	3.269
	$Z_2$	-	-	-	-	-	-
	$Z_3$	16.06	198.4	29.62	109.3	28.73	3.269
Mode 3	$Z_1$	28.86	356.0	5.335	42.91	5.150	1.494
	$Z_2$	41.05	506.5	5.335	42.91	5.150	1.494
	$Z_3$	28.86	356.0	5.335	42.91	5.150	1.494

**Figure 5.** FRF for the displacements (at the position of the maximum modal deflection) and voltages around mode 1(a,b), 2(c,d) and 3(e,f) of the simply supported beam with three piezoelectric absorbers. In (a,c,e) the solid, dashed and dashed-dotted curves is for the tuning based on the modal, static and blocked capacitance, respectively, while the horizontal dashed lines indicate the DAFs. In (b,d,f) the black, blue and red lines indicates the voltage  $V_1$ ,  $V_2$  and  $V_3$  over each absorber.

plateaus are at  $|V_2||Q_1|_2 \simeq 0.5$  for shunt  $Z_2$  and  $|V_1||Q_1|_1 = |V_3||Q_1|_3 \simeq 0.25$  for shunt  $Z_1$  and  $Z_3$ , which corresponds to the fractions  $(\hat{V}_r)_i(Q_r)_i / (\{\hat{V}_r\}^t \{Q_r\})$  appearing in the characteristic equation (27). This fraction also determines the ratio between the effective and modified effective EMCCs in

(11) and thus quantifies the amount of damping provided by each piezoelectric shunt. For mode 2 in Figure 5(d) it is seen that the first ( $Z_1$ ) and third ( $Z_3$ ) piezoelectric absorbers each provide half of the total damping, while the second absorber ( $Z_2$ ) instead contributes the most to the damping of mode 3.

### Two-modes damping

Simultaneous damping of the resonant vibration modes 1 and 2 in Figure 4(a,b) is now considered. The second piezoelectric absorber ( $Z_2$ ) is tuned to vibration mode 1, for which it is optimally positioned, while the first ( $Z_1$ ) and third ( $Z_3$ ) absorbers are tuned to vibration mode 2. In the following the calibration strategies for the single-mode in the section **Single-mode calibration**, the modified single-mode in **Modified single-mode calibration** and the multi-mode in **Multi-mode calibration with non-resonant absorbers** are applied.

The single-mode tuning parameters are provided in Table 3, with the second absorber ( $Z_2$ ) tuned to mode 1 and the first ( $Z_1$ ) and third ( $Z_3$ ) absorbers tuned to mode 2. According to (36), the single-mode calibration causes a decrease in the obtained damping ratio and ultimately a higher maximum DAF at resonance. It may therefore be beneficial to use the resistance tuning from the modified effective EMCC (37), which gives

$$\tilde{\kappa}_1^2 = \frac{(Q_1)_2(\hat{V}_1)_2}{\omega_1^2} = 0.70\%, \quad (44)$$

$$\tilde{\kappa}_2^2 = \frac{(Q_2)_1(\hat{V}_2)_1 + (Q_2)_3(\hat{V}_2)_3}{\omega_2^2} = 1.53\%$$

for the two modes. The optimum tuning of shunts  $\tilde{Z}_1$ ,  $\tilde{Z}_2$  and  $\tilde{Z}_3$  is provided in Table 4 and determined by using the modified single-mode calibration from the second row of Table 1.

Finally, the multi-mode calibration method presented in the third row of Table 1 is considered. This method requires the evaluation of two eigenvalue problems for each target mode, in order to obtain more representative effective EMCCs and modal charges and voltages. The two eigenvalue problems for the first target mode ( $r = 1$ ) is obtained by grounding all absorber electrodes  $V_1 = V_2 = V_3 = 0$  in the SC case, while subsequently removing the constraint on the second absorber electrode  $V_1 = Q_2 = V_3 = 0$  in the OC case. For the second target mode ( $r = 2$ ), the SC eigenvalue

problem is defined by keeping the second absorber in the OC condition, while the first and third absorbers are shorted:  $V_1 = Q_2 = V_3 = 0$ , while the OC eigenvalue problem has all absorbers in their OC condition:  $Q_1 = Q_2 = Q_3 = 0$ . Hereby, the corresponding two effective EMCCs are

$$\kappa_1^2 = 0.70\%, \quad \kappa_2^2 = 1.53\% \quad (45)$$

corresponding exactly to those in (44) obtained by the modified single-mode calibration. The new modal charges and voltages are provided in Table 4 together with the optimum parallel and series shunt tuning determined by the formulas in the third row of Table 1.

It can be seen from Table 4 that the modified single-mode and the multi-mode shunt tuning of  $Z_1$  and  $Z_3$  to mode 2 are identical and equal to the single-mode calibration in Table 3. This is because the second piezoelectric absorber ( $Z_2$ ) does not influence mode 2. The single-mode calibration is therefore valid in this case without any reduction in attainable damping. The optimum tuning of the second shunt  $Z_2$  to mode 1 is however seen to differ from the single-mode calibration in Table 3, because of the influence from the first ( $Z_1$ ) and third ( $Z_3$ ) piezoelectric absorbers on the effective EMCC. The inductance tuning for the modified single-mode and the multi-mode calibrations in Table 4 are almost equal to those for the single-mode calibration in Table 3, since the effective EMCC only plays a minor role in the corresponding tuning formulas and the new modal charge and voltage only alter the inductance tuning of  $Z_2$  slightly. However, the resistance tuning for the modified single-mode and multi-mode calibrations in Table 4 are significantly different for mode 1 compared to those for the single-mode calibration in Table 3, due to the new effective EMCCs in (44) and (45).

The effect of using the three different shunt tuning methods is now analyzed by inspecting the FRFs in Figure 6 to a load with a spatial distribution equal to either the first or second resonant vibration modes. It can be seen from the FRF around the first resonant frequency in Figure 6(a) that the single-mode calibration (dashed-dotted curve) causes a non flat plateau with a maximum DAF accurately determined from the reduced damping ratio in (36) (horizontal dashed-dotted line). When instead using the modified single-mode calibration (dashed curve) and the multi-mode calibration (solid curve), flat plateaus are observed for the corresponding FRFs in Figure 6(a). For the shunt voltage in Figure 6(b), the multi-mode calibration (solid curve) gives a slightly more flat plateau in the FRF compared to the modified single-mode calibration (dashed curve). It can be seen from the FRF around the second resonant frequency in Figure 6(c) that the three-shunt calibrations give identical responses, as  $Z_2$  has no influence on mode 2. For the mode 2 shunt voltage in Figure 6(d), it is furthermore seen that the first ( $Z_1$ ) and third ( $Z_3$ ) absorbers contribute equally to the mitigation of mode 2 in Figure 5(d).

The simultaneous shunt tuning and damping of modes 1 and 2 of the simply supported beam is now analyzed by considering a dynamic point load located at the center point in Figure 3, of the first piezoelectric absorber where it spatially excites both vibration modes 1 and 2.

The FRF to the point load is seen in Figure 7 in a frequency spectrum capturing the first two resonances of the simply supported beam. As observed for the response to the

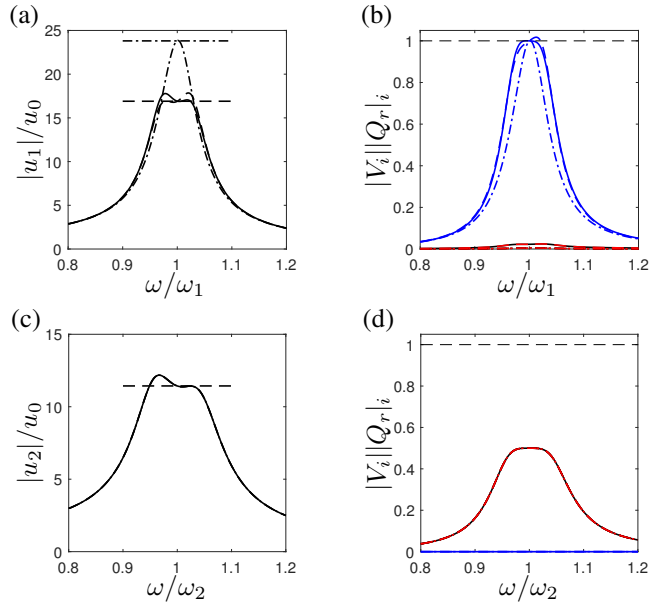


**Figure 6.** FRF to modal loads in mode 1 (a,b) and 2 (c,d), for parallel multi-mode (—), modified single-mode (---) and single-mode (-.-.) tuning of the piezoelectric absorbers. In (a,c) the horizontal dashed and dashed-dotted lines indicate, the DAFs based on the damping ratios (43) and (36), while the black, blue and red curves in (b,d) indicate the voltage responses  $V_1$ ,  $V_2$  and  $V_3$ , respectively.

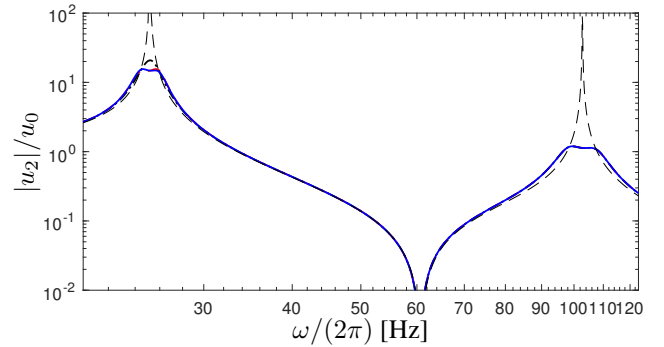


**Figure 7.** FRF for simply supported beam with point load in Figure 3, for parallel multi-mode tuning (—), modified single-mode tuning (---), single-mode tuning (-.-.), and for the SC structure (- - -).

modal loads in Figure 6, it can be seen in Figure 7 that the optimum vibration suppression is obtained around mode 2 for all three tuning methods, while optimum suppression of vibration mode 1 requires the use of the modified single-mode tuning or the full multi-mode calibration. In all cases, the three piezoelectric absorbers suppress both resonant peaks significantly.

### Three-modes damping

Simultaneous damping of the first three resonant vibration modes of the simply supported beam in Figure 3 is now considered and realized by tuning the first piezoelectric absorber ( $Z_1$ ) to mode 2, the second ( $Z_2$ ) to mode 3 and the third ( $Z_3$ ) to mode 1. Again, all three tuning methods are considered and compared. The single-mode

**Table 4.** Modal charge and voltage and optimum modified single  $\tilde{Z}_i$  and multi-mode  $\underline{Z}_i$  parallel and series shunt tuning for the second piezoelectric absorber tuned to mode 1 and the first and third absorbers tuned to mode 2.

Shunt	$ Q_r _i$ $\left[ \frac{(mC)}{m\sqrt{kg}} \right]$	$ \hat{V}_r _i$ $\left[ \frac{(kV)}{m\sqrt{kg}} \right]$	$L_i^p$ [H]	$R_i^p$ [k $\Omega$ ]	$L_i^s$ [H]	$R_i^s$ [k $\Omega$ ]	
Mode 1	$\tilde{Z}_2$	3.781	46.64	493.0	656.8	482.8	9.130
	$\underline{Z}_2$	3.781	46.32	489.6	654.5	479.4	9.035
Mode 2	$\tilde{Z}_1$	16.07	198.41	29.62	109.3	28.73	3.269
	$\tilde{Z}_3$	16.07	198.41	29.62	109.3	28.73	3.269
	$\underline{Z}_1$	16.07	198.41	29.62	109.3	28.73	3.269
	$\underline{Z}_2$	16.07	198.41	29.62	109.3	28.73	3.269
	$\underline{Z}_3$	16.07	198.41	29.62	109.3	28.73	3.269

calibration follows from Table 3, while the modified single-mode calibration follows from determination of the modified effective EMCC in (37), obtained for the three vibration modes as

$$\begin{aligned} \tilde{\kappa}_1^2 &= \frac{(Q_1)_3(\hat{V}_1)_3}{\omega_1^2} = 0.35\%, \\ \tilde{\kappa}_2^2 &= \frac{(Q_2)_1(\hat{V}_2)_1}{\omega_2^2} = 0.76\%, \\ \tilde{\kappa}_3^2 &= \frac{(Q_3)_2(\hat{V}_3)_2}{\omega_3^2} = 0.90\% \end{aligned} \quad (46)$$

The corresponding optimum tuning of the parallel and series shunt  $\tilde{Z}_i$  are provided in Table 5. The multi-mode calibration requires the evaluation of individual eigenvalue problems in order to determine three new SC and OC resonance frequencies and the corresponding modal charges and voltages. The SC and OC eigenvalue problems (40) and (41) are respectively established for target mode  $r = 1$  by  $V_1 = V_2 = V_3 = 0$  and  $V_1 = V_2 = Q_3 = 0$ , for target mode  $r = 2$  by  $V_1 = V_2 = Q_3 = 0$  and  $Q_1 = V_2 = Q_3 = 0$  and for target mode  $r = 3$  by  $Q_1 = V_2 = Q_3 = 0$  and  $Q_1 = Q_2 = Q_3 = 0$ . The corresponding effective EMCCs are then found as

$$\underline{\kappa}_1^2 = 0.35\%, \quad \underline{\kappa}_2^2 = 0.76\%, \quad \underline{\kappa}_3^2 = 0.89\% \quad (47)$$

while three new modal charge and voltage amplitudes are provided in Table 5. Finally, the optimum multi-mode parallel and series shunt tuning are given in Table 5.

It can be seen from Table 5 that the parallel shunt inductance for the modified single-mode calibration is identical to the single-mode calibration in Table 3 because the corresponding tuning formula (30) is independent of the effective EMCC. For the multi-mode calibration the inductance is slightly altered due to the new modal charges and voltages. As also found for the double mode damping, the optimum resistances in Table 5 are significantly different from the single-mode calibration values in Table 3, mainly due to the new effective EMCCs in (46) and (47). The three tuning methods are analyzed by inspecting the corresponding FRFs produced by applying modal loads for the respective three resonant vibration modes, shown for the parallel shunts in Figure 8.

It can be seen from Figure 8(a,c,e) that the maximum DAF at resonance is accurately determined from the reduced damping ratio (dashed line) in (36), when the single-mode

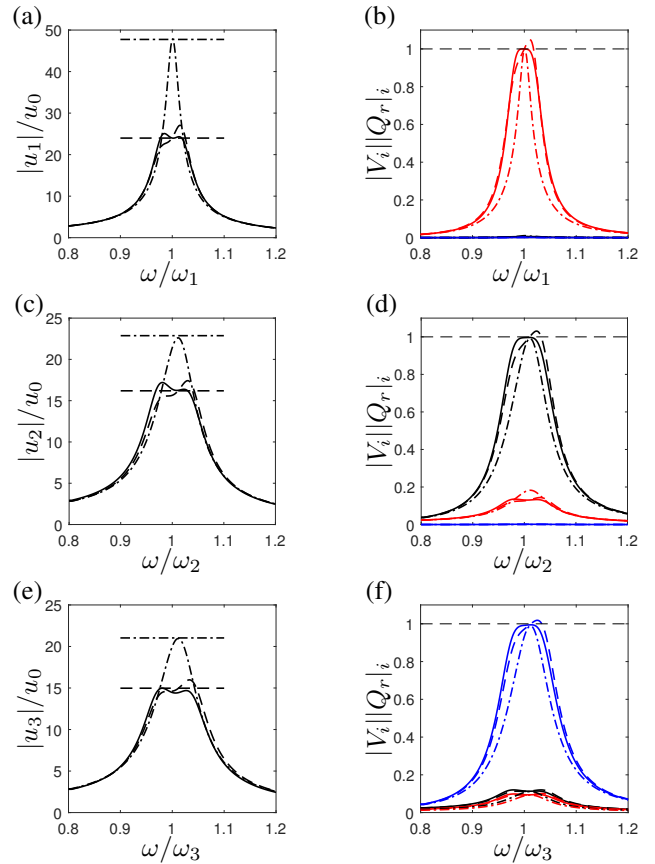


**Figure 8.** FRF to modal loads in mode 1 (a,b), 2 (c,d) and 3 (e,f), for parallel multi-mode (—), modified single-mode (---) and single-mode (-.-.) calibrations. In (a,c,e) the horizontal dashed and dashed-dotted lines indicate the DAFs based on the damping ratios (43) and (36), and in (b,d,f) the black, blue and red curves indicate the voltage responses  $V_1$ ,  $V_2$  and  $V_3$ , respectively.

calibration in Table 3 is used. Both the modified single-mode and multi-mode calibration give almost flat plateaus in the FRF based on the damping ratio in (43). A slightly higher amplitude may be observed for the modified single-mode calibration, due to the inaccuracy of the modal charges and voltages. For the shunt voltage in Figure 8 it is similarly observed that the multi-mode calibration (solid curves) is

**Table 5.** Modal charge and voltage and optimum single and multi-mode parallel and series shunt tuning for the three piezoelectric absorbers dedicated to damp resonant vibration mode 2, 3 and 1, respectively.

Shunt	$ Q_r _i$ $\left[ \frac{(mC)}{m\sqrt{kg}} \right]$	$ \hat{V}_r _i$ $\left[ \frac{(kV)}{m\sqrt{kg}} \right]$	$L_i^p$ [H]	$R_i^p$ [k $\Omega$ ]	$L_i^s$ [H]	$R_i^s$ [k $\Omega$ ]	
Mode 1	$\tilde{Z}_3$	2.670	32.94	493.0	930.1	484.5	6.470
	$\underline{Z}_3$	2.670	32.58	487.6	925.0	485.9	6.420
Mode 2	$\tilde{Z}_1$	16.07	198.4	29.62	154.6	28.95	2.329
	$\underline{Z}_1$	16.14	198.4	29.25	153.5	29.03	2.332
Mode 3	$\tilde{Z}_2$	41.05	506.5	5.335	60.50	5.195	1.069
	$\underline{Z}_2$	41.07	506.5	5.286	60.45	5.238	1.073

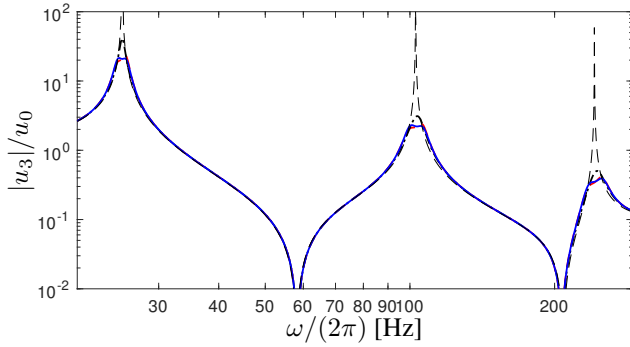


**Figure 9.** FRF for simply supported beam with point load in Figure 3, for parallel multi-mode (—), modified single-mode (---) and single-mode (-.-.) calibrations, and for the SC structure (- - -).

closer to the ideally balanced calibration with completely flat plateaus compared to the response of the modified single-mode calibration (dashed curves).

Finally, the performance of the shunt tuning provided in Table 3 and 5 are again analyzed by the FRF in Figure 9 for the harmonic point load in Figure 3. It can be seen from Figure 9 that the multi-mode calibration (blue solid curve) leads to the most flat plateaus around the resonant frequencies. The modified single-mode calibration (red dashed curve) provides almost the same vibration suppression around the three resonant frequencies and may thus be beneficial, as it avoids the evaluation of additional eigenvalue problems. The single-mode calibration (black dashed-dotted curve) is seen to cause non-flat plateaus around the resonant frequencies and a larger DAF, which is however still significantly reduced compared to the DAF for the SC structure (black dashed curve).

## Conclusion

A resonant piezoelectric shunt calibration principle accounting for the influence of non-resonant vibration modes is proposed for multiple shunted piezoelectric domains (absorbers) attached to a flexible structure. The method requires the evaluation of two eigenvalue problems associated with the SC and OC conditions of the piezoelectric domains, from which the frequencies, modal charges and modal voltages are determined, constituting the required shunt tuning parameters. The evaluation of the modal charge and voltage also permits the direct evaluation of a new effective

modal capacitance, that contains the effects of non-resonant vibration modes. When only a subset of the piezoelectric shunts are tuned with respect to the target vibration mode the tuning becomes non-optimal and the attainable damping decreases. In this case, an enhanced shunt tuning may be obtained by the determination of a modified effective EMCC, which only considers the piezoelectric absorbers tuned with respect to the target vibration mode. Finally, the tuning method is generalized to multi-mode vibration suppression, for which the corresponding optimum shunt tuning requires the evaluation of additional eigenvalue problems to account for the influence from piezoelectric absorbers tuned to modes below and above the target mode.

The three shunt calibration methods are tested on a simple numerical example concerning a simply supported beam with three pairs of shunted piezoceramic patches (absorbers). First, it is demonstrated that the tuning of the three piezoelectric absorbers to the same resonant vibration mode provides significant vibration suppression and reduces the maximum DAF to the level predicted by an estimated modal damping ratio. It is found that the tuning parameters for the three shunts are indistinguishable, except for the tuning of the second absorber to the second vibration mode, since this absorber is exactly located at the nodal point of mode 2.

Secondly, simultaneous damping of vibration modes 1 and 2 is considered. It is demonstrated that the single-mode calibration of the second piezoelectric absorber causes a non-optimal response around mode 1, while a flat plateau is obtained around mode 2, damped by the piezoelectric absorbers 1 and 3. For the first vibration mode the influence from absorber 1 and 3 on the effective EMCC causes the non-optimum damping. The single-mode calibration, however, remains valid for the second vibration mode, as the second absorber is located in nodal point. The optimum tuning to the first resonant mode may be enhanced by using the modified effective EMCC or the multi-mode calibration, where improved accuracy of the latter comes at the cost of evaluating additional eigenvalue problems.

Finally, simultaneous damping of the first three resonant vibration modes is considered. In this case, the single-mode calibration leads to non-optimum shunt damping for all three vibration modes with a maximum DAF accurately estimated from a reduced modal damping ratio. However, when using the modified single-mode or the multi-mode calibrations, flat plateaus around the resonant frequencies are obtained

in the corresponding FRFs. The results of the numerical example therefore indicate that it may be beneficial to use the modified single-mode calibration method, by which an optimum tuning and vibration suppression is obtained without the evaluation of the additional eigenvalue problems required in the full multi-mode calibration.

An experimental implementation and validation of the proposed shunt tuning method is of great interest and may be achieved by determine the shunt tuning from actual measurements of the SC current and OC voltage. As the effective modal capacitance is independent of the mode shapes normalization through the modal charge to voltage ratio, this is obtained and used to determine a precise inductance tuning. By evaluating the optimum shunt tuning directly from measurements on the actual piezoelectric absorber any uncertainties associated with the numerical model and evaluation of the shunt tuning may be seemingly avoided. The experimental validation of the proposed tuning method is considered in future work.

## Funding

This research has been supported by the Danish Council for Independent Research via the project ‘Resonant Piezoelectric Shunt Damping of Structures’.

## Acknowledgements

The authors are grateful to Prof. Ayeche Benjeddou for his valuable comments and corrections, which have improved the final paper.

## References

- Anderson EH and Hagood NW (1994) Simultaneous piezoelectric sensing/actuation: Analysis and application to controlled structures. *Journal of Sound and Vibration* 174: 617-639.
- Berardengo M, Thomas O, Giraud-Audine C and Manzoni S (2016) Improved resistive shunt by means of negative capacitance: new circuit, performances and multi-mode control. *Smart Materials and Structures* 25: 075033(23pp).
- Berardengo M, Manzoni S, Thomas O, and Vanali M (2018) Piezoelectric resonant shunt enhancement by negative capacitances: Optimisation, performance and resonance cancellation. *Journal of Intelligent Material Systems and Structures* 29(12): 25812606.
- Caruso G (2001) A critical analysis of electric shunt circuits employed in piezoelectric passive vibration damping. *Smart Materials and Structures* 10: 1059-1068.
- de Marneffe B and Preumont A (2008) Vibration damping with negative capacitance shunts: theory and experiment. *Smart Materials and Structures* 17: 035015.
- Ducarne J, Thomas O and Deü JF (2010) Structural Vibration Reduction by Switch Shunting of Piezoelectric Elements: Modeling and Optimization. *Journal of Intelligent Material Systems and Structures* 21: 797816.
- eFunda Portal (2019) Lead Zirconate Titanate (PZT-5H). Available at: [http://www.efunda.com/materials/piezo/material\\_data/matdata\\_output.cfm?Material\\_ID=PZT-5H](http://www.efunda.com/materials/piezo/material_data/matdata_output.cfm?Material_ID=PZT-5H) (accessed 1 July 2019).
- Fleming AJ, Behrens S and Moheimani SOR (2000) Synthetic impedance for implementation of piezoelectric shunt-damping circuits. *Electronics Letters* 36: 1525-1526.
- Forward RL (1979) Electronic damping of vibrations in optical structures. *Applied Optics* 18: 690-697.
- Gardonio P and Casagrande D (2017) Shunted piezoelectric patch vibration absorber on two-dimensional thin structure: tuning considerations. *Journal of Sound and Vibration* 395: 26-47.
- Hagood NW and von Flotow A (1991) Damping of structural vibrations with piezoelectric materials and passive electrical networks. *Journal of Sound and Vibration* 146: 243-268.
- Høgsberg J and Krenk S (2012) Balanced calibration of resonant shunt circuits for piezoelectric vibration control. *Journal of Intelligent Material Systems and Structures* 23: 1937-1948.
- Høgsberg J and Krenk S (2017) Calibration of piezoelectric RL shunts with explicit residual mode correction. *Journal of Sound and Vibration* 386: 65-81.
- Hollkamp JJ (1994) Multimodal passive vibration suppression with piezoelectric materials and resonant shunts. *Journal of Intelligent Material Systems and Structures* 5: 49-57.
- IEEE Inc. (1988) *Standards on piezoelectricity* ANS/IEEE Std 176-1987 USA.
- Krenk S and Høgsberg J (2016) Tuned resonant mass or inerter-based absorbers: Unified calibration with quasi-dynamic flexibility and inertia correction. *Proceedings of the Royal Society* 472: 20150718(23pp).
- Krenk S and Høgsberg J (2013) Equal modal damping design for a family of resonant vibration control formats. *Journal of Vibration and Control* 19: 1294-1315.
- Larbi W and Deü JF (2019) Reduced order finite element formulations for vibration reduction using piezoelectric shunt damping. *Applied Acoustics* 147: 111-120.
- Lossouarn B, Aucejo M, Deü JF and Multon B (2017) Design of inductors with high inductance values for resonant piezoelectric damping. *Sensors and Actuators A: Physical* 259: 68-76.
- Lossouarn B, Aucejo M, Deü JF and Cunefare K A (2018) Design of a passive electrical analogue for piezoelectric damping of a plate. *Journal of Intelligent Material Systems and Structures* 29(7): 13011314.
- Park CH and Inman DJ (1999) Uniform model for series R-L and parallel R-L shunt circuits and power consumption. *SPIE Proceedings* 3668: 797-804.
- Preumont A (2011) *Vibration Control of Active Structures. An Introduction* 3rd edition Springer Heidelberg.
- Soltani P, Kerschen G, Tondreau G and Deraemaeker A (2014) Piezoelectric vibration damping using resonant shunt circuits: an exact solution. *Smart Materials and Structures* 23: 125014(11pp).
- Thomas O, Ducarne J and Deü JF (2012) Performance of piezoelectric shunts for vibration reduction. *Smart Materials and Structures* 21: 015008(16pp).
- Toftækær JF, Benjeddou A, Høgsberg J and Krenk S (2018) Optimal piezoelectric RL shunt damping of plates with residual mode correction. *Journal of Intelligent Material Systems and Structures* 29: 3346-3370.
- Toftækær JF, Benjeddou A and Høgsberg J (2019) General numerical implementation of a new piezoelectric shunt tuning method based on the effective electromechanical coupling coefficient. *Mechanics of Advanced Materials and Structures*. Epub ahead of print 25 January 2019. <https://doi.org/10.1080/15376494.2018.1549297>.

- Wu SY (1996) Piezoelectric shunts with a parallel R-L circuit for structural damping and vibration control. *SPIE proceedings* 2720: 259-269.
- Wu SY (1998) Method for multiple mode piezoelectric shunting with single PZT transducer for vibration control. *Journal of Intelligent Material Systems and Structures* 12: 991-998.
- Yamada K, Matsuhisa H, Utsuno H and Sawada K (2010) Optimum tuning of series and parallel LR circuits for passive vibration suppression using piezoelectric elements. *Journal of Sound and Vibration* 329: 5036-5057.

Finally, the characteristic equation (51) may be expressed in the generic form of (25) by division with  $(1 + \kappa_r^2)^2$  and introduction of the OC frequency from (7), which leads to (33).

## Appendix I

The square brackets in (19) may be multiplied by  $i\omega[Z(\omega)]\{Q_r\}$ , whereby the characteristic equation can be written as

$$\left(1 - \frac{\omega^2}{\omega_r^2}\right) \left( i\omega \frac{\{\hat{V}_r\}^t [C_r] [Z(\omega)] \{Q_r\}}{\{\hat{V}_r\}^t \{Q_r\}} + 1 \right) + i\omega \frac{\{Q_r\}^t [Z(\omega)] \{Q_r\}}{\{Q_r\}^t [C_r]^{-1} \{Q_r\}} \kappa_r^2 = 0 \quad (48)$$

after using (23) and dividing by  $\omega_r^2$ . The series impedance (32) and effective capacitance (22) are now inserted in (48), whereby the characteristic equation can be written as

$$\begin{aligned} & \left(1 - \frac{\omega^2}{\omega_r^2}\right) \left( \omega^2 \sum_{i=1}^{N_p} \frac{(\hat{V}_r)_i (Q_r)_i}{\{\hat{V}_r\}^t \{Q_r\}} L_i^s \frac{(Q_r)_i}{(\hat{V}_r)_i} \right. \\ & \left. - i\omega \sum_{i=1}^{N_p} \frac{(\hat{V}_r)_i (Q_r)_i}{\{\hat{V}_r\}^t \{Q_r\}} R_i^s \frac{(Q_r)_i}{(\hat{V}_r)_i} + 1 \right) \\ & + \omega^2 \sum_{i=1}^{N_p} \frac{(\hat{V}_r)_i (Q_r)_i}{\{\hat{V}_r\}^t \{Q_r\}} L_i^s \frac{(Q_r)_i}{(\hat{V}_r)_i} \kappa_r^2 \\ & - i\omega \sum_{i=1}^{N_p} \frac{(\hat{V}_r)_i (Q_r)_i}{\{\hat{V}_r\}^t \{Q_r\}} R_i^s \frac{(Q_r)_i}{(\hat{V}_r)_i} \kappa_r^2 = 0 \end{aligned} \quad (49)$$

It is convenient to divide (49) with  $\sum_{i=1}^{N_p} \frac{(\hat{V}_r)_i (Q_r)_i}{\{\hat{V}_r\}^t \{Q_r\}} L_i^s \frac{(Q_r)_i}{(\hat{V}_r)_i} \omega_r^2$ , which then can be written as

$$\begin{aligned} & \left(1 - \frac{\omega^2}{\omega_r^2}\right) \left( \frac{\omega^2}{\omega_r^2} - i \frac{\omega}{\omega_r} \frac{\sum_{i=1}^{N_p} (Q_r)_i^2 R_i^s}{\sum_{i=1}^{N_p} (Q_r)_i^2 L_i^s \omega_r} \right. \\ & \left. + \sum_{i=1}^{N_p} \frac{\{\hat{V}_r\}^t \{Q_r\}}{(\hat{V}_r)_i (Q_r)_i} \frac{1}{L_i^s} \frac{(\hat{V}_r)_i}{(Q_r)_i \omega_r^2} \right) \\ & + \frac{\omega^2}{\omega_r^2} \kappa_r^2 - i \frac{\omega}{\omega_r} \frac{\sum_{i=1}^{N_p} (Q_r)_i^2 R_i^s}{\sum_{i=1}^{N_p} (Q_r)_i^2 L_i^s \omega_r} \kappa_r^2 = 0 \end{aligned} \quad (50)$$

By expanding the expressions in (50), it can be written as

$$\begin{aligned} & \frac{\omega^4}{\omega_r^4} - \left(1 + \kappa_r^2 - \sum_{i=1}^{N_p} \frac{\{\hat{V}_r\}^t \{Q_r\}}{(\hat{V}_r)_i (Q_r)_i} \frac{1}{L_i^s} \frac{(\hat{V}_r)_i}{(Q_r)_i \omega_r^2}\right) \frac{\omega^2}{\omega_r^2} \\ & - \sum_{i=1}^{N_p} \frac{\{\hat{V}_r\}^t \{Q_r\}}{(\hat{V}_r)_i (Q_r)_i} \frac{1}{L_i^s} \frac{(\hat{V}_r)_i}{(Q_r)_i \omega_r^2} \\ & + i \frac{\omega}{\omega_r} \frac{\sum_{i=1}^{N_p} (Q_r)_i^2 R_i^s}{\sum_{i=1}^{N_p} (Q_r)_i^2 L_i^s \omega_r} \left(1 + \kappa_r^2 - \frac{\omega^2}{\omega_r^2}\right) = 0 \end{aligned} \quad (51)$$



P4

Experimental validation of piezoelectric shunt tuning method with residual mode correction for damping of plate-like structures

Johan Frederik Toftekær and Jan Høgsberg

*Journal of Intelligent Material Systems and Structures*

Submitted, JIM-19-388



# Experimental Validation of Piezoelectric Shunt Tuning with Residual Mode Correction: Damping of Plate-Like Structures

Journal Title  
XX(X):1-17  
©The Author(s) 2016  
Reprints and permission:  
sagepub.co.uk/journalsPermissions.nav  
DOI: 10.1177/ToBeAssigned  
www.sagepub.com/

SAGE

Johan Frederik Toftekær<sup>1</sup> and Jan Høgsberg<sup>1</sup>

## Abstract

The effective vibration mitigation properties of piezoceramic patches with inductive-resistive (LR) shunts are investigated experimentally. A shunt tuning method is proposed, in which a consistent correction for the influence from residual vibration modes is included by an effective modal capacitance, evaluated from measured charge and voltage amplitudes in short- and open circuit (SC and OC) conditions, respectively. The robustness of the proposed method is verified experimentally for both a free beam and plate structure with four shunted piezoceramic patch pairs. A stable and fully passive inductor is produced by winding a copper wire around a magnetic coil, which requires precise inductance tuning to determine the final number of turns. It is demonstrated that the effective modal capacitance interpolates consistently between the blocked and static capacitances, commonly used for single-mode tuning of piezoelectric LR shunts. By imposing pseudo-random vibrations, the piezoelectric current and voltage signals are measured and evaluated by their frequency response functions (FRF). Spectrum peak values determine the apparent SC charge to OC voltage ratio for each shunt, which directly determines the shunt components by explicit tuning formulas. Good correlation between numerical and experimental results are obtained for the free beam, while for the free plate experiment effective multi-mode shunt tuning is obtained by a modified effective electromechanical coupling coefficient.

## Keywords

Piezoelectric shunt damping, shunt calibration, residual mode correction, electromechanical coupling coefficient, modal capacitance, experimental validation

## Introduction

Flexible plate-like structures may be vulnerable to excessive vibrations caused by dynamic harmonic loads with frequencies close to a resonance in the structure. This may cause structural failure, fatigue or lead to undesirable acoustic problems. The introduction of resonant absorber devices calibrated to a single or several dominating resonant modes of the structure may therefore be required. For vibration mitigation of plate-like structures, a convenient absorber consists of co-located piezoceramic patches, with strong electromechanical coupling properties, wired to resonant shunts. The resonant shunt consists of an inductance ( $L$ ) tuned to secure a proper absorber frequency and a resistor ( $R$ ) chosen to obtain optimum energy dissipation around the targeted resonant frequency, as proposed and experimentally demonstrated by Forward (1979). A tuning procedure based on a single mode approximation of the electromechanical structure has been derived subsequently for the series (Hagood and von Flotow, 1991) and parallel (Wu, 1996) LR-shunts, while a comparison of the two shunt configurations have been provided by Park and Inman (1999) and Caruso (2001). Alternative methods for the series and parallel resonant shunt tuning has been suggested in Thomas et al. (2012); Yamada et al. (2010); Høgsberg and Krenk (2012); Soltani et al. (2014), all relying on a pure single-mode truncation of the structural dynamics. A consequence of the single mode assumption

is that the optimum inductance tuning is evaluated directly from the inherent blocked piezoelectric capacitance  $C_p^S$ , in order to obtain the desired absorber frequency. However, due to the effect of non-resonant vibration modes this will in many cases lead to a non-optimum inductance and shunt tuning.

The effect of the (non-resonant) residual vibration modes has rarely been considered in neither numerical or experimental validations of shunt tuning procedures. In numerical validations the influence from residual mode is ignored by simply applying a single-mode structural model when producing frequency response curves for the electromechanical structure (Caruso, 2001; Soltani et al., 2014), while in experiments it is seldom stated precisely which piezoelectric capacitance is measured and thereby used in the shunt tuning. However, in Wu and Bicos (1997) it is stated that the capacitance of a piezoceramic patch bonded to a structure is only slightly different than the inherent blocked

<sup>1</sup>Department of Mechanical Engineering  
Technical University of Denmark  
Nils Koppels Allé, Building 404, DK-2800 Kgs. Lyngby, Denmark

## Corresponding author:

Johan F. Toftekær, Department of Mechanical Engineering  
Technical University of Denmark, Nils Koppels Allé, Building 404, DK-2800 Kgs. Lyngby, Denmark  
Email: jotof@mek.dtu.dk

capacitance, which is therefore used as the governing shunt tuning parameter. Furthermore, in [Porfiri et al. \(2007\)](#); [de Marneffe and Preumont \(2008\)](#); [Preumont \(2011\)](#) the effective capacitance of a piezoelectric element bonded to a vibrating structure is discussed in greater detail. Furthermore, [Porfiri et al. \(2007\)](#) distinguishes between the original free and blocked capacitances and the two additional capacitances, referred to as the free modal and the blocked modal capacitance of the piezoelectric patch bonded to the vibrating host structure. The free modal capacitance can be measured when the structure is free to deform, whereby it becomes representative in the low-frequency limit and thus in [de Marneffe and Preumont \(2008\)](#); [Preumont \(2011\)](#) referred to as the static capacitance  $C_p^0$ . Oppositely, the blocked modal capacitance is representative in the high-frequency limit, whereby its evaluation in principle requires the blocking of all modal coefficients. This makes the blocked modal capacitance difficult to evaluate from experimental campaigns. However, as described in [Porfiri et al. \(2007\)](#) the optimum shunt tuning should be based on this blocked modal capacitance, since it inherently contains the contributions from (non-resonant) residual vibration modes. Finally, methods for evaluating the blocked modal capacitance is proposed and discussed in [Porfiri et al. \(2007\)](#).

The influence and importance of residual vibration modes on resonant  $LR$  shunt tuning has recently been addressed. In [Høgsberg and Krenk \(2017\)](#) explicit flexibility and inertia correction terms, initially derived for tuned mass- and inerter based absorbers in [Krenk and Høgsberg \(2016\)](#), have been proposed. In [Berardengo et al. \(2016, 2018\)](#) the inherent capacitance of the bonded piezoelectric element is modified by the influence from higher vibration modes, while a theoretical study of the influence from an increasing number of vibration modes on the shunt tuning has been provided in [Gardonio and Casagrande \(2017\)](#). An electrical analogy to the flexibility and inertia correction terms in [Høgsberg and Krenk \(2017\)](#) has been proposed in [Toftekær et al. \(2018\)](#), in which it is demonstrated that the corresponding electric capacitance and inductance correction terms, together with the inherent blocked piezoelectric capacitance, determine an effective dynamic capacitance, used to evaluate and improve the traditional shunt inductance tuning. It is illustrated in [Toftekær et al. \(2019\)](#) that for typical patch configurations the apparent inertia correction from residual modes is insignificant compared to the corresponding flexibility effect. Therefore, an alternative effective capacitance, based on the electric response to a short and an open circuit (SC and OC) eigenvalue problem, is proposed in [Toftekær and Høgsberg \(2019a\)](#). It defines a tuning method that is easy to implement in commercial finite element (FE) software ([Toftekær et al. \(2019\)](#)), as it only requires the evaluation of two eigenvalue problems and thus avoids matrix manipulations or the determination of an exhaustive number of residual mode frequencies and shapes. As demonstrated in the following, this method is also suitable for experimentally based shunt tuning.

The present paper provides experimental validation of the shunt tuning procedure proposed in [Toftekær and Høgsberg \(2019a\)](#) and demonstrates experimentally the influence from

residual vibration modes by comparison with the shunt tuning based on both the blocked, the static and the proposed effective modal capacitance ([Toftekær and Høgsberg \(2019a\)](#)). The shunt circuits are designed as pure passive electrical circuits with use of a passive inductor, designed by winding a copper wire around a closed magnetic coil ([Lossouarn et al. \(2017\)](#)), connected in series with a potentiometer, which is easily adjusted to the specific resistance tuning. As discussed in the paper, the use of the passive inductor increases the importance of a precise prior inductance tuning, since subsequent re-adjustment of the final passive inductance is not as straightforward, as for the typical synthetic inductor. Finally, the multi-mode piezoelectric shunt tuning proposed in [Toftekær and Høgsberg \(2019a\)](#) is also implemented and demonstrated experimentally.

The paper is organized in three main sections. In the first section, the numerical shunt tuning method proposed in [Toftekær and Høgsberg \(2019a\)](#) is briefly summarized for the series shunt, used in the experiments. Furthermore, the numerical results for the initial experimental setup, concerning a free beam with four shunted piezoceramic patch pairs, is presented for the subsequent comparison with experimental results. In the second section, it is demonstrated how the required shunt tuning parameters can be evaluated experimentally by measurements of the piezoelectric SC current and OC voltage signals to a specific dynamic excitation imposed by a fifth piezoelectric patch pair. The passive inductor is then briefly presented, requiring a precise prior tuning that includes the influence from the residual vibration modes. The third section considers the two experimental setups, with a free beam and a free plate structure, each damped by four pairs of shunted piezoceramic patches. The components in the four shunts are for both structures determined from the experimentally evaluated tuning parameters. Finally, the shunt damping performance is verified by considering the frequency response functions (FRFs) for both the structural displacements and the piezoelectric absorber voltage response around the targeted resonance frequencies.

## Numerical shunt tuning

This section presents the numerical model and shunt tuning method ([Toftekær and Høgsberg \(2019a\)](#)) to be validated experimentally in the subsequent sections.

In a frequency domain representation with angular frequency  $\omega$ , the general vibration problem for an elastic structure with attached piezoelectric domains may be described as ([Toftekær et al. \(2019\)](#))

$$\left( \begin{bmatrix} K^E & k_{me}^E \\ (k_{me}^E)^t & -C_p \end{bmatrix} - \omega^2 \begin{bmatrix} M & 0 \\ 0 & 0 \end{bmatrix} \right) \begin{Bmatrix} U \\ V \end{Bmatrix} = \begin{Bmatrix} 0 \\ -Q \end{Bmatrix} \quad (1)$$

in which  $[K^E]$  is the elastic stiffness matrix of the structure with SC piezoelectric electrodes and  $[M]$  is the mass matrix. The coupling between the mechanical and the electrical domains is governed by the coupling matrix  $[k_{me}^E]$  with rows equal to the number of mechanical degrees of freedom (dofs) and columns equal to the number of independent piezoelectric shunts  $N_p$ , while  $(\dots)^t$  represents the transpose operation. A piezoelectric shunt  $Z_i$  may be wired to several piezoelectric domains whereby the shunted domains act as

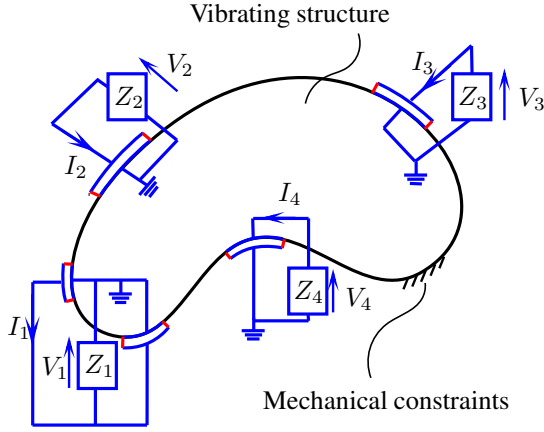


**Figure 1.** Vibrating structure with piezoelectric domains comprised by  $N_p = 4$  piezoelectric absorbers with independent shunt impedance  $Z_i$ . (Toftekær and Høgsberg, 2019a)

a single resulting piezoelectric absorber, see Figure 1. The electrical domain is hereby described by a diagonal matrix  $[C_p]$  containing the resulting blocked capacitance  $(\bar{C}_p^S)_i$  for each piezoelectric absorber (Toftekær et al., 2019). In (1) the vector  $\{U\}$  contains the  $N$  mechanical degrees of freedom (dofs),  $\{V\}$  contains the  $N_p$  electric dofs given by the voltage between the shunted electrodes, while  $\{Q\}$  represents the stored electric charge on each of the shunted electrodes, alternatively expressed by the flow of current

$$I_i = -i\omega Q_i \quad (2)$$

with  $i = \sqrt{-1}$  being the imaginary unit.

The proposed shunt tuning method in Toftekær and Høgsberg (2019a) considers the two limiting eigenvalue problems from (1) with either SC and OC piezoelectric electrodes. The SC eigenvalue problem is obtained by direct wiring of the piezoelectric electrodes ( $Z_i = 0$ ), whereby  $\{V\} = \{0\}$  in (1) directly gives

$$([K^E] - \omega_j^2[M])\{U_j\} = \{0\} \quad (3)$$

introducing the SC natural frequency  $\omega_j$  and the mode shape  $\{U_j\}$  for mode  $j$ . The electric absorber response from the second equation in (1) is then obtained as a modal charge

$$\{Q_j\} = -[k_{me}^E]^t\{U_j\} \quad (4)$$

obtained alternatively as  $\{Q_j\} = \{I_j\}/(i\omega_j)$  from the current  $\{I_j\}$  in (2) with  $\omega = \omega_j$ , which can be readily measured in experiments. The OC limit corresponds to infinite shunt resistance ( $Z_i \rightarrow \infty$ ), implying a vanishing flow of current or  $\{Q\} = \{0\}$ . Elimination of  $\{V\}$  in the upper equation of (1) then determines the OC eigenvalue problem as

$$\left([K^E] + [k_{me}^E][C_p]^{-1}[k_{me}^E]^t - \hat{\omega}_j^2[M]\right)\{\hat{U}_j\} = \{0\} \quad (5)$$

defining the OC frequency  $\hat{\omega}_j$  and mode shape vector  $\{\hat{U}_j\}$ . For  $\{Q\} = \{0\}$  the second equation of (1) defines the modal voltage

$$\{\hat{V}_j\} = [C_p]^{-1}[k_{me}^E]^t\{\hat{U}_j\} \quad (6)$$

as the associated electric response amplitude. The evaluation of the two limiting (SC and OC) eigenvalue problems respectively determine the SC frequencies  $\omega_j$  and modal charge amplitudes  $\{Q_j\}$  and the corresponding OC frequencies  $\hat{\omega}_j$  and modal voltages in  $\{\hat{V}_j\}$ . These four modal parameters constitute the basis of the present shunt tuning procedure (Toftekær and Høgsberg, 2019a), which is verified in the following by experimental analysis.

The derivation of the tuning procedure applies a mixed modal projection of the SC and OC mode shapes, which expresses the effective EMCC

$$\kappa_j^2 = \frac{\hat{\omega}_j^2 - \omega_j^2}{\omega_j^2} = \frac{\{Q_j\}^t\{\hat{V}_j\}}{\tilde{m}_j\omega_j^2} \quad (7)$$

in terms of the modal charge, modal voltage and an intermediate modal mass  $\tilde{m}_j = \{U_j\}^t[M]\{U_j\}$ , which is approximately equal to the SC modal mass  $m_j = \{U_j\}^t[M]\{U_j\}$  for most practical cases with a limited change in the mode shape because of the inherent SC to OC stiffness increase. The modal equations are derived from a decoupling of the general vibration problem (1) by the modal representation  $\{U\} = [U]\{v\}$  with the SC mode shapes  $\{U_j\}$  contained as columns in the modal matrix  $[U]$  and the modal coordinates  $v_j$  collected in the vector  $\{v\}$ . Hereby, the upper mechanical equation in (1) uncouples as

$$(\omega_j^2 - \omega^2)v_j - \frac{\{Q_j\}^t}{m_j}\{V\} = 0 \quad (8)$$

for all vibration modes  $j = 1, 2, \dots, N$ , while the bottom electric equation in (1),

$$\sum_{j=1}^N \{Q_j\}v_j = \{Q\} - [C_p]\{V\} \quad (9)$$

still depends on the full range of modal coordinates  $v_j$ .

The influence from the non-resonant vibration modes on the optimum shunt tuning arises from the linear combination of modal charges in (9), which is undesirable to fully evaluate. Since (8) states that  $v_j$  is proportional to the voltage  $\{V\}$ , the influence from the non-resonant vibration modes around a target mode  $j = r$  may be approximated by an additional term to the blocked piezoelectric capacitance as

$$\begin{aligned} \{Q_r\}v_r &= \{Q\} - \left([C_p] + \sum_{j \neq r}^N \frac{\{Q_j\}\{Q_j\}^t}{m_j\omega_j^2} \frac{\omega_j^2}{\omega_j^2 - \omega^2}\right)\{V\} \\ &\simeq \{Q\} - [C_r]\{V\} \end{aligned} \quad (10)$$

The introduced effective modal capacitance matrix  $[C_r]$  is in the following assumed to be diagonal (Toftekær and Høgsberg, 2019a). An effective modal capacitance is evaluated by considering the modal equations (8) and (10) in the OC limit and then introducing the latter representation of the effective EMCC in (7). This results in the modal effective capacitance

$$(C_r)_i \simeq -\frac{(Q_r)_i}{(\hat{V}_r)_i} \quad (11)$$

for the  $i$ 'th piezoelectric absorber when  $\tilde{m}_j \simeq m_j$  is assumed. Upon introduction of the impedance relation

**Table 1.** Pure and modified single-mode calibration expressions for series shunt  $i$  components and effective EMCCs.

Method	Inductance ( $L_r$ ) <sub><math>i</math></sub>	Resistance ( $R_r$ ) <sub><math>i</math></sub>	EMCC $\kappa_r^2, \tilde{\kappa}_r^2$
Single	$\frac{ \hat{V}_r _i}{ Q_r _i \hat{\omega}_r^2 (1 + \kappa_r^2)}$	$\frac{ \hat{V}_r _i \sqrt{2\kappa_r^2}}{ Q_r _i \hat{\omega}_r (1 + \kappa_r^2)}$	$\frac{\hat{\omega}_r^2 - \omega_r^2}{\omega_r^2}$
Modified	$\frac{ \hat{V}_r _i}{ Q_r _i \hat{\omega}_r^2 (1 + \tilde{\kappa}_r^2)}$	$\frac{ \hat{V}_r _i \sqrt{2\tilde{\kappa}_r^2}}{ Q_r _i \hat{\omega}_r (1 + \tilde{\kappa}_r^2)}$	$\sum_{i=1}^{n_p} \frac{(Q_r)_i (\hat{V}_r)_i}{\{Q_r\}^t \{\hat{V}_r\}} \kappa_r^2$

$\{V\} = -i\omega\{Z(\omega)\}\{Q\}$  for the piezoelectric absorbers and the non-resonant modal approximation in (10), a governing characteristic equation for the target mode  $r$ ,

$$\left( \frac{\omega^2}{\omega_r^2} - i \frac{\omega}{\omega_r} \sum_{i=1}^{N_p} \frac{(\hat{V}_r)_i (Q_r)_i}{\{\hat{V}_r\}^t \{Q_r\}} \frac{1}{Z_i(\omega)(C_r)_i \omega_r} \right) \times \left( 1 - \frac{\omega^2}{\omega_r^2} \right) + \kappa_r^2 \frac{\omega^2}{\omega_r^2} = 0 \quad (12)$$

is then obtained from (8). In the present analysis the series  $LR$  shunt with  $Z_i(\omega) = R_i + i\omega L_i$  is preferred because the intrinsic resistance of the passive inductors used in the experiments can then be directly accounted for by  $R_i$  (Lossouarn et al., 2017). The modal characteristic equation is now obtained by substitution of  $Z_i(\omega) = R_i + i\omega L_i$  into (12), from which the principle of equal modal damping (Krenk and Høgsberg, 2013) then determines the effective single-mode tuning expressions presented in Table 1. The applied tuning procedure accounts for the influence from residual vibration modes directly by the modal voltage to charge ratio  $|\hat{V}_r|_i/|Q_r|_i$  contained in the derived calibration expressions (Toftekær and Høgsberg, 2019a).

When a subset  $n_p \leq N_p$  of all piezoelectric absorbers targets a specific vibration mode  $j = r$ , the presented single-mode calibration becomes non-optimal, as discussed in Toftekær and Høgsberg (2019a). The limited authority of the reduced number of absorbers can however be represented by a modified effective EMCC

$$\tilde{\kappa}_r^2 = - \sum_{i=1}^{n_p} \frac{(Q_r)_i (\hat{V}_r)_i}{\tilde{m}_r \omega_r^2} = \sum_{i=1}^{n_p} \frac{(Q_r)_i (\hat{V}_r)_i}{\{Q_r\}^t \{\hat{V}_r\}} \kappa_r^2 \quad (13)$$

which mainly alters the optimum shunt resistance, as seen from the tuning formulas in the bottom row of Table 1.

## Numerical results

The performance of the presented shunt tuning strategy is initially demonstrated numerically for the experimental setup with a free beam and five pairs of piezoceramic patches. The four piezoceramic patch pairs are shunted for vibration damping, while the fifth piezoceramic patch pair is used to induce structural vibrations. Dimensions and material properties of the beam and the piezoceramic patches are provided in the section Experiments. For the present numerical analysis the commercial FE-software

**Table 2.** Free beam with four piezoceramic patch pairs: Numerical SC and OC frequencies, effective EMCC, modal capacitances and optimum shunt components.

Flex. mode	1	2	3	4	5
$\omega/(2\pi)$ [Hz]	160.6	439.6	852.3	1398	2076
$\hat{\omega}/(2\pi)$ [Hz]	162.4	443.1	859.7	1410	2110
$\kappa_r^2$ [%]	2.31	2.06	1.72	1.77	3.26
$(C_r)_1$ [nF]	31.4	31.5	31.6	31.6	3.09
$(C_r)_2$ [nF]	31.4	31.5	30.9	32.0	31.1
$(C_r)_3$ [nF]	31.4	-	31.6	-	31.3
$(C_r)_4$ [nF]	31.4	31.6	33.2	30.8	31.3
$(L_r)_1$ [H]	29.85	4.01	1.07	0.396	0.179
$(L_r)_2$ [H]	29.86	4.02	1.09	0.391	0.177
$(L_r)_3$ [H]	29.86	-	1.07	-	0.176
$(L_r)_4$ [H]	29.87	4.01	1.01	0.406	0.176
$(R_r)_1$ [ $\Omega$ ]	6549	2263	1068	660.1	604.2
$(R_r)_2$ [ $\Omega$ ]	6551	2267	1095	651.3	599.1
$(R_r)_3$ [ $\Omega$ ]	6552	-	1070	-	596.0
$(R_r)_4$ [ $\Omega$ ]	6555	2262	1017	676.1	595.0

ANSYS is used, see Toftekær et al. (2019) for details on the implementation. The beam is discretized by  $180 \times 12 \times 3$  3D Solid186 elements, while each piezoceramic patch is modeled by  $12 \times 12 \times 1$  3D Solid226 coupled field elements. The natural frequencies and corresponding tuning parameters are for the lowest six modes determined by evaluation of the SC and OC eigenvalue problems in (3) and (5), respectively. The natural frequencies, effective modal capacitances (11) and series shunt components are summarized in Table 2. In the following section Experiments, the experimental shunt tuning results are compared by a percentage deviation to these numerical benchmark values. It should be noted that only the flexural vibration modes are considered in Table 2.

**Modal load** For the present free beam example the four piezoelectric absorbers target the flexural vibration modes 2 to 5, with the curves for the frequency response functions (FRFs) obtained by a full harmonic analysis of the discretized structure in ANSYS. Initially, the ideal modal load case  $\{f_r\} = [M]\{U_r\}$  is considered to verify the equal modal damping principle used to derive the present shunt tuning method in Table 1. The FRFs around the four target flexural vibration modes 2 to 5 can be seen in Figure 2(a,c,e,g) for the structure with the piezoelectric absorbers in OC condition (black dashed curves), with pure  $L$ -shunts (blue curves) and with optimum series  $LR$ -shunts (red curves). For each vibration mode  $r = 2$  to 5 in Figure 2, all four piezoelectric absorbers  $i = 1$  to 4 are calibrated specifically to that mode, as seen from the corresponding absorber voltage response in Figure 2(b,d,f,h).

Figure 2(a,c,e,g) shows that the vibration reduction provided by the  $LR$ -shunted piezoelectric absorbers (red curves) agrees well with the dynamic amplification factor  $1/(2\zeta_r)$ , estimated by the modal damping ratio  $\zeta_r = \sqrt{1/8\kappa_r^2}$  from Toftekær and Høgsberg (2019a) with the effective EMCC  $\kappa_r^2$  given in Table 1. For a proper inductance tuning the three (dashed, blue and red) curves in Figure 2(a,c,e,g) intersect for two neutral frequencies, at which the structural response magnitude is independent of the applied shunt resistance. Furthermore, the pure  $L$ -shunt

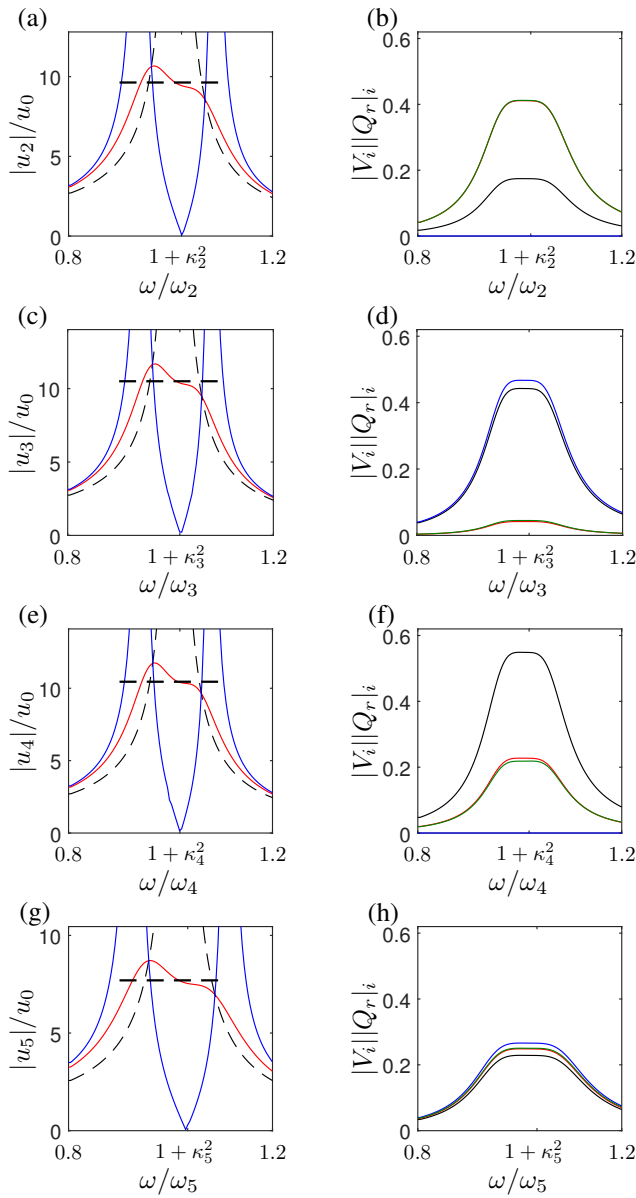


**Figure 2.** FRFs for free beam with 4 piezoelectric absorbers and modal load: Maximum modal displacements and voltages for damping of mode  $r = 2$  (a,b), 3(c,d), 4(e,f), 5(g,h). (a,c,e,g): black, blue and red curves are FRFs for OC condition,  $L$ - and  $LR$ -shunted absorbers, respectively. Horizontal dashed lines is  $1/(2\zeta_r)$ . (b,d,f,h): Black, red, blue and green curves represent voltage response for absorbers 1 to 4, respectively.

(blue curve) exhibits a clear anti-resonance point at  $\omega = \omega_r(1 + \kappa_r^2)$ , around which the two resonance frequencies of the blue curve are inverse points (Toftekær et al., 2019). Therefore, the FRFs for the pure  $L$ -shunt are in the following included to specifically assess the inductance calibration. The response curves in Figure 2(a,c,e,g) are not completely flat because the equal modal damping calibration (Krenk and Høgsberg, 2013) implies a slight declination towards higher frequencies. However, the equal modal damping principle secures a fully flat plateau in absorber response amplitude with a unit magnitude when normalized appropriately by the applied modal load  $\{f_r\}$ . Figure 2(b,d,f,h) verifies this condition, as the absorber voltage amplitudes at each resonance are exactly flat and add

up to unity. The flatness of the voltage FRFs are therefore a convenient indicator for the accuracy of the underlying shunt tuning.

**Electromechanical point load** In the experimental setups in the section Experiments a pair of piezoceramic patches is placed locally on the structure to excite structural vibrations. This load is modeled in ANSYS by applying an electric potential on the non-grounded interface electrode of the fifth piezoceramic patch pair (Toftekær et al., 2019). For this piezoelectric excitation, the FRFs around the four target vibration modes 2 to 5 are shown in Figure 3(a,c,e,g) for the tip beam displacements with the piezoelectric absorbers in OC condition (black dashed curves), with pure  $L$ -shunts (blue curves) and with the optimum  $LR$ -shunts (red curves). The corresponding voltage response amplitude curves are shown in Figure 3(b,d,f,h) for the absorbers 1 to 4.

For the electromechanical point load imposed by the fifth piezoceramic patch pair, the FRFs for the voltage response in Figure 3(b,d,f,h) are not entirely flat and thus non-optimal, while the tip displacement FRFs (red curves) in Figure 3(a,c,e,g) do not recover the precise inclination, presented for the ideal modal load case in Figure 2(a,c,e,g). However, as the absorber voltage amplitudes (b,d,f,h) are almost flat and the displacement amplitudes (a,c,e,g) are effectively reduced, the performance is practically optimal, even for this specific load case that inherently activates other non-targeted vibration modes. Furthermore, the blue curves for the pure  $L$ -shunt recover both the correct anti-resonance frequency  $\omega_r(1 + \kappa_r^2)$  and the neutral points. Thus, the numerical results in Figure 3 constitute an important benchmark for the assessment of the actual experimental results, presented in the section Experiments.

## Experimental shunt tuning

The experimental method follows the approach of the numerical implementation, in which the modal parameters are evaluated in the two limiting situations associated with SC and OC piezoelectric electrodes. The structure is excited by the fifth piezoelectric patch pair with a pseudo-random vibration signal within a given frequency interval and a certain intensity. In terms of noise, it has been found that this type of signal appears superior to other random excitation methods. For each shunt the electric current  $I(t)$  and the voltage  $V(t)$  response signals are then measured for the SC and OC conditions, respectively. The measurements are acquired over a sufficiently long time-span and fast sampling rate to gather sufficiently detailed experimental FRFs by a spectrum analyzer to obtain the natural frequencies and electrical amplitudes to be used in the tuning procedure. The FRF for the electric charge is obtained from the measured FRF for the electric current by simply applying (2). Thus, the required modal shunt tuning parameters are directly obtained from the resonant peaks in the charge and voltage FRFs, which are available from the shunt terminals without any assessment of the structural response.

## Influence of residual mode correction

The modal charge to voltage ratio, used (11) to estimate the effective modal capacitance, may be determined

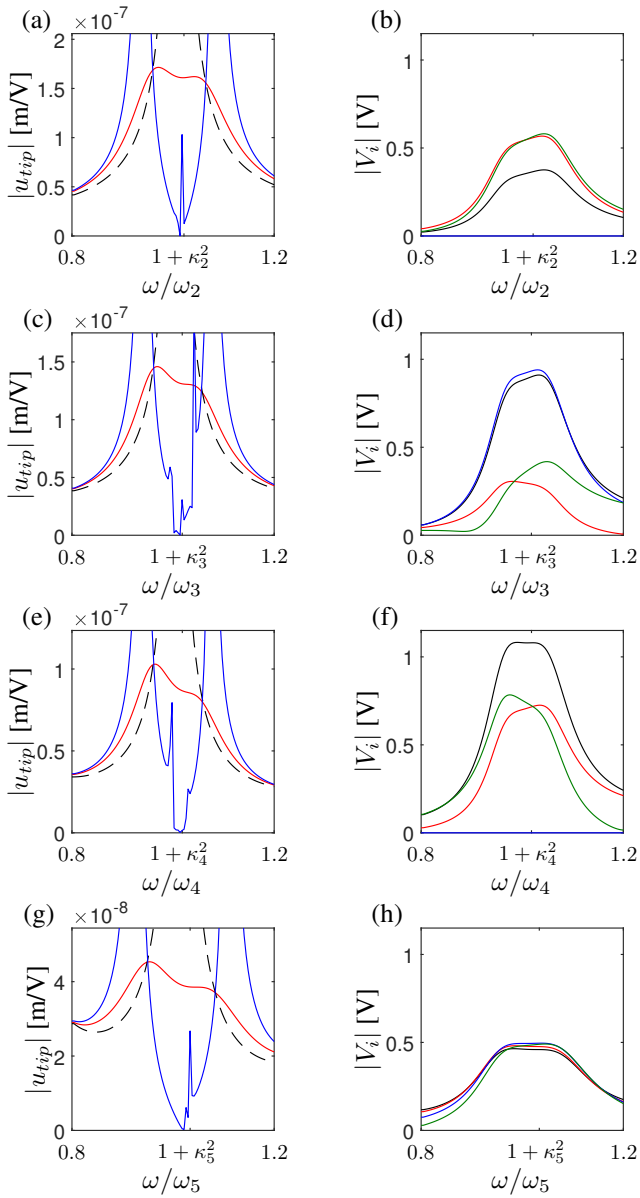


**Figure 3.** FRFs for free beam with 4 piezoelectric absorbers and electromechanical point load: Tip displacements and voltages for damping of mode  $r = 2$ (a,b), 3(c,d), 4(e,f), 5(g,h). (a,c,e,g): black, blue and red curves are FRFs for OC condition,  $L$ - and  $LR$ -shunted absorbers, respectively. (b,d,f,h): black, red, blue and green curves represent voltage response for absorbers 1 to 4, respectively.

experimentally by the ratio between the peaks in the charge and voltage FRFs. The effective modal capacitance  $(C_r)_i$  is the main shunt tuning parameter and in particular a precise inductance tuning is crucial for the final damping performance of the piezoelectric absorber.

For the series shunt inductance, the optimal tuning expression from Table 1 can be written in the traditional form

$$(L_r)_i = \frac{1}{(C_r)_i \hat{\omega}_r^2 (1 + \kappa_r^2)} \quad (14)$$

for which any tuning error is comprised by the modal capacitance  $(C_r)_i$ . For the traditional inductance tuning, based on a single-mode approximation without residual mode correction, the inductance is obtained by the similar

expression

$$(L_r^S)_i = \frac{1}{(\bar{C}_p^S)_i \hat{\omega}_r^2 (1 + \kappa_r^2)} \quad (15)$$

where the effective modal capacitance is simply replaced by the resulting blocked capacitance  $(\bar{C}_p^S)_i$ , which is usually evaluated from the stress-free piezoelectric capacitance  $C_p^T$  and the relevant coupling coefficient  $k$  provided by the manufacturer,

$$C_p^S = C_p^T (1 - k^2) \quad (16)$$

This resulting blocked capacitance is the actual blocked capacitance for a single piezoelectric element, while the resulting blocked capacitance depends on the specific wiring between several piezoelectric patches connected to a single shunt.

As mentioned in the Introduction, the literature describes the difference between the blocked capacitance  $C_p^S$  and a static capacitance  $C_p^0$ , measured at low frequencies when the piezoelectric element is bonded to the structure. The static capacitance is inherently larger than the blocked capacitance, yet smaller than the stress-free capacitance  $C_p^S < C_p^0 < C_p^T$ , as the boundaries of the piezoelectric element bonded to a flexible structure are only partially constrained in reality (Porfiri et al., 2007; de Marneffe and Preumont, 2008). For the shunt tuning to lower resonance frequencies this static capacitance will therefore provide a more accurate inductance tuning by

$$(L_r^0)_i = \frac{1}{(C_p^0)_i \hat{\omega}_r^2 (1 + \kappa_r^2)} \quad (17)$$

while the use of the blocked capacitance may instead be more accurate for damping of very high-frequency modes, since  $(C_r)_i \rightarrow (\bar{C}_p^S)_i$  for  $\omega \rightarrow \infty$  (de Marneffe and Preumont, 2008).

A common practice in experimental piezoelectric shunt tuning has been to determine an optimum inductance tuning based on either the blocked or the static capacitance, while the final fine-tuning has been performed by implementing the pure  $L$ -shunt and ensuring that the two split mode frequencies match the inverse frequency relation to the original target frequency (Toftekær et al., 2018). This has been a feasible method as the adjustable synthetic inductor (Fleming et al., 2000) has been widely used to emulate the required shunt inductance. However, recently it has been demonstrated that relatively large inductance values may in fact be realized passively by winding a copper wire around a magnetic core (Lossouarn et al., 2017). Whereas this provides a promising opportunity for the design of pure passive  $LR$ -shunts, it obviously eliminates the possibility to fine-tune and therefore requires a very precise prior inductance tuning, providing the desired number of wire turns in the passive inductor. Thus, it is the aim of this paper to demonstrate that the effective modal capacitance  $(C_r)_i$  in (11) secures an adequate and robust inductance tuning from (14) for the design of the passive inductor.

### The passive inductor

This section summarizes the main properties of and practical experiences with the design of the passive inductors introduced in Lossouarn et al. (2017), to which the reader



**Figure 4.** Passive inductor: (a) RM-core parts and (b) assembled inductor with  $n$  wire turns around center coil.

is referred for further details. In the present application a so-called RM-core is considered, see [Figure 4](#). It consists of the two parts in [Figure 4\(a\)](#) that are assembled around a coil with  $n$  wire turns to create the passive inductor shown in [Figure 4\(b\)](#). The passive inductor is designed to obtain the required inductance properties in an electric circuit, defined by the following ratio between the voltage and the rate of current,

$$L = \frac{V}{\omega I} \quad (18)$$

The voltage  $V$  may also be described in the frequency domain by the total flux  $\varphi$  through the  $n$  turns of the coil:  $V = n\omega\varphi$ . The magnetic flux then follows from the current as  $\varphi = n\mu(A_e/l_e)I$ , where the effective permeability  $\mu$ , the magnetic cross section  $A_e$  and the magnetic patch length  $l_e$  are properties provided by the core manufacturer. By combining these expressions, the inductance of the wounded coil becomes proportional to the square of  $n$ ,

$$L = A_L n^2 \quad , \quad A_L = \frac{\mu A_e}{l_e} \quad (19)$$

with  $A_L$  being the permeance or constant inductance factor.

It is a challenge in the manufacturing of passive inductors to achieve a tight and proper winding arrangement. For this purpose a CNC Guitar Pickup Mini Coil Winder has been used, which permits a sufficiently fine adjustment of coil and wire size, and furthermore winds the exact number of desired turns. Once the desired coil wire arrangement is achieved, it is furthermore important to fully clamp the RM-core to the coil. Even small variations in the clamping has been observed to significantly deteriorate the achieved inductance. It is strongly advised to the purchase RM-cores with a center hole that enables the use of adjustment screws for the fine-tuning of the inductance.

In the present experimental setup, the RM-cores in [Figure 4\(a\)](#) are without a center hole, whereby adequate fine-tuning has been performed by use of scotch and strips. Furthermore, an exact measurement of the realized inductance is important, as this may vary with frequency ([Lossouarn et al. , 2017](#)), temperature ([Darleux et al. , 2018](#)) and magnitude of the current ([Lossouarn et al. , 2018](#)). In the present case, the inductance has been measured by considering the voltage-current relation for the electric circuit inductor (18). By applying a suitable alternating voltage between the poles of the inductor, while measuring the flow of current with a high-quality multimeter, the achieved inductance is determined precisely for the specific excitation frequency. [Figure 5\(a\)](#) shows a measured electric current to a specific voltage excitation for the RM-core T38 with material properties provided in [Table 3](#) and  $n = 400$  wire turns. The theoretical inductance for these properties are

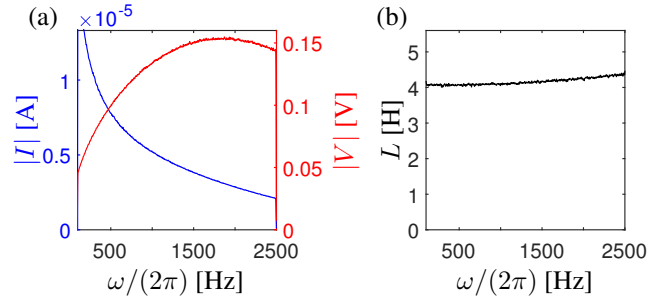


**Figure 5.** Effective inductance of passive inductor: (a) voltage excitation (red curve) and current response (blue curve) give effective inductance in (b).

**Table 3.** Geometry and properties of magnetic core.

RM-core	$A_e$ [mm <sup>2</sup> ]	$l_e$ [mm]	$B_{sat}$ [T]	$\mu_e$ [-]*	$A_L$ [ $\mu$ H]
T38	145	46	0.43	7070	28

\* $\mu_e = \mu/\mu_0$  with vacuum permeability  $\mu_0 = 0.4\pi\mu\text{H/m}$

$L = A_L n^2 = 4.48\text{H}$ , while the actual inductance obtained by measurements with (18) is shown in [Figure 5\(b\)](#) as function of the excitation frequency. It is found that the measured inductance is slightly lower than the theoretical estimate, corresponding to an inductance factor  $A_L \simeq 25\mu\text{H}$  that is smaller than the theoretical value ( $28\mu\text{H}$ ) in [Table 3](#) over the frequency interval of interest. Details on practical limitations of the passive inductors can be found in [Lossouarn et al. \(2017\)](#).

## Experiments

Experimental piezoelectric shunt damping of two plate-like structures is analyzed in the present section, where the data which reproduces the results presented in the following are available at [Toftekær and Høgsberg \(2019b\)](#). The general experimental setup can be seen in [Figure 6\(a\)](#), while [Figure 6\(b,c\)](#) shows the free beam and the free plate structure, each with five pairs of piezoceramic patches. In both experimental setups the fifth piezoceramic patch pair is connected to a power amplifier, which is controlled by the Laser Doppler Vibrometer acquisition software Polytec. The acquisition of the velocities measured by the Laser Doppler Vibrometer is also controlled by the Polytec acquisition software, whereby FRFs and mode shapes of the tested structures are readily available.

The shunt tuning of the piezoelectric absorbers is based on FRFs for current and voltage, as discussed in the section [Experimental shunt tuning](#). These FRFs are obtained by a 34465A Keysight Digital Multimeter, see [Figure 6\(a\)](#), which supports high-resolution acquisition of the direct current and voltage time histories. The precise geometries and material properties for the free beam and plate structures are presented in the following subsections. The free beam is primarily used to validate the numerical results obtained with the ANSYS 3D FE-model presented in the section [Numerical shunt tuning](#), while multi-modal damping of closely spaced vibration modes is addressed by the subsequent free plate experiment.

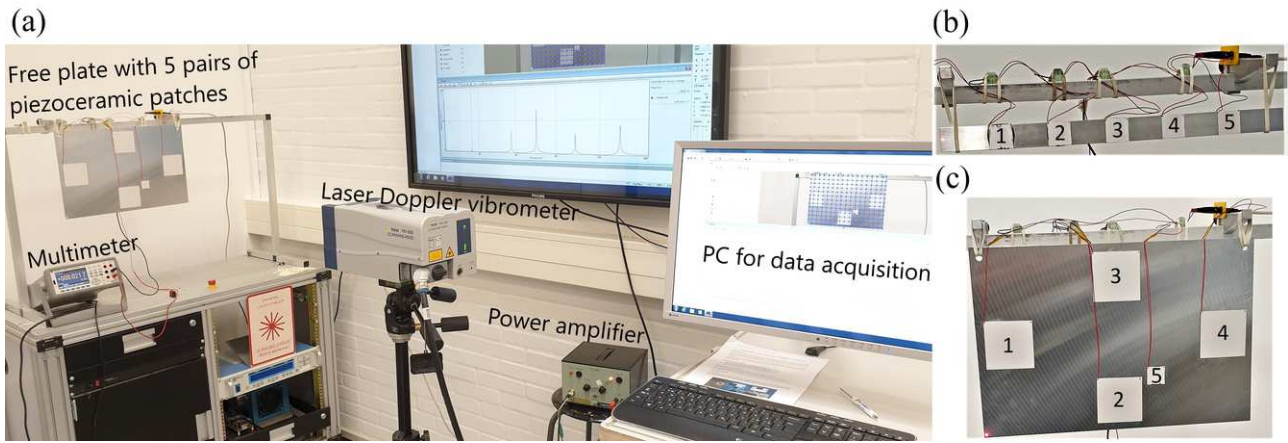


**Figure 6.** (a) Experimental setup and close-up of the tested free beam (b) and free plate (c), both with five pairs of piezoceramic patch pairs (1-5). Red points indicate location of laser deflection measurement at left beam tip in (b) and bottom left plate corner in (c).

### Free beam

The experimental results for the free beam with five pairs of piezoceramic patches in [Figure 6\(b\)](#) are presented and discussed in the present section. To realize free boundary conditions, the beam is hanging in two rubber bands ([Figure 6\(b\)](#)). The beam dimensions are  $450 \times 30 \times 6\text{mm}^3$  and the material is aluminum with a Young's modulus  $E_b = 71\text{GPa}$ , Poisson's ratio  $\nu_b = 0.33$  and density  $\rho_b = 2710\text{kg/m}^3$ . The five piezoceramic patches all have the same dimensions  $30 \times 30 \times 6\text{mm}^3$  and they are bonded to the beam with their center points placed in the one-sixth locations along the beam. The piezoceramic material is PZT 3265HD, purchased from [CTS \(2019\)](#), with full 3D material properties presented in [Table 4](#). The free capacitance  $C_p^T$  and in-plane coupling coefficient  $k_p$  for each piezoceramic patch have furthermore been provided by the manufacturer, while the mean values used in the experimental analysis are given in [Table 4](#). For each pair the two piezoceramic patches are glued with non-conductive EPO-TEK 320 epoxy to both sides of the sanded aluminum beam, followed by a one hour curing at  $130^\circ\text{C}$ . The non-conductive adhesive is used to avoid the risk of spill-over epoxy short-circuiting the electrodes of the thin piezoceramic patches. However, as each patch pair must be connected in series, the two inner electrodes must be electrically connected. This is ensured by applying a sufficient mechanical pressure during the curing to establish an electric connection between the inner electrodes and the aluminum beam, which then acts as the conductor between the two piezoceramic patches. Multi-filament cables are then soldered to the two outer piezoelectric electrodes, which can then be connected to the electric shunt. When bonded to the structure, the static capacitance ( $C_p^0$ ) of each pair of piezoceramic patches may be determined by an LCR-meter. The static capacitance may also be evaluated numerically by applying a unit static voltage to each pair of piezoceramic patches in the FE code ANSYS, while the corresponding charge (capacitance per unit voltage) is obtain as the corresponding electric response. Both the experimental and numerical (ANSYS) static capacitances  $C_p^0$  are provided in [Table 4](#). As previously discussed in the section [Experimental shunt tuning](#), the value of  $C_p^0$  appears between the free ( $\bar{C}_p^T$ ) and the blocked ( $\bar{C}_p^S$ )

**Table 4.** Stiffness components, stress piezoelectric coupling coefficients and blocked dielectric constants for PZT 3265HD ([CTS , 2019](#)).

Stiffness components [GPa]	Piezoelectric coupling [C/m <sup>2</sup> ]
$C_{11}^E, C_{22}^E$	$e_{31}, e_{32}$ -16.5
$C_{33}^E$	$e_{33}$ 30.3
$C_{12}^E$	$e_{24}, e_{15}$ 21.7
$C_{13}^E, C_{23}^E$	Blocked dielectric constants
$C_{44}^E, C_{55}^E$	$\varepsilon_{11}^S, \varepsilon_{22}^S$ $2465\varepsilon_0$
$C_{66}^E$	$\varepsilon_{33}^S$ $2100\varepsilon_0$
Material density [kg/m <sup>3</sup> ]	Plane coupling coefficient [-]
$\rho_{PZT}$ 8220	$k_p$ 0.66
Free, blocked and static capacitance (ANSYS) [nF]	
$\bar{C}_p^T = C_p^T/2$ 46.7	
$\bar{C}_p^S = \bar{C}_p^T(1 - k_p^2)$ 23.4	
$C_p^0$ 32.1	
Free, blocked and static capacitance (Experiment) [nF]	
$\bar{C}_p^T = C_p^T/2$ 47.2	$k_p$ [-] 0.54
$\bar{C}_p^S = \bar{C}_p^T(1 - k_p^2)$ 33.4	
$(C_p^0)_i$ 38.1	37.5 35.7 36.2

$\varepsilon_0 = 8.854 \times 10^{-12}\text{F/m}$ ; see [IEEE inc. \(1988\)](#)

capacitances, with  $\bar{(\ )}$  denoting the resulting capacitance from the series connection of the two patches in each piezoceramic pair.

**Experimental shunt tuning** The experimental shunt tuning method presented in the section [Experimental shunt tuning](#) is now applied, by initially imposing a pseudo-random vibration excitation to the free beam, while the piezoceramic patch pairs 1 to 4 are placed in the SC and OC conditions, respectively. In the present case the considered frequency range of the pseudo-random excitation is 100 – 2500Hz, while the excitation intensity is set to 2V. By use of a multimeter, the corresponding SC current and OC voltage time histories are measured between the outer electrodes of the piezoceramic patch pairs 1 to 4, with a sampling interval of  $1/(2 \times 2500\text{Hz}) = 200\mu\text{s}$  for a total of  $2^{20}$  samples. The Matlab build-in spectrum generator *pspectrum* is then used on the electric current and voltage time series to obtain the corresponding FRFs. [Figure 7\(a-d\)](#) shows the FRFs for the SC charge  $Q$  and OC voltage  $V$  for the piezoelectric

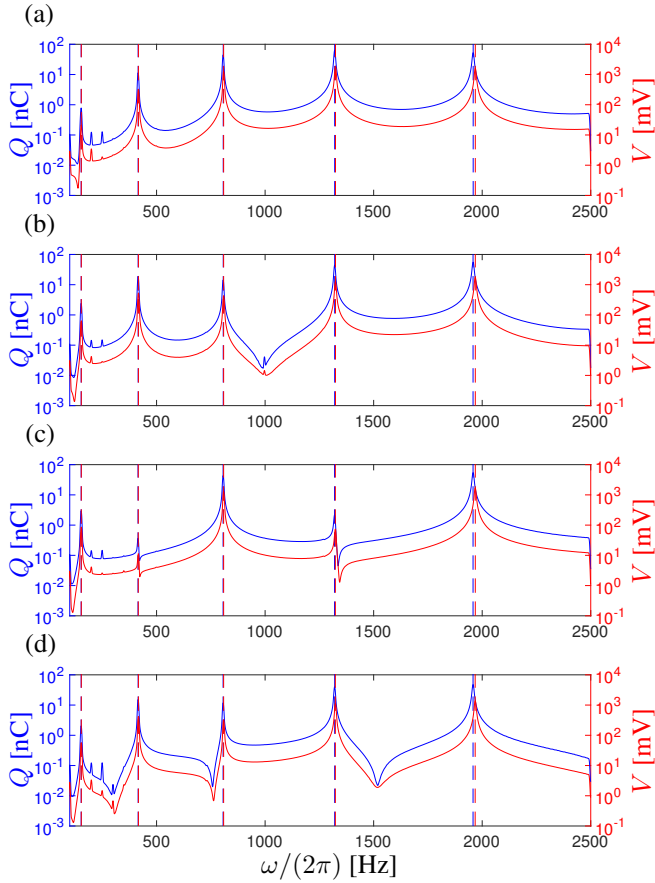


**Figure 7.** FRFs for measured SC charge (blue) and OC voltage (red) for piezoelectric absorbers 1-4 (a-d) on free beam.

absorbers 1 to 4. The charge FRF is obtained from the measured FRF of the electric current by the relation in (2).

The FRFs of the SC charge and OC voltage in **Figure 7** for the piezoelectric absorbers 1 to 4 contain all the information needed for conducting the shunt tuning to any target vibration mode in the analyzed frequency spectrum. It can immediately be seen that five resonant vibration modes may be targeted in the analyzed frequency spectrum, for which the modal charge and voltage are determined as the peak resonance values indicated in **Figure 7** by the vertical dashed blue and red lines, while the SC and OC frequencies are identified by the dashed lines intersections with the frequency axis. From the measured charge and voltage peak values the corresponding effective capacitances are then determined by (11) and provided in **Table 5**. The magnitude of the individual peak charge and voltage furthermore reveal which piezoelectric absorbers are suitably targeting which vibration mode. It is seen that the third piezoelectric absorber in **Figure 7(c)** may not be used to damp modes 2 and 3, while a closer inspection of the resonance peak values in **Figure 7(b,d)** indicate that the piezoelectric absorbers 2 and 4 are inadequate for damping of mode 3. An overview of all tuning values for all target modes is provided in **Table 5**. The table entries in red indicate which patch pairs are suitable for vibration damping of the particular mode 1 to 5.

As a supplement to the electric FRF, the physical response of the free beam has been measured using the Laser Doppler Vibrometer in **Figure 6**, which produces the experimental mode shapes in **Figure 8**. From these mode shapes and the

**Table 5.** Free beam with four piezoceramic patch pairs: Experimental SC and OC frequencies, effective EMCC, modal capacitances and optimum shunt tuning components based on charge and voltage FRFs in **Figure 7**.

Flex. mode	1	2	3	4	5
$\omega/(2\pi)$ [Hz]	152.6	415.0	806.8	1320	1958.0
$\hat{\omega}/(2\pi)$ [Hz]	153.2	416.2	808.9	1324	1968.1
$\kappa_r^2$ [%]	0.80	0.59	0.53	0.53	1.03
$(C_r)_1$ [nF]	36.7	35.6	35.1	33.6	33.0
$(C_r)_2$ [nF]	37.6	35.5	32.9	34.8	32.0
$(C_r)_3$ [nF]	34.4	32.3	33.1	29.5	32.6
$(C_r)_4$ [nF]	36.9	36.1	36.1	35.8	34.4
$(L_r)_1$ [H]	29.2	4.08	1.10	0.427	0.196
$(L_r)_2$ [H]	28.5	4.09	1.17	0.413	0.202
$(L_r)_3$ [H]	31.1	4.52	1.16	0.487	0.198
$(L_r)_4$ [H]	29.0	4.02	1.05	0.402	0.185
$(R_r)_1$ [ $\Omega$ ]	3550	1160	532	375	343
$(R_r)_2$ [ $\Omega$ ]	3470	1160	568	362	364
$(R_r)_3$ [ $\Omega$ ]	3800	1280	651	427	358
$(R_r)_4$ [ $\Omega$ ]	3540	1140	588	322	330

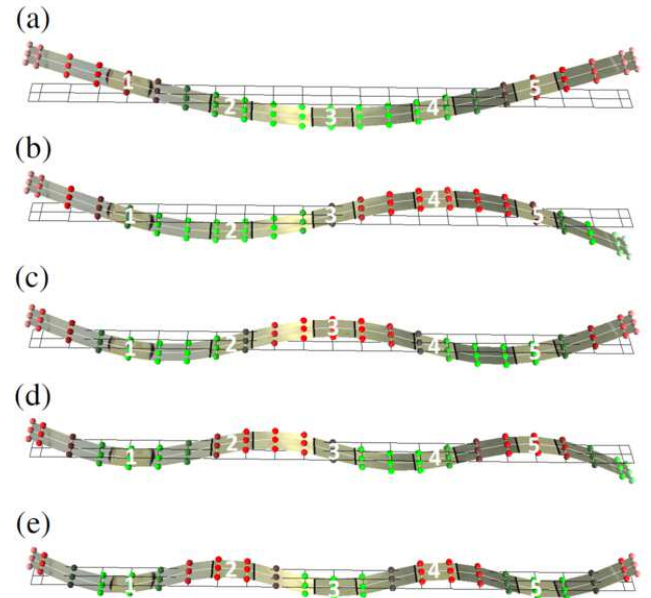


**Figure 8.** Experimental flexural mode shapes 1-5 (a-e) of the free beam with five pairs of SC piezoceramic patches.

position of the piezoelectric absorbers 1-4 it is seen that the (optimal) red entries in **Table 5** correspond to the cases, where the specific patch pair is located at a point with large curvature of the associated mode shape. Furthermore, it is seen that the homogeneous distribution of the piezoelectric absorbers along the beam is particularly optimal for the electromechanical coupling of mode 5 in **Figure 8(e)**, for which all absorbers experience almost maximum curvature.

When comparing the numerical results in **Table 2** to the experimental results in **Table 5**, it is seen that there is a noticeable deviation on the effective EMCC  $\kappa_r^2$ . This is due to the large experimental capacitances in **Table 5** and to the quality of the gluing of the piezoelectric patches to the aluminum beam, which is considered ideal in the numerical ANSYS model. The quality of the gluing is highly sensitive to small differences in the amount of epoxy and

also to the pressure applied during the curing process. In the present case generally too much epoxy have been applied between patches and beam, whereby a considerable amount of strain energy may be stored in the epoxy layer. However, besides the deviation in effective EMCC, a good agreement is observed for the resonance frequencies, the effective modal capacitances and the shunt tuning components. For the higher vibration modes the deviation between the numerical model and the experimental results increases slightly, which might occur because more FE elements are required in the numerical model to obtain the same accuracy on the higher vibration modes. However, an advantage of the present experimental shunt tuning method is that the tuning is based entirely on the piezoelectric absorber response, whereby the bonding quality and eventual material imperfections are inherently accounted for in the procedure.

**FRF analysis** The performance of the optimum shunt tuning is now analyzed by studying the FRFs based on the time response of the tip displacements, measured when the structure is excited with pseudo-random vibrations by the fifth piezoelectric patch pair. Four different damping cases are considered, in which all piezoelectric absorbers 1-4 are collectively shunted in turn to one of the target modes 2, 3, 4 and 5. Each resonant shunt is composed of the passive inductor presented in the section **The passive inductor**, connected in series with a potentiometer permitting an easy adjustment of the shunt resistance. The passive inductors are designed to achieve inductance values as close to the predetermined optimum tuning as possible. The required number of wire turns  $n$  are calculated by (19) with the constant attainable inductance factor  $A_L \simeq 25\mu\text{H}$  measured for the RM-core T38. The inductors to the target vibration modes 2, 3, 4 and 5 are designed with  $n = 400, 200, 130, 90$  wire turns, respectively. The fine-adjustment for each piezoelectric absorber tuning is subsequently done by simply changing the tightness of the RM-core clamping, as discussed in the section **The passive inductor**. Finally, the obtained inductance values are measured using the method presented in the section **The passive inductor**, from which the mean value and relative standard deviation (Std) in a frequency interval  $(0.8\omega_r - 1.2\omega_r)$  are determined and provided in **Table 6**. The deviation (Dev) between the exact tuning in **Table 5** and the passively obtained inductance around the target modes is also provided in **Table 6**, indicating a relatively good accuracy of the produced passive inductors.

The FRFs for the tip displacements around the target modes 2, 3, 4 and 5 with the piezoelectric absorber 1 to 4 shunted only by the passive inductors can be seen in **Figure 9(a,c,e,g)** by the blue solid curves, while the blacked dashed curves indicate the original OC response. Subsequently, the potentiometers are connected in series with the passive inductors and adjusted to the resistance values provided in **Table 6**. It is seen from the relative deviation to the optimum resistance tuning in **Table 5** that the implemented resistances are considerably lower than the optimum tuning. This is due to the inherent resistance of the passive inductor, which will not be analyzed in further detail. The FRFs for the tip displacements with the optimum  $LR$ -shunted absorbers can be seen in **Figure 9(a,c,e,g)** by the

**Table 6.** (Top) Passive inductances with relative standard deviations (Std) and (bottom) shunt resistance with relative deviation (Dev.) to desired optimum shunt tuning in **Table 5**.

Flex. mode	2	3	4	5
$(L_r)_1$ [H]	4.09	1.07	0.428	0.193
Std [%]	(0.43)	(0.30)	(0.39)	(0.48)
Dev.	0.31%	-2.54%	0.07%	-1.96%
$(L_r)_2$ [H]	4.07	-	0.411	0.203
Std [%]	(0.38)	-	(0.42)	(0.44)
Dev.	-0.61%	-	-0.56%	0.39%
$(L_r)_3$ [H]	-	1.17	-	0.201
Std [%]	-	(0.53)	-	(0.32)
Deviation	-	0.43%	-	1.15%
$(L_r)_4$ [H]	4.02	-	0.400	0.186
Std [%]	(0.32)	-	(0.45)	(0.46)
Dev.	-0.06%	-	-0.63%	-1.56%
$(R_r)_1$ [ $\Omega$ ]	750	250	250	250
Dev.	-35%	-53%	-33%	-27%
$(R_r)_2$ [ $\Omega$ ]	750	-	250	250
Dev.	-35%	-	-31%	-31%
$(R_r)_3$ [ $\Omega$ ]	-	250	-	250
Dev.	-	-62%	-	-3%
$(R_r)_4$ [ $\Omega$ ]	750	-	250	250
Dev.	-34%	-	-22%	-24%

red solid curves, while the corresponding absorber voltage responses for the piezoelectric absorbers 1 to 4 are provided in **Figure 9(b,d,f,h)**.

As discussed in the section **Numerical shunt tuning**, the present shunt tuning method is based on the principle of equal modal damping, which results in slightly inclined plateaus in the FRF for the displacements around the target resonant frequencies, see numerical results in **Figure 3(a,c,e,g)**. However, the method implies completely flat plateaus for the absorber voltage response in the case of an ideal modal load (**Figure 2(b,d,f,h)**) and almost flat plateau for an electromechanical point load case (**Figure 3(b,d,e,f)**). Therefore the validation of the experimental shunt tuning method is best performed by inspecting the absorber voltage response in **Figure 9(b,d,e,f)**, from which it can be seen that the FRF for the four absorbers around the four target frequencies are relatively flat, with the exception of the absorber response around target mode 3 in **Figure 9(d)**, in which the inductances for absorber 1 and 3 seem, respectively, too low and too high. However, this tendency is seen to agree with the deviation for the implemented passive inductors in the third column of **Table 6**. Small deviations from the optimum flat plateau may also be encountered for the other three target modes, but in all cases the tendency seem to follow the deviation between the optimum inductances in **Table 5** and the implemented inductances in **Table 6**. By inspection of the FRFs for the tip displacements with the implemented  $LR$ -shunts (red curves) in **Figure 9(a,c,e,g)** it is seen that these have the same form as those obtained in the numerical example in **Figure 3**. For target modes 2,3 and 4 in **Figure 9(a,c,e)** the plateau inclination is however too large, while the opposite inclination for target mode 5 in **Figure 9(g)** occurs because of a too large inductance. The present FRFs for

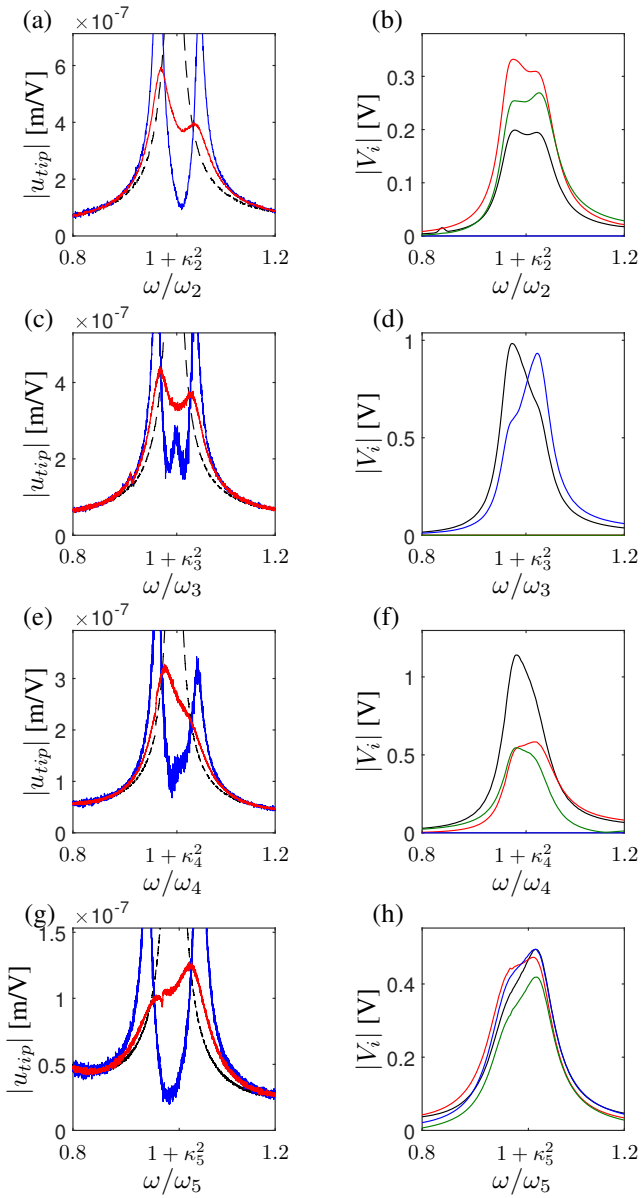


**Figure 9.** Experimental FRFs for free beam with 4 piezoelectric absorbers and electromechanical point load. Tip displacements and voltages for damping of mode  $r = 2$  (a,b), 3(c,d), 4(e,f), 5(g,h). (a,c,e,g): black, blue and red curves are FRFs for OC,  $L$ - and  $LR$ -shunted absorbers, respectively. (b,d,f,h): black, red, blue and green curves represent voltage response for absorbers 1 to 4, respectively.

the free beam experiment show that the proposed shunt tuning method, based on experimental FRFs for the charge and voltage signals from the four piezoelectric absorbers, appears robust, as it approximately recovers the desired frequency response characteristics across the full frequency range, with deviations likely associated with inaccuracies in the produced passive inductances.

*Inductance from blocked and static capacitance* As discussed in the section **Experimental shunt tuning** it is particular important to obtain a precise inductance tuning, as even small deviations may substantially detune the shunt absorbers and because the use of passive inductors will not allow any straightforward fine tuning. The inductance tuning in (17) and in (15) is based on the static capacitance

**Table 7.** Shunt inductance tuning based on the experimental static  $(C_p^0)_i$  and blocked  $\bar{C}_p^S$  capacitances (Table 4). Deviation (Dev) relative to the tuning in Table 5 based on effective modal capacitance  $(C_r)_i$ .

Flex. mode	1	2	3	4	5
$(L_r^0)_1$ [H]	28.1	3.82	1.01	0.378	0.170
$(L_r^0)_2$ [H]	28.5	3.87	1.03	0.383	0.172
$(L_r^0)_3$ [H]	30.0	4.07	1.08	0.400	0.181
$(L_r^0)_4$ [H]	29.0	4.02	1.06	0.397	0.179
Mean Dev. [%]	-1.3	-5.4	-6.6	-9.3	-10
$(L_r^S)_i$ [H]	32.0	4.35	1.15	0.430	0.194
Mean Dev. [%]	8.7	4.1	2.7	-0.6	-1.4

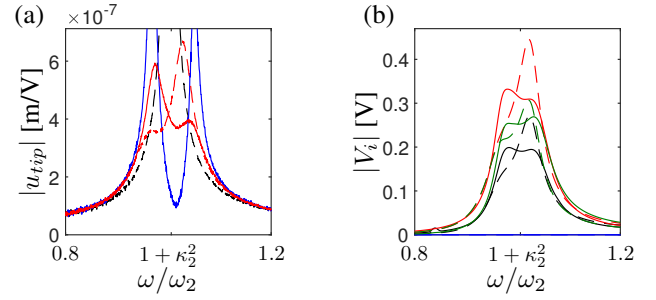


**Figure 10.** Experimental FRF for mode  $r = 2$  for free beam with 4 piezoelectric absorbers and electromechanical point load. Absorbers tuned with effective modal capacitance  $(C_r)_i$  (red solid curves) and with static capacitance  $C_p^S$  (red dashed curves). Corner displacements in (a), voltage response in (b) for absorbers 1 (black) and 4 (green) for the tuning based on  $(C_r)_i$  (solid curves) and  $C_p^S$  (dashed curves).

$(C_p^0)_i$  and the blocked capacitance  $\bar{C}_p^S$ , respectively. These inductances in Table 7 are determined based on the measured capacitances in Table 4 and used to illustrate the potential detuning associated with the exclusion of the residual mode contribution contained in the effective modal capacitance  $(C_r)_i$  in (11). It can be seen from Table 7 that the inductance tuning based on the static capacitance  $C_p^0$  is relatively accurate for the lower-frequency modes, while the blocked capacitance  $C_p^S$  becomes better for target modes with higher frequencies. This agrees with the tendency of the dynamic capacitance, which approaches the blocked capacitance for increasing frequency. However, the use of either the static or the blocked capacitance for the inductance tuning may therefore cause errors in the high- or low-frequency limits, respectively.

Figure 10 shows the FRF for the tip beam deflection (a) and shunt voltage (b) for target mode  $r = 2$ . The red solid curve represents the present tuning based on the effective modal capacitance  $(C_r)_i$ , while the red dashed curve is for the associated blocked capacitance  $C_p^S$ . The passive inductors used in the experiment for the tuning based on the blocked capacitance are designed with  $n = 415$  wire turns, whereby the inductance values are  $(L_2)_1 = 4.33\text{H}$ ,  $(L_2)_2 = 4.36\text{H}$  and  $(L_2)_4 = 4.32\text{H}$ , with a relative standard deviation to the numerical values of 0.46%, 0.43% and 0.51%, respectively. The present tuning based on  $(C_r)_i$  results in an increased inclination of the plateau in the response FRF in Figure 10(a), whereas the inductance tuning based on the blocked capacitance  $C_p^S$  has an entirely opposite inclination,

indicating a substantially detuning. For the voltage FRF in [Figure 10\(b\)](#) the present tuning method provides almost flat plateaus, while for the blocked capacitance tuning the dashed curves exhibit substantial peaks.

### Free plate

The second experiment concerns the free plate with five pairs of piezoceramic patches in [Figure 6\(c\)](#). The plate dimensions are  $450 \times 300 \times 6\text{mm}^3$  and it is made of aluminum with a Young's modulus  $E_b = 71\text{GPa}$ , Poisson's ratio  $\nu_b = 0.33$  and material density  $\rho_b = 2710\text{kg/m}^3$ . The piezoceramic material is the same as in the previous experiment with full 3D material properties provided in [Table 4](#). In the present setup the fifth pair of piezoceramic patches with dimensions  $30 \times 30 \times 0.5\text{mm}^3$  is used to excite structural vibrations, while the remaining pairs 1 to 4 with the dimensions  $75 \times 75 \times 0.5\text{mm}^3$  are shunted for vibration mitigation. The piezoelectric patch pairs 1 and 4 are centered along the vertical y-axis (short plate side), while their center is located respectively 50mm from the left and right plate edges. Similarly, the piezoelectric patch pair 2 and 3 are centered along the horizontal x-axis (long plate side), with the patch center located 50mm from the bottom and top plate edges, respectively. Finally, the fifth piezoceramic patch pair is placed with its center at respectively 287.5mm and 87.5mm along the x and y directions from the bottom left plate corner. All the piezoceramic patches are glued to the aluminum plate using the approach described for the free beam experiment in the previous subsection.

The free capacitance and in-plane piezoelectric coupling coefficient of the piezoceramic patches (pair 1 to 4) have been provided by [CTS \(2019\)](#), from which the resulting free  $\bar{C}_p^T$  and blocked  $\bar{C}_p^S$  capacitances for the series connected patch pairs are determined and summarized in [Table 8](#). Furthermore, the static capacitances  $(C_p^0)_i$  of the piezoceramic patch pairs 1-4 have been measured and provided in [Table 8](#).

It can be seen that the four static capacitances  $(C_p^0)_i$  in [Table 8](#) appear as expected between the blocked  $\bar{C}_p^S$  and free  $\bar{C}_p^T$  capacitances. However, in the present case the static capacitances are in general closer to the free capacitance, which indicates a poorer bonding between the patches and the plate, whereby the patches become less constrained. The reason for the poor bonding is mainly due to insufficient pressure applied on to the fairly large piezoelectric patches during the curing process.

**Experimental shunt tuning** The shunt tuning procedure in the section [Experimental shunt tuning](#) is now applied by initially exciting plate vibrations with a pseudo-random vibration signal in the frequency interval from 100 – 800Hz. The SC current and OC voltage response signals are then measured between the interface electrodes of the

**Table 8.** Free, blocked and static capacitance of the piezoceramic patch pairs 1-4 in [Figure 6\(c\)](#).

Free, blocked and static capacitance (Experiment) [nF]				
$\bar{C}_p^T = C_p^T/2$	298	$k_p$ [-]	0.62	
$\bar{C}_p^S = \bar{C}_p^T(1 - k_p^2)$	185			
$(C_p^0)_i$	254	245	233	252

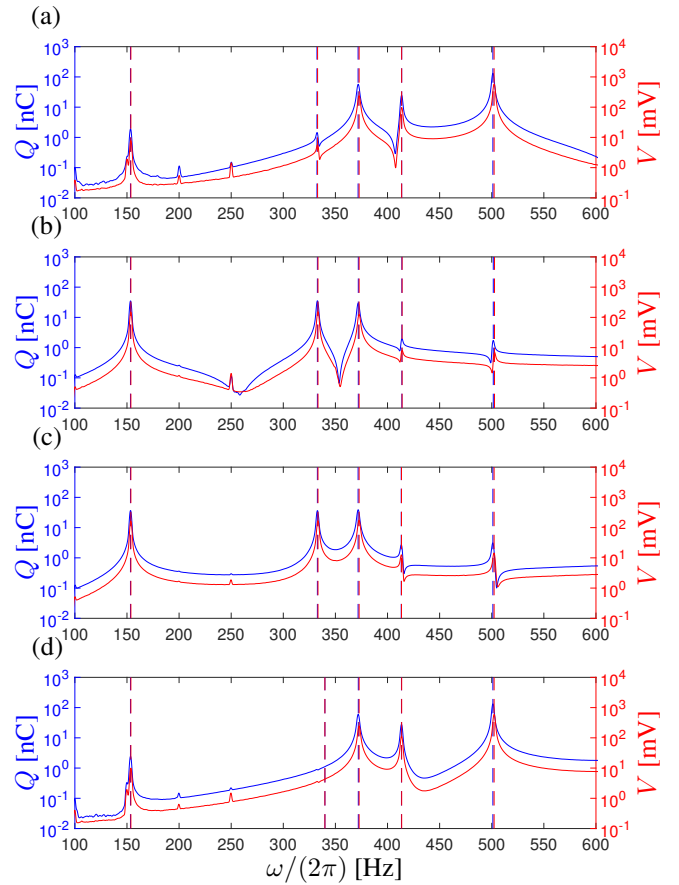


**Figure 11.** FRF for measured SC charge (blue) and OC voltage (red) for piezoelectric absorbers 1-4 (a-d) on free plate.

piezoelectric absorbers 1-4. The electric absorber response is measured with a sampling interval of  $1/(2 \times 800\text{Hz}) = 625\mu\text{s}$  for a total of  $2^{19}$  samples. Subsequently, the build-in Matlab spectrum generator *pspectrum* is used on the absorber current and voltage time series to obtain the corresponding FRFs shown in [Figure 11](#). The FRF for the charge is obtained by (2) from the FRF of the measured electric current.

It can be seen from the FRFs of the SC charge and OC voltage in [Figure 11](#) that five resonant vibration modes are excited in the analyzed frequency interval. The vibration response of the plate is measured by the Laser Doppler Vibrometer and the first six modes are shown in [Figure 12](#). It is found that the first free plate mode in [Figure 12\(a\)](#) at 149.5Hz is not apparent in the FRFs for the measured current and voltage in [Figure 11](#), since the four piezoelectric absorbers are either exposed to in-plane shear or located in a nodal point of the vibration mode in [Figure 12\(a\)](#).

The shunt tuning parameters for the vibration modes 2 to 6 are now determined directly from the FRFs for charge and voltage by their respective peak values, indicated by the vertical dashed lines in [Figure 11](#), which also determine the corresponding SC and OC frequencies. The effective modal capacitances  $(C_r)_i$  are then evaluated from the peak charge and voltage values according to (11). They are given in [Table 9](#) together with the optimum series shunt tuning parameters. It is seen from the peak charge and voltage values that the absorber 1 and 4 in [Figure 11\(a,d\)](#) are not applicable for damping of modes 2 and 3, while the absorbers

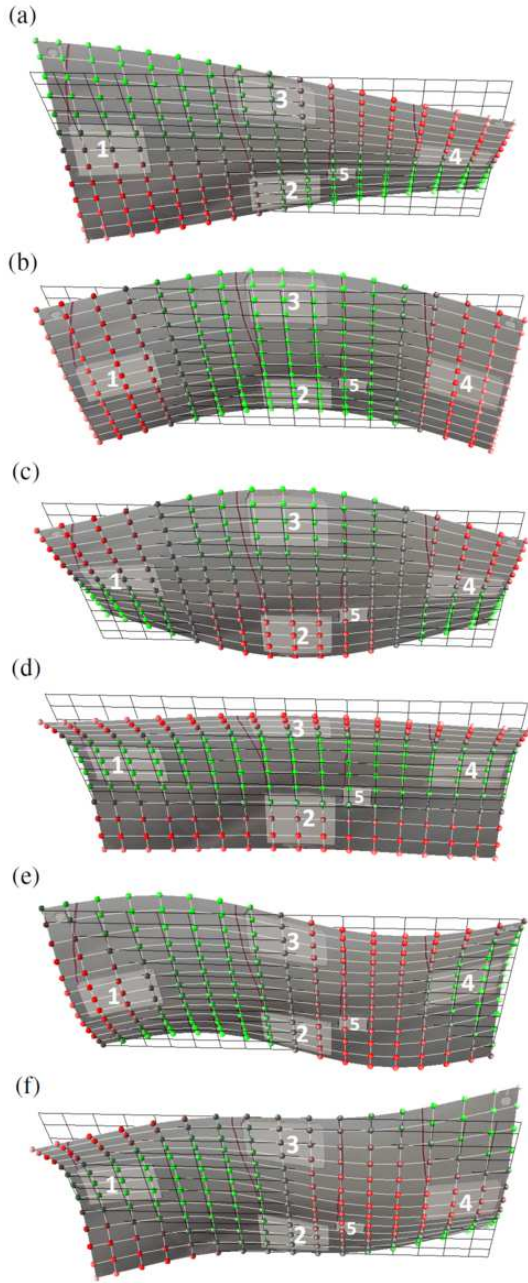


**Figure 12.** Resonant vibration modes 1-6 (a-f) of the free plate with SC piezoceramic patches.

2 and 3 in [Figure 11\(b,c\)](#) have very limited authority on modes 5 and 6. An overview of all tuning values for all target modes is provided in [Table 5](#), in which those values in red constitute the suitable shunt configurations.

The passive inductors are designed according to the procedure in the section [The passive inductor](#) with the aim of achieving the optimum inductance tuning provided in [Table 9](#) for the targeted modes 2, 3, 4 and 6 with considerable electromechanical coupling. For each of the four targeted modes the inductors emphasized in red in [Table 9](#) have been wound with  $n = 420, 450$  turns for mode 2,  $n = 198, 200$  turns for mode 3, four times  $n = 180$  turns for mode 4 and  $n = 125, 127$  turns for mode 6. [Table 10](#) provides the corresponding mean inductance values around the target frequencies ( $0.8\omega_r - 1.2\omega_r$ ), the relative standard deviation

**Table 9.** Free plate with four piezoceramic patch pairs: Experimental SC and OC frequencies, effective EMCC, modal capacitances and optimum shunt tuning components based on charge and voltage FRFs in [Figure 11](#).

Mode	Experimental results				
	2	3	4	5	6
$\omega/(2\pi)$ [Hz]	153.4	332.7	371.9	413.5	501.1
$\hat{\omega}_2/(2\pi)$ [Hz]	153.7	333.3	372.7	413.6	502.3
$\kappa_r^2$ [%]	0.51	0.35	0.47	0.05	0.47
$(C_r)_1$ [nF]	243.7	250.4	<b>239.8</b>	<b>252.5</b>	<b>223.6</b>
$(C_r)_2$ [nF]	<b>235.8</b>	<b>230.6</b>	<b>235.0</b>	240.7	244.5
$(C_r)_3$ [nF]	<b>225.7</b>	<b>217.9</b>	<b>223.4</b>	213.7	216.1
$(C_r)_4$ [nF]	246.9	259.3	<b>243.2</b>	<b>245.1</b>	<b>222.3</b>
$(L_r)_1$ [H]	4.38	0.907	<b>0.756</b>	<b>0.586</b>	<b>0.446</b>
$(L_r)_2$ [H]	<b>4.52</b>	<b>0.986</b>	<b>0.771</b>	0.613	0.408
$(L_r)_3$ [H]	<b>4.72</b>	<b>1.04</b>	<b>0.812</b>	0.693	0.462
$(L_r)_4$ [H]	4.32	0.876	<b>0.745</b>	<b>0.604</b>	<b>0.449</b>
$(R_r)_1$ [ $\Omega$ ]	427	159	<b>172</b>	<b>149</b>	<b>137</b>
$(R_r)_2$ [ $\Omega$ ]	<b>441</b>	<b>173</b>	<b>175</b>	156	125
$(R_r)_3$ [ $\Omega$ ]	<b>461</b>	<b>183</b>	<b>184</b>	176	141
$(R_r)_4$ [ $\Omega$ ]	421	151	<b>169</b>	<b>153</b>	<b>138</b>

**Table 10.** (Top) Passive inductances with relative standard deviations (Std) and (bottom) shunt resistance with relative deviation (Dev.) to desired optimum shunt tuning in [Table 9](#).

Mode	2	3	4	6
$(L_r)_1$ [H]	-	-	0.760	0.444
Std [%]	-	-	(0.62)	(0.62)
Deviation	-	-	0.48%	-0.64%
$(L_r)_2$ [H]	4.53	0.986	0.790	-
Std [%]	(0.41)	(0.54)	(0.53)	-
Deviation	0.29%	0.06%	2.30%	-
$(L_r)_3$ [H]	4.70	1.05	0.811	-
Std [%]	(0.53)	(0.44)	(0.66)	-
Deviation	-0.47%	0.41%	-0.19%	-
$(L_r)_4$ [H]	-	-	0.751	0.446
Std [%]	-	-	(0.57)	(0.44)
Deviation	-	-	0.60%	-0.77%
$(R_r)_1$ [ $\Omega$ ]	-	-	100	80
Deviation	-	-	-42%	-41%
$(R_r)_2$ [ $\Omega$ ]	250	100	100	-
Deviation	-43%	-42%	-43%	-
$(R_r)_3$ [ $\Omega$ ]	250	100	100	-
Deviation	-46%	-45%	-46%	-
$(R_r)_4$ [ $\Omega$ ]	-	-	100	80
Deviation	-	-	-41%	-42%

and the deviation relative to the optimum inductance tuning in [Table 9](#).

**FRF analysis** The deviations in [Table 10](#) indicate that the produced passive inductors are in good agreement with the desired optimum shunt tuning in [Table 9](#). [Figure 13](#) shows the FRFs for the measured corner (cor) displacement of the free plate structure in (a,c,e,g) and the corresponding voltage across the patch electrodes in (b,d,f,h). The blue solid curves in [Figure 13\(a,c,e,g\)](#) represent the pure  $L$ -shunts for the absorbers 1 to 4, which appear to have two well-separated peaks with a minimum close to  $\omega = \omega_r(1 + \kappa_r^2)$ . When introducing the shunt resistance from [Table 10](#) in series with

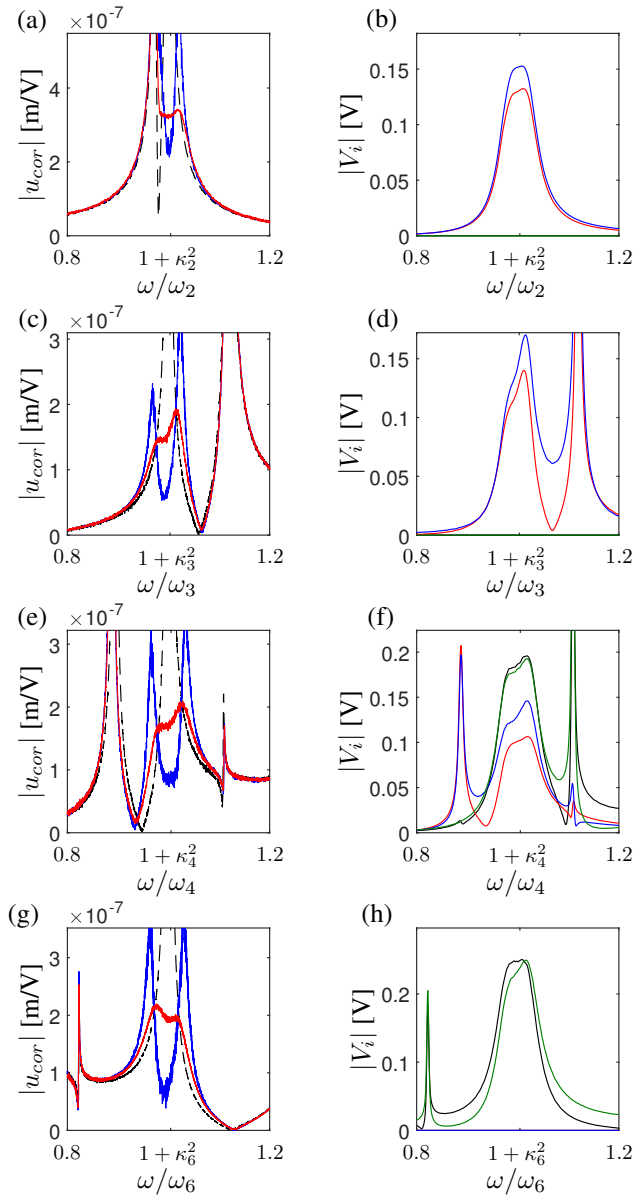


**Figure 13.** Experimental FRF for free plate with 4 piezoelectric absorbers. Corner displacements and voltages for damping of mode  $r = 2$ (a,b), 3(c,d), 4(e,f), 5(g,h). (a,c,e,g): black, blue and red curves are FRFs for OC,  $L$ - and  $LR$ -shunted absorbers, respectively. (b,d,f,h) black, red, blue and green curves represent voltage response for absorbers 1 to 4, respectively.

the passive inductors, the red curves in [Figure 13](#)(a,c,e,g) become almost flat around resonance. Furthermore, the absorber voltage response in [Figure 13](#)(b,d,f,h) is practically flat, which indicates a proper shunt tuning.

A pronounced resonance peak in the FRF for the plate corner displacement can be seen around the target mode 2 in [Figure 13](#)(a), which occurs because of the closely spaced resonant mode 1 in [Figure 12](#)(a), not damped by the piezoelectric absorbers. To avoid the influence of mode 1, the response for target mode 2 may instead be analyzed by considering the FRF for the displacements of the center point on the left plate edge, where mode 1 in [Figure 12](#)(a) has a nodal point. [Figure 14](#)(a) shows the FRF for this new measuring point, which exhibits a flat plateau around target mode 2.

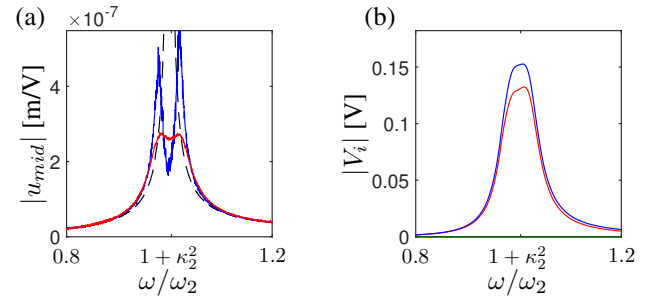


**Figure 14.** Experimental FRF for mode  $r = 2$  for free plate with 4 piezoelectric absorbers. (a) Displacement at center point on the left plate edge and (b) voltage response. (a): black, blue and red curves are FRFs for OC, and  $L$ - and  $LR$ -shunted absorbers, respectively. (b): black, red, blue and green curves represent voltage response for absorbers 1 to 4, respectively.

### Inductance based on blocked and static capacitance

The influence of neglecting the residual mode contributions in the shunt inductance tuning is analyzed by tuning the inductances based on the static  $(C_p^0)_i$  and blocked  $C_p^S$  capacitances in [Table 8](#). These inductance values are provided in [Table 11](#) along with the mean deviations relative to the optimum inductance tuning in [Table 9](#). The comparison in [Table 11](#) shows that the static capacitance  $(C_p^0)_i$  is most accurate for the lower modes, while its deviation increases with frequency, confirming the observations from the previous free beam experiments. The opposite tendency is found for the tuning based on the blocked capacitance  $C_p^S$ , which becomes less imprecise for higher target modes.

The influence on the damping performance, when using the inductance based on the static capacitance, is finally analyzed by considering the FRF for the plate corner displacements around target mode 6 shown in [Figure 15](#)(a) with the corresponding absorber voltage response in [Figure 15](#)(b). The exactly implemented inductors used in the experiment have mean inductance values around the target mode 6 given by  $(L_6^0)_1 = 0.399\text{H}$  and  $(L_6^0)_4 = 0.406\text{H}$ , thus slightly larger than the tuning values indicated in red for mode 6 in [Table 11](#). It is clearly seen in [Figure 15](#) that the piezoelectric absorbers are severely detuned when the inductances are based on the static capacitances (red dashed curves) compared to the response with optimally tuned absorbers (red solid curves) based on the effective modal capacitances. This demonstrates the importance of

**Table 11.** Shunt inductance tuning based on the experimental static  $(C_p^0)_i$  and blocked  $C_p^S$  capacitances in [Table 8](#) and the mean relative deviation (Dev) to the optimum tuning with residual mode contribution in [Table 9](#).

Flex. mode	2	3	4	5	6
$(L_r^0)_1$ [H]	4.19	0.893	<b>0.713</b>	<b>0.581</b>	<b>0.392</b>
$(L_r^0)_2$ [H]	<b>4.35</b>	<b>0.926</b>	<b>0.740</b>	0.603	0.407
$(L_r^0)_3$ [H]	<b>4.57</b>	<b>0.974</b>	<b>0.777</b>	0.634	0.428
$(L_r^0)_4$ [H]	4.23	0.901	<b>0.719</b>	<b>0.587</b>	<b>0.396</b>
Mean Dev. [%]	-3.3	-2.8	-4.4	-3.4	-7.9
$(L_r^S)_i$ [H]	5.78	1.23	0.981	0.800	0.540
Mean Dev. [%]	29	29	27	28	23

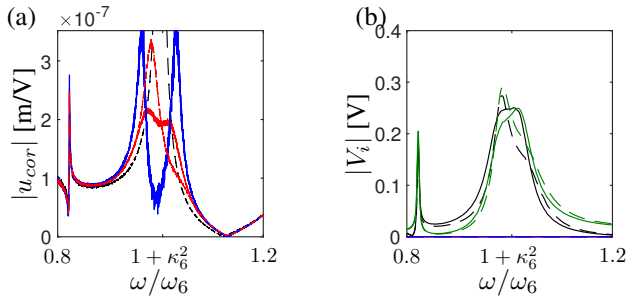


**Figure 15.** Experimental FRF for mode  $r = 6$  for free plate with 4 piezoelectric absorbers. Absorbers tuned with effective modal capacitance  $(C_r)_i$  (red solid curves) and with static capacitance  $C_p^S$  (red dashed curves). Corner displacements in (a), voltage response in (b) for absorbers 1 (black) and 4 (green) for the tuning based on  $(C_r)_i$  (solid curves) and  $C_p^S$  (dashed curves).

**Table 12.** Modified effective EMCC and corresponding series shunt tuning of the plate bonded piezoelectric absorbers 1 to 4 in Figure 6(c). (...): Implemented resistances.

Mode	Multi-mode tuning			
	3 and 4	Dev.	2, 3, 4 and 6	Dev.
$\tilde{\kappa}_3^2$ [%]	-		0.23	-51%
$\tilde{\kappa}_3^3$ [%]	0.35	-0.1%	0.16	-53%
$\tilde{\kappa}_4^2$ [%]	0.34	-27%	0.27	-47%
$\tilde{\kappa}_6^2$ [%]	-		0.18	-62%
$(L_r)_1$ [H]	0.758	0.1%	0.448	0.2%
$(L_r)_2$ [H]	0.988	0.0%	0.987	0.2%
$(L_r)_3$ [H]	1.043	0.0%	4.735	0.2%
$(L_r)_4$ [H]	0.747	0.1%	0.748	0.2%
$(R_r)_1$ [ $\Omega$ ]	147(70)	-16%	96(50)	-30%
$(R_r)_2$ [ $\Omega$ ]	172(100)	0.0%	119(50)	-31%
$(R_r)_3$ [ $\Omega$ ]	183(100)	0.0%	337(125)	-27%
$(R_r)_4$ [ $\Omega$ ]	144(70)	-16%	105(40)	-38%

considering the residual mode contributions by the shunt tuning contained in the effective modal capacitances  $(C_r)_i$  obtained by (11).

**Multi-mode damping** Simultaneous damping of several vibration modes is now considered by calibrating the piezoelectric absorbers to different target modes. Initially, simultaneous damping of the closely spaced vibration modes 3 and 4 is considered by tuning the absorbers 2 and 3 to mode 3, while absorbers 1 and 4 target mode 4. Subsequently, the four piezoelectric absorbers 1 to 4 are respectively tuned to modes 6, 3, 2 and 4, for simultaneous damping of all four vibration modes.

As discussed in the section **Numerical shunt tuning** the optimum multi-mode shunt tuning is based on the same charge and voltage FRF curves, by evaluating the modified effective EMCC  $\tilde{\kappa}_r^2$  in (13), which only considers the coupling of the piezoelectric absorber(s) tuned to the specific targeted mode. Therefore, the multi-mode shunt tuning of the piezoelectric absorbers is based on the FRFs for measured charge and voltage in Figure 11, which has also previously been used for the single-mode tuning. Table 12 provides the modified effective EMCC, the corresponding  $LR$ -shunt tuning and its deviation from the basic single-mode tuning for simultaneous damping of modes 3 and 4 and for simultaneous damping of modes 2, 3, 4 and 6.

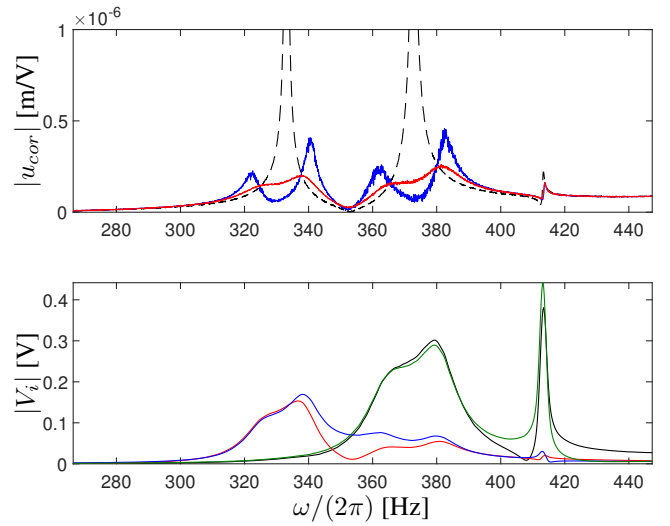


**Figure 16.** Experimental FRF for (a) the plate corner displacements with OC (dashed),  $L$ -shunt (blue) and  $LR$ -shunt (red) and (b) the voltage response of the absorbers 2 (red), 3 (blue) tuned to mode 3, and absorber 1 (black), 4 (green) tuned to mode 6.

For the simultaneous damping of modes 3 and 4 it is seen that the modified effective EMCC for mode 3 in Table 12 is equal to the original effective EMCC, which is the case because the piezoelectric absorbers 1 and 4 have limited coupling with mode 3. The remaining effective EMCCs are as expected seen to be somewhat lower than the original effective EMCC, as fewer piezoelectric absorbers now contribute to the overall coupling of a targeted mode. For all cases it can be seen in Table 12 that the influence from the modified effective EMCC on the inductance tuning is negligible, whereby the same passive inductors from the single-mode tuning can in fact be implemented for multi-mode damping. The optimum resistances are however seen to be significantly altered, since their values are proportional to the square root of the modified effective EMCC, see Table 1. The new resistances used for the experimental multi-mode shunt tuning are thus in Table 12 provided in parentheses for comparison. These implemented values are as well smaller than the optimum tuning, mainly because of the inherent resistance in the passive inductors. However, the deviation between the optimal and the implemented resistances are seen to have approximately the same magnitude as for the single-mode tuning, which indicates that the modified effective EMCC successfully modifies the shunt resistance.

The FRF for the plate corner displacements and the corresponding absorber voltage response can be seen in Figure 16 for the simultaneous damping of modes 3 and 4 and in Figure 17 for the damping of modes 2, 3, 4 and 6. It can be seen from the FRF for the plate corner displacements in Figure 16(a) that both modes 3 and 4 are optimally damped by the  $LR$ -shunted absorbers (red curves) with flat plateaus around the two target modes. Furthermore, it can be seen in Figure 16(b) that there is almost no absorber voltage response for absorber 1 (black) and 4 (green) around mode 3 and for absorber 2 (red) and 3 (blue) around mode 4. This limited spill-over to non-targeted modes indicates precise

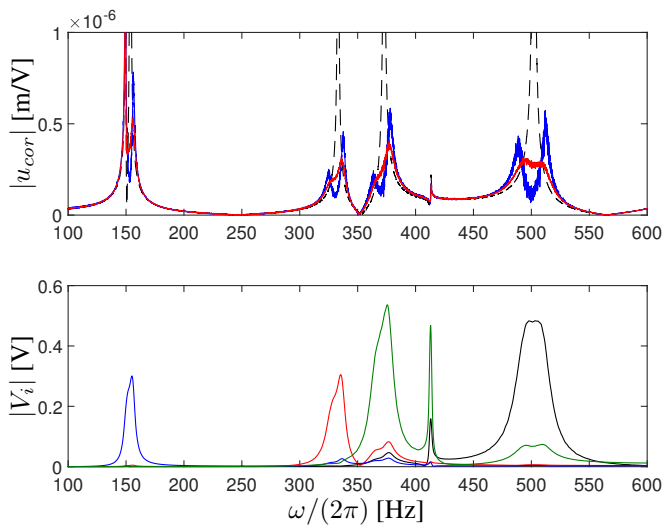


**Figure 17.** Experimental FRF for (a) the plate corner displacements with OC (dashed),  $L$ -shunt (blue) and  $LR$ -shunt (red) and (b) the voltage response of the piezoelectric absorbers 1(black), 2(red), 3(blue) and 4(green) tuned to modes 6, 3, 2 and 4, respectively.

tuning of the individual absorbers to their respective target modes.

Similar characteristics can be seen for the simultaneous damping of modes 2, 3, 4, and 6 in **Figure 17**, in which flat plateaus around the target modes can be observed in the FRF for the plate corner displacements in **Figure 17(a)**, except for the first resonance peak of the undamped first free plate mode in **Figure 12(a)**. Furthermore, it is clearly seen from the FRF for the absorber voltage in **Figure 17(b)**, that significant voltage amplitudes are present only around the respective target modes of the individual piezoelectric absorbers.

## Conclusion

The use of passive inductors for resonant piezoelectric shunt tuning requires a precise prior inductance tuning, accounting for the influence from residual vibration modes. This effect is included in a recently proposed shunt tuning method, based on the evaluation of an effective modal capacitance determined from a modal SC charge and OC voltage, obtained by the evaluation of the two corresponding eigenvalue problems. In the present paper, it is demonstrated how this method can as well be applied from simple measurements of the piezoelectric absorber SC current and OC voltage response to a simple pseudo-random vibration excitation of the electromechanical structure. By acquiring the current and voltage measurements with a suitable sample interval and time-span the corresponding FRFs may be obtained with sufficiently high accuracy. From the FRF for the electric current the corresponding FRF for electric charge is obtained, and the shunt tuning is then entirely based on the measured FRFs for the absorber charge and voltage responses. The modal charge and voltage are then found as the peak amplitudes in the FRFs, while SC and OC frequencies are obtained as resonances along the frequency axis. The effective modal capacitance is finally evaluated from the proposed charge to voltage ratio, which

is subsequently used for the shunt tuning instead of the traditional blocked or static capacitances.

The experimental shunt tuning method is demonstrated for both a free beam and free plate structure with five pairs of piezoceramic patches. In both cases one piezoceramic patch pair is used to excite structural vibrations, while the remaining four patch pairs are connected in series with a tuned resonant shunt. Hereby, the shunted patch pairs act as four individual piezoelectric vibration absorbers. For the free beam the tuning and damping of four resonant vibration modes is considered and found to be in good agreement with the corresponding numerical results obtained with a full 3D FE analysis conducted in ANSYS. Similar results have been obtained for the free plate experiment, for which optimum multi-mode shunt damping is further demonstrated by tuning the piezoelectric absorbers to different target modes, while altering the resistance tuning by a modified effective EMCC. Finally, it is shown that tuning of the shunt inductance based on the blocked capacitance for the second beam mode and on the static capacitance for the sixth plate mode may cause severe detuning of the piezoelectric shunts, reducing the attainable damping performance. Thus, it can be concluded that a precise inductance tuning is vital for the shunt damping performance, especially for pure passive resonant shunts, for which the re-adjustments of the shunt inductance is not straightforward. A precise prior tuning is therefore required and may be ensured by taking into account the contribution from residual vibration modes.

## Funding

This research has been supported by the Danish Council for Independent Research via the project ‘Resonant Piezoelectric Shunt Damping of Structures’. The help by the technicians at CTS is highly appreciated.

## References

- Berardengo M, Thomas O, Giraud-Audine C and Manzoni S (2016) Improved resistive shunt by means of negative capacitance: new circuit, performances and multi-mode control. *Smart Materials and Structures* 25:075033(23pp).
- Berardengo M, Manzoni S, Thomas O, and Vanali M (2018) Piezoelectric resonant shunt enhancement by negative capacitances: Optimisation, performance and resonance cancellation. *Journal of Intelligent Material Systems and Structures* 29(12):25812606.
- Caruso G (2001) A critical analysis of electric shunt circuits employed in piezoelectric passive vibration damping. *Smart Materials and Structures* 10:1059-1068.
- CTS (2019) List of piezoelectric materials *PZT 3265HD*. [https://www.ctscorp.com/wp-content/uploads/CTS\\_-PZT-Materials\\_Complete-Properties\\_20180829.pdf](https://www.ctscorp.com/wp-content/uploads/CTS_-PZT-Materials_Complete-Properties_20180829.pdf)
- Darleux R, Lossouarn B, Deü JF (2018) Passive self-tuning inductor for piezoelectric shunt damping considering temperature variations. *Journal of Sound and Vibration* 432:105-118
- de Marneffe B and Preumont A (2008) Vibration damping with negative capacitance shunts: theory and experiment. *Smart Materials and Structures* 17:035015.

- Fleming AJ, Behrens S and Moheimani SOR (2000) Synthetic impedance for implementation of piezoelectric shunt-damping circuits. *Electronics Letters* 36:1525-1526.
- Forward RL (1979) Electronic damping of vibrations in optical structures. *Applied Optics* 18:690-697.
- Gardonio P and Casagrande D (2017) Shunted piezoelectric patch vibration absorber on two-dimensional thin structure: tuning considerations. *Journal of Sound and Vibration* 395:26-47.
- Hagood NW and von Flotow A (1991) Damping of structural vibrations with piezoelectric materials and passive electrical networks. *Journal of Sound and Vibration* 146:243-268.
- Høgsberg J and Krenk S (2012) Balanced calibration of resonant shunt circuits for piezoelectric vibration control. *Journal of Intelligent Material Systems and Structures* 23:1937-1948.
- Høgsberg J and Krenk S (2017) Calibration of piezoelectric RL shunts with explicit residual mode correction. *Journal of Sound and Vibration* 386:65-81.
- IEEE Inc. (1988) *Standards on piezoelectricity* ANS/IEEE Std 176-1987 USA.
- Krenk S and Høgsberg J (2016) Tuned resonant mass or inerter-based absorbers: Unified calibration with quasi-dynamic flexibility and inertia correction. *Proceedings of the Royal Society A: Mathematical, Physical and Engineering Sciences* 472:20150718(23pp).
- Krenk S and Høgsberg J (2013) Equal modal damping design for a family of resonant vibration control formats. *Journal of Vibration and Control* 19:1294-1315.
- Lossouarn B, Aucejo M, Deü JF and Multon B (2017) Design of inductors with high inductance values for resonant piezoelectric damping. *Sensors and Actuators A: Physical* 259:68-76.
- Lossouarn B, Deü JF, Kerschen G (2018) A fully passive nonlinear piezoelectric vibration absorber *Philosophical Transactions of the Royal Society A: Mathematical, Physical and Engineering Sciences* 376:20170142.
- Park CH and Inman DJ (1999) A uniform model for series R-L and parallel R-L shunt circuits and power consumption. *SPIE Proceedings* 3668:797-804.
- Porfiri M, Maurini C and Pouget J (2007) Identification of electromechanical modal parameters of linear piezoelectric structures. *Smart Materials and Structures* 16:323-331.
- Preumont A (2011) *Vibration Control of Active Structures. An Introduction* 3rd edition Springer Heidelberg.
- Soltani P, Kerschen G, Tondreau G and Deraemaeker A (2014) Piezoelectric vibration damping using resonant shunt circuits: an exact solution. *Smart Materials and Structures* 23:125014(11pp).
- Thomas O, Ducarne J and Deü JF (2012) Performance of piezoelectric shunts for vibration reduction. *Smart Materials and Structures* 21:015008(16pp).
- Toftækær JF, Benjeddou A, Høgsberg J and Krenk S (2018) Optimal piezoelectric RL shunt damping of plates with residual mode correction. *Journal of Intelligent Material Systems and Structures* 29:3346-3370.
- Toftækær JF, Benjeddou A and Høgsberg J (2019) General numerical implementation of a new piezoelectric shunt tuning method based on the effective electromechanical coupling coefficient. *Mechanics of Advanced Materials and Structures*. Epub ahead of print 25 January 2019. <https://doi.org/10.1080/15376494.2018.1549297>.
- Toftækær JF and Høgsberg J (2019) Multi-Mode Piezoelectric Shunt Damping with Residual Mode Correction by Evaluation of Modal Charge and Voltage. *Journal of Intelligent Material Systems and Structures*. Submitted, JIM-19-319.
- Toftækær JF and Høgsberg J (2019) Experimental Data for Validation of Piezoelectric Shunt Tuning with Residual Mode Correction: Damping of Plate-Like Structures, *Mendeley Data*, Epub 30 September 2019, <http://dx.doi.org/10.17632/c4zgfwdwvk7.1>
- Wu SY (1996) Piezoelectric shunts with a parallel R-L circuit for structural damping and vibration control. *SPIE Proceedings* 2720:259-269.
- Wu SY and Bicos AS (1997) Structural vibration damping experiments using improved piezoelectric shunts. *SPIE Proceedings* 3045:40-50.
- Yamada K, Matsuhisa H, Utsuno H and Sawada K (2010) Optimum tuning of series and parallel LR circuits for passive vibration suppression using piezoelectric elements. *Journal of Sound and Vibration* 329:5036-5057.



# C1

New piezoelectric shunt tuning method based on the effective electromechanical coupling coefficient: Validation and 3D implementation

Johan Frederik Toftækær, Aych Benjeddou and Jan Høgsberg

*Proceedings of 7th International Symposium on Aircraft Materials*  
April 24-26, 2018, Compiègne, France



## New piezoelectric shunt tuning method based on the effective electromechanical coupling coefficient: validation and 3D implementation

Johan Frederik Toftekær<sup>1</sup>, Ayech Benjeddou<sup>2,3</sup> and Jan Høgsberg<sup>1</sup>

<sup>1</sup>Department of Mechanical Engineering  
Technical University of Denmark

Nils Koppels Allé, Building 404, DK-2800 Kgs. Lyngby, Denmark  
e-mail: jotof@mek.dtu.dk, jhg@mek.dtu.dk

<sup>2</sup> Université de Technologie de Compiègne, CNRS, ROBERVAL  
Centre de Recherche Royallieu, CS 60319, 60203 Compiègne CEDEX, France  
e-mail: ayech.benjeddou@utc.fr

<sup>3</sup>SUPMECA, 3 Rue Fernand Hainaut, 93407 Saint Ouen CEDEX, France  
e-mail: benjeddou@supmeca.fr

### Abstract

In the present work, a newly proposed resonant shunt tuning method is implemented in the commercial ANSYS<sup>®</sup> finite element (FE) code. For this purpose, the tuning method is written in a more general format that does not explicitly contain the resulting plane stress-reduced piezoelectric coupling coefficient. This new compact format of the proposed shunt tuning method is demonstrated suitable for implementation in ANSYS<sup>®</sup>. Further, ANSYS<sup>®</sup> three-dimensional (3D) modelling has allowed the assessment of an earlier developed plate-patches simplified two-dimensional (2D) FE model and the validation of the corresponding piezoelectric smart beam and plate benchmarks. It was found that the formerly established 2D model, using Kirchhoff plate and purely in-plane FEs, approximates the smart structures rather accurately, when the vertical masses from the piezoceramic patches are included. At last, it was found that the optimal shunt tuning, beneficially can be based on the effective electromechanical coupling coefficient, short circuit target resonant frequency and the associated modal sensed charge of the electromechanical structure.

### 1 Introduction

Piezoelectric transducers attached locally to a structure have the ability to dissipate converted mechanical energy into heat in a supplemental resonant shunt circuit. The latter is often designed as a series or parallel connection of a resistance ( $R$ ) and an inductance ( $L$ ). The  $RL$ -shunt circuit was first suggested and experimentally demonstrated by Forward [1]. Actual calibration procedures were subsequently derived first for the series [2] and since for the parallel shunt circuit [3]. Both calibration methods are based on a single mode representation of the electromechanical structure and are governed by the resonant frequency of a target vibration and the capacitive properties of the piezoelectric transducer(s). As it has been demonstrated recently in [4] and [5], the presence of the electric shunt alters the original resonant vibration, whereby the non-resonant vibration modes influence the response and ultimately the shunt tuning. This influence can be described by flexibility and inertia contributions, derived in [6], which modify the capacitive effect of the piezoelectric transducer(s). The modified capacitance yields a modified modal electromechanical coupling coefficient (EMCC), which in the case of exact determination

of the flexibility and inertia effects from the non-resonant modes equals the effective (or generalized) EMCC. The latter has led to the derivation of a new shunt tuning method based on the effective EMCC [5], that is defined by the relative difference between the short circuit (SC) and open circuit (OC) frequencies of the electromechanical structure [7]. It is further an indicator of the level of attainable damping, and has thus often been used as the objective function for the design and position optimization of piezoelectric transducers [8].

In the present work the newly proposed shunt tuning method based on the effective EMCC is implemented in the commercial ANSYS® finite element (FE) code. The tuning formulas are written in a more general format in order to allow simple and direct implementation in ANSYS® via reading APDL scripts. ANSYS® supports three-dimensional (3D) coupled analysis of electromechanical structures, which previously has been used in the assessment of two-dimensional (2D) and 3D evaluated effective EMCCs [9]. Also full 3D analysis of, for instance, a CD-ROM drive base with shunted piezoelectric patches [10] has been performed in ANSYS®. The possibility of exporting system matrices and vectors is further utilized in [11] to determine optimal shunt calibration and in [12] for optimal patch positioning, using optimization functions written in Matlab. Here, the implementation of the new shunt calibration method in ANSYS® is used to perform full 3D analysis of the two benchmarks presented in [5] and to validate the earlier established 2D FE model, using Kirchhoff plate and in-plane FEs [5].

## 2 FE-model and shunt tuning

This section is devoted to the notations and general structure of the ANSYS® 3D FE model. This is presented in order to clarify the implementation of the new shunt calibration procedure [5]. The latter is further briefly recapped in the present notation, also serving the purpose of presenting the modification to the tuning formulas in order to not explicitly contain the plane stress-reduced piezoelectric coupling coefficient.

### 2.1 Constitutive equations

Initially, the full 3D constitutive equations for piezoceramic materials with transverse isotropic piezoelectric behaviour are presented. The constitutive relations can be written in four different forms depending on the choice of independent variables. The most implemented form in commercial softwares, including ANSYS®, is the  $e$ -form, which defines the stresses  $T_p$  and electric displacements  $D_k$  from the mechanical strains  $S_q$  and electric fields  $E_l$  ( $p, q = 1, \dots, 6$ ;  $k, l = 1, 2, 3$ ), as (for a polarization along the 3-direction)

$$\begin{Bmatrix} T_1 \\ T_2 \\ T_3 \\ T_4 \\ T_5 \\ T_6 \end{Bmatrix} = \begin{bmatrix} c_{11}^E & c_{12}^E & c_{13}^E & 0 & 0 & 0 \\ c_{12}^E & c_{11}^E & c_{13}^E & 0 & 0 & 0 \\ c_{13}^E & c_{13}^E & c_{33}^E & 0 & 0 & 0 \\ 0 & 0 & 0 & c_{55}^E & 0 & 0 \\ 0 & 0 & 0 & 0 & c_{55}^E & 0 \\ 0 & 0 & 0 & 0 & 0 & c_{66}^E \end{bmatrix} \begin{Bmatrix} S_1 \\ S_2 \\ S_3 \\ S_4 \\ S_5 \\ S_6 \end{Bmatrix} - \begin{bmatrix} 0 & 0 & e_{31} \\ 0 & 0 & e_{31} \\ 0 & 0 & e_{33} \\ 0 & e_{15} & 0 \\ e_{15} & 0 & 0 \\ 0 & 0 & 0 \end{bmatrix} \begin{Bmatrix} E_1 \\ E_2 \\ E_3 \end{Bmatrix} \quad (1)$$

$$\begin{Bmatrix} D_1 \\ D_2 \\ D_3 \end{Bmatrix} = \begin{bmatrix} 0 & 0 & 0 & 0 & e_{15} & 0 \\ 0 & 0 & 0 & e_{15} & 0 & 0 \\ e_{31} & e_{31} & e_{33} & 0 & 0 & 0 \end{bmatrix} \begin{Bmatrix} S_1 \\ S_2 \\ S_3 \\ S_4 \\ S_5 \\ S_6 \end{Bmatrix} + \begin{bmatrix} \epsilon_{11}^S & 0 & 0 \\ 0 & \epsilon_{11}^S & 0 \\ 0 & 0 & \epsilon_{33}^S \end{bmatrix} \begin{Bmatrix} E_1 \\ E_2 \\ E_3 \end{Bmatrix} \quad (2)$$

Here  $c_{pq}^E$ ,  $e_{kq}$  and  $\epsilon_{kl}^S$  are the SC elastic stiffness components, stress piezoelectric coupling coefficients and dielectric constants under constant (nil) strains, respectively. When the piezoceramic patch is thin and therefore dominated by in-plane deformations, a good approximation of the material behaviour is given by the plane stress-reduced electromechanical properties which were used in [5], see appendix. This approximation generally causes a slight decrease of the natural frequencies compared to those evaluated from the corresponding 3D model, as demonstrated in [9].

## 2.2 FE formulation

In the following, mechanically unloaded harmonic vibrations are considered. The variational formulation for the electromechanical structure can thus be written as

$$\int_{\Omega} \{\delta S\}^t \{T\} d\Omega - \omega^2 \int_{\Omega} \{\delta u\}^t \rho \{u\} d\Omega - \int_{\Omega} \{\delta E\}^t \{D\} d\Omega = \int_{\Gamma_q} \delta \phi q d\Gamma_q \quad (3)$$

assuming harmonic solutions of the form  $\{u\} = \{u\}e^{i\omega t}$ . In (3),  $\rho$  denotes the material mass density,  $\delta\phi$  and  $q$  the electric potential and surface charge density,  $\omega$  the radial frequency,  $\Omega$  the material domain and  $\Gamma_q$  the electrode covered part of the electric boundary on which  $q$  is applied or measured. Finally, superscript  $t$  denotes the transpose operation.

Substituting the constitutive relations (1) and (2) in to (3), the stresses and electric displacements no longer appear explicitly. The relations between the mechanical strains  $S_q$  and displacements  $u_k$  and the electric field  $E_l$  and potential  $\phi$  can further be introduced

$$S_q = u_{k,k}, \quad q = k = 1, 2, 3 \quad (4)$$

$$S_q = u_{k,l} + u_{l,k}, \quad l \neq k, \quad q = 9 - (k + l) \quad (5)$$

$$E_l = -\phi_{,l} \quad (6)$$

Hereby, after approximating the continuous displacements  $\{u\}$  and electric potential  $\phi$  through shape functions and element degrees of freedom (dofs), the discrete vibration problem associated with (3) can be written as

$$\left( \begin{bmatrix} K_U^E & K_{U\varphi}^E \\ (K_{U\varphi}^E)^t & -K_{\varphi}^{\epsilon^S} \end{bmatrix} - \omega^2 \begin{bmatrix} M & 0 \\ 0 & 0 \end{bmatrix} \right) \begin{Bmatrix} U \\ \varphi \end{Bmatrix} = \begin{Bmatrix} 0 \\ -Q_{\varphi} \end{Bmatrix} \quad (7)$$

where  $[K_U^E]$ ,  $[K_{U\varphi}^E]$  and  $[K_{\varphi}^{\epsilon^S}]$  contain the stiffness components associated with the mechanical displacements, electromechanical coupling and electric potentials, while  $M$  contains the mechanical masses. Further, the dofs in the vectors  $\{U\}$ ,  $\{\varphi\}$  and  $\{Q_{\varphi}\}$  contain the mechanical displacements, electric potentials and external electric charges, respectively.

The equipotential condition is now applied to all electric potential dofs forming a continuous electrode. In the present work, thin piezoceramic patches with two in-plane electrodes are considered. Further, only one patch or one connection of two symmetrically colocalized patches are assumed. Hereby, only a single electrode electric potential dof remains unconstrained after grounding one of the non wired (interface) electrodes. The discrete vibration problem (7) can thus be decomposed as

$$\left( \begin{bmatrix} K_U^E & \bar{K}_{U\varphi}^E & K_{UV}^E \\ (\bar{K}_{U\varphi}^E)^t & -\bar{K}_{\varphi}^{\epsilon^S} & -K_{\varphi V}^{\epsilon^S} \\ (K_{UV}^E)^t & -(K_{\varphi V}^{\epsilon^S})^t & -C_p^{\epsilon^S} \end{bmatrix} - \omega^2 \begin{bmatrix} M & 0 & 0 \\ 0 & 0 & 0 \\ 0 & 0 & 0 \end{bmatrix} \right) \begin{Bmatrix} U \\ \varphi \\ V \end{Bmatrix} = \begin{Bmatrix} 0 \\ 0 \\ -Q \end{Bmatrix} \quad (8)$$

Here,  $[\bar{K}_{U\varphi}^E]$  and  $[\bar{K}_{\varphi}^{\epsilon^S}]$  contain the electromechanical and electric stiffness contributions associated with the electric potential dofs which are not part of an electrode. Oppositely,  $\{K_{UV}^E\}$  contains the electromechanical stiffness contributions associated with the electric potential dofs that are part of an electrode, while  $C_p^{\epsilon^S}$  contains the effective capacitive property of the piezoceramic patch(es). The latter is a scalar quantity due to the assumption of a single piezoceramic patch or a single system of connected patches. Further, the electric potential on the ungrounded non wired (interface) electrode defines the difference in the electric potential or voltage  $V$ , while  $Q$  is equivalent to the applied/measured charge difference between the two non wired (interface) electrodes. At last,  $\{K_{\varphi V}^{\epsilon^S}\}$  contains the coupling between the electric potential dofs of non-electroded and electroded parts. The vibration problem (8) is now beneficially written in the condensed format

$$\left( \begin{bmatrix} K^E & k_{me}^E \\ (k_{me}^E)^t & -\bar{C}_p^{\epsilon^S} \end{bmatrix} - \omega^2 \begin{bmatrix} M & 0 \\ 0 & 0 \end{bmatrix} \right) \begin{Bmatrix} U \\ V \end{Bmatrix} = \begin{Bmatrix} 0 \\ -Q \end{Bmatrix} \quad (9)$$

obtained by inserting  $\{\varphi\}$  from the second equation of (8) into its first and third equations. Hereby the system matrices and coupling vectors are defined as

$$[K^E] = [K_U^E] + [\bar{K}_{U\varphi}^E][\bar{K}_{\varphi}^{\epsilon^S}]^{-1}[\bar{K}_{U\varphi}^E]^t, \quad \{k_{me}^E\} = \{K_{UV}^E\} - [\bar{K}_{U\varphi}^E][\bar{K}_{\varphi}^{\epsilon^S}]^{-1}\{K_{\varphi V}^{\epsilon^S}\} \quad (10)$$

while the resulting modified capacitance follows as

$$\bar{C}_p^{\epsilon^S} = C_p^{\epsilon^S} - \{K_{\varphi V}^{\epsilon^S}\}^t [\bar{K}_{\varphi}^{\epsilon^S}]^{-1} \{K_{\varphi V}^{\epsilon^S}\} \quad (11)$$

The vibration problem (9) is equivalent to that in [5, eq. 57], with  $\{k_{me}^E\} \propto [W]k_c \bar{e}_{31}$ .

### 2.3 The effective EMCC

The effective EMCC is a measure of the effective coupling between the electric and mechanical domains of an electromechanical structure. It is determined as the rate of convertible energy by the piezoelectric material and given by the difference between the modal strain energies associated with SC and OC piezoceramic patch(es) electrodes. The modal strain energies are proportional to the eigenvalues of the SC and OC eigenvalue problems [9], here given by (9) with  $V = 0$  and  $Q = 0$ , respectively. The SC eigenvalue problem can thus be written as

$$([K^E] - \omega_j^2[M]) \{U\}_j = \{0\} \quad (12)$$

for mode  $j$ . The last electric equation of (9) further provides the modal sensed charge as

$$Q_j = -\{k_{me}^E\}^t \{U\}_j \quad (13)$$

which will be used subsequently. It is noted that the mode shape vectors  $\{U\}_j$  are normalised in order to obtain unit modal masses such that

$$\{U\}_j^t [M] \{U\}_j = 1, \quad \{U\}_j^t [K^E] \{U\}_j = \omega_j^2 \quad (14)$$

The OC eigenvalue problem is given by (8), when  $Q = 0$ , as

$$\left( \left( [K^E] + \{k_{me}^E\} (\bar{C}_p^{\epsilon^S})^{-1} \{k_{me}^E\}^t \right) - \hat{\omega}_j^2 [M] \right) \{\hat{U}\}_j = \{0\} \quad (15)$$

with condensed system matrices in order to avoid zeros in the diagonal of the mass matrix.

The SC stiffness matrix  $[K^E]$  is in (15) seen altered by the piezoelectric coupling vector  $\{k_{me}^E\}$  and the inverse of the modified capacitance  $\bar{C}_p^{\epsilon^S}$ . The OC piezoceramic patch(es) therefore provide(s) a stiffening effect on the electromechanical structure, thus  $\hat{\omega}_j^2 \geq \omega_j^2$ . Finally, the effective EMCC for resonant mode  $j = r$  can be determined as

$$\kappa_e^2 = \frac{\hat{\omega}_r^2 - \omega_r^2}{\omega_r^2} \quad (16)$$

where the difference between the squared OC and SC frequencies is an indicator of the convertible energy in the piezoelectric domain.

#### 2.4 Modal reduced equations

In the following, the modal reduced equations from (9) are derived in order to obtain the proposed shunt tuning method in the form used for the implementation in ANSYS®. The mechanical part of (9) can be decoupled in terms of the mode shapes  $\{U\}_j$  by representing the displacements  $\{U\}$  as a linear combination of the SC mode shapes collected column-wise in  $[U]$  and the modal coordinates in the vector  $\{v\}$  by

$$\{U\} = [U]\{v\} \quad (17)$$

Introducing (17) in (9), followed by pre-multiplication with the transpose of the mode shapes matrix, the coupled mechanical and electric modal equations can be written as

$$([\omega_n^2] - \omega^2[I_n])\{v\} = \{Q\}V, \quad \{Q\}^t\{v\} + \bar{C}_p^{\epsilon^S}V = Q \quad (18)$$

Here  $[\omega_n^2]$  contains the squared resonant frequencies in the diagonal,  $[I_n]$  is the identity matrix and the vector  $\{Q\}$  contains the SC modal sensed charges (13). The modal coordinates in (18a) can now be determined as

$$\{v\} = ([\omega_n^2] - \omega^2[I_n])^{-1}\{Q\}V \quad (19)$$

Introducing an electric shunt between the grounded and ungrounded electrodes, the charge  $Q$  in the right hand side of (18b) can be eliminated by the generalised Ohm's law

$$V = -i\omega Z_{sh}(\omega)Q \quad (20)$$

Using (20) and inserting the modal coordinates (19) in (18b) one obtains

$$\left( \{Q\}^t ([\omega_n^2] - \omega^2[I_n])^{-1} \{Q\} + \bar{C}_p^{\epsilon^S} + \frac{1}{i\omega Z_{sh}(\omega)} \right) V = 0 \quad (21)$$

The first product in the governing equation (21) is alternatively written as a sum over the number of vibration modes, which further here is approximated by considering the correction terms derived in [6]. Hereby, the sum can be written similarly to [4, 5] as

$$\sum_j \frac{\omega_j^2}{\omega_j^2 - \omega^2} \frac{Q_j^2}{\omega_j^2} \simeq \frac{\omega_r^2}{\omega_r^2 - \omega^2} \frac{Q_r^2}{\omega_r^2} + C'_r - \frac{1}{\omega_r^2 L'_r} \frac{\omega_r^2}{\omega^2} \quad (22)$$

by noting that  $\bar{e}_{31}^2/k_r$  in [5] is equivalent to  $Q_r^2/\omega_r^2$ . This is emphasized by considering the units of the normalised modal stiffness in [5]  $[kg/(m^2s^2)]$  and the present squared modal charge  $[C^2/(m^2kg)]$ .

Introducing the approximation (22) in (21) one obtains

$$\left( \frac{\omega_r^2}{\omega_r^2 - \omega^2} \frac{Q_r^2}{\omega_r^2} + \bar{C}_p^{\epsilon^S} + C_r' - \frac{1}{\omega_r^2 L_r'} \frac{\omega_r^2}{\omega^2} + \frac{1}{i\omega Z_{sh}(\omega)} \right) V = 0 \quad (23)$$

From (23) the system's characteristic equation can finally be identified as

$$\left( \frac{\omega_r^2 \omega^2}{\omega_r^2 - \omega^2} + \frac{\omega^2 - \omega_r^2}{\kappa_r^2} \right) \kappa_e^2 + \left( 1 - i\omega \frac{1}{Z_{sh}(\omega)} \frac{\kappa_e^2}{Q_r^2} \right) \omega_r^2 = 0 \quad (24)$$

by introducing  $C_r = C_p^{\epsilon^S} + C_r'$  and  $C_L = C_r - 1/(\omega_r^2 L_r')$  from [5] and the effective and inertia reduced EMCCs as

$$\kappa_e^2 \simeq Q_r^2 / (C_L \omega_r^2) \quad , \quad \kappa_r^2 \simeq Q_r^2 / (C_r \omega_r^2) \quad (25)$$

The latter (25b) denotes in the present work the inertia reduced EMCC as it corresponds to the effective EMCC without the inertia contribution for the non-resonant modes.

### 2.5 Optimum parallel shunt tuning

In the present work parallel  $RL$ -shunts are considered, as the corresponding balanced calibration formulas here imply no approximations, see [4]. Applying the balanced calibration procedure [4, 5, 6] to (24), yields optimum inductance tuning, when the term in the last bracket of (24) equals zero

$$L = \frac{\kappa_e^2}{Q_r^2} \quad (26)$$

The optimum inductance (26) is equivalent to that in [5] as  $\bar{e}_{31}^2/m_r$  and  $Q_r^2$  are equivalent.

Representing the optimum inductance (26) by the impedance relation  $Z_{sh}(\omega) = i\omega L$  in (24), the characteristic equation reduces to

$$\omega^4 - (2 + \kappa_r^2) \omega_r^2 \omega^2 + \omega_r^4 = 0 \quad (27)$$

which is a second order polynomial in  $\omega^2$  with solutions  $\omega_+^2$  and  $\omega_-^2$ , that bound the SC frequency  $\omega_r$  and define the inertia reduced EMCC as

$$\kappa_r^2 = \frac{(\omega_+ - \omega_-)^2}{\omega_+ \omega_-} \quad (28)$$

The objective is now to determine the two squared circular frequencies  $\omega_+^2$  and  $\omega_-^2$  by solving the corresponding eigenvalue problem for the electromechanical structure with the pure  $L$ -shunt. In this case, the generalized Ohm's law can be written as in (20) with  $Z_{sh}(\omega) = i\omega L$ . Thus, inserting this relation in (9) one obtains the eigenvalue problem

$$\left( \left[ \begin{array}{cc} K^E & k_{me}^E \\ 0 & 1 \end{array} \right] - \omega^2 \left[ \begin{array}{cc} M & 0 \\ -(k_{me}^E)^t & \bar{C}_p^{\epsilon^S} L \end{array} \right] \right) \left\{ \begin{array}{c} U \\ V/L \end{array} \right\} = \left\{ \begin{array}{c} 0 \\ 0 \end{array} \right\} \quad (29)$$

The choice of  $V/L$  as variable is here motivated by obtaining  $\bar{C}_p^{\epsilon^S} L$  in the second matrix diagonal, which is noted to have the dimension of  $1/\omega^2$ .

The eigenvalues of (29) are then determined from which  $\omega_+^2$  and  $\omega_-^2$  are identified. The inertia reduced EMCC finally follows from (28) and the optimum resistance according to the balanced calibration procedure [5]

$$R = \frac{\kappa_r^2 \omega_r}{Q_r^2} \sqrt{\frac{1}{2\kappa_r^2}} \quad (30)$$

The optimum resistance may beneficially be approximated by using the effective EMCC  $\kappa_e^2$  in (30) instead of the inertia reduced EMCC  $\kappa_r^2$ . This is because the shunt performance is less sensitive to deviations in the resistance [5]. Thus, near optimum damping may be attained using the effective EMCC for the resistance tuning. The approximate tuning is beneficial as it avoids solving the eigenvalue problem (29).

### 3 Implementation in ANSYS®

This section is devoted to demonstrating the implementation of the presented calibration procedure in ANSYS®. The key steps of the approach are shown in the flow chart of Figure 1 and further outlined in the following.

The first step is to define the geometry, material properties, element types and mesh partitions of the analysed electromechanical structure. In the present work, SOLID186 and SOLID226 3D 20 node elements are used for the discretization of respectively the host structure and piezoceramic patch(es). Next, the boundary conditions (BCs) and equipotential (EP) conditions for all continuous electrodes are imposed to the discretized model. For each continuous electrode, the EP condition is defined in a master node which is stored and saved for later use.

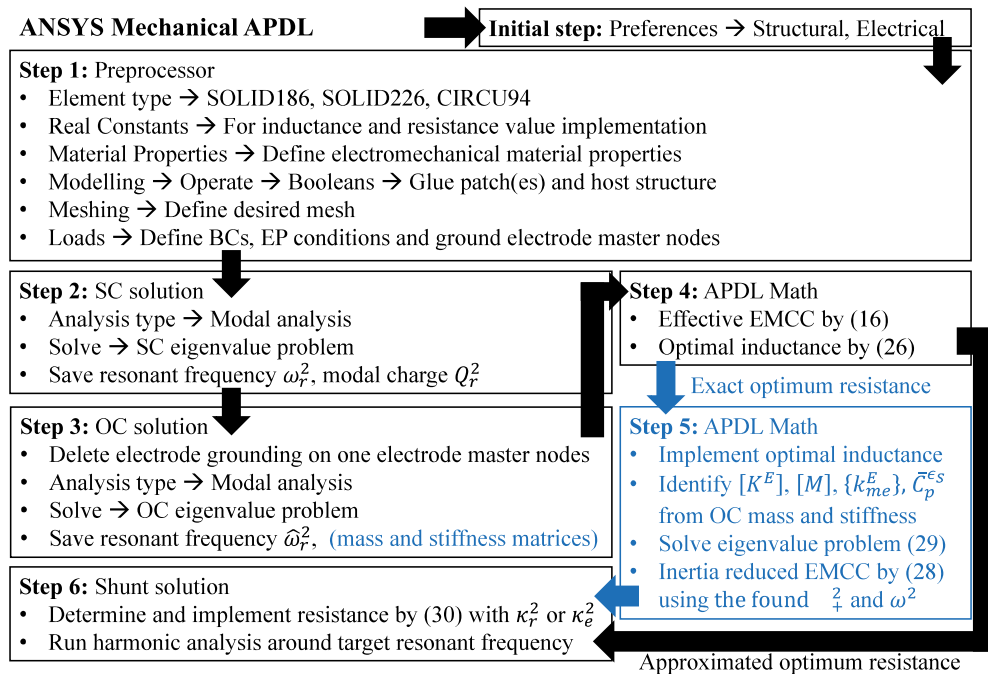


Figure 1: Flow chart illustrating ANSYS® implementation of the new optimum shunt tuning procedure

In the second step, zero electric potential is applied to the master nodes to obtain SC piezoceramic patch(es). A modal analysis is then conducted to determine and store the target SC resonant frequency  $\omega_r^2$ , modal sensed charge  $Q_r^2$  and mode shape  $\{U\}_r$ .

The third step is to delete the electric potential constraint on one of the master nodes to obtain OC piezoceramic patch(es). A modal analysis is then conducted to find and save the target OC resonant frequency  $\hat{\omega}_r^2$ . Further, for exact evaluation of the shunt resistance the OC mass and stiffness matrices may be saved.

The fourth step is to determine the effective EMCC using (16), whereby the optimum inductance value is determined by (26) using the effective EMCC and SC modal charge.

The fifth step is to implement the optimum inductance between the grounded and ungrounded master nodes according to the patch(es) configuration and polarization, see [5]. The electronic components are implemented using CIRCU94 elements which are compatible with SOLID226 piezoelectric elements. Inductive or resistive properties are implemented using key options and by defining their associated real constants. The matrices  $[K^E]$  and  $[M]$  and the effective capacitance  $\bar{C}_p^{eS}$  are identified next. Further, the coupling vector  $\{k_{me}^E\}$  is found as the column of the OC stiffness matrix corresponding to the voltage dof of the unconstrained master node, without the row entry of the same dof. The eigenvalue problem (29) is then established and solved in APDL to determine the eigenvalues  $\omega_+^2$  and  $\omega_-^2$ . Finally, the inertia reduced EMCC is determined by (28).

The sixth and final step is to determine and implement the optimum resistance. Either the exact (30), or the approximate ((30) with  $\kappa_r^2 = \kappa_e^2$ ) resistance can be used, where the approximation leads to the possibility of omitting step five. At last, the optimum resistance is implemented between the same master nodes as the inductance, to obtain the parallel shunt circuit configuration.

## 4 Benchmark examples

In the present section the smart beam and plate benchmarks analysed in [5] are modelled with 3D FEs in ANSYS® in order to verify the formerly established 2D FE model and determine the shunt tunings. For both benchmarks, the reader is referred to [5] for the geometries of the patches and host structures and their materials properties. Due to lack of provided information for the 3D FE simulations, it is in the present work chosen to use well defined piezoceramic materials. For the beam benchmark the piezoceramic material PIC151 is used, with full 3D material properties provided in [13]. For the plate benchmark, the PZT 5H piezoceramic is used, for which the material properties can be accessed through the 'eFunda portal' [14]. Finally, the plane stress-reduced properties used in the 2D FE model [5] are determined from the 3D properties according to the appendix.

### 4.1 Cantilever beam

For the cantilever beam example, optimum *RL*-shunt tuning is determined and analysed for the first eight vibration modes using, respectively, a 3D FE model in ANSYS® and the formerly established 2D model [5]. The discretization used in [5] has been applied to the 3D FE model in ANSYS®. A convergence study has been performed in ANSYS®, yielding relative errors on the first eight resonant frequencies around and below 1% with the present discretization, which is thus regarded sufficient for the present purposes. The SC frequencies, effective and inertia reduced EMCCs and optimum *RL*-shunt tunings are provided in Table 1. Furthermore, the table also provides the relative deviations between the 2D and 3D evaluated SC frequencies and optimum *RL*-shunt tunings. It is noted that

**Table 1:** SC frequencies, effective and inertia reduced EMCCs, optimum  $RL$ -shunt tunings and relative deviations, for a cantilever beam with a pair of oppositely poled and series wired piezoceramic patches, modelled respectively by 3D FEs in ANSYS® (ANS) and 2D FEs in Matlab (Mat).

Mode (type)	Model	$f$ [Hz] (dev[%])	$\kappa_e^2$ [%]	$\kappa_r^2$ [%]	$L$ [H] (dev[%])	$R$ [k $\Omega$ ] (dev[%])
1 (x-z bending)	3D(ANS)	48.83	-	2.65	1486	1981
	2D(Mat)	48.84 (-0.02)	-	2.79	1480 (0.40)	1923 (2.96)
2 (x-z bending)	3D(ANS)	336.0	-	3.13	32.25	271.5
	2D(Mat)	336.7 (-0.21)	-	3.34	32.05 (0.60)	261.6 (3.66)
3 (x-y bending)	3D(ANS)	603.5	-	-	-	-
	2D(Mat)	- (-)	-	-	- (-)	- (-)
4 (x-z bending)	3D(ANS)	949.9	-	2.92	4.159	101.9
	2D(Mat)	955.1 (-0.55)	-	3.18	4.117 (1.01)	97.19 (4.64)
5 (Torsion)	3D(ANS)	1008	-	-	-	-
	2D(Mat)	1028 (-2.00)	-	-	- (-)	- (-)
6 (x-z bending)	3D(ANS)	1827	-	1.82	1.157	68.83
	2D(Mat)	1843 (-0.88)	-	1.98	1.141 (1.41)	65.67 (4.58)
7 (x-z bending)	3D(ANS)	2968	-	0.49	0.442	82.45
	2D(Mat)	3015 (-1.60)	-	0.49	0.430 (2.83)	80.91 (1.86)
8 (Torsion)	3D(ANS)	3025	-	-	-	-
	2D(Mat)	3062 (-1.23)	-	-	- (-)	- (-)

\*dev[%]=100x(3D-2D)/3D

the patches vertical mass contributions are included in the 2D FE model, see [5].

Good correlations between the SC frequencies of the electromechanical beam structure can be seen in Table 1, yielding the approximations made in [5] to be reasonable for the given thin beam structure. It is seen that the third vibration mode which is an x-y bending mode is not obtained with the 2D FE model as this model does not contain in-plane dofs. Shunt tunings are seen obtained only for the x-z bending modes. This is due to the position and configuration of the piezoceramic patches, which yield no electromechanical energy conversion when the structure is excited in the remaining torsional and in-plane bending modes. The relative deviations on the x-z bending modes are all seen below 2%. Further, the relative deviations on the optimum inductances are seen to be maximum 2.83% for the seventh resonant mode. This shows that near optimal shunt tunings are obtained by use of the previous simple FE model in [5]. The relative deviations on the shunt resistance are seen to be higher but less than 4.7%. However, as shown in the subsequent example, the shunt performance is less sensitive to deviations on the resistance, thus the present 2D shunt tuning can still be found close to the optimum. The influence of using the effective EMCC for the tuning of the shunt resistance is not investigated here. This is because the relative deviations between the effective and inertia reduced EMCCs are negligible, thus the resistance could beneficially be evaluated from (30) with  $\kappa_r^2 = \kappa_e^2$ .

#### 4.2 Simply supported plate

The second example concerns the simply supported plate described in [5] but with PZT-5H patches. Again, the same 2D and 3D discretizations are used after verifying the model with results obtained with refined mesh. The first eight SC frequencies, effective and inertia reduced EMCCs and shunt tunings are provided in Table 2, together with the relative deviations between the 2D and 3D evaluated SC frequencies and shunt tunings.

Again, good correlation between the SC frequencies of the 2D and 3D models can be seen from Table 2, with relative deviations below 1.6%. In the present case all vibration modes are predicted with the 2D model as expected since only pure plate bending modes are present. As it was found in [5], high attainable damping is only achievable for three out

**Table 2:** SC frequencies, effective and inertia reduced EMCCs, optimum  $RL$ -shunt tunings and relative deviations, for a simply supported plate with a pair of same poled and parallel wired piezoceramic patches, modelled respectively by 3D FEs in ANSYS® (ANS) and 2D FEs in Matlab (Mat).

Mode (type)	Model	$f$ [Hz] (dev[%])	$\kappa_e^2$ [%]	$\kappa_r^2$ [%]	$L$ [H] (dev[%])	$R$ [k $\Omega$ ] (dev[%])
<b>1 (1,1)</b>	<b>3D(ANS)</b>	<b>35.95</b>	<b>1.93</b>	<b>1.92</b>	<b>36.00</b>	<b>41.33</b>
	<b>2D(Mat)</b>	<b>35.89</b> (0.15)	<b>1.94</b>	<b>1.93</b>	<b>35.45</b> (1.55)	<b>40.52</b> (1.95)
2 (2,1)	3D(ANS)	80.77	0.10	0.10	7.080	78.05
	2D(Mat)	80.12 (0.80)	0.10	0.10	7.067 (1.55)	79.46 (-1.23)
3 (1,2)	3D(ANS)	112.0	0.12	0.11	3.603	49.79
	2D(Mat)	111.1 (0.81)	0.11	0.11	3.602 (0.03)	50.98 (-2.38)
<b>4 (3,1)</b>	<b>3D(ANS)</b>	<b>155.0</b>	<b>2.38</b>	<b>2.35</b>	<b>1.941</b>	<b>8.593</b>
	<b>2D(Mat)</b>	<b>154.5</b> (0.35)	<b>2.26</b>	<b>2.23</b>	<b>1.917</b> (1.25)	<b>8.699</b> (-1.23)
5 (2,2)	3D(ANS)	165.8	0.02	0.01	2.023	67.50
	2D(Mat)	164.4 (-0.86)	0.02	0.01	2.034 (-0.54)	57.03 (15.5)
6 (3,2)	3D(ANS)	230.8	0.04	0.02	0.743	21.83
	2D(Mat)	228.6 (0.96)	0.02	0.01	0.758 (-2.03)	34.37 (-57.5)
<b>7 (1,3)</b>	<b>3D(ANS)</b>	<b>242.7</b>	<b>2.09</b>	<b>1.99</b>	<b>0.814</b>	<b>5.928</b>
	<b>2D(Mat)</b>	<b>241.2</b> (0.61)	<b>1.95</b>	<b>1.87</b>	<b>0.801</b> (1.53)	<b>6.027</b> (-1.67)
8 (4,1)	3D(ANS)	252.7	0.00	0.00	0.989	81.52
	2D(Mat)	248.8 (1.57)	0.03	0.00	1.088 (-9.98)	22.19 (72.8)

\*dev[%]=100x(3D-2D)/3D

**Table 3:** Exact ( $R$ ) and approximate ( $R_r$ ) optimum resistance values and associated relative deviations.

Mode (type)	<b>1 (1,1)</b>	2 (2,1)	3 (1,2)	<b>4 (3,1)</b>	5 (2,2)	6 (3,2)	<b>7 (1,3)</b>	8 (4,1)
$R$ [k $\Omega$ ]	<b>41.33</b>	78.50	49.79	<b>8.593</b>	67.50	21.83	<b>5.928</b>	81.52
$R_r$ [k $\Omega$ ]	<b>41.39</b>	79.54	51.53	<b>8.659</b>	109.5	36.39	<b>6.070</b>	189.1
$100 \times \frac{R_r - R}{R}$ [%]	<b>0.15</b>	1.33	3.49	<b>0.77</b>	62.2	66.8	<b>2.39</b>	132

of the first eight vibration modes (in bold in Table 2) with the given piezoceramic patches position and dimensions. This can be seen by considering the effective EMCC for the remaining five resonant modes (in non-bold in Table 2) which squared values are below 0.12% and thus electromechanically uncoupled. It is seen that the relative deviations on the shunt tunings are low for the three modes with high effective EMCC, while significant relative deviations can be observed for the shunt tunings to the remaining five uncoupled vibration modes. This is because the relative errors increases for decreasing effective and inertia reduced EMCCs (see [15]). The shunt tunings for the five electromechanically uncoupled vibration modes are thus practically useless, but provided to demonstrate the effect of the inertia contribution on the resistance calibration and to recognize the increasing importance of a precise numerical model for decreasing effective EMCCs.

It is now investigated how well the approximated resistance ((30) with  $\kappa_r^2 = \kappa_e^2$ ) estimates the exact resistance (30) and which influence it has on the shunt performance. In Table 3, the exact ( $R$ ) and approximated ( $R_r$ ) resistances and their relative deviations are provided. For the three vibration modes with strong electromechanical coupling (in bold in Table 3), it is seen that the relative deviations between the exact and approximated resistances are relatively low. For the five electromechanically uncoupled vibration modes (in non-bold in Table 3) significant relative deviations can be observed with an increasing tendency concurrent with the decrease of the effective and inertia-reduced EMCCs.

The performance of the resonant shunt damping using approximated resistance values is now analysed by looking at the corresponding harmonic responses to harmonic modal loads in the sixth and seventh resonant modes, shown in Figure 2. For the seventh vibration mode Figure 2(b), with strong electromechanical coupling, no significant deviations

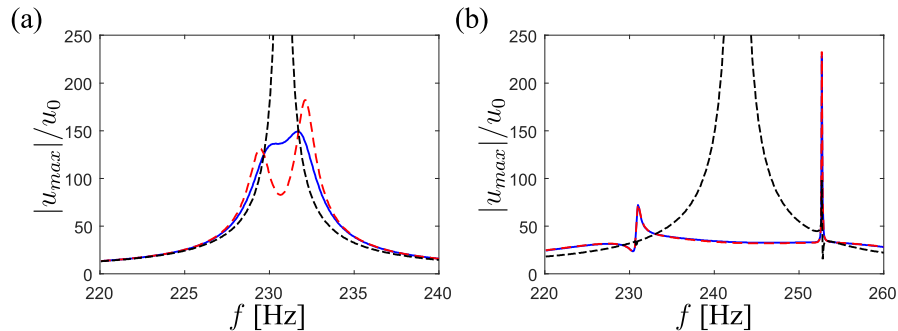


**Figure 2:** Responses to modal harmonic loads around (a) 6th and (b) 7th resonant modes. Solid lines: optimum shunt tuning, dashed line: shunt with approximated resistance and dashed-dotted lines: SC response.

can be observed between the shunt with exact (solid line) and approximate (dashed line) resistance values. This concludes the statement that the shunt performance is little sensitive to deviations in the resistance. Considering the frequency response plot around the electromechanically uncoupled sixth resonant mode Figure 2(a), it can be seen that there are notable differences between the responses with exact (solid line) and approximated (dashed line) resistance values. This demonstrates, for the case of low effective EMCC values, that not only a precise numerical model is important, but also an accurate evaluation of the resistance based on the inertia-reduced EMCC. However, in all practical cases with a strong electromechanical coupling, it is thought that using the effective EMCC only, provides a sufficiently precise shunt tuning.

## 5 Conclusion

In the present work a newly proposed shunt calibration procedure based on the effective EMCC is generalized and demonstrated suitable for implementation in the commercial ANSYS® FE code. A formerly established 2D FE model is subsequently verified through 3D FE modelling and analysis of two smart beam and plate benchmarks. The 2D FE model is found to sufficiently represent thin beam and plate structures with a pair of surface-bonded piezoceramic patches, as long as the vertical mass contribution from the patches is included. Small deviations between the 2D and 3D FE models were found on the frequencies and shunt tunings for the electromechanically coupled modes, while deviations on the shunt resistances were observed for the uncoupled modes. However, as demonstrated in the plate example, the shunt performance is less sensitive to deviations on the resistance. Thus, the shunt tuning based on the 2D FE model is in case of high effective and inertia-reduced EMCCs found adequate. At last, the influence, on the shunt performance, of using exact and approximated (based on the effective EMCC) resistance values were investigated. It is found, for electromechanically uncoupled modes, that the importance of exact resistance evaluation increases, along with the need for a precise numerical model. However, since these uncoupled modes are out of interest for shunt damping, it can be concluded that the shunt resistance is sufficiently tuned from the effective EMCC.

## Acknowledgement

This research has been supported by the Danish Council for Independent Research via the project ‘Resonant Piezoelectric Shunt Damping of Structures’.

## References

- [1] Forward R.L. Electronic damping of vibrations in optical structures. *Appl. Optics* **18**(1979) 690-697.
- [2] Hagood N.W., von Flotow A. Damping of structural vibrations with piezoelectric materials and passive electrical networks. *J. Sound Vib.* **146**(1991) 243-268.
- [3] Wu S.Y. Piezoelectric shunts with a parallel R-L circuit for structural damping and vibration control. *In Proc. SPIE* **2720**(1996) 259-269.
- [4] Høgsberg J., Krenk S. Calibration of piezoelectric RL shunts with explicit residual mode correction. *J. Sound Vib.*, **386**(2017) 65-81
- [5] Toftekær J.F., Benjeddou A. Høgsberg J., Krenk S., Optimal piezoelectric RL shunt damping of plates with residual mode correction. *J. Intell. Mater. Syst. Struct.* Submitted, JIM-17-459 (2017).
- [6] Krenk S., Høgsberg J., Tuned resonant mass or inerter-based absorbers: Unified calibration with quasi-dynamic flexibility and inertia correction. *Proc. R. Soc. A*, **472**(2016) 20150718.
- [7] Trindade M., Benjeddou A. Effective electromechanical coupling coefficients of piezoelectric adaptive structures: critical evaluation and optimization. *Mech. Adv. Mater. Struct.* **16**(2009) 210-223.
- [8] Belloli A., Ermanni P. Optimum placement of piezoelectric ceramic modules for vibration suppression of highly constrained structures. *Smart Mater. Struct.* **16**(2007) 16621671.
- [9] Benjeddou A. Modal effective electromechanical coupling approximate evaluations and simplified analyses: Numerical and experimental assessments. *Acta Mech.* **225**(2014) 2721-2742.
- [10] Choi S. B., Kim H. S. Park J. S., Multi-mode vibration reduction of a CD-ROM drive base using a piezoelectric shunt circuit. *J. Sound Vib.* **300**(2007) 160-175.
- [11] Seba B., Ni J., Ni Lohmann, B. Vibration attenuation using a piezoelectric shunt circuit based on finite element method analysis. *Smart Mater. Struct.* **15**(2006) 509-517.
- [12] Bachmann F., Bergamini A. E. Ermanni P., Optimum piezoelectric patch positioning: A strain energy-based finite element approach. *J. Intell. Mater. Syst. Struct.* **23**(2012) 1575-1591.
- [13] Becker J., Fein O., Maess M., Gaul L. Finite element-based analysis of shunted piezoelectric structures for vibration damping *Comp. Struct.* **84**(2006) 2340-2350.
- [14] eFunda Portal *Lead Zirconate Titanate (PZT-5H)* (2017), (available: [http://www.efunda.com/materials/piezo/material\\_data/matdata\\_output.cfm?Material\\_ID=PZT-5H](http://www.efunda.com/materials/piezo/material_data/matdata_output.cfm?Material_ID=PZT-5H)).
- [15] Chevallier G., Benjeddou A. Couplage lectromcanique effectif dans les structures pizoelectriques composites. *Revue Comp. Matr. Avancs* **19**(2009) 239-264.

## Appendix: Plane stress-reduced piezoelectric coefficients

When a piezoceramic patch is dominated by in-plane shearless deformations, a good approximation of the material behaviour is given by the plane stress-reduced mechanical and electrical properties. Plane stress assumption yields no transverse stresses  $T_3 = T_4 = T_5 = 0$ , whereby (1) and (2) can be reduced to

$$\begin{Bmatrix} T_1 \\ T_2 \\ T_6 \end{Bmatrix} = \begin{bmatrix} \bar{c}_{11}^E & \bar{c}_{12}^E & 0 \\ \bar{c}_{12}^E & \bar{c}_{11}^E & 0 \\ 0 & 0 & c_{66}^E \end{bmatrix} \begin{Bmatrix} S_1 \\ S_2 \\ S_6 \end{Bmatrix} - \begin{Bmatrix} \bar{e}_{31} \\ \bar{e}_{31} \\ 0 \end{Bmatrix} E_3, \quad D_3 = \langle \bar{e}_{31} \quad \bar{e}_{31} \quad 0 \rangle \begin{Bmatrix} S_1 \\ S_2 \\ S_6 \end{Bmatrix} + \bar{e}_{33}^S E_3 \quad (31)$$

with the plane stress-reduced SC stiffness, coupling coefficients and dielectric constant

$$\bar{c}_{11}^E = c_{11}^E - \frac{(c_{13}^E)^2}{c_{33}^E}, \quad \bar{c}_{12}^E = c_{12}^E - \frac{(c_{13}^E)^2}{c_{33}^E}, \quad \bar{e}_{31} = e_{31} - e_{33} \frac{c_{13}^E}{c_{33}^E}, \quad \bar{e}_{33}^S = e_{33}^S + \frac{e_{33}^2}{c_{33}^E} \quad (32)$$

These plane stress-reduced properties are those implemented in the 2D FE-model [5].

## C2

Resonant piezoelectric shunt tuning based on the electric current and voltage response to pseudo-random vibration excitation

Johan Frederik Toftekær and Jan Høgsberg

*Proceedings of 9th ECCOMAS Thematic Conference on Smart Structures and Materials*

July 8-11, 2019, Paris, France



# RESONANT PIEZOELECTRIC SHUNT TUNING BASED ON THE ELECTRIC CURRENT AND VOLTAGE RESPONSE TO PSEUDO-RANDOM VIBRATION EXCITATION

JOHAN FREDERIK TOFTEKÆR\* AND JAN HØGSBERG\*

\*Department of Mechanical Engineering, Technical University of Denmark  
Nils Koppels Allé, Building 404, DK-2800 Kgs. Lyngby, Denmark  
e-mail: jotof@mek.dtu.dk, jhg@mek.dtu.dk

**Key words:** *RL* shunts, Piezoelectric damping, Structural dynamics, Experimental analysis, ANSYS®

**Abstract.** A tuning procedure for resonant piezoelectric shunt damping based on measurable experimental data is proposed. The procedure is derived from a proposed resonant shunt tuning method designed for the implementation in commercial finite element (FE) software, including the contribution from non-resonant vibration modes. It has been found that this procedure is robust and effective for vibration mitigation in both beam and plate structures. In the present procedure a pseudo-random excitation signal is imposed on a structure with attached piezoceramic patches, while the piezoelectric electrodes are respectively in short- or open circuit. In both cases a time record of respectively the electric current and voltage is measured with a high quality multimeter. A Fast-Fourier-Transform is then used on these time records in order to determine the electric current and voltage frequency response functions. Finally, the optimum resonant shunt inductances and resistances are determined from the corresponding modal properties, which are extracted from the two frequency response functions. The method is demonstrated for a free beam with two pairs of piezoceramic patches, one pair used for the vibration excitation and the other for vibration mitigation. The experimental results are found to be in good agreement with the results from a corresponding numerical model build up in the commercial FE-software ANSYS®.

## 1 INTRODUCTION

The concepts of resonant piezoelectric shunt damping origin from the work by Forward [1], in which the mechanical equivalence to an electric capacitance, resistance and inductance are presented. It is then suggested that the shunt inductance ( $L$ ) is tuned in order to neutralize the inherent capacitance of the piezoelectric material, whereby the damping introduced by the shunt resistance ( $R$ ) is maximized. A concrete procedure for the optimum tuning of the resonant  $LR$ -shunt circuit was subsequently proposed by Hagood and von Flotow [2]. The method assumes the structural response around a target resonant frequency to be sufficiently represented by the corresponding modal properties. The tuning formulas are thus derived from a representative two degrees of freedom coupled electromechanical system. In [2] the series shunt circuit is considered, while the parallel shunt circuit was suggested later by Wu [3]. Alternative methods for the precise series and parallel shunt tuning have been suggested subsequently [4, 5], all based on the modal approximation. In recent years several authors have discussed the influence from the non-resonant vibration modes on the structural response, which alternate the optimum piezoelectric shunt tuning [6, 7, 8]. In [9] the influence from the non-resonant modes was described by a flexibility and

an inertia correction terms and the influence on the optimum tuning of tuned mass and inerter-based absorbers was demonstrated. In [8] the equivalence to resonant piezoelectric shunt damping was presented and in [10] an alternative formulation suitable for implementation in commercial software was suggested. In the present work, it is the aim to demonstrate the latter method through experiments carried out on a free beam employed with two pairs of piezoceramic patches.

The experimental design with a free beam is chosen in order to achieve high correlation between the experimental and numerical results. Disparancies between numerical and experimental results have been encountered in numerous contributions [2, 3, 4], where one of the common uncertainties is associated with an inaccurate numerical or theoretical approximation of the actual boundary conditions of the experimental setup. This can be dealt with by updating the finite element (FE) model according to the experimental results as proposed in [11]. However, such a procedure can be rather cumbersome, hence the free beam is chosen in the present case.

## 2 NUMERICAL SHUNT TUNING

In the present section the optimum shunt tuning procedure presented in [10] is summarized and an alternative way of determining the effective electromechanical coupling coefficient (EMCC) presented, where the latter becomes useful when reformulating the tuning formulas for subsequent experimental implementation. Optimum tuning of one shunt circuit is considered, which however may be connected to a network of several piezoceramic patches glued on to a mechanical structure. The coupled vibration problem of a mechanical structure with interconnected and shunted piezoceramic patches may be written according to [10], as

$$\left( \begin{bmatrix} K^E & k_{me}^E \\ (k_{me}^E)^t & -\tilde{C}_p^{\epsilon^S} \end{bmatrix} - \omega^2 \begin{bmatrix} M & 0 \\ 0 & 0 \end{bmatrix} \right) \begin{Bmatrix} U \\ V \end{Bmatrix} = \begin{Bmatrix} 0 \\ -Q \end{Bmatrix} \quad (1)$$

where  $[K^E]$  is the elastic stiffness matrix of the structure with short circuit (SC) piezoceramic patch(es),  $[M]$  is the mass matrix,  $\{k_{me}^E\}$  the electromechanical coupling vector and  $\tilde{C}_p^{\epsilon^S}$  the resulting modified capacitance of the piezoceramic patch(es).

The vibration problem Eq. (1) is limited by two eigenvalue problems associated with, respectively, SC and open circuit (OC) piezoceramic patch electrodes. When having SC electrodes the voltage vanishes  $V = 0$  and the associated eigenvalue problem can be written as

$$([K^E] - \omega_j^2[M]) \{U\}_j = \{0\} \quad (2)$$

for a particular vibration mode  $j$  with circular frequency  $\omega_j$ . The second equation in Eq. (1) further provides the (sensed) modal charge

$$\tilde{Q}_j = -\{k_{me}^E\}^t \{U\}_j \quad (3)$$

When no current can flow between the interface electrodes, the piezoceramic patch(es) is(are) said to be in OC. Vanishing current implies that the charge is zero, whereby the corresponding eigenvalue problem follows from Eq. (1), with  $Q = 0$ , as

$$\left( [K^E] + \frac{1}{\tilde{C}_p^{\epsilon^S}} \{k_{me}^E\} \{k_{me}^E\}^t - \hat{\omega}_j^2[M] \right) \{\hat{U}\}_j = \{0\} \quad (4)$$

while the second equation of Eq. (1) provides an OC modal voltage given as

$$\tilde{V}_j = \frac{1}{\tilde{C}_p^{\epsilon^S}} \{k_{me}^E\}^t \{\hat{U}\}_j \quad (5)$$

Table 1: Numerical parallel and series shunt tuning to target vibration mode  $r$ .

Parallel ( $p$ )	Series ( $s$ )
$L_p = \frac{\kappa_r^2}{Q_r^2}$ , $R_p = \frac{\kappa_r^2 \omega_r}{Q_r^2} \sqrt{\frac{1}{2\kappa_r^2}}$	$L_s = \frac{\kappa_r^2}{Q_r^2(1 + \kappa_r^2)^2}$ , $R_s = \frac{\kappa_r^2 \omega_r}{Q_r^2} \sqrt{\frac{2\kappa_r^2}{(1 + \kappa_r^2)^3}}$

The authority of the piezoceramic patch(es) on a given vibration mode of the electromechanical structure is associated with the relative difference between the SC and OC modal strain energies and defined by the effective EMCC. The effective EMCC is for resonant vibration mode  $j = r$ , given as

$$\kappa_r^2 = \frac{\hat{\omega}_r^2 - \omega_r^2}{\omega_r^2} \quad (6)$$

Pre-multiplying Eq. (2) with  $\{\hat{U}\}_r^t$  and Eq. (4) with  $\{U\}_r^t$ , the terms involving  $[K^E]$  may be eliminated such that the effective EMCC alternatively can be expressed as

$$\kappa_r^2 = \frac{\{U\}_r^t \{k_{me}^E\} \{k_{me}^E\}^t \{\hat{U}\}_r}{\omega_r^2 \bar{C}^{\epsilon^S} \{U\}_r^t [M] \{\hat{U}\}_r} \quad (7)$$

Introducing the SC modal charge Eq. (3) and OC voltage Eq. (5), the effective EMCC Eq. (7) can be written as

$$\kappa_r^2 = \frac{\tilde{Q}_r \tilde{V}_r}{\omega_r^2 \{U\}_r^t [M] \{\hat{U}\}_r} = \frac{Q_r V_r}{\omega_r^2} \quad (8)$$

The latter expression in Eq. (8) follows by normalizing the modal charge and voltage from Eqs. (3) and (5) by the intermediate modal mass  $\tilde{m}_r = \{U\}_r^t [M] \{\hat{U}\}_r$  in the denominator of Eq. (8) as

$$Q_r = \frac{\tilde{Q}_r}{\sqrt{\tilde{m}_r}} \quad , \quad V_r = \frac{\tilde{V}_r}{\sqrt{\tilde{m}_r}} \quad (9)$$

In regard to experiments, the intermediate modal mass  $\tilde{m}_r$  may beneficially be determined from Eq. (8),

$$\tilde{m}_r = \frac{\tilde{Q}_r \tilde{V}_r}{\omega_r^2 \kappa_r^2} \quad (10)$$

In reality the intermediate modal mass  $\tilde{m}_r$  would be close to both the modal mass of the SC or OC electromechanical structure, since the corresponding mode shapes are almost identical and the mass distribution remains virtually unchanged.

In [10], a reduced order model was introduced in order to determine the optimum parallel and series resonant  $RL$  shunt tuning. The tuning formulas are provided in Table 1 for clarity, while the reader is referred to [10] for the extensive derivations. It is noted that the inertia effect from the non-resonant vibration modes on the shunt tuning is neglected according to [10].

The tuning formulas provided in Table 1 are favorable in terms of FE-analysis since the mode shapes and modal charge can be normalized in order to obtain unit modal masses as described in [10]. In terms of tuning based on experimental data it become beneficial to reformulate these tuning formulas as demonstrated subsequently in section 3.

### 3 EXPERIMENTAL SHUNT TUNING

In this section the resonant shunt tuning procedure in section 2 is reformulated to be dependent on measurable experimental data. The experimental procedure is very simple and consists of two steps. First, the electromechanical structure is excited by a pseudo-random excitation signal with a given frequency bandwidth and intensity, while the piezoceramic patch(es) are in SC condition. The SC condition is realized by connecting the interface electrodes of the piezoceramic patch(es) to a multimeter measuring the time record of the corresponding electric current  $I(t)$ . In the second step, a random excitation signal with the same frequency bandwidth and intensity is applied to the electromechanical structure with the piezoceramic patches in OC condition. The OC condition is realized by adjusting the multimeter to measure electric voltage  $V(t)$ , whereby an infinitely large resistance is imposed between the interface electrodes. From the measured current and voltage time records two frequency response functions (FRF) can be determined using a fast Fourier transform (FFT), from which the SC and OC frequencies and modal current and voltage amplitudes are read for each vibration mode in the analyzed frequency band.

The modal voltage is found directly as the resonant peaks  $\tilde{V}_j = \tilde{V}(\hat{\omega}_j)$  in the generated frequency response, while the measured electric current time response  $I(t)$  is used to determine the corresponding charge  $\tilde{Q}(t)$ . The electric current is given as the time derivative ( $\dot{(\cdot)} = d/dt$ ) of the electric charge

$$I(t) = \dot{Q}(t) \quad (11)$$

Assuming harmonic solutions, the electric current and charge time functions may be expressed as

$$I(t) = \tilde{I}e^{i\omega t} \quad , \quad Q(t) = \tilde{Q}e^{i\omega t} \quad (12)$$

with the complex amplitudes  $\tilde{I}$  and  $\tilde{Q}$ . Inserting (12) into (11) the relationship between the complex amplitudes of the current and charge may be written as

$$\tilde{I} = i\omega\tilde{Q} \quad (13)$$

Finally the modal charge are found as the resonant peaks  $\tilde{Q}_j = \tilde{Q}(\omega_j)$  of the corresponding FRF.

The shunt tuning then follows by determining the effective EMCC Eq. (6) and the intermediate modal mass from Eq. (10), while the shunt tuning formulas in Table 1 can be reformulated by inserting  $\kappa_r^2$  from Eq. (8) in the tuning formulas. For the parallel inductance tuning this gives

$$L_p = \frac{|V_r|}{|Q_r|\omega_r^2} = \frac{|\tilde{V}_r|}{|\tilde{Q}_r|\omega_r^2} \quad (14)$$

which is seen to be independent of any normalization of the modal charge and voltage and also does not require determination of the OC frequency and effective EMCC. The series inductance tuning and tuning of the optimum resistances follow similarly from inserting the effective EMCC  $\kappa_r^2$  (Eq. (8)) into the tuning formulas provided in Table 1. The reformulated tuning formulas for the experimental  $RL$  shunt design are provided in Table 2 for both the parallel and series shunt circuits.

### 4 SYNTHETIC INDUCTOR

In the subsequent experimental verification of the tuning procedure presented in section 3, a so-called synthetic inductor is used to emulate the required shunt inductance. It consists of an Antoniou circuit [12] with the modification proposed in [13]. The circuit diagram of the modified Antoniou circuit and the prototype of the synthetic inductor used in the experiment can be seen in Figure 1.

Table 2: Experimental parallel and series shunt tuning to target vibration mode  $r$ .

Parallel ( $p$ )		Series ( $s$ )	
$L_p = \frac{ \tilde{V}_r }{ \tilde{Q}_r \omega_r^2}$	$R_p = \frac{ \tilde{V}_r }{ \tilde{Q}_r \omega_r} \sqrt{\frac{1}{2\kappa_r^2}}$	$L_s = \frac{ \tilde{V}_r }{ \tilde{Q}_r \hat{\omega}_r^2 \hat{\omega}_r^2} \omega_r^2$	$R_s = \frac{ \tilde{V}_r }{ \tilde{Q}_r \hat{\omega}_r \hat{\omega}_r^2} \omega_r^2 \sqrt{2\kappa_r^2}$

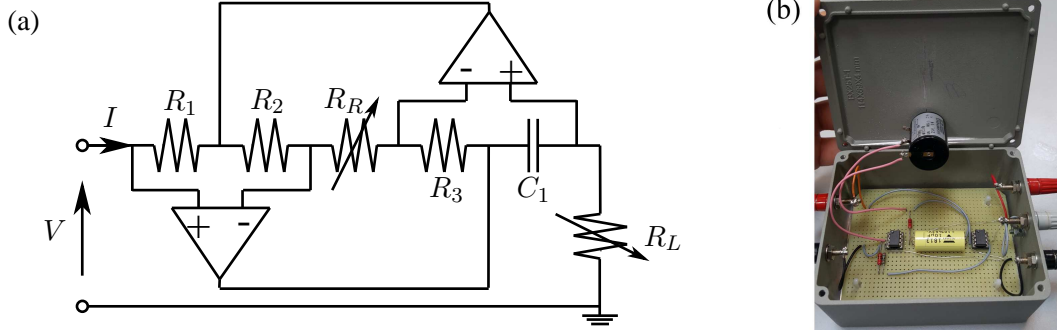


Figure 1: Synthetic inductor, circuit diagram (a) and prototype (b).

Details about the original Antoniou circuit can be found in [14], while the modification is given by the addition of the variable resistance  $R_R$ , see Figure 1(a). The latter permits the addition of negative resistance to the circuit impedance, added in order to compensate for eventual parasitic losses. The original Antoniou circuit was designed in order to emulate the effect of an inductance by keeping a constant current to voltage relationship at the circuit terminal defined as

$$V(t) = L\dot{I}(t) \quad (15)$$

Assuming harmonic solutions, the electric current may be expressed as in Eq. (12a) with a similar representation for the voltage,

$$V(t) = \tilde{V}e^{i\omega t} \quad (16)$$

Inserting Eqs. (12a) and (16) into Eq. (15) the emulated inductance can be defined as

$$L = \frac{|\tilde{V}|}{\omega|\tilde{I}|} \quad (17)$$

Analyzing the circuit diagram Figure 1(a), it may thus be found that the emulated inductance is given as

$$L = \frac{C_1 R_1 R_3}{R_2} R_L \quad (18)$$

The full effective impedance of the modified Anoniou circuit can further be determined as

$$Z = i\omega \frac{C_1 R_1 R_3}{R_2} R_L - \frac{R_1}{R_2} R_R \quad (19)$$

which is seen to correspond to the impedance of an inductance connected in series with a negative resistance. The properties of the constant electronic components are given by  $R_1 = 2\text{k}\Omega$ ,  $R_2 = 1\text{k}\Omega$ ,

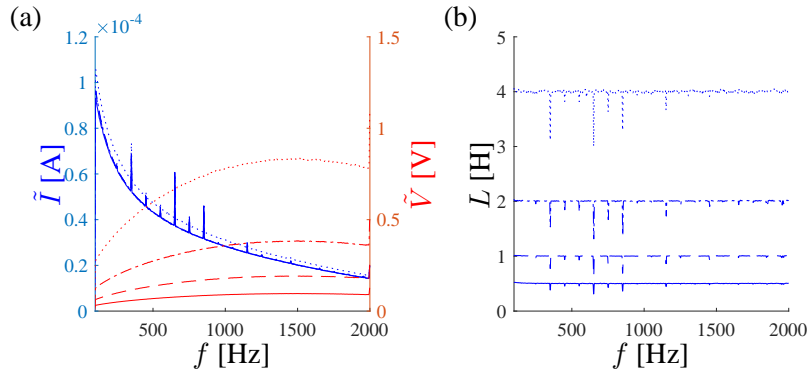


Figure 2: Verification of synthetic inductor (a) FRF for the current and voltage and (b) the corresponding emulated inductance value, for  $R_L = 25\Omega$  (—),  $50\Omega$  (---),  $100\Omega$  (-.-.),  $200\Omega$  (.....).

$R_3 = 1\text{k}\Omega$  and  $C_1 = 10\mu\text{F}$ , whereby the inductance and negative resistance can be determined by constant factors multiplied by respectively the variable resistances  $R_L$  and  $R_R$  ( $0 - 1\text{k}\Omega$ ), as

$$L = (0.02\text{H}/\Omega)R_L \quad , \quad R = -2R_R \quad (20)$$

In order to verify the analytic expression Eq. (20a) for the emulated inductance, the terminal of the synthetic inductor is excited by a pseudo-random voltage signal for different  $R_L$  values, while the resistance  $R_R$  is kept constant to zero. The corresponding electric current time record is then measured with a high quality multimeter connected in series with the synthetic inductor. Finally, an FFT is used on the voltage and current time records in order to obtain the corresponding FRFs. In Figure 2(a) the FRFs corresponding to  $R_L$  values of  $25\Omega$ ,  $50\Omega$ ,  $100\Omega$  and  $200\Omega$  are provided, while the corresponding emulated inductance values determined from Eq. (17) are shown in Figure 2(b). It is seen that the input voltage signal is increased for the tests with larger  $R_L$ -values, in order to minimize the effect of the electric hums that are clearly visible in the FRF of the electric current. Disregarding these electric hums, it is seen from Figure 2(b) that the emulated inductance values agree well with the values predicted from Eq. (20a) and are almost constant in the analyzed frequency band.

The synthetic inductor is further tested at higher  $R_L$  values of  $400\Omega$ ,  $800\Omega$ ,  $1600\Omega$  and  $3200\Omega$  for which the FRFs of the current and voltage and corresponding emulated inductance can be seen in Figure 3. Again, the electric hums are clearly apparent in the FRF of the current and corresponding emulated inductance. Again, disregarding this noise, constant emulated inductance values predicted by Eq. (20a) are observed in the considered frequency band, except for the case of  $R_L = 3200\Omega$  where a slight decrease in the emulated inductance is noted at higher frequencies. This may indicate that the emulated inductance becomes slightly non-linear for large  $R_L$  values at high frequencies. However, larger  $R_L$  and corresponding inductance is only relevant for piezoelectric shunt tuning to low frequent vibrations, since the optimum inductance tuning is inversely proportional to the target resonant frequency, see Table 2. It is thus verified that Eq. (20a) precisely predicts the emulated inductance of the synthetic inductor.

## 5 EXPERIMENTAL VERIFICATION

In this section, the optimum piezoelectric shunt tuning to a free beam with two pairs of piezoceramic patches is determined according to the tuning procedure presented in section 3. The free beam and the position of the two piezoceramic patch pairs can be seen in Figure 4, while the exact dimensions and

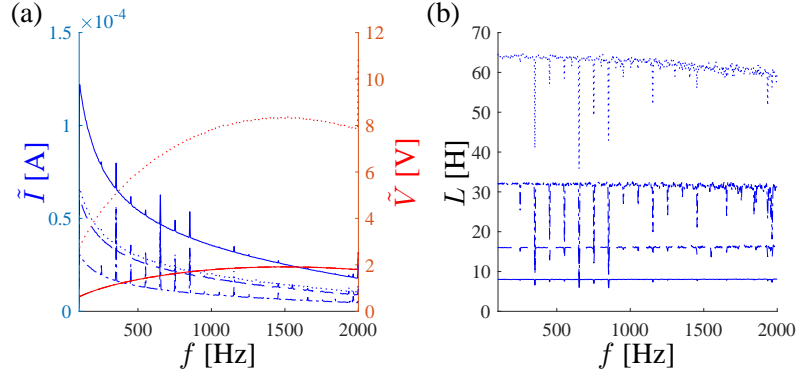


Figure 3: Verification of synthetic inductor (a) FRF for the current and voltage and (b) the corresponding emulated inductance value, for  $R_L = 400\Omega$ (—),  $800\Omega$ (- - -),  $1600\Omega$ (- · - ·),  $3200\Omega$ ( · · · ·).

Table 3: Dimensions and material properties for free beam and piezoceramic patches.

	Beam		Piezoceramic patches NCE51 (CTS)			
Length (mm)	$l$	260	$l_p$	30	Center patch to center beam	
Width (mm)	$w$	30	$w_p$	30	(mm)	
Thickness (mm)	$t$	2	$t_p$	1	$x_p$	22
Density (kg/m <sup>3</sup> )	$\rho$	2710	$\rho_p$	7850	Stress piezoelectric coefficient	
Young's Modulus (GPa)	$E$	71	Stiffness Components (GPa)		(10 <sup>-12</sup> m/V)	
Poisson's ratio (-)	$\nu$	0.33	$C_{11}^E, C_{22}^E$	134	$e_{31}, e_{32}$	-6.06
			$C_{12}^E$	88.9	$e_{33}$	17.2
			$C_{13}^E, C_{23}^E$	90.9	$e_{24}, e_{15}$	13.7
			$C_{33}^E$	121	Relative permittivity*	
			$C_{44}^E, C_{55}^E$	20.5	$\epsilon_{11}^p, \epsilon_{22}^p$	906 $\epsilon_0$
			$C_{66}^E$	22.4	$\epsilon_{33}^p$	823 $\epsilon_0$

\*Reference vacuum permittivity  $\epsilon_0 = 8.854 \times 10^{-12}$ F/m

material properties of the beam and piezoceramic patches are provided in Table 3. It is noted that the piezoceramic patches of each patch pair are oppositely poled and connected in series. As indicated in Figure 4 the left piezoceramic patch pair is used for vibration excitation, while the right patch pair mitigates vibrations by connecting it to an optimally tuned resonant shunt.

The experimental setup can also be seen in Figure 4, where the left piezoceramic patch pair is connected to a power amplifier, while the right patch pair is connected to a multimeter. Both power amplifier and multimeter are connected to a PC used for data acquisition. A Laser Doppler Vibrometer is used to measure the dynamic response of the free beam.

Following the steps presented in section 3 a pseudo-random voltage excitation signal is imposed between the interface electrodes of the left piezoceramic patch pair, while the right patch pair is connected to a multimeter set to measure respectively current, whereby the right patch pair is in its SC condition, and voltage corresponding to the OC condition. The bandwidth of the pseudo-random excitation signal is set to 2kHz and the sample rate of the multimeter to 250 $\mu$ s. The tip velocity is further measured by the

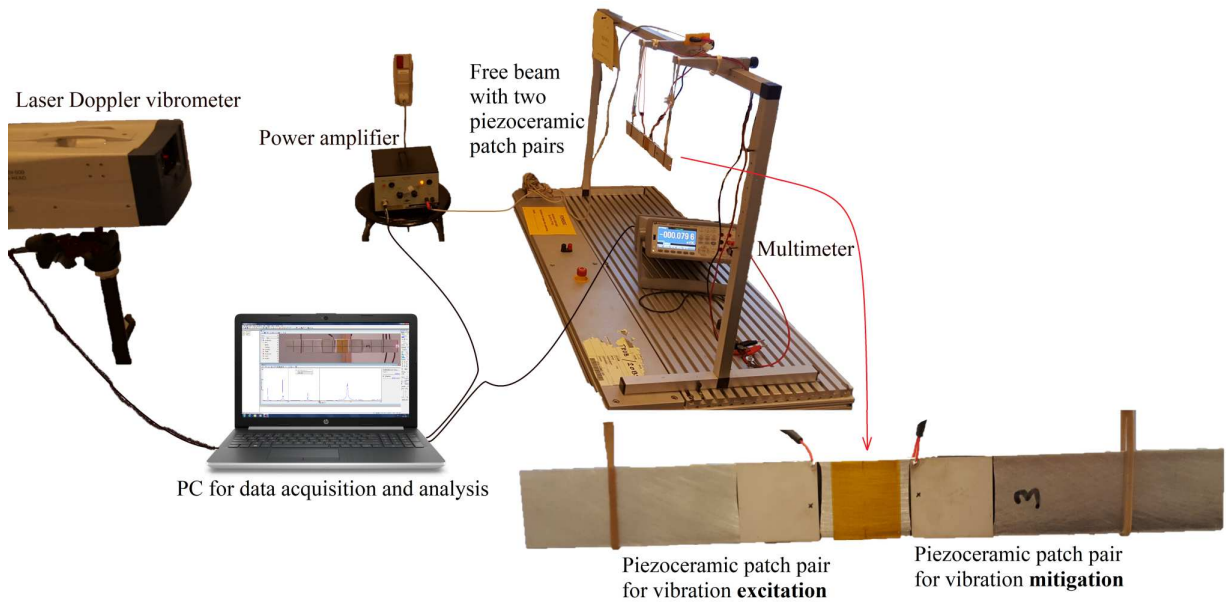


Figure 4: Free beam with two pairs of piezoceramic patches, experimental setup.

Laser Doppler Vibrometer in order to compare the mechanical response of the free beam and the electric response of the right piezoceramic patch pair. An FFT is performed on both mechanical and electrical time records, whereby the FRFs for, respectively, the tip displacements (determined from the tip velocity) in SC and OC condition and the electric current and voltage are obtained and shown in Figure 5.

It can be seen from Figure 5 that the mechanical and electrical responses correspond very well and that four resonant vibration modes appear in the investigated frequency band. In order to determine the optimum piezoelectric shunt tuning, only the FRFs for the electric charge and voltage in Figure 5(b) are considered, from which the SC and OC natural frequencies and modal charge and voltage are determined and provided in Table 4. The optimum shunt tuning then follows by the tuning formulas provided in Table 2 giving the optimum parallel and series shunt tuning listed in Table 4. For comparison, the free beam with the two piezoceramic patch pairs has been modeled in ANSYS®, where the SC and OC eigenvalue problems have been evaluated in order to determine the SC and OC frequencies and modal charge and voltage, which are also provided in Table 4. The FE-model used in ANSYS® consist of  $225 \times 8 \times 4$  SOLID186 3D elements discretizing the beam and  $100 \times 8 \times 2$  SOLID226 3D electromechanical elements discretizing each of the four piezoceramic patches. Finally, the equipotential condition is enforced for each piezoelectric electrode by applying a coupling constraint to the concerned electrical dofs, while the opposite polarization is obtained by using opposite signs for the stress piezoelectric coefficients in each piezoceramic patch pair.

It can be seen from Table 4 that there is a good correlation between the experimental and numerical SC and OC frequencies, except for the fourth torsional vibration mode predicted by the ANSYS® model, which can not be excited by the driving force from the left piezoceramic patch pair. The use of the left piezoceramic patch pair as the driving force for the vibrations means that only the flexural vibration modes are easily activated. Furthermore, the position of the patch pairs also influences how well each vibration mode may be sounded and damped. The mode shapes corresponding to the four flexural resonant frequencies in Table 4 and based on the measurement with the Laser Doppler Vibrometer can be

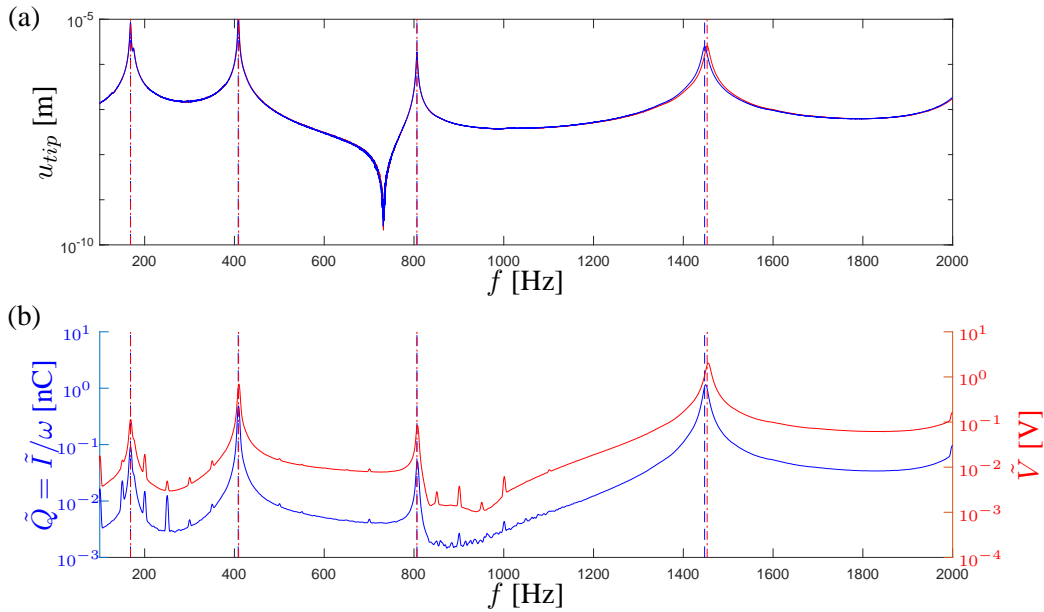


Figure 5: FRF for (a) the tip displacement and (b) the electric charge and voltage with respectively SC (blue line) and OC (red line) piezoceramic patch electrodes.

Table 4: Frequencies, effective EMCC, modal charge and voltage and optimum shunt tuning to the resonant vibration modes between 0 – 2kHz

Mode	Model	$f$ [Hz]	$\hat{f}$ [Hz]	$\kappa_r^2$ [%]	$Q_r$ [mC]	$V_r$ [MV]	$L_p$ [H]	$R_p$ [k $\Omega$ ]	$L_s$ [H]	$R_s$ [k $\Omega$ ]
1 Flex	ANS	170.9	171.4	0.52	6.618	0.907	118.9	1251	117.6	12.93
	Exp	168.5	169.0	0.58	7.242	0.899	110.7	1088	109.4	12.52
2 Flex	ANS	409.1	410.1	0.50	15.52	2.141	20.88	535.2	20.67	5.341
	Exp	409.3	409.8	0.24	10.38	1.522	22.18	825.3	22.07	3.928
3 Flex	ANS	813.5	813.7	0.03	7.224	0.992	5.256	1147	5.253	0.629
	Exp	807.8	807.8	0.02*	5.506	0.936	6.598	1674	6.532	0.670
4 Tors	ANS	958.6	958.6	0.00	-	-	-	-	-	-
	Exp	-	-	-	-	-	-	-	-	-
5 Flex	ANS	1446.6	1454.4	1.07	80.05	11.08	1.675	103.9	1.640	2.195
	Exp	1449.6	1455.4	0.81	61.70	10.89	2.129	152.3	2.095	2.438

\* Effective EMCC based on frequencies determined from the FRF for the tip displacements, see Figure 5(a).

seen in Figure 6. The location of the piezoceramic patches are here indicated by the red arrows, and it can thus be seen that the third vibration mode is both hardly excited and damped since the two patch pairs are located close to a nodal point of the corresponding mode shape in Figure 6(c). This is also apparent by the corresponding effective EMCC in Table 4, which is close to zero. Oppositely, the largest effective EMCC is obtained for the fourth flexural vibration mode, for which it can be seen that the piezoceramic patches are located near a position of maximum curvature (Figure 6(d)) and therefore have good authority on the corresponding vibrations. The position of the piezoceramic patches with respect to the first and second vibration modes in Figure 6(a,b) are seen to be moderately good, also indicated

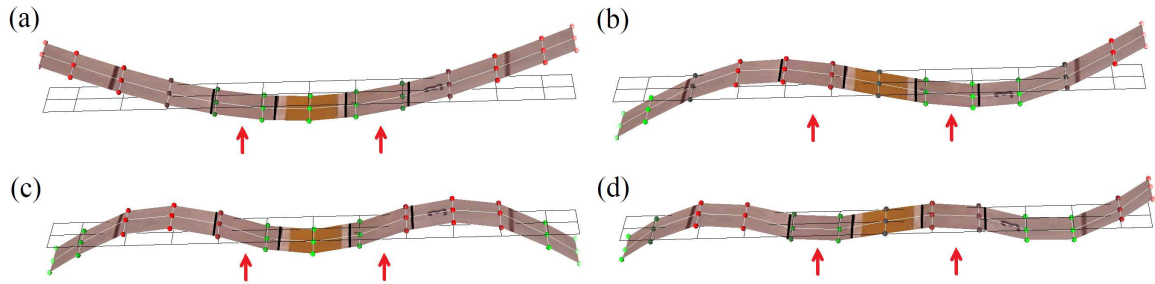


Figure 6: First four flexural mode shapes (a)-(d) of the free beam with two piezoceramic patch pairs located as indicated by the red arrows.

by the effective EMCCs in Table 4. Common for all the effective EMCCs is that there is a significant relative deviation between the numerical and experimental results. This may be explained by several uncertainties associated with the experimental setup, for instance the gluing of the piezoceramic patches to the beam, the actual electromechanical properties and eventual hysteretic behavior of the piezoceramic material, which is not considered in the tuning and numerical FE-model. Finally, it can be seen from Table 4 that there is good correlation between the numerical and experimental modal charge and voltage and the corresponding optimum parallel and series shunt tuning. The normalized modal charge and voltage are for the experiment determined from the measured modal charge and voltage amplitudes with Eq. (9), in which the intermediate modal mass is equated with Eq. (10).

It is now analyzed how well the optimum piezoelectric shunt tuning performs, when each individual shunt circuit for the four flexural vibration modes are wired in series to the right piezoceramic patch pair. The optimum inductance is emulated by the synthetic inductor described in section 4, which is further connected in series with a variable resistor. It is found that the optimum inductance values must be slightly altered in order to obtain the most optimum damping properties. The optimum inductance values are  $L_1 = 128\text{H}$ ,  $L_2 = 24.2\text{H}$ ,  $L_3 = 6.6\text{H}$  and  $L_5 = 2.0\text{H}$ . The deviation between these values and the series tuning provided in Table 4 may be due to the neglect of structural damping in the tuning formulas and the fact that the forcing from the left piezoceramic patch pair does not act as an ideal modal load. However, the deviations are relatively small, in particularly for the fourth flexural vibration mode with the largest effective EMCC. Regarding the resistance tuning to the first three flexural vibration modes, it is found that the parasitic loss in the synthetic inductor seems to exceed the optimum resistance tuning, even when negative resistance is added to the system through  $R_R$ . For the shunt circuit tuned to the fourth flexural vibration mode, the variable resistance is set to  $R_4 = 2.4\text{k}\Omega$ , approximately equal to the optimum series tuning in Table 4. With the respective implementation of these four shunt circuits the corresponding FRFs for both the tip displacements and electric voltages are determined using the FFT on the corresponding time records to a pseudo-random vibration excitation with the same frequency bandwidth and intensity as used previously. The FRFs can be seen in Figure 7.

It can be seen from Figure 7(a)-(d) that considerable amplitude reduction is obtained around each of the four flexural resonant frequencies when implementing the respective resonant shunt circuits. In particular, flexural vibration mode 4 in Figure 7(d) is seen to be highly damped and an almost flat plateau around the corresponding resonant frequency is obtained. The lowest vibration reduction is found for mode 3 in Figure 7(c), as expected due to the corresponding insignificant electromechanical coupling. Looking at the voltage responses in Figure 7(e)-(h), it can be seen that the damper response is increased around the resonant frequencies when implementing the resonant shunt circuits. This may be interpreted

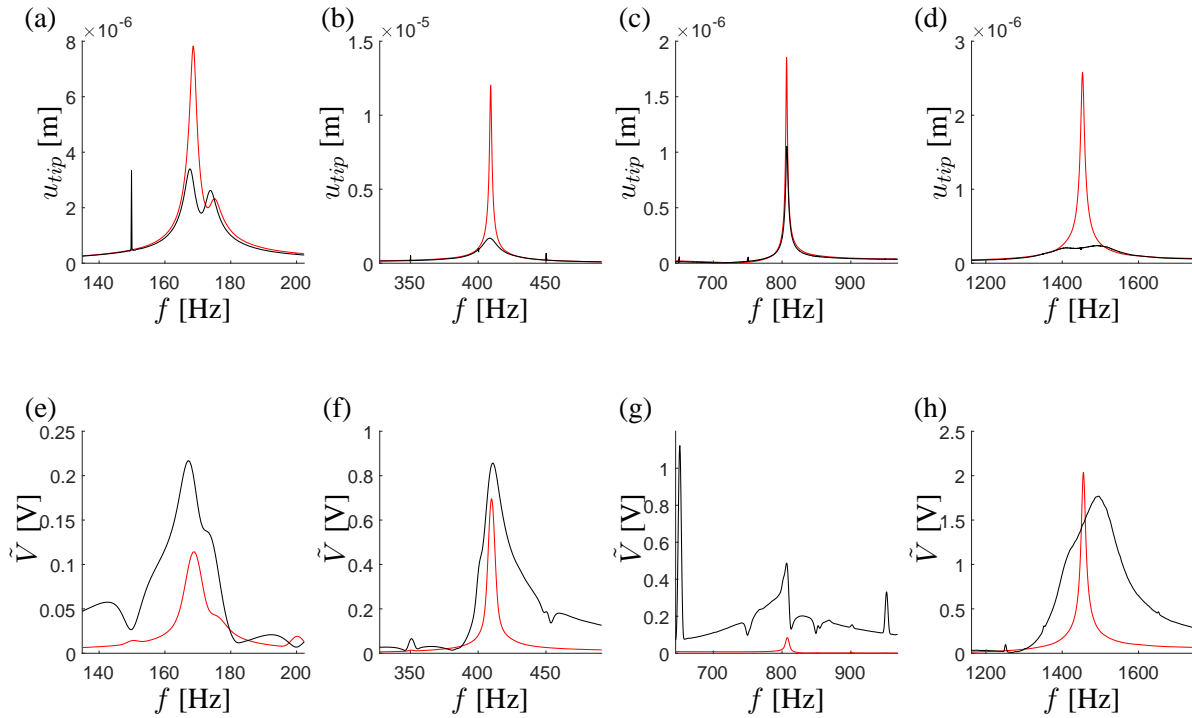


Figure 7: FRF for (a)-(d) the tip displacements and (e)-(f) shunt voltage, for OC (—) and optimally shunted to respectively flexural mode 1-4 (—) piezoceramic patches.

as an increase in the amount of energy dissipated by the shunt resistance. For the fourth flexural vibration mode in Figure 7(h) an almost flat plateau around the resonant frequency for the voltage is obtained, which agrees well with the theoretical damper response of the tuned piezoelectric shunt damper [10].

Although small deviations between the optimum and implemented shunt tuning has been encountered, the experimental shunt tuning method presented in section 3 has proven to be accurate and easy to implement, as the optimum shunt tuning to any resonant vibration mode in a given frequency band may be determined from only current and voltage responses to a pseudo-random vibration excitation.

## 6 CONCLUSIONS

A piezoelectric shunt tuning method based on measurable experimental data has been proposed. The procedure consists in imposing pseudo-random vibrations to a mechanical structure while the electric current and voltage responses are measured between the electrodes of an attached piezoelectric domain. A FFT is then used on the electric time records to obtain the FRF for the corresponding charge and voltage. The SC and OC natural frequencies and modal charge and voltage may finally be determined for each vibration mode in the analyzed frequency band, and the corresponding shunt circuit components optimally tuned. The method is verified by the analysis of a free beam with two pairs of piezoceramic patches, one pair used to excite the structure, while the second pair is connected to a shunt circuit optimally tuned to a target resonant vibration mode. The FRF for the electric charge and voltage have

been determined and the optimum shunt tuning evaluated for the first four flexural vibration modes of the free beam. Finally, it is found that the obtained optimum shunt tuning values are very close to the shunt tuning, which delivers the most substantial damping to the structure around the target resonant frequencies. The proposed method is beneficial as the necessary tuning parameters are determined from two FRF obtained by imposing pseudo-random vibrations to the investigated structure. Furthermore, the inductance tuning is independent of the relative difference between the SC and OC frequencies, which may be hard to determine. Instead, it relies on the ratio between the modal voltage and charge.

## REFERENCES

- [1] Forward, R.L. Electronic damping of vibrations in optical structures. *Appl. Opt.* **18**(1979) 690-697.
- [2] Hagood, N.W. and von Flotow, A. Damping of structural vibrations with piezoelectric materials and passive electrical networks. *J. Sound Vib.* **146**(1991) 243-268.
- [3] Wu, S.Y. Piezoelectric shunts with a parallel R-L circuit for structural damping and vibration control. *In Proc. SPIE* **2720**(1996) 259-269.
- [4] Thomas, O., Ducarne, J. and Deü, J.-F. Performance of piezoelectric shunts for vibration reduction. *Smart Mater. Struct.* **21**(2012) 015008.
- [5] Soltani, P., Kerschen, G. Tondreau, G. and Deraemaeker, A. A Piezoelectric vibration damping using resonant shunt circuits: an exact solution. *Smart Mater. Struct.*, **23**(2014) 125014.
- [6] Berardengo, M., Thomas, O. Giraud-Audine C, Manzoni S., Improved resistive shunt by means of negative capacitance: new circuit, performances and multi-mode control. *Smart Mater. Struct.* **25**(2016) 075033.
- [7] Gardonio, P. and Casagrande, D. Shunted piezoelectric patch vibration absorber on two-dimensional thin structure: tuning considerations. *J. Sound Vib.* **395**(2017) 2647.
- [8] Høgsberg, J. and Krenk, S. Calibration of piezoelectric RL shunts with explicit residual mode correction. *J. Sound Vib.*, **386**(2017) 65-81
- [9] Krenk, S. and Høgsberg, J. Tuned resonant mass or inerter-based absorbers: Unified calibration with quasi-dynamic flexibility and inertia correction. *Proc. R. Soc. A*, **472**(2016) 20150718.
- [10] Toftekær, J.F., Benjeddou, A. and Høgsberg, J. General numerical implementation of a new piezoelectric shunt tuning method based on the effective electromechanical coupling coefficient. *Mech. Adv. Mater. Struct.* (2019).
- [11] Hamdi, M., Ghanmi, S. Benjeddou, A. and Nasri, R., Robust electromechanical finite element updating for piezoelectric structures effective coupling prediction, *J. Intell. Mater. Syst. Struct.* **25**(2014) 137-154.
- [12] Antoniou, A. Realization of Gytrators Using Operational Amplifiers, and their Use in RC-Active-Network Synthesis. *In Proc. of IEEE* **116**(1969) 1838-1850
- [13] Von Wangeheim, L. Modification of the classical GIC structure and its application to RC-oscillators. *Electron. lett.* **32**(1)(1996) 6-8
- [14] Sedra, A.S. and Smith, K.C. *Microelectronic Circuits*, 5th Edition, Oxford University Press (2007).



DTU Mechanical Engineering  
Section of Solid Mechanics  
Technical University of Denmark

Nils Koppels Allé, Bld. 404  
DK-2800 Kgs. Lyngby  
Denmark  
Tlf.: +45 4525 4250  
Fax: +45 4525 1961

[www.mek.dtu.dk](http://www.mek.dtu.dk)

September 2019

ISBN: 978-87-7475-583-8

**DCAMM**  
**Danish Center for Applied Mathematics**  
**and Mechanics**

Nils Koppels Allé, Bld. 404  
DK-2800 Kgs. Lyngby  
Denmark  
Phone (+45) 4525 4250  
Fax (+45) 4525 1961

[www.dcammm.dk](http://www.dcammm.dk)

DCAMM Special Report No. S269

ISSN: 0903-1685